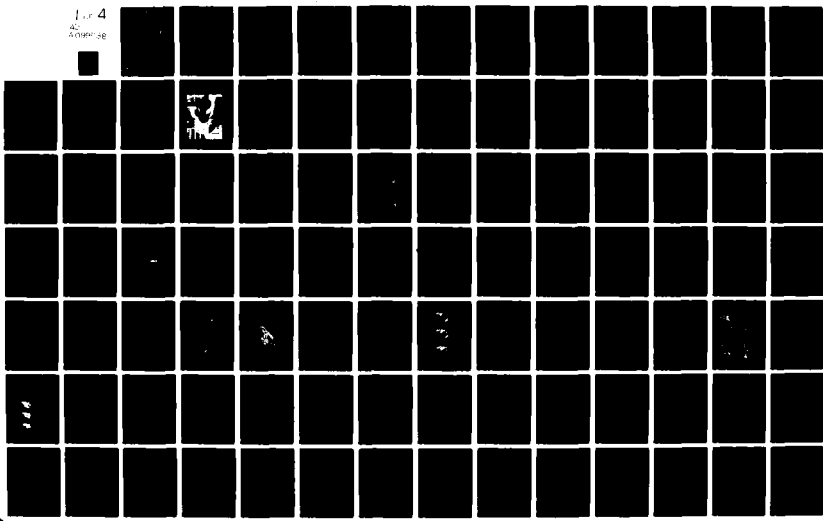


AD-A099 998 SRI INTERNATIONAL MENLO PARK CA
PROCEEDINGS OF THE SUMMER EQUATORIAL EXPERIMENT DATA REVIEW MEE--ETC(U)
NOV 80 D R McDANIEL F/G 22/2
DNA001-78-C-0379

UNCLASSIFIED NL

DNA-5528P

For 4
etc
McDaniel



5U
6
ADA099998

LEVEL IV

12-26-11
DNA 5528P

PROCEEDINGS OF THE SUMMER EQUATORIAL EXPERIMENT DATA REVIEW MEETING, 18 MARCH 1980,

Dan R. McDaniel Compiler

SRI International

333 Ravenswood Avenue

Menlo Park, California 94025

1 November 1980

12323

Proceedings

DTIC
ELECTRONIC
S JUN 10 1981
C

115
CONTRACT No. DNA 001-78-C-0379

APPROVED FOR PUBLIC RELEASE;
DISTRIBUTION UNLIMITED.

THIS WORK SPONSORED BY THE DEFENSE NUCLEAR AGENCY
UNDER RDT&E RMSS CODE B322078462 125AAXHK63803 H2590D.

DTIC FILE COPY

Prepared for
Director
DEFENSE NUCLEAR AGENCY
Washington, D. C. 20305

816 10 015

Destroy this report when it is no longer
needed. Do not return to sender.

PLEASE NOTIFY THE DEFENSE NUCLEAR AGENCY,
ATTN: STTI, WASHINGTON, D.C. 20305, IF
YOUR ADDRESS IS INCORRECT, IF YOU WISH TO
BE DELETED FROM THE DISTRIBUTION LIST, OR
IF THE ADDRESSEE IS NO LONGER EMPLOYED BY
YOUR ORGANIZATION.



UNCLASSIFIED

SECURITY CLASSIFICATION OF THIS PAGE (When Data Entered)

REPORT DOCUMENTATION PAGE		READ INSTRUCTIONS BEFORE COMPLETING FORM
1. REPORT NUMBER DNA 5528P	2. GOVT ACCESSION NO. <i>AD-A099 998</i>	3. RECIPIENT'S CATALOG NUMBER
4. TITLE (and Subtitle) PROCEEDINGS OF THE SUMMER EQUATORIAL EXPERIMENT DATA REVIEW MEETING, 18 MARCH 1980	5. TYPE OF REPORT & PERIOD COVERED Proceedings	
7. AUTHOR(s) Dan R. McDaniel, Compiler	6. PERFORMING ORG. REPORT NUMBER SRI Project 7745	
9. PERFORMING ORGANIZATION NAME AND ADDRESS SRI International 333 Ravenswood Avenue Menlo Park, California 94025	10. PROGRAM ELEMENT, PROJECT, TASK AREA & WORK UNIT NUMBERS Subtask I25AAXHX638-03	
11. CONTROLLING OFFICE NAME AND ADDRESS Director Defense Nuclear Agency Washington, D.C. 20305	12. REPORT DATE 1 November 1980	
14. MONITORING AGENCY NAME & ADDRESS (if different from Controlling Office)	13. NUMBER OF PAGES 326	
	15. SECURITY CLASS (of this report) UNCLASSIFIED	
	15a. DECLASSIFICATION/DOWNGRADING SCHEDULE	
16. DISTRIBUTION STATEMENT (of this Report) Approved for public release; distribution unlimited.		
17. DISTRIBUTION STATEMENT (of the abstract entered in Block 20, if different from Report)		
18. SUPPLEMENTARY NOTES This work sponsored by the Defense Nuclear Agency under RDT&E RMSS Code B322078462 I25AAXHX63803 H2590D.		
19. KEY WORDS (Continue on reverse side if necessary and identify by block number) Equatorial Ionosphere Spread F Electron Density Mass Spectroscopy	Electric-Field Measurements Incoherent Scatter Radio-Frequency Beacons Field-Aligned Structure	
20. ABSTRACT (Continue on reverse side if necessary and identify by block number) A rocket-borne probe experiment was conducted at Kwajalein Atoll in August 1979. The probes were launched into nighttime spread F to penetrate a plume or depleted region. The probe payloads carried a pair of electron density probes, an E-field sensor, an ion mass spectrometer, and a four-frequency RF beacon. Two probes were launched: the first probe was successful even though the C-band tracking beacon failed, and in the second probe, -		

DD FORM 1 JAN 73 1473 / EDITION OF 1 NOV 65 IS OBSOLETE

UNCLASSIFIED

SECURITY CLASSIFICATION OF THIS PAGE (When Data Entered)

UNCLASSIFIED

SECURITY CLASSIFICATION OF THIS PAGE(When Data Entered)

L ✓ the rf-beacon experiment was unsuccessful because the payload and rocket second stage failed to separate. These proceedings report the results of data analysis through June 1980.

Accession For	
NTIS GRA&I	<input checked="" type="checkbox"/>
DTIC TAB	<input type="checkbox"/>
Unannounced	<input type="checkbox"/>
Justification	
By _____	
Distribution/	
Availability Codes	
Dist	Avn - Snd -
A	Sp - ml

UNCLASSIFIED

SECURITY CLASSIFICATION OF THIS PAGE(When Data Entered)

TABLE OF CONTENTS

	<u>Page</u>
INTRODUCTION	3
ROCKET RF-BEACON EXPERIMENT FOR THE SUMMER 1979 KWAJALEIN CAMPAIGN, J. Petriceks	9
THE PULSED PLASMA-PROBE EXPERIMENT: IN-SITU MEASUREMENTS OF ELECTRON DENSITY, TEMPERATURE, AND DENSITY FLUCTUATION OF POWER SPECTRA, E. Szuszczewicz, J. Holmes	33
ALTAIR RADAR MEASUREMENTS IN SUPPORT OF THE PLUMEX ROCKET CAMPAIGN, R. Tsunoda	51
OPTICAL STUDIES IN SUPPORT OF THE JULY 1979 KWAJALEIN EQUATORIAL SPREAD-F CAMPAIGN, D. Sipler, M. Biondi, R. Hake	73
A COMPARATIVE ANALYSIS OF EQUATORIAL IRREGULARITY STRUCTURES AS MEASURED BY WIDEBAND, AE-E, AND IN-SITU ROCKET PROBES, C. Rino, R. Livingston, J. Petriceks	97
PLASMA-DENSITY AND ELECTRIC-FIELD MEASUREMENTS MADE DURING THE PLUMEX I ROCKET FLIGHT, K. Baker, J. Ulwick, L. Jensen, M. Kelley, R. Pfaff, J. Petriceks	137
PLUMEX I--COINCIDENT RADAR AND ROCKET OBSERVATIONS OF EQUATORIAL SPREAD F, E. Szuszczewicz, R. Tsunoda, R. Narcisi, J. Holmes	181
PLUMEX II--A SECOND SET OF COINCIDENT RADAR AND ROCKET OBSERVATIONS OF EQUATORIAL SPREAD F, E. Szuszczewicz, R. Tsunoda, R. Narcisi, J. Holmes	195
BACKSCATTER MEASUREMENTS OF 11-cm EQUATORIAL SPREAD-F IRREGULARITIES, R. Tsunoda	211
ON THE GENERATION AND GROWTH OF EQUATORIAL BACKSCATTER PLUMES, R. Tsunoda, B. White	227
A THEORETICAL EXPLANATION FOR 11-cm IRREGULARITIES DURING EQUATORIAL SPREAD F, J. Huba, S. Ossakow	247
NUMERICAL SIMULATIONS OF EQUATORIAL SPREAD F, USING ALTAIR INCOHERENT- BACKSCATTER-MEASURED ELECTRON-DENSITY PROFILES, S. Zalesak, S. Ossakow .	257
NONLINEAR EVOLUTION OF THE COLLISIONAL RAYLEIGH-TAYLOR INSTABILITY FOR INTERMEDIATE WAVELENGTHS IN THE 17 JULY 1979 KWAJALEIN DESCENDING SPREAD-F IONOSPHERE, M. Keskinen, S. Ossakow	277
STRUCTURE AND COMPOSITION MEASUREMENTS IN EQUATORIAL IONOSPHERIC BUBBLES, R. Narcisi, E. Trzcinski, G. Federico, L. Wlodyka, P. Bench . .	291

INTRODUCTION

A. Background

During the summers of 1977 and 1978, the Defense Nuclear Agency sponsored experimental programs at Kwajalein Missile Range. The purpose of these programs was to launch an instrumented rocket payload into the equatorial ionosphere to make *in-situ* measurements in conjunction with Wideband satellite measurements. Because of rocket system failures, the rocket-borne experiments failed in both campaigns.

In the summer of 1978, DNA sponsored a High-Altitude Nuclear Weapons Effects Summer Study at Los Alamos, New Mexico. The study provided a forum so that researchers could work collectively on problems associated with propagation through ionospheric environments that high-altitude nuclear explosions might produce. The proceedings of this summer study contain the recommendations of the Field Experiments Working Group. They recommended, in part, that during the months of July and August 1979, a series of heavily instrumented rockets be fired from Kwajalein through the equatorial backscatter plumes. This experiment was carried out, and these proceedings contain the results of data analysis compiled through July 1980.

B. The Experiment

The experiment consisted of two instrumented rocket payloads that were to be fired into a fully developed F-region "plume," or depleted region. The payload, depicted in Figure 1, consisted of an ion mass spectrometer, a pair of pulsed plasma probes, an E-field sensor, and a multifrequency beacon. In addition to this primary instrumentation in the payload, there was a C-band tracking beacon, telemetry, and an attitude control system. The rocket system was a Terrier-Malemute two-stage sounding rocket, which was designed to fly the instrumented payload to an altitude of 600 km.

The ALTAIR radar was used to locate and track the plumes, thus providing the information necessary to make launcher settings and to launch the rockets.

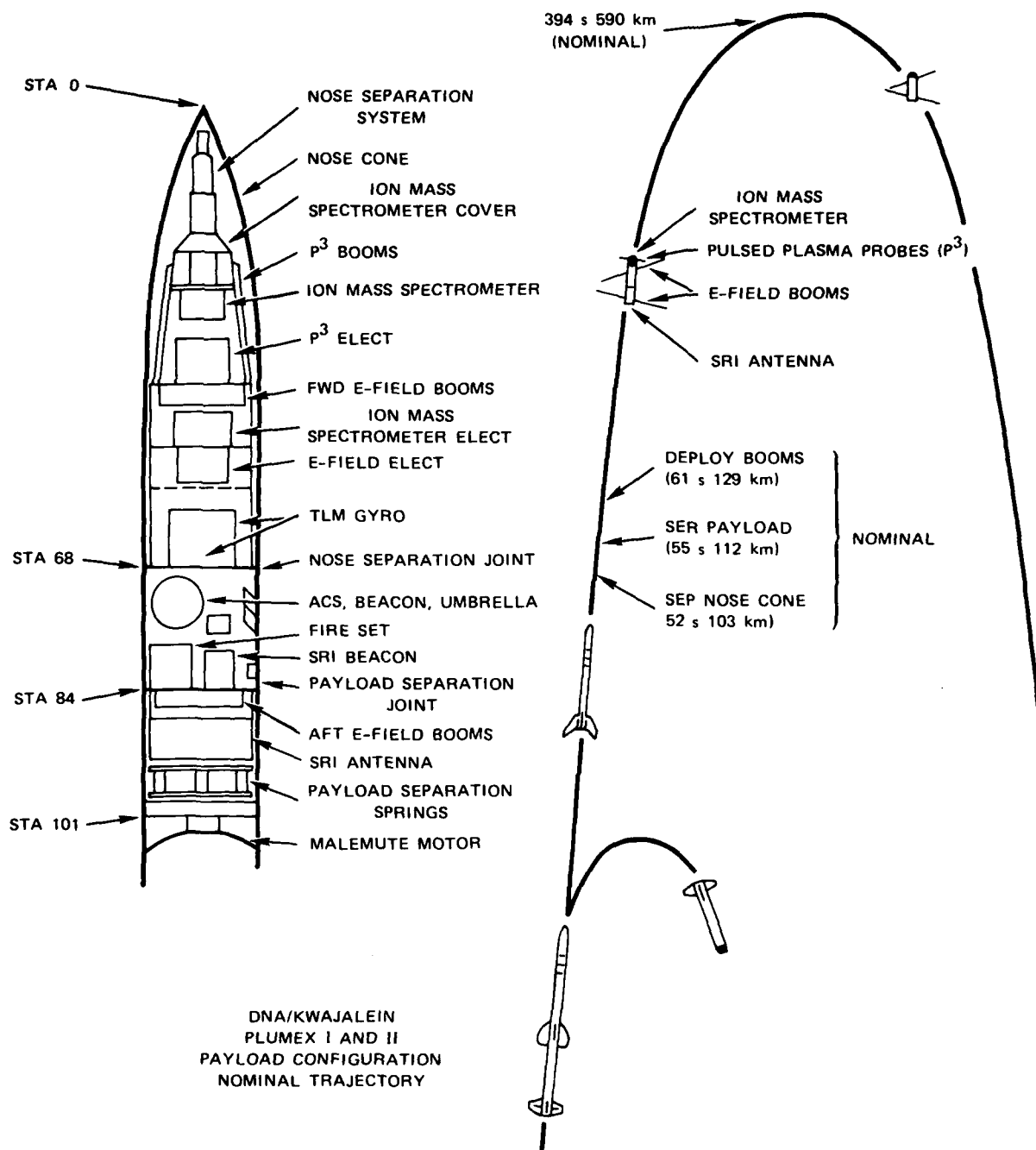


FIGURE 1 PLUMEX PAYLOAD INSTRUMENTATION AND FLIGHT FUNCTIONS

In addition to the ALTAIR, the TRADEX radar was used to look for L-band scintillations, an ionosonde was operated to measure the general characteristics of the ionosphere, and a Fabry-Perot interferometer was used to measure neutral-wind motions.

The rockets were launched on an azimuth of 28° true, because that was the only safe direction of fire. Fortunately, this azimuth provided a favorable geometry because of the easterly drift of the plumes. Figure 2 shows the rocket safety zone.

C. Launch Operations

The first rocket was launched from the Roi Namur launch facility at 1231:30 UT on 17 July 1979. All experiments onboard the rocket functioned and telemetry data were excellent. The MPS-36 radars did not acquire the C-band beacon, and no metric data were obtained. The rocket trajectory was plotted, however, based on telemetry antenna pointing angles and a brief appearance of the rocket in the ALTAIR beam. The payload penetrated an extremely active region of the ionosphere.

The second rocket was launched at 0957:30 UT on 23 July 1979. Excellent telemetry data were obtained, and metric tracking was accomplished for the duration of the flight. The payload failed to separate from the second stage rocket, severely compromising this mission. The multifrequency beacon antenna was not exposed, and this experiment failed, as a result. The aft E-field booms could not deploy; however data were obtained on the front booms. The payload tumbled because the presence of the burned-out second stage caused a large error in the location of the center of gravity. Data were obtained on the plasma probe and mass spectrometer experiments, but interpretation was difficult because of the lack of the stable platform reference.

D. Participation

Responsibilities in this program were as follows:

Rockets, payload integration--Sandia National Laboratories

Multifrequency beacon--SRI International

Pulsed plasma probe--Naval Research Laboratory

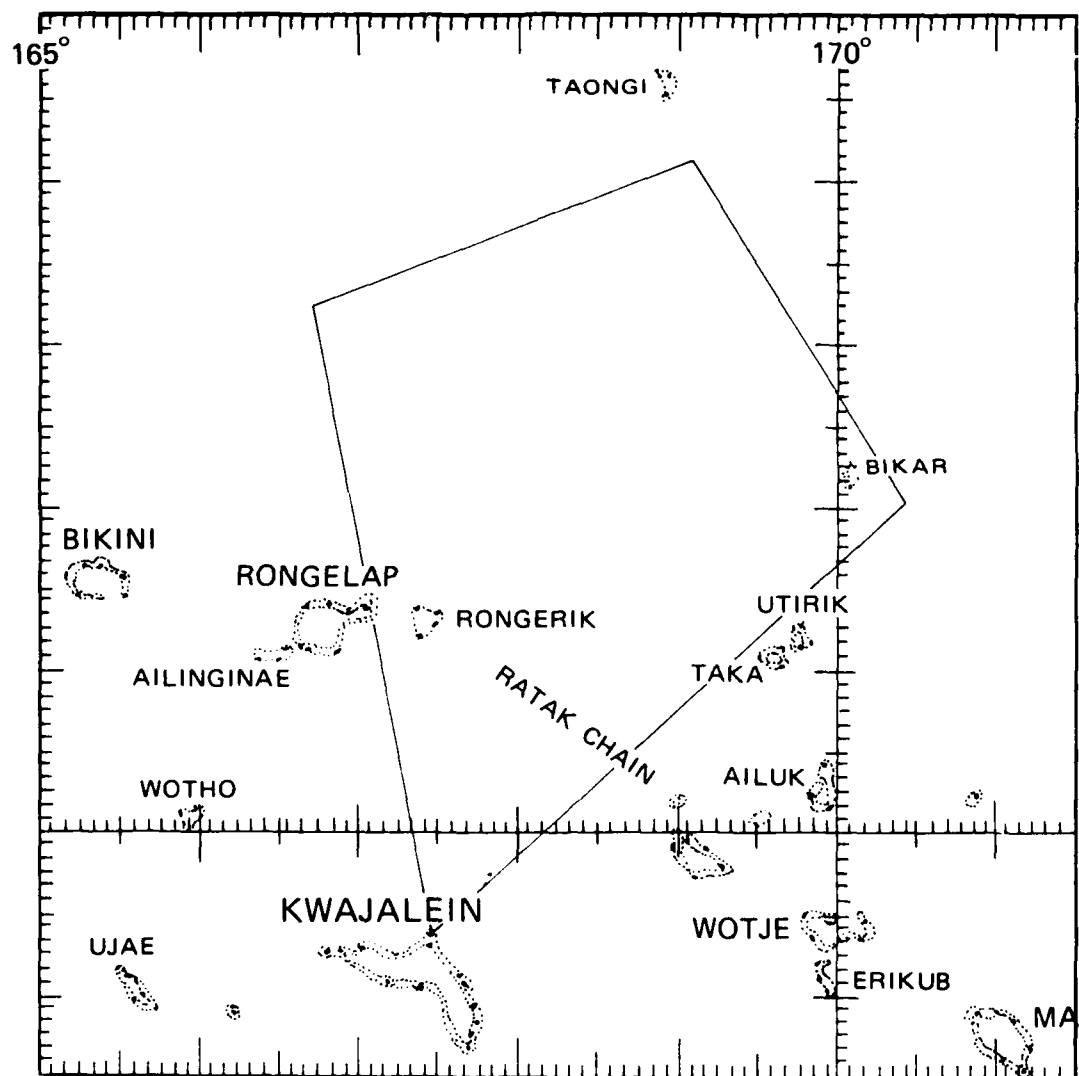


FIGURE 2 ROCKET SAFETY ZONE

Mass spectrometer--Air Force Geophysical Laboratory
Ionosonde--SRI International
ALTAIR/TRADEX radars--SRI International
Fabry-Perot interferometer--SRI International, University of
Pittsburgh
Overall planning and coordination--SRI International
Range support--Kwajalein Missile Range.

This experiment was carried out under the sponsorship of the Defense Nuclear Agency.

ROCKET RF-BEACON EXPERIMENT FOR THE SUMMER 1979 KWAJALEIN CAMPAIGN

Juris Petriceks
Radio Physics Laboratory
SRI International
Menlo Park, CA 94025

ABSTRACT

SRI International fielded the RF-Beacon Experiment during the Summer 1979 Kwajalein Campaign. The rocket payload equipment consisted of a four-frequency phase-coherent beacon and a broadband circularly polarized antenna. The receiving antenna was located almost at the foot of the rocket trajectory. A phase-locked receiver and digital data-acquisition system collected amplitude and dispersive-phase data.

Subsequently, the data were converted from a temporal grid to a spatial grid and then detrended to separate the slow trend-like variations from the more rapid scintillation-like variations. The filtered output ($\lambda > 50$ km) of the upleg dispersive-phase data was used to estimate the large-scale electron density structure. The detrended ($\lambda < 50$ km) phase and amplitude data were analyzed to characterize the structure of the equatorial spread-F ionosphere. The characterization was in terms of the intensity scintillation index, S_4 , the phase scintillation index, σ , and the phase spectral strength and slope (index), T_z and p_z^ϕ , respectively.

The results of the data analysis are discussed in the companion report entitled, "A Comparative Analysis of Equatorial Irregularity Structures as Measured by Wideband, AE-E, and In-Situ Rocket Probes," by C. L. Rino, R. C. Livingston, and J. Petriceks.

I INTRODUCTION

Radio beacon propagation experiments have been performed many times. The Summer 1979 Kwajalein Campaign presented an opportunity to use spare beacons from the SECEDE II program in a unique geometry. Section III describes the background, concept, and objectives of this experiment.

The RF-Beacon Experiment was conducted in two phases. The first phase dealt with data collection. In preparation for data collection, the hardware was procured, assembled, and tested; the rf beacon and the transmitting antenna were integrated into the rocket payload; and the receiving equipment was installed on Roi-Namur Island. The launch of the first payload was successful and resulted in a good data set. Section IV describes the data collection phase.

The second phase dealt with data analysis. In preparation for data analysis the collected data were reviewed and equipment effects were removed; the data were converted from an equally spaced temporal grid onto an equally spaced spatial grid; and the data were partitioned by using a sharp-cutoff digital filter to separate slow trend-like variations from scintillation-like variations. Section V describes the process of data preparation for analysis.

Subsequently, the slow trend-like variations of the dispersive-phase data were used to derive large-scale electron density variations as a function of altitude. The scintillation-like phase and amplitude data were used to describe the equatorial spread-F ionosphere in terms of scintillation indices and spectral parameters. Section VI describes the data analysis effort.

II EXPERIMENT DESIGN

A. Background

In 1971 SRI fielded an rf-beacon experiment in conjunction with the SECEDE II barium release series. A rocket was launched carrying a multi-frequency beacon behind a barium cloud as seen from receiving stations at fixed locations on the ground. The ground-based receivers measured amplitude fluctuations and dispersive phase of the received signals.

The dispersive phase was measured by using the highest transmitted frequency signal as a reference. From the dispersive phase the total electron content was obtained. Extraction of electron density profiles

from the dispersive-phase data was considered a by-product of the SECEDE II results.

B. Concept

For the summer 1979 Kwajalein campaign the rf-beacon experiment geometry was designed to give the electron density profile as a primary result. The rocket carrying the instrument payload was launched with a take-off angle of less than 10° from vertical. To take advantage of this trajectory the ground-based coherent receiver and data acquisition system were located near the rocket launch pad.

The experiment geometry assured that during the rocket upleg trajectory the beacon signal path remained unchanged except for an incremental increase in the payload altitude as a function of time. Because dispersive phase is related to the integral of electron density as

$$\delta\phi = -r_e \lambda \int_{z_0}^{v_z t} N_e(\eta) d\eta \left[1 - \left(f/f_r \right)^2 \right] \quad (1)$$

where r_e is the classical electron radius, λ is the measurement wavelength, v_z is the rocket velocity, which lies essentially along the propagation path, N_e is the electron density, and f_r is the reference frequency. Clearly, the differentiation of the dispersive phase with respect to distance will yield the electron density along the payload trajectory. The only assumption involved in so deriving the electron density is that the ionosphere remains time-invariant along the path for the duration of the measurement.

In addition to the phase effects, which could be converted into electron density profiles to the extent that the intervening ionosphere is time-invariant, patchy or localized plasma disturbances could be detected by phase and amplitude fluctuations. The size of the amplitude fluctuations relative to the phase fluctuations depends upon the location of the perturbing region along the signal path--it is largest when the region is half-way along the path and tends to zero at the ends.

Thus the rf-beacon measurements could yield the electron density along the rocket payload upleg trajectory and could detect both in-situ and remote electron density fluctuations. It also could provide some information concerning the location of the fluctuations.

C. Objectives

The RF-Beacon Experiment had two main objectives. One was to obtain an accurate profile of electron density along the rocket upleg trajectory and to estimate the time-invariance of the electron density. The other was to measure the amount of amplitude and phase scintillation owing to the disturbed plasma regions penetrated. On the downleg trajectory the measured amount of scintillation could be used to estimate the location of scintillation producing regions, which need not necessarily be penetrated by the rocket payload.

In addition, both the electron density and scintillation measurements would be compared with results obtained by in-situ probes. As these results were being compared, it became clear that the rf-beacon measurements could provide valuable information about the time-variant ionosphere along the rocket upleg trajectory.

III DATA COLLECTION

A. Hardware

The basic equipment for this experiment consisted of a four-frequency radio beacon and transmitting antenna onboard the rocket payload and a receiving antenna, receiver, and data acquisition system on the ground. Because this experiment was based on the same measurement techniques as the rf propagation experiment carried out by SRI during the SECEDE II program most of the equipment was already on hand. However, new transmitting antennas had to be procured because of the geometrical orientation of the rocket payload relative to the receiving site. Similarly, the data acquisition system had to be adapted to record digital data in the field.

1. Rocket Payload Equipment

The radio beacon signals were coherent in the ratios 1:2:3:6. The emitted power levels and frequencies were 1 W at 145.7644 MHz and 2 W each at 291.5288, 437.2932, and 874.5864 MHz. A four-way power combiner was used to feed the transmit antenna.

Because the receiving site was at the foot of the rocket trajectory, the transmitting antenna had to have the main beam centered along the long axis of the rocket payload. To avoid using an antenna (antennas) that would have to be deployed or would be attached permanently to the exterior of the payload body, we used a cavity backed spiral antenna that could be mounted at the base of the payload. Figure 1 is a photograph of the payload, including the beacon antenna. The antenna was designed to have a 70° 3-dB beamwidth and sufficient bandwidth to cover all four beacon frequencies.

2. Ground-Based Equipment

The receiving antenna was a cross log periodic that covered the beacon frequency band and had a 70° 3-dB beamwidth. The antenna output was fed to a distribution network and then branched into separate low-noise amplifiers for each beacon frequency.

The dispersive-phase and amplitude measurement receiver consisted of down-converters, multichannel tracking filters, and a frequency synthesizer. A large amount of measurement redundancy had been built into the equipment. Either the 874- or 437-MHz signal could be used as the reference for the dispersive phase measurements. Also any of the lower-frequency to reference-frequency signal pairs provided the desired dispersive phase measurement.

The digital data acquisition system consisted of a multiplexer, analog-to-digital converter, interface, minicomputer, and digital tape deck. A system, previously used in the MISERS BLUFF program, was made available and adapted for use in this experiment. To provide some redundancy, an analog tape deck was included in the data acquisition

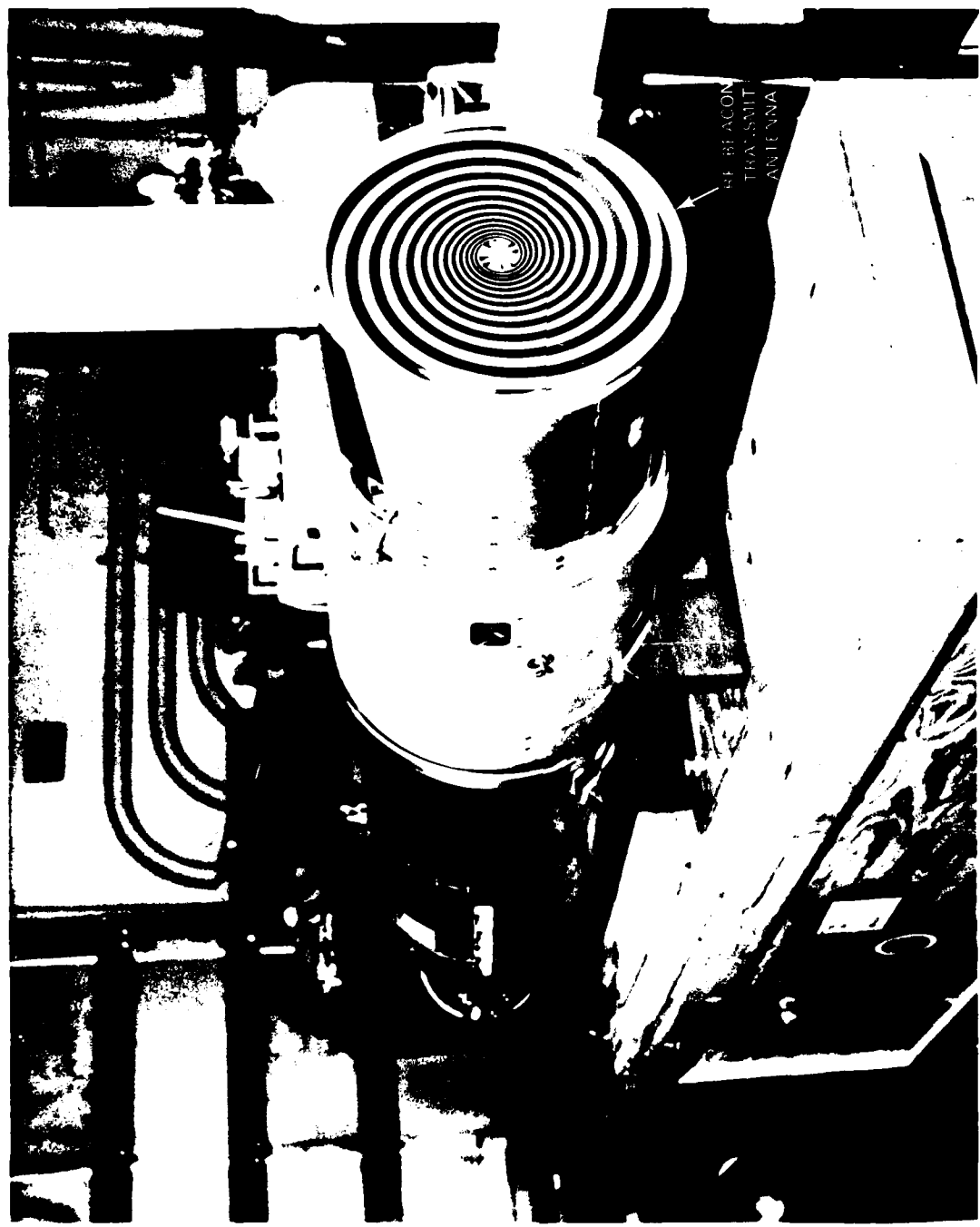


FIGURE 1 ROCKET PAYLOAD

system for recording the amplitude and dispersive phase data signals prior to analog-to-digital conversion.

B. Fielding

The radio beacon, power combiner, and transmit antenna were integrated into the rocket payloads by Sandia Laboratories. At Sandia checks were conducted to insure that no cross-experiment interference would occur in the payload. Similarly, all time-sequencer and telemetry signals were checked to insure proper operation of all four experiments aboard the payload.

The rf-beacon ground-based equipment was installed in the Launch Operations Control Building (LOCB) on Roi Namur Island. The LOCB is located \approx 100 m from the payload assembly building and the rocket launch pad. The cross log periodic antenna was placed on the roof of the LOCB and aligned with the upleg portion of the planned rocket trajectory.

To verify the operation of the RF-Beacon Experiment equipment the radio beacon was activated to emit 0.1 mW at each of the four frequencies. The rocket payload assembly building had sufficient openings to let some of the signal leak out. The proximity of the LOCB and the placement of the receiving antenna resulted in the necessary signal strength to check the performance of the receiver.

C. Operations

On rocket-launch count down days further experiment verification was performed. When pad operations did not require radio silence, the rf beacon was activated and the performance of the receiver was checked. When the count down reached $T_0 - 20$ min, the receiver was calibrated and the calibration data was recorded.

On 17 July 1979 at 12:30:30 UT the first rocket lifted off. At $T_0 + 55$ s payload separation from the second stage occurred and 6 s later the rf beacon was switched to high power output. Immediately thereafter the rf-beacon signals were received and dispersive-phase and amplitude data recording was started.

All four frequency amplitude signals were recorded. The three lowest frequency beacon signals of the dispersive phase were recorded with the highest frequency signal serving as the reference. Because two quadrature components needed to be measured to resolve the signal phase, a total of ten data channels had to be recorded. In addition time code generator output was also recorded. Figure 2 shows a sample output of amplitude and one of the phase quadrature signals at each of the three lowest frequencies. The data were sampled and recorded at the rate of 500 samples per second. The sampling rate was more than adequate for the 150-Hz loop bandwidth of the phase-locked receiver.

The signal-to-noise ratio for all four received signals was designed to be between 40 and 20 dB for the expected range of 130 to 600 km from the payload to the receiver. Both the transmitting and receiving antennas had 3-dB beamwidths of 70°. The broad beamwidths assured that any payload attitude variation would not be translated into received signal amplitude variations. Furthermore the 70° beamwidth guaranteed adequate signal strength until the payload reached the troposphere and disintegrated. The received-signal-strength measurement validated the design. The rf-beacon signals were not lost until $T_0 + 814$ s when the payload was at an altitude of ≈ 22 km and at a range of ≈ 272 km. After loss of data signals another receiver calibration was done.

The second rocket lift-off occurred on 24 July 1979 at 09:57:30 UT. However, the payload separation from the second stage did not occur. As a result of this failure the rf-beacon experiment transmitting antenna aboard the payload was not uncovered and no beacon signals were received.

IV DATA ANALYSIS PREPARATION

A. Verification

The raw phase and amplitude records were reviewed for obvious equipment malfunction effects. This was done most conveniently by displaying the amplitude data for the four beacon signals and the dispersive-phase data for the three lowest frequency beacon signals. Figure 3 shows the

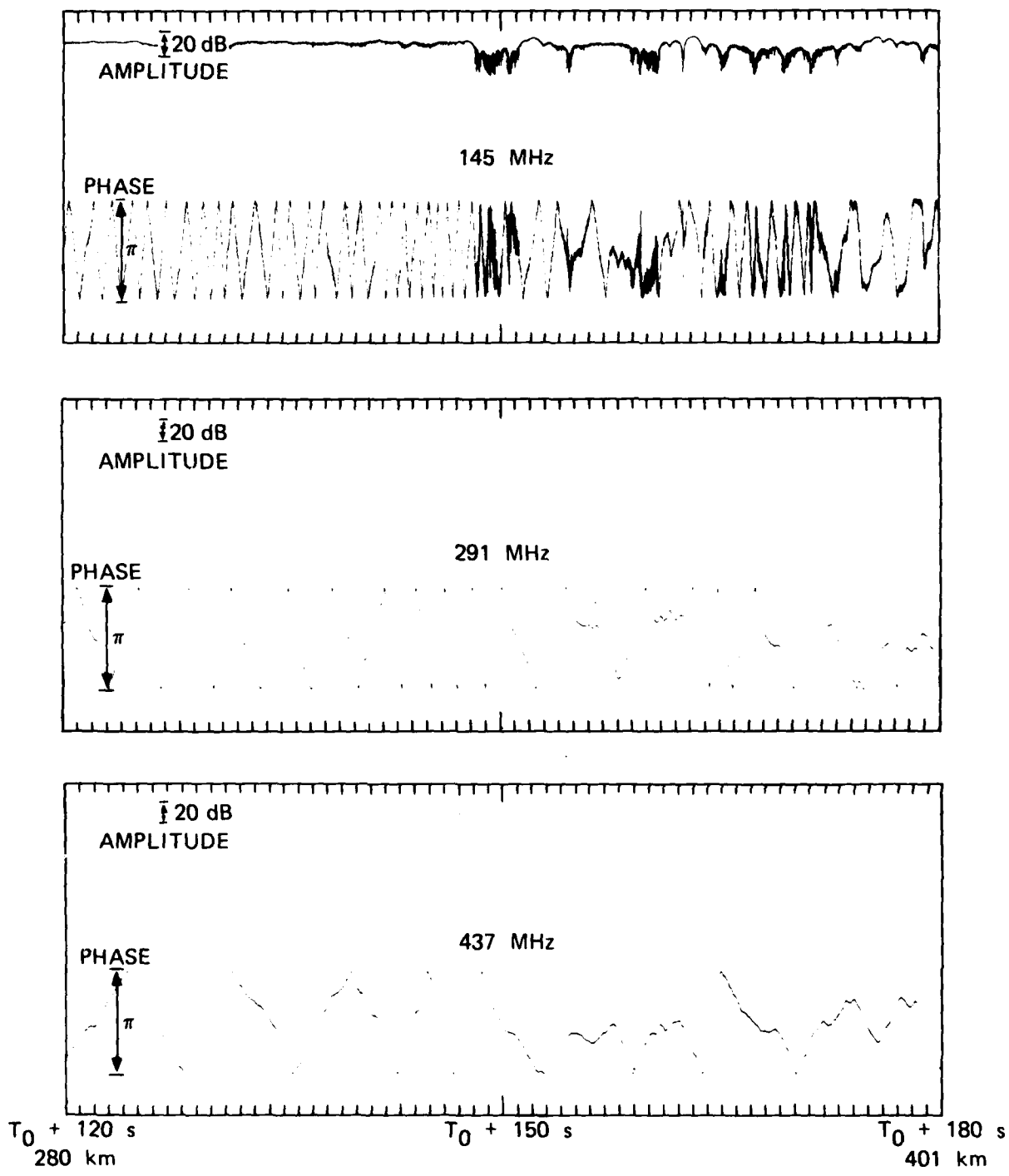


FIGURE 2 RAW DATA SAMPLE

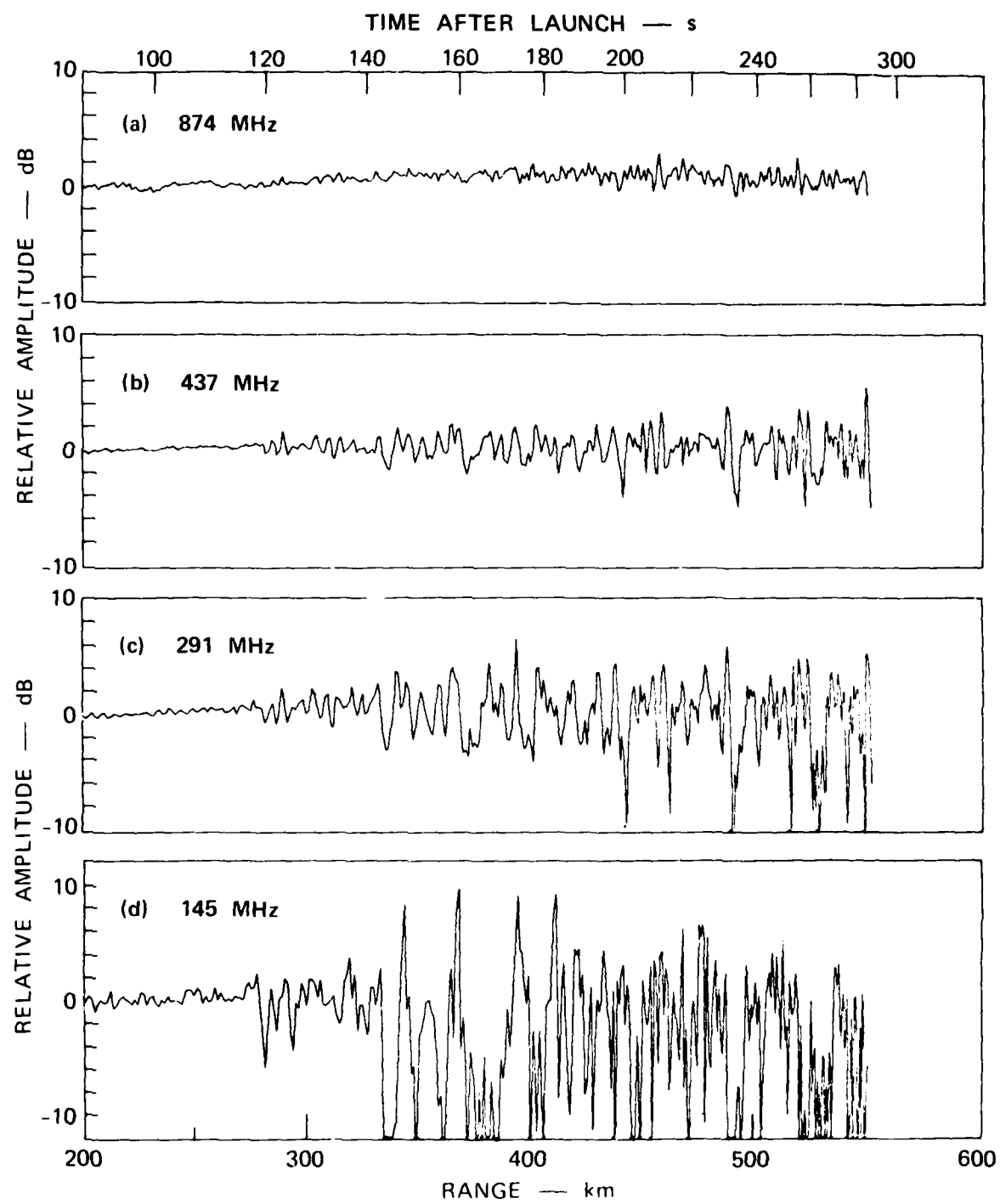


FIGURE 3 AMPLITUDE DATA

amplitude data at 874, 437, 291 and 145 MHz. The data displayed has had the slow trend-like amplitude variation removed. Figure 4 shows the dispersive phase data at 437 and 291 MHz. Again the slow trend-like phase variation has been removed. The only equipment effects observed are in the 291 MHz phase data near the range of 550 km. Cycle slippage can occur in the phase-locked loop when deep amplitude fades are encountered.

Statistical analysis of the six channels of phase data revealed small biases and gain nonlinearities in all six channels. The bias and nonlinearity effects were removed from the data.

Another effect, which was removed from the data, resulted from the spin of the payload. Each revolution of the payload introduced 360° of phase at all four frequencies. However, the desired dispersive-phase measurement is linear with wavelength. Therefore, before the dispersive phase was processed that part introduced by the payload spin had to be removed. With the spin rate provided by Sandia Laboratories, the phase-data correction was a straightforward matter.

B. Temporal-to-Spatial Conversion

The data were recorded at a constant rate of 500 samples per second. Because the payload velocity varied as a function of time the spatial sampling rate was not constant. To simplify the derivation of electron density as a function of height the data were converted from an equally spaced temporal grid onto an equally spaced spatial grid. This conversion was also necessary to avoid introducing any effects from the changing velocity into the data spectral analysis.

To simplify the temporal-to-spatial conversion we developed an analytic expression to fit the payload trajectory data supplied by Sandia. Fitting of an analytic ballistic trajectory expression to the trajectory data (starting at the end of the second stage burn) did not give satisfactory results. Subsequently, a trial and error method of compressing the time scale resulted in the use of an effective time in the analytic expression, which is related to the true time, as follows

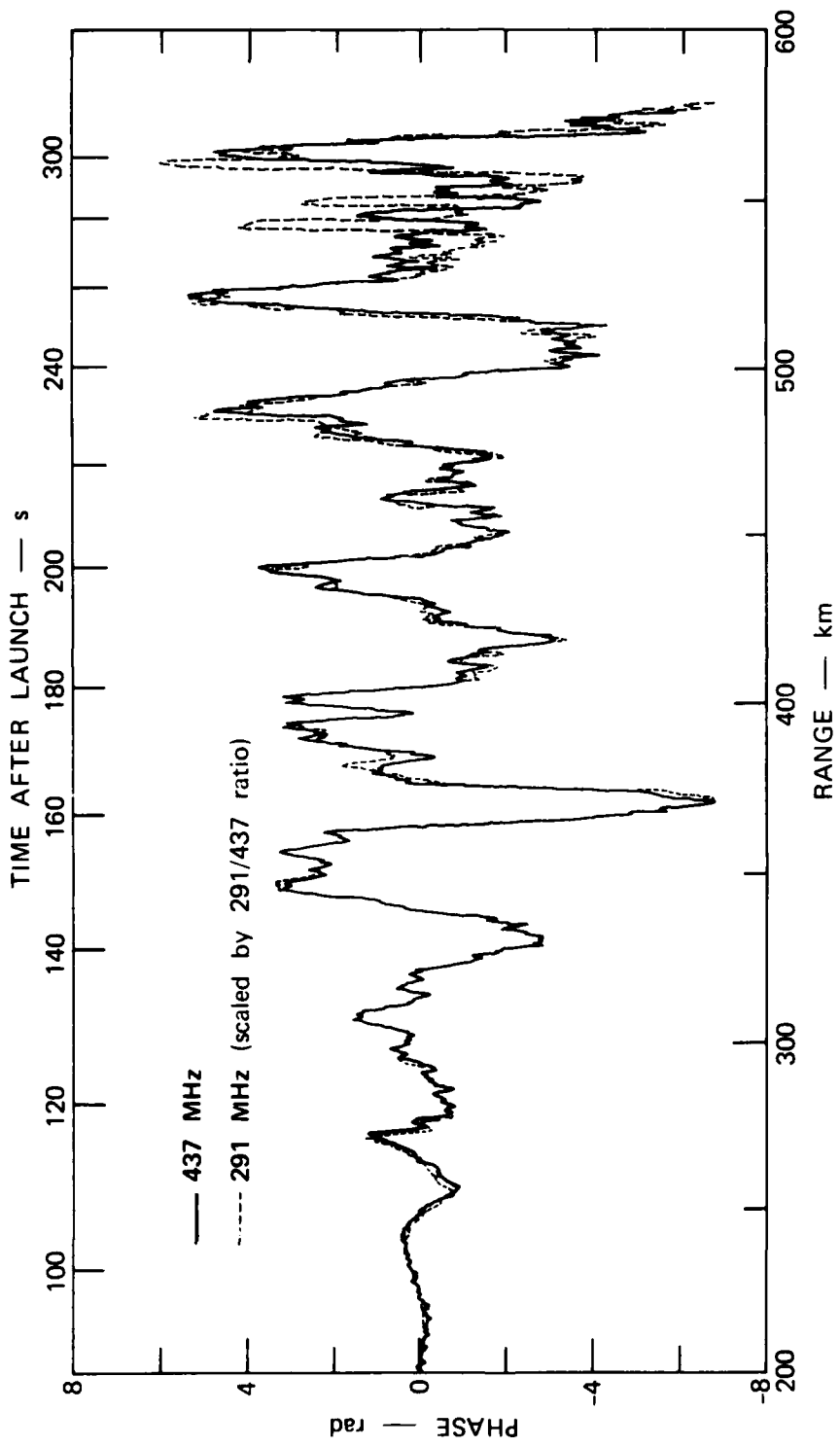


FIGURE 4 PHASE DATA

$$t_{\text{eff}} = \frac{t_{\text{true}}}{(1.0 + t_{\text{true}}/10^5)^{3.8} + 0.063}$$

The reason for the apparent time contraction could be the regular firing of the payload attitude control jets. Figure 5 shows the match in payload heights as given by the analytic trajectory expression and the trajectory data supplied by Sandia. A positive deviation from zero indicates an overestimation of the height by the analytic expression.

A computer program was then written to interpolate the equally spaced temporal grid data onto an equally spaced spatial grid. The spatial sampling rate used was 100 samples per km. Because the payload velocity varied between ≈ 3 km/s and 0.3 km/s the data conversion process was essentially a decimation process.

C. Detrending

To separate the slow trend-like features of phase and amplitude variation from the fast scintillation-like variations the data were detrended using a digital filter with a 50-km cutoff. The effect of the detrending process was to preserve in the detrended data all Fourier components with spatial wavelengths shorter than 50 km. As an example, Figure 6 shows the raw, filtered, and detrended phase data of the 437-MHz channel. Figure 7 shows the same components of the amplitude data for the same channel.

Some of the data channels were also detrended using filters with 20-km, 10-km, and 1-km cutoffs.

V DATA ANALYSIS RESULTS

A. Electron Density

The dispersive-phase measured is proportional to the integrated density along the propagation path. If we assume that the ionosphere along the measurement path is time-invariant, electron density can be

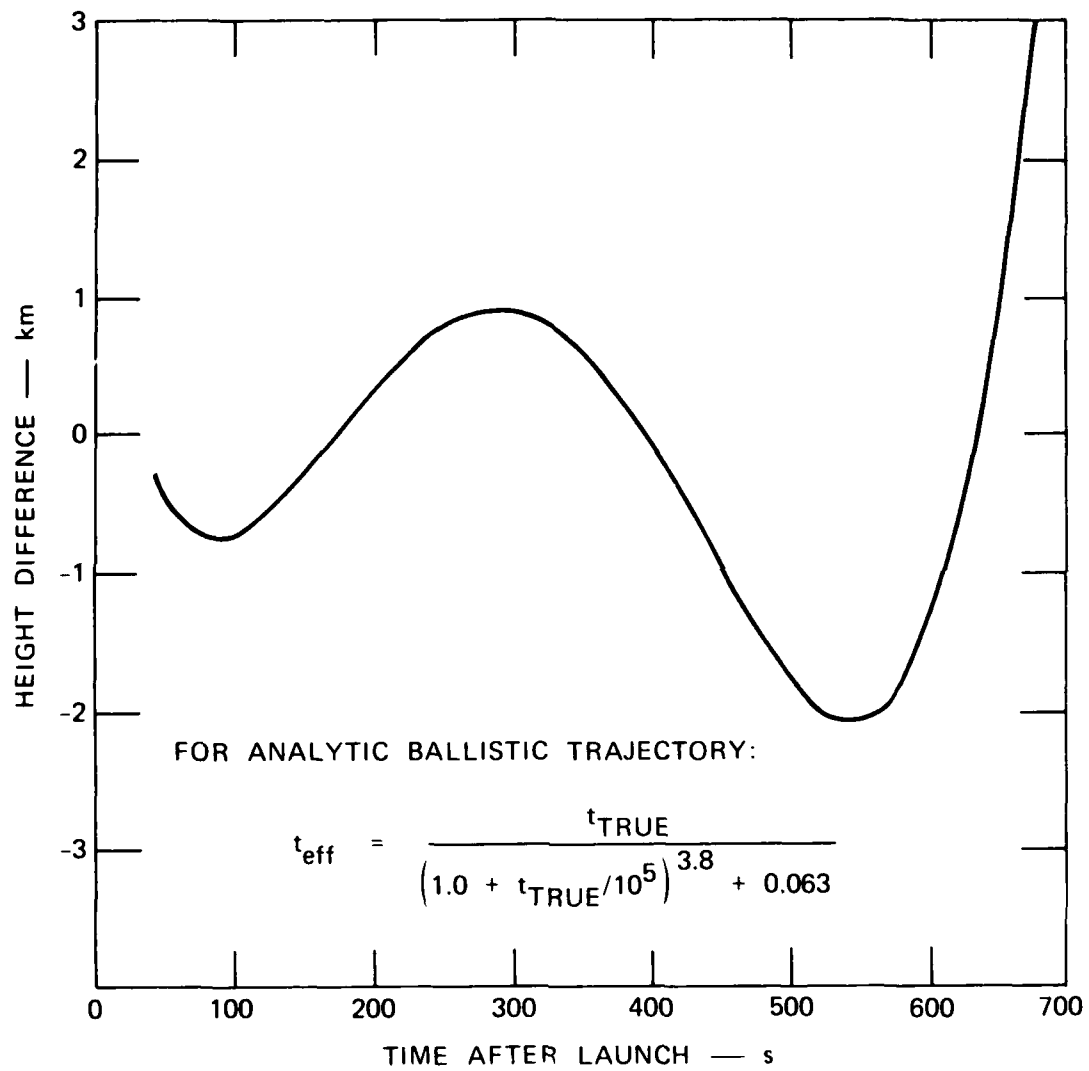


FIGURE 5 HEIGHT DIFFERENCE OF ANALYTIC AND RADAR-DERIVED TRAJECTORIES

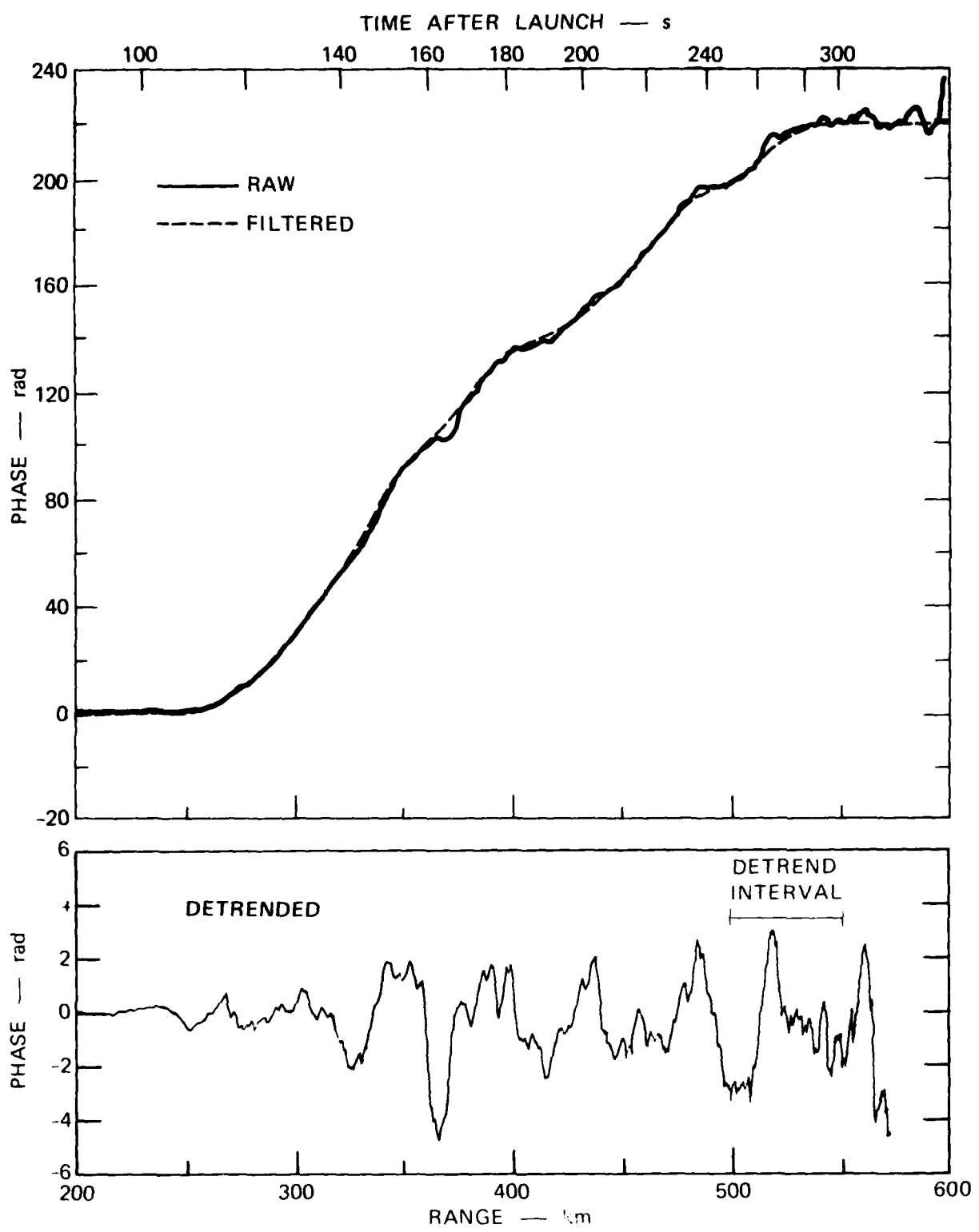


FIGURE 6 PHASE DATA — 437 MHz (Raw, Filtered, and Detrended)

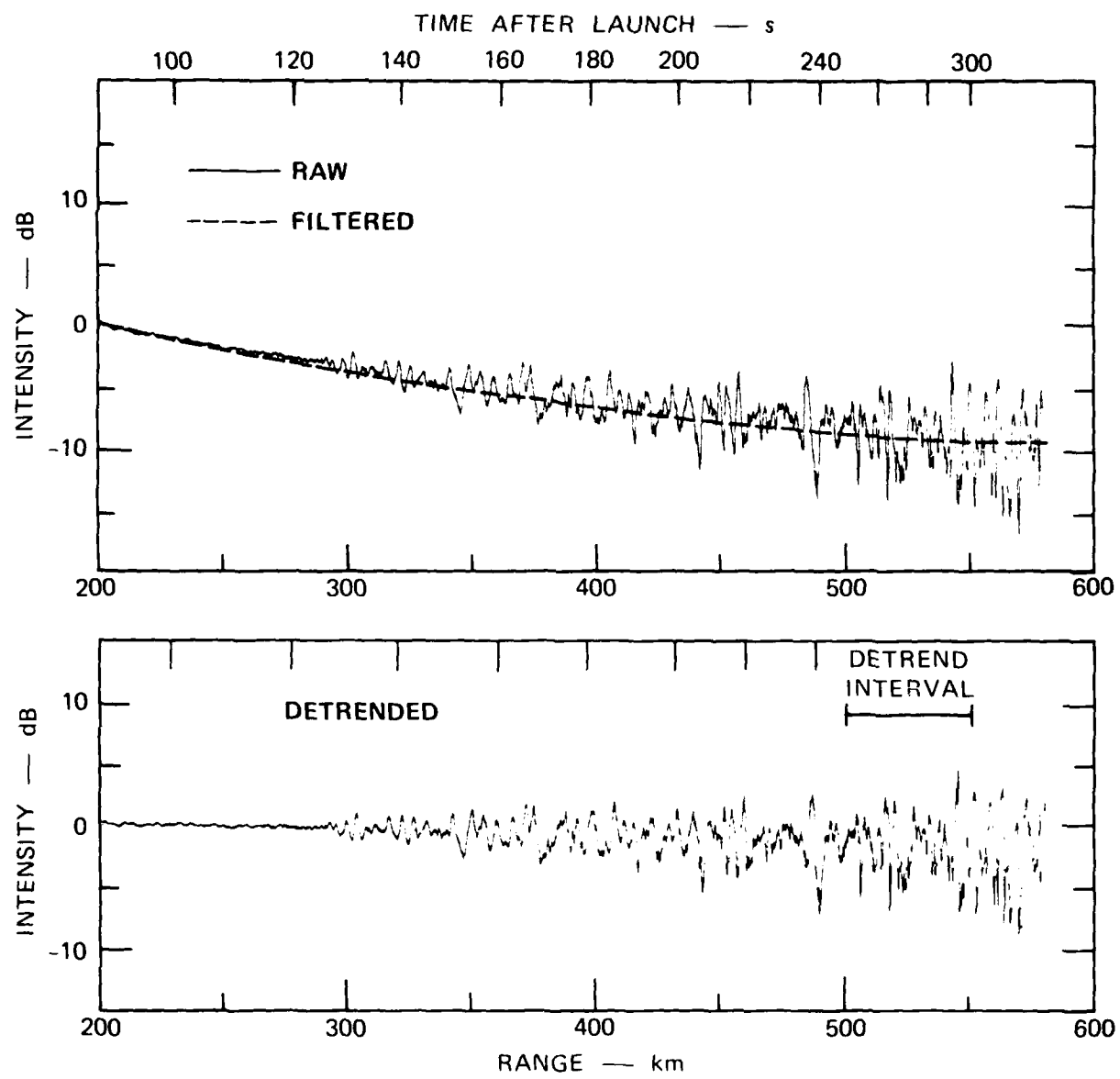


FIGURE 7 AMPLITUDE DATA — 437 MHz (Raw, Filtered, and Detrended)

derived by differentiating the dispersive phase, corrected for the finite reference frequency, with respect to distance as

$$N_e = \frac{\Delta\phi}{\Delta z} \frac{1}{r_e \lambda} \quad (2)$$

where r_e is the classical electron radius and λ is the measurement wavelength [Eq. (1)].

The slow trend-like phase data measured at 437 MHz was differentiated to obtain the large-scale electron density structure. The results are compared with the in-situ Langmuir probe measurements in Figure 8. The electron density scale was calibrated from the incoherent-scatter data measurement made with the ALTAIR radar. Absolute density calibration will have to await the results of the high-resolution electron density probe.

If the electron density structure remained stationary and time-invariant over the interval that the rf-beacon phase data were being accumulated, the two curves in Figure 8 would track. Up to the range of ≈ 370 km (≈ 368 km height) the electron density measured by the Langmuir probe and the rf-beacon compare very well.

The departure of the beacon-derived electron density from the Langmuir probe measurement of electron density at ranges in excess of ≈ 370 km (≈ 165 s into the rocket flight) gives a measure of the time-variant electron density structure along the propagation path from the rocket payload to the receiving equipment at the foot of the rocket trajectory. The ALTAIR radar backscatter maps* show that a region of increased backscatter (indicative of electron density depletion) moved into and out of the measurement path between $T + 120$ s and $T + 240$ s.

The results presented are for the upleg portion of the payload flight. During this portion of the flight the unique geometry of an essentially unchanging measurement path held true. Comparable results

*c.f. Roland Tsunoda's paper in this Proceedings.

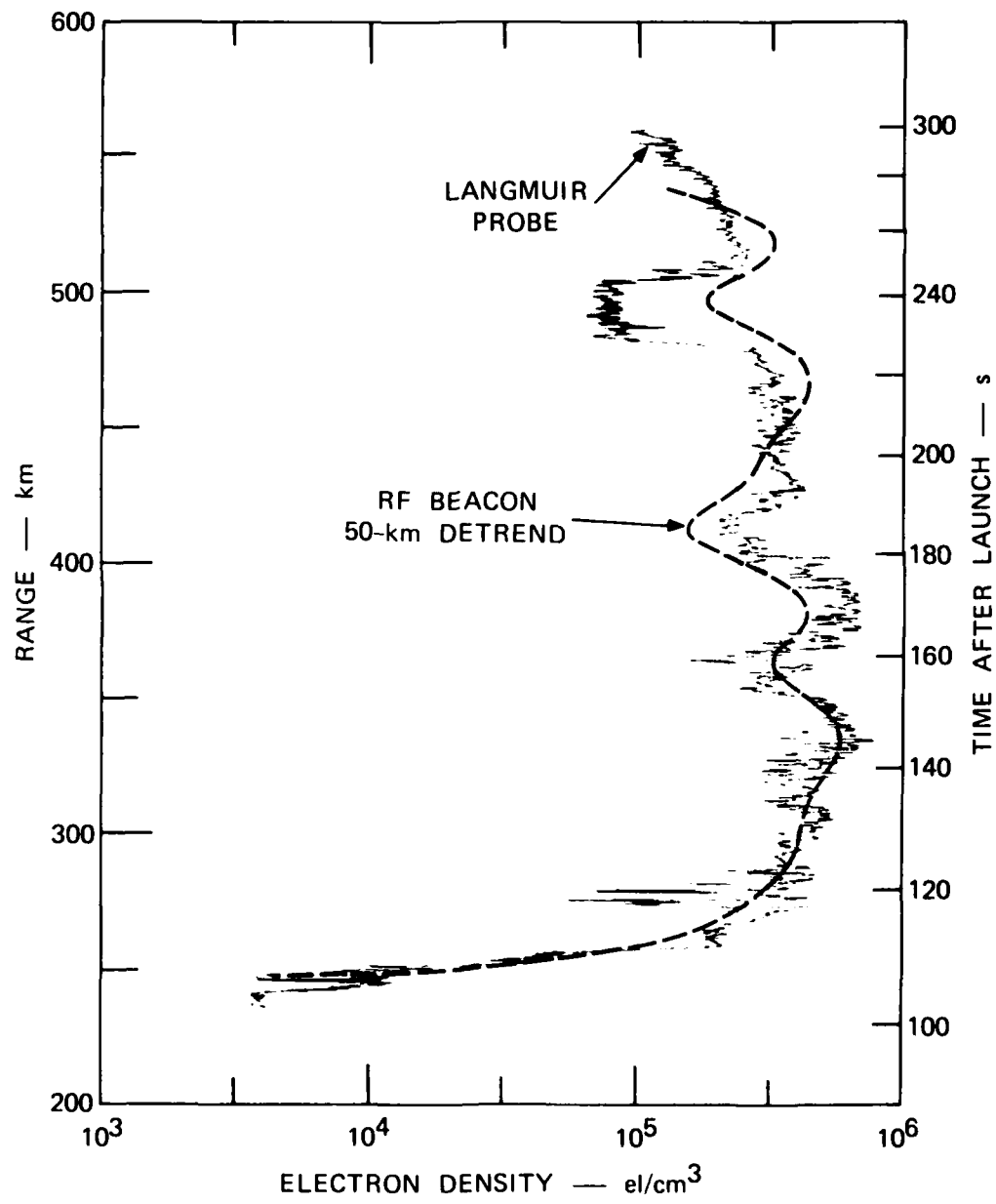


FIGURE 8 ELECTRON DENSITY COMPARISON

could not be obtained for the downleg portion of the flight because the propagation path from the payload to the receiving equipment changed continuously.

B. Scintillation Indices

The detrended scintillation-like variations of both the amplitude and phase data were analyzed to obtain the intensity-scintillation index S_4 and the phase-scintillation index σ_ϕ . Both the upleg and downleg data were analyzed using overlapping 40-km data intervals with a 5-km step for each new data set. The intensity scintillation index, S_4 , was computed for the 145-, 291-, and 437-MHz signals and the phase-scintillation index, σ_ϕ , was computed for the 291- and 437-MHz signals.

Figure 9 shows the phase-scintillation index for the upleg portion of the payload trajectory. If the ionospheric structure along the propagation path were time-invariant, we would expect the σ_ϕ index to increase monotonically. The decrease of σ_ϕ at ranges $> \approx 370$ km indicates that at $\approx T_o + 165$ s, a scintillation producing region of the ionosphere was replaced by less disturbed structure. This observation supports the electron density measurement results discussed earlier. The 291 MHz data have been scaled by the 291/437 ratio to demonstrate the expected linear dependence of σ_ϕ on wavelength. The failure of the two curves to track around 550 km results from the cycle slippage in the phase measurement at 291 MHz discussed earlier.

Figure 10 shows the intensity-scintillation index for the upleg portion of the payload flight. As was the case for the phase-scintillation index, the intensity scintillation index also decreases at ranges $> \approx 370$ km. Therefore, the measured electron density and scintillation indices not only describe the propagation environment along the measured path, but also provide information about changes in that environment. The extremely high values of S_4 at 145 MHz in the range from 370 to 400 km result from the severe, prolonged amplitude fade in that range region.

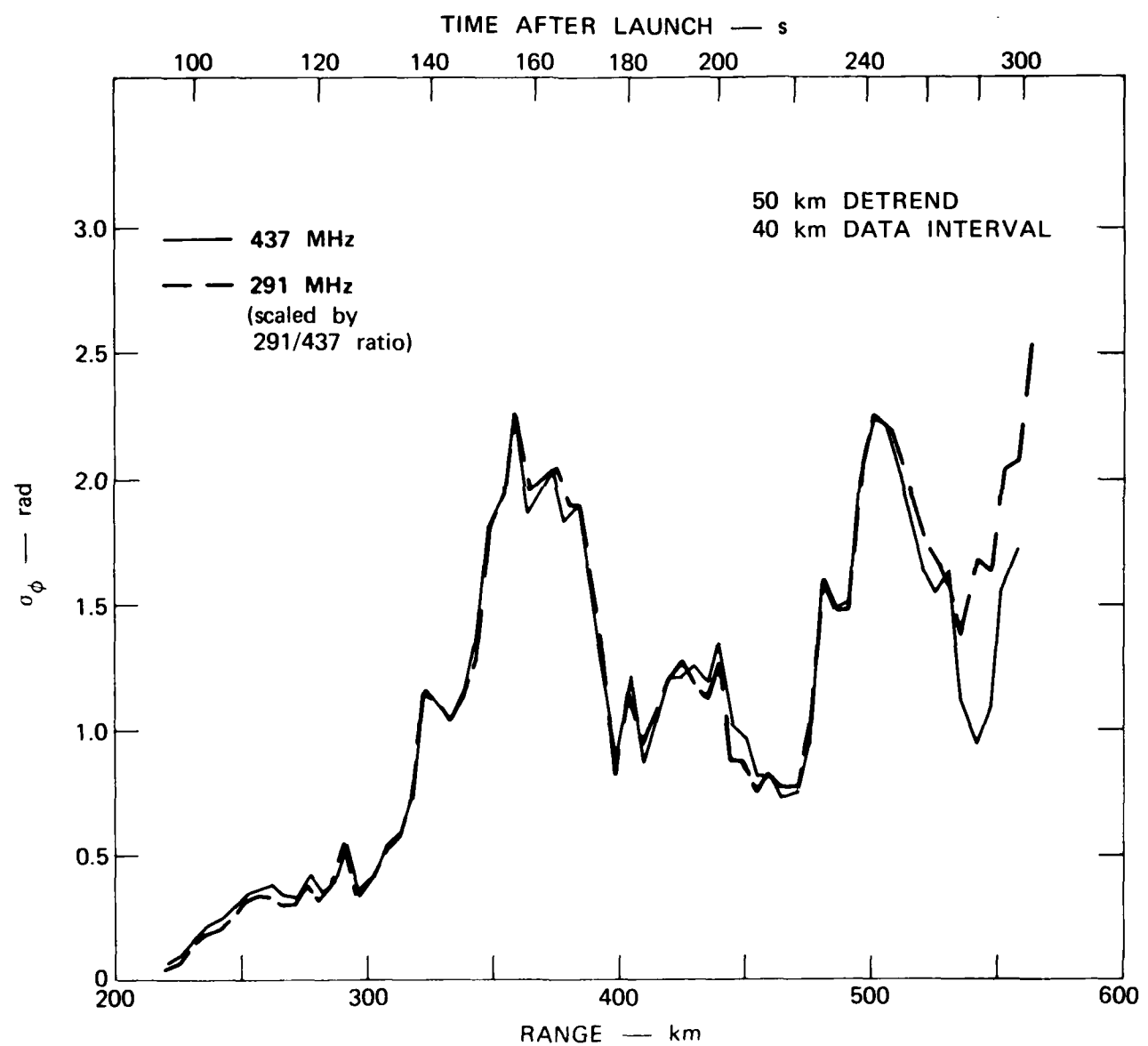


FIGURE 9 PHASE SCINTILLATION INDEX, σ_ϕ

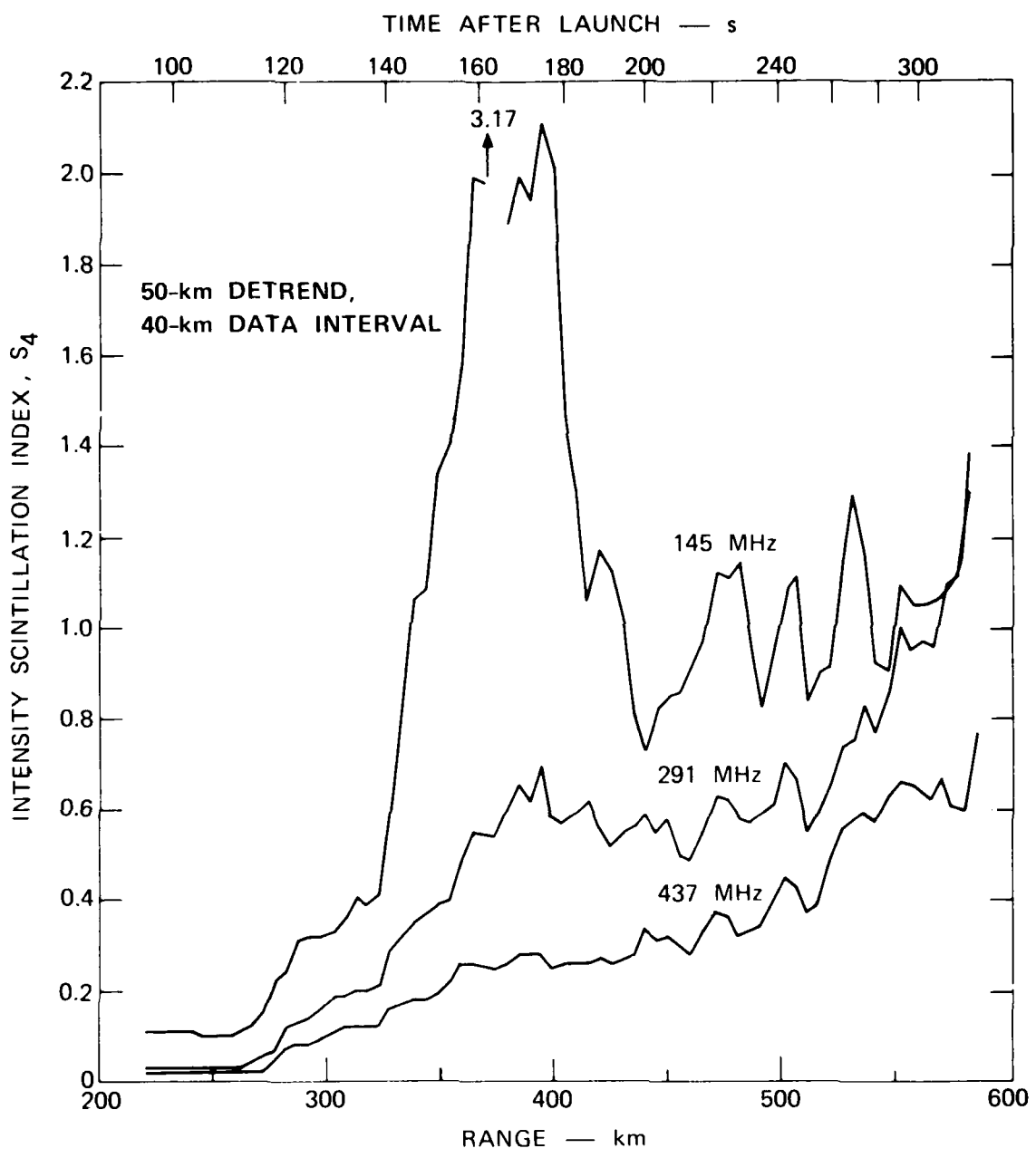


FIGURE 10 INTENSITY SCINTILLATION INDEX, S_4

C. Spectral Analysis

Spectral analysis was performed on the detrended 291 and 437 MHz phase data. Both the upleg and downleg data were analyzed using 40-km data intervals with a 5-km step for each new data set. The top panel of Figure 11 shows an example of the spectral analysis program output. A least-square log-linear fit is made to the power spectral density function to characterize the phase-spectrum by the strength and slope (index) parameter T_z and p_z , respectively. T_z and p_z are defined such that

$$\Phi(f) = T_z f^{-p_z} . \quad (3)$$

The effect of the detrend filter cutoff is illustrated in the lower panel of Figure 11, for which 10-km detrended data were used. The significance of the RF-Beacon Experiment measurements and the measured values of T_z and p_z are presented in the companion report titled, "A Comparative Analysis of Equatorial Irregularity Structures as Measured by Wideband, AE-E and In-Situ Rocket Probes," by C. L. Rino, R. C. Livingston, and J. Petriceks.

ACKNOWLEDGMENTS

Acknowledgement for the basic concept of this experiment goes to Alan A. Burns; the experimental effort was directed by Charles L. Rino; many of the data analysis programs were adapted from Robert C. Livingston's work; and data collection assistance in the field was given by Russell N. Scofield. The Langmuir probe electron density data presented were provided by Michael C. Kelley of Cornell University. This work was sponsored by the Defense Nuclear Agency under Contract DNA001-79-C-0128.

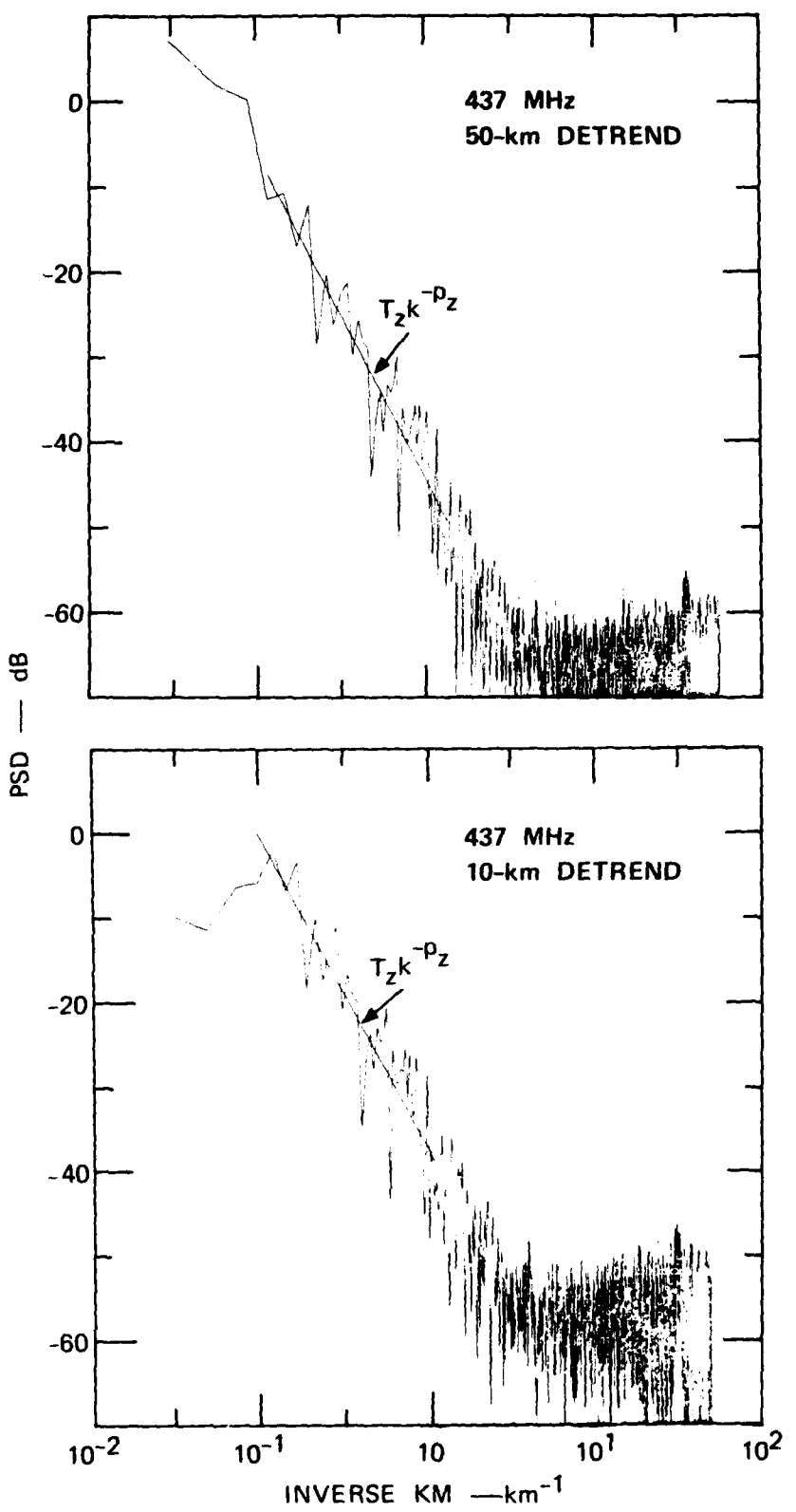


FIGURE 11 TYPICAL POWER SPECTRAL DENSITY DISPLAY

THE PULSED PLASMA-PROBE EXPERIMENT: IN-SITU MEASUREMENTS OF ELECTRON DENSITY, TEMPERATURE, AND DENSITY FLUCTUATION OF POWER SPECTRA

E. P. Szuszczewicz and J. C. Holmes

E. O. Hulbert Center for Space Research
Naval Research Laboratory
Washington, DC 20375

ABSTRACT

The NRL pulsed plasma-probe experiment was successfully flown on each of the two PLUMEX rockets during July 1979. The experiment provided direct measurements of absolute density, N_e , temperature T_e , and density fluctuation power spectra with a maximum Nyquist frequency of 1 KHz (1-m resolution at a 1-km/s rocket velocity). In the first operation, a number of major depletions ($\Delta N_e/N_e^0 \lesssim 0.90$) were distributed throughout the F region, from its bottomside gradient centered near 260 km, through the F peak, to a topside altitude of 500 km. The F peak was at 375 km, with $N_e^{\max} = 1.3 \times 10^6 \text{ cm}^{-3}$ ($\pm 250\text{K}$) with no obvious signatures of energy redistribution in and around the depletions. The most intense in-situ irregularities occurred on the bottomside ledge where gradient scale lengths were found to vary between 2 and 25 km. The power spectral density in this region of intense irregularities on the bottomside was dominated by a $k^{-2.5}$ power law over the intermediate wavelength domain $k = 2\pi/1000 \text{ m}^{-1}$ to $k = 2\pi/25 \text{ m}^{-1}$. This result supports the role of the collisional Rayleigh-Taylor instability in generating intermediate-wavelength irregularities during the occurrence of equatorial spread F.

I INTRODUCTION

The DNA/PLUMEX rocket payloads launched into the equatorial ionosphere during the July 1979 campaign carried a complement of plasma diagnostics that included a quadrupole ion mass spectrometer, a pair of pulsed plasma probes, vector electric-field sensors and a four-frequency beacon. The pair of pulsed plasma probes not only provided simultaneous measurements of electron density, N_e , temperature, T_e , and density

fluctuation power spectra, $P_n(k)$, but also provided the capability for a running measurement of relative variations in mean ion mass, $\langle M_i \rangle$.

The measurements of N_e and T_e form the basic information on the laminar condition of the ionosphere, allowing for the determination of the ionospheric plasma response to varying geophysical conditions (solar and magnetic activity, winds, gravity waves, etc.) and the detection of triggering mechanisms (e.g., steep density gradients in N_e) for ionospheric irregularities.

The measurements of δN_e , giving $P_n(k)$, yield important test information for signal channel models as well as possible instability mechanisms (e.g., collisional drift modes, $\bar{E} \times \bar{B}$ and Rayleigh-Taylor), which might be active in the ionospheric plasma.

In this paper we describe the experimental technique, payload configuration, and launch scenarios. We also present additional experimental results that complement companion papers.^{1,2*}

II TECHNICAL OVERVIEW

A. Introduction

The pulsed plasma probe, or P^3 , technique is a unique diagnostic tool that is capable of high spatial and temporal resolution of plasma parameters. The instrument is a Langmuir-type probe using a special electronic procedure for generating the current-voltage characteristic.^{3,4} The result is greatly improved reliability and expanded versatility in Langmuir probe measurements. As a diagnostic tool, the P^3 technique reduces commonly found distortions in derived electron densities and energy distribution functions. A unique feature of the technique is its ability to measure simultaneously the electron temperature, density, and the density-fluctuation power spectrum. Successful applications of the P^3 technique include not only rocket, but also satellite^{5,6} and

*References are listed at the end of this paper.

laboratory beam-plasma studies⁷ of turbulent charged-particle environments.

Figure 1 shows two types of probe operation. Figure 1(a) depicts a linear sawtooth sweep voltage that represents the conventional approach to Langmuir probe operation in which some form of continuous voltage sweep is applied between voltage limits V_- and V_+ . Figure 1(b) shows the pulse-modulated sweep that has been used with P³. The voltage pulses that follow the sawtooth envelope generate the current-voltage characteristic of the probe. During the interpulse period, at constant voltage, V_B , the collected probe current, I_B , provides a direct measure of variations in the probe-plasma system. The pulse duty cycle is short so that the probe rests at its baseline potential, V_B , for a period much longer than the pulse width. Figure 2 shows pulse and baseline durations identified as τ_{on} and τ_B , respectively. So that sweep voltage transients will not affect the value of probe current, the probe current is sampled at the termination of Subinterval τ_i within the sweep pulse and at the center of the baseline Interval τ_B .

With τ_{on} much shorter than either τ_B or the time constant of the probe surface contamination layer,⁴ the pulse procedure will maintain the surface condition and associated voltage drop at a more nearly constant level than if a continuous, slowly-varying sweep voltage was used. The resulting current-voltage characteristic can then be separated from the plasma-density fluctuations (I_B) so that the electron temperature and density are determined uniquely. In addition, the I_B values provide the raw data from which density-fluctuation power spectra are determined.

B. Payload Configuration and P³ Characteristics

A pair of pulsed probes were extended diametrically from the forward end of the rocket payload (Figure 3). The sensing elements, constructed from tungsten wire, were isolated from their extension booms by coaxial guard electrodes that were driven at the same potential as the probes themselves. One of the probes, defined as the I probe, operated with $V_B \approx 1$ V, yielding net ion baseline current of I_B^i . The

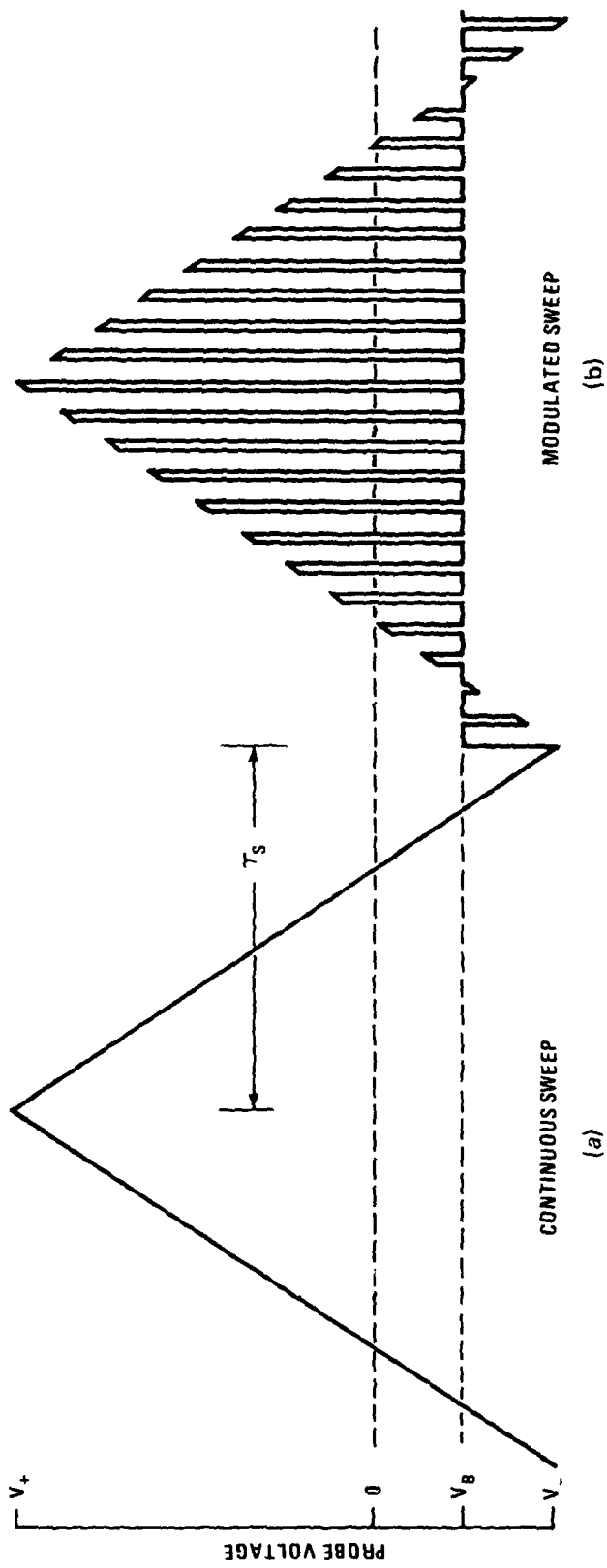


FIGURE 1 CONTINUOUS AND PULSED MODES OF PROBE OPERATION. (a) represents the conventional approach and (b) shows the modulated sweep utilized in the P^3 technique.

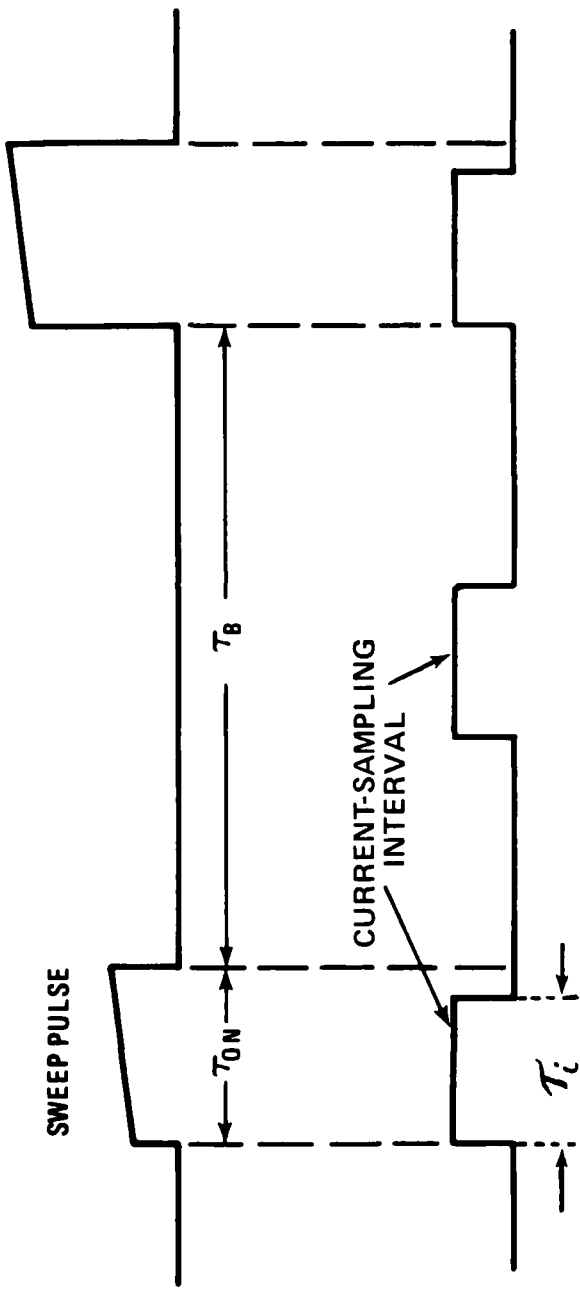


FIGURE 2 THE SWEEP PULSES (FIGURE 1) SHOWN ON AN EXPANDED SCALE TO ILLUSTRATE THE PROBE-CURRENT SAMPLING INTERVALS.

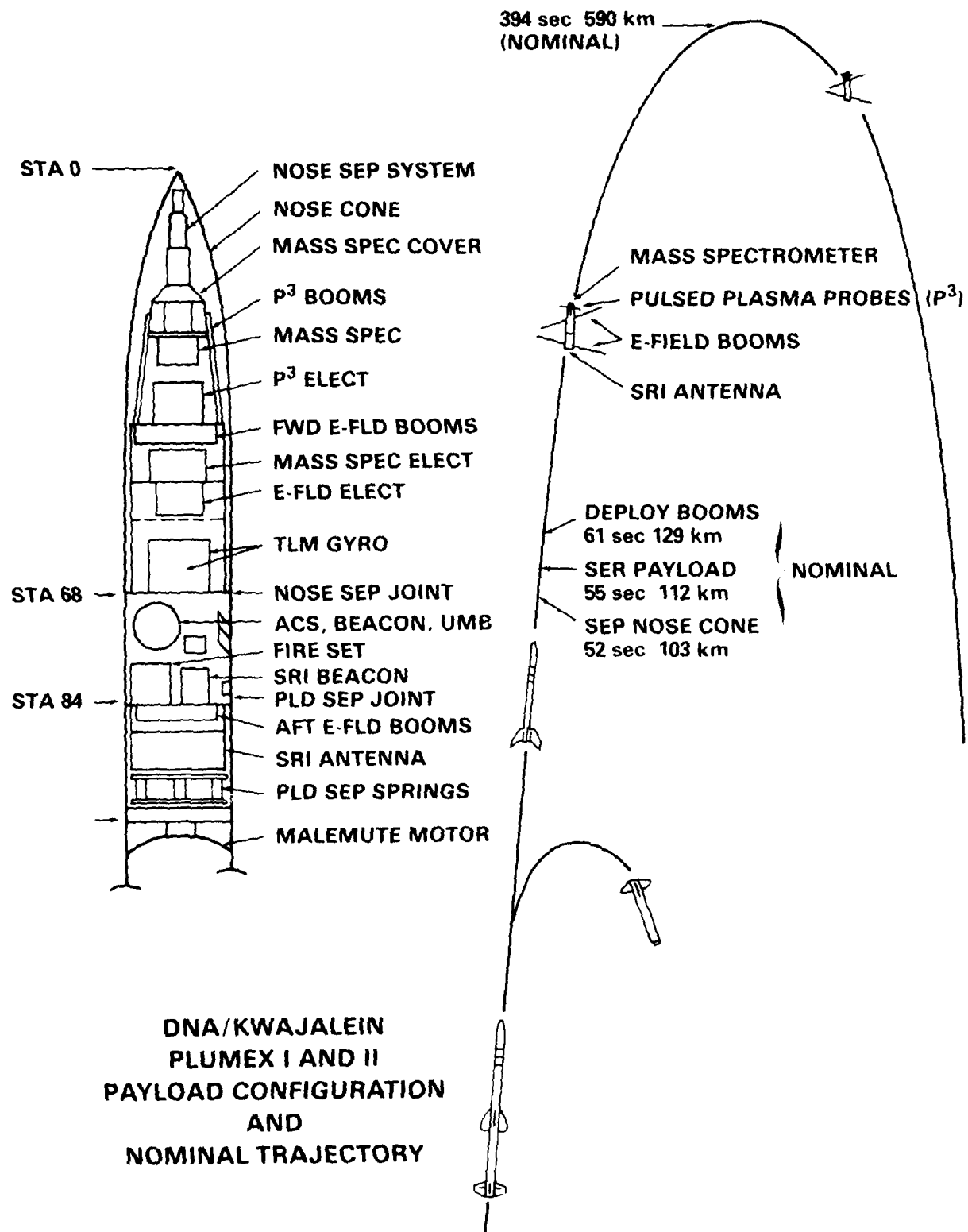


FIGURE 3 PLUMEX I AND II PAYLOAD CONFIGURATION AND NOMINAL TRAJECTORY.
(This figure has been adapted from a Sandia report.)

other probe, defined as the E probe, operated with $V_B \approx 2$ V, yielding net electron baseline current of I_B^e . Both probes generated complete current-voltage characteristics in ≈ 400 ms, yielding absolute values of N_e and T_e at an approximate 2.5-Hz rate. Maximum I_B sampling occurred at 2048 Hz, resulting in 0.5 m spatial resolution for relative electron density fluctuations at a vehicle velocity of 1 km/s.

Probe electrometers were set to operate over a dynamic range extending from 4×10^{-10} to 2.5×10^{-4} A, with automatic switching over 8 ranges maintaining 9-bit accuracy for all anticipated ionospheric conditions. The automatic ranging is best illustrated in Figure 4: an actual in-flight analog record of telemetry channel outputs for the probe currents and applied voltages; the roll magnetometer for magnetic aspect determinations; and pitch, yaw, and roll monitors on the ACS jets. The data sample presented in Figure 4 was collected when the payload was 55 s into flight while the probe electrometers were being driven through a load resistor for calibration. The operation of the probe alternated between a fixed-bias mode and a pulsed-sweep mode, with absolute currents determined by a simple algorithm that coupled the switching 0 to 5 V TM signal on PCM channel 26-1 with the sweep current range monitor on channel 27-1. The record format in Figure 4 helped provide field estimates of density profiles without distortions of magnetic aspect sensitivities and attitude control jets.

III RESULTS

A. Density Profiles and Irregularity Structures

By 2100 LT on the night of the first rocket launch (PLUMEX I) the bottomside of the F region had risen to an approximate altitude of 400 km. The F region then began a downward drift with a simultaneous onset of spread F. The downward drifting and spread-F conditions continued. When the bottomside F layer had descended to an altitude below 300 km, the rocket was launched (1231:30 UT on day 198; 0031:30 LT, 17 July 1979).

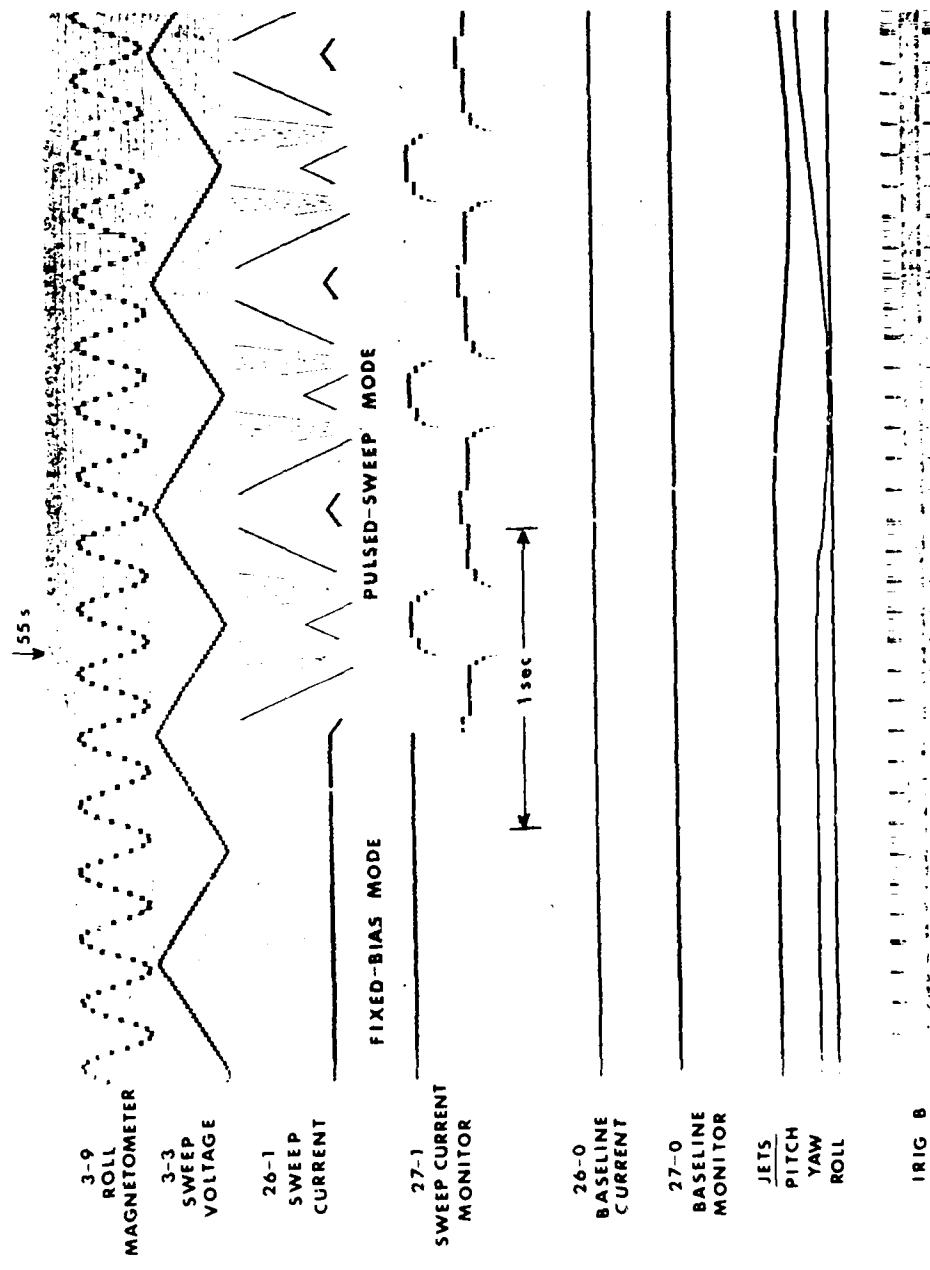


FIG 8

FIGURE 4 ANALOG RECORD OF PLUMEX 1 TELEMETRY CHANNELS (3-9 AND 3-3) ILLUSTRATING PULSED PLASMA-PROBE OUTPUTS AND RELEVANT VEHICLE INFORMATION (ROLL MAGNETOMETER, ATTITUDE CONTROL JETS AND IRIG B TIMING). The probe electrometers (26-1) cover six decades of current in 8 automatic-switching ranges (26-1 above shows automatic ranging, and 27-1 identifies each range through a simple algorithm). A 9-bit accuracy is maintained throughout.

Figure 5 displays the upleg measurements of relative electron density as presented by correlated ion- (I_B^i) and electron-saturation $I_e^i(V^+)$ currents. The ordinate has a linear scale for time-after-launch with altitude superimposed at 50-s increments. Because ion and electron saturation currents have significantly different sensitivities to velocity, sheath, and magnetic-field effects,⁷ variations in I_B^i and $I_e^i(V^+)$, not mutually corroborated, were attributed to the various aspect sensitivities and excluded from Figure 5. This approach made analysis easier, reduced computer time, and established the credibility of the interpretation of the curves as relative electron-density profiles.

The results in Figure 5 show that a number of major depletions ($\Delta N_e / N_e^0 \lesssim 0.9$) were distributed throughout the F region. Each of the large-scale depletions (identified alphabetically) has its own distribution of irregularities, illustrated in Figure 6 by the expanded view of Regions C, D, H, and I. It is clear that Region C is not a single narrow bite-out, but a collection of rather large irregular structures extending over a total altitude domain of about 12 km. (Vehicle velocity in Region C was 2.4 km/s.) To develop a quantitative view of irregularity fluctuations observed in the F region, continuous linear detrends were executed throughout the entire upleg trajectory. The variations about those linear detrends were then plotted in Figure 5 as "Irregularity Intensity," with a maximum relative scale of ± 4 . A fluctuation as great as ± 4 approximately represents a ± 80 -percent fluctuation about the linear detrend. (Correlation of these results with macroscale gradients and ALTAIR backscatter contours are discussed in a companion paper.¹)

B. Absolute Density and Temperature

Absolute values of electron density and temperature were determined by conventional analyses of Langmuir probe characteristics³ with appropriate care to eliminate perturbing effects of surface contamination,⁴ density fluctuations,^{5,10} and magnetic-field effects.⁶ Approximately 25 characteristics were analyzed over the F layer from 340 to 560 km. In each case a conversion coefficient, $a = N_e / I_e(V^+)$, with N_e measured in electrons/cm³ and I_e in amperes, was determined so that the $I_e(V^+)$

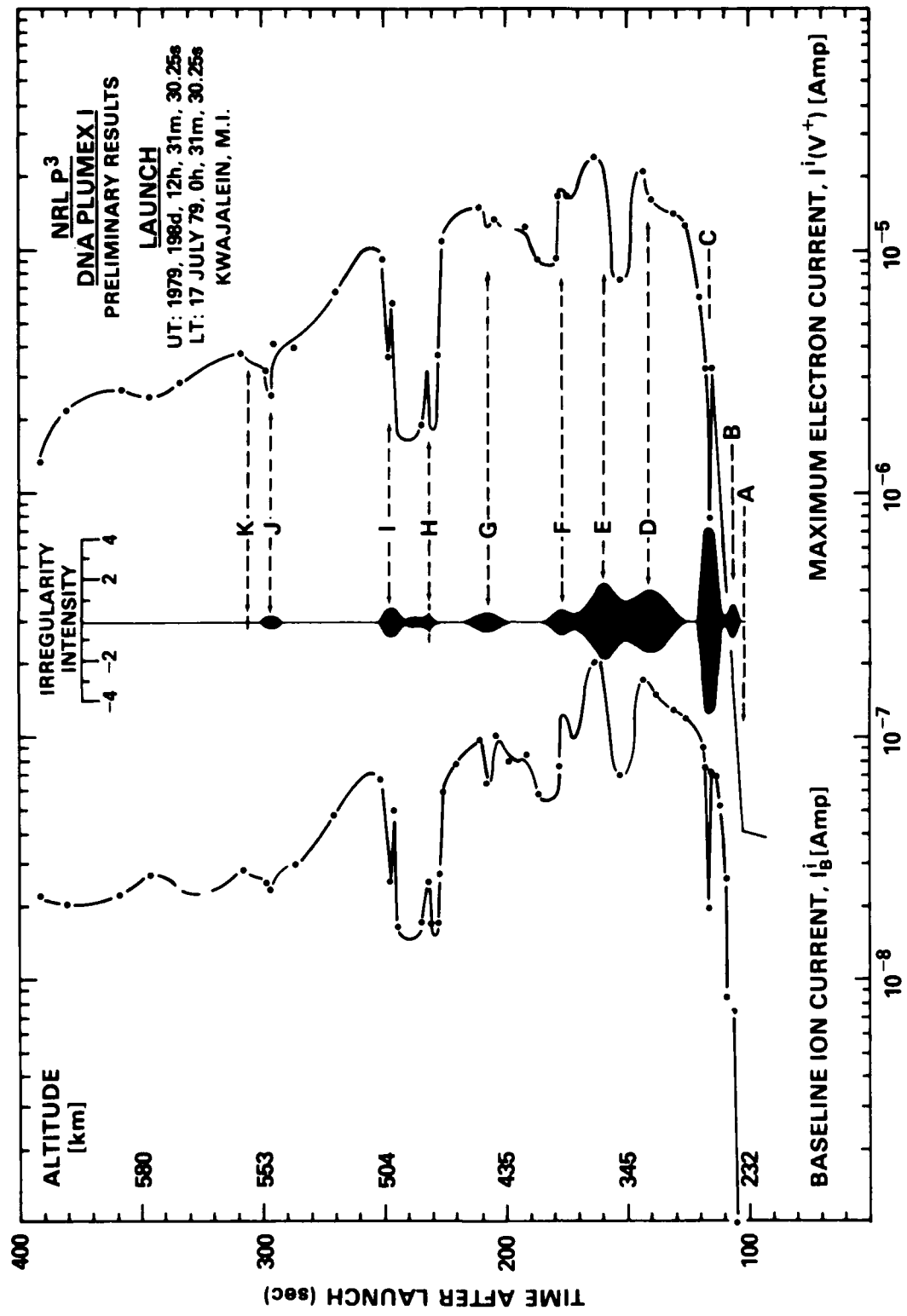


FIGURE 5 RELATIVE ELECTRON-DENSITY PROFILE OF MACROSCALE FEATURES AS MEASURED SIMULTANEOUSLY BY ION- AND ELECTRON-SATURATION PROBE CURRENTS COLLECTED ON THE UPLEG TRAJECTORY OF PLUMEX I. The "irregularity intensity" provides a measure of smaller scale structure with a ± 4 intensity approximately equal to ± 80 -percent fluctuations about a linear detrend.

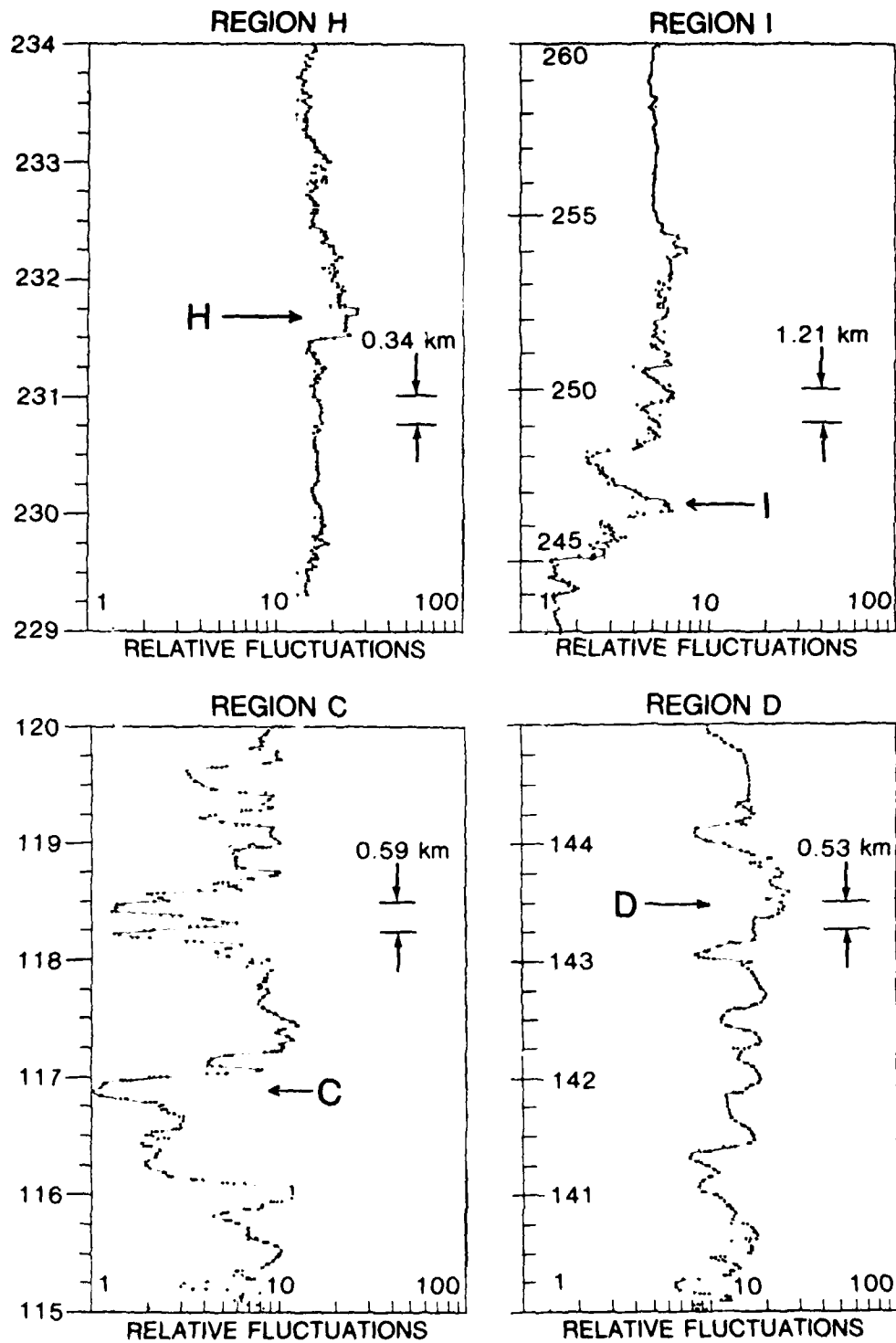


FIGURE 6 EXPANDED VIEWS OF DENSITY FLUCTUATIONS OBSERVED IN REGIONS C, D, H, AND I OF FIGURE 5.

profile in Figure 5 could be directly scaled to absolute electron densities. This procedure yielded $a = 5.5 \times 10^{10}$ electrons $\text{cm}^{-3}\text{A}^{-1}$ ($\pm 10\%$).

The upleg profile has been reconstructed in Figure 7 with relative and absolute electron density plotted as a function of altitude. The result shows the F peak at 375 km, with a maximum density of 1.3×10^6 cm^{-3} ($\pm 10\%$).

Analysis of the retarding-field region of the same set of current-voltage characteristics yielded $T_e = 1350$ K (± 250 K), with no obvious signatures of electron energy redistribution in and around the depletions.

C. Intermediate Wavelength Power Spectra

The pulsed-probe data provided an excellent opportunity for comparison with the numerical simulations¹¹ of the collisional Rayleigh-Taylor (R-T) instability at intermediate wavelengths. Attention is focused on the bottomside F-layer gradient and Region C, which is believed representative of the midphase development of the R-T process.¹ Typically, computer simulations employ several values for the zero-order gradient scale length

$$L = \left(\frac{1}{N_e^0} \frac{dN_e^0}{dy} \right)^{-1}$$

and initiate the code with some two-dimensional perturbation superimposed. In the work of Keskinen et al.,¹¹ L was selected at 5, 10, and 15 km and the perturbation took the form¹¹:

$$\frac{\delta N_e(x, y, t=0)}{N_e^0} = \sin(k_y y) \cos(k_x x) \times 10^{-4} + 2 \sin(2k_y y) \times 10^{-6}$$

Under actual conditions encountered in PLUMEX I (Figure 7), the bottomside F-layer gradient extended from 240 to 290 km. The question of gradient scale length can be studied in Figure 8 in which it is

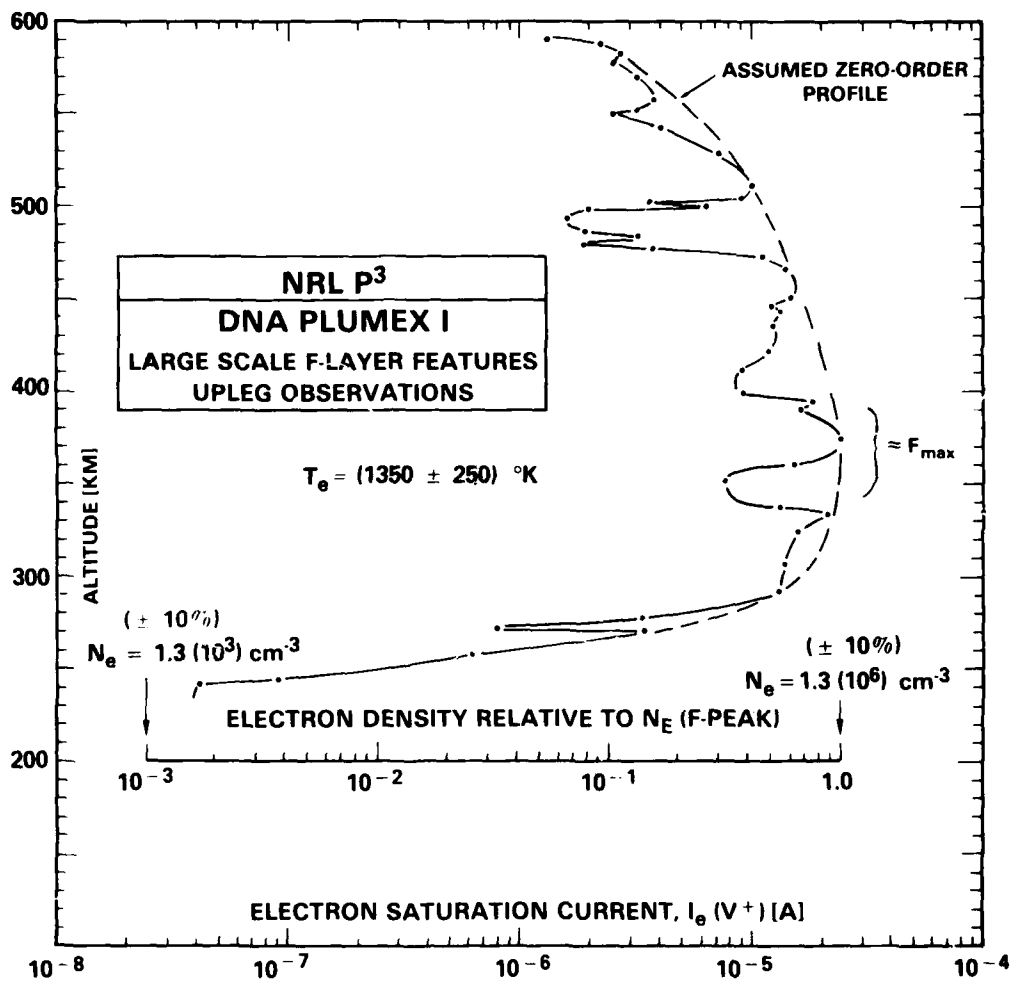


FIGURE 7 RELATIVE AND ABSOLUTE PROFILE OF ELECTRON DENSITY (PLUMEX I UPLEG).

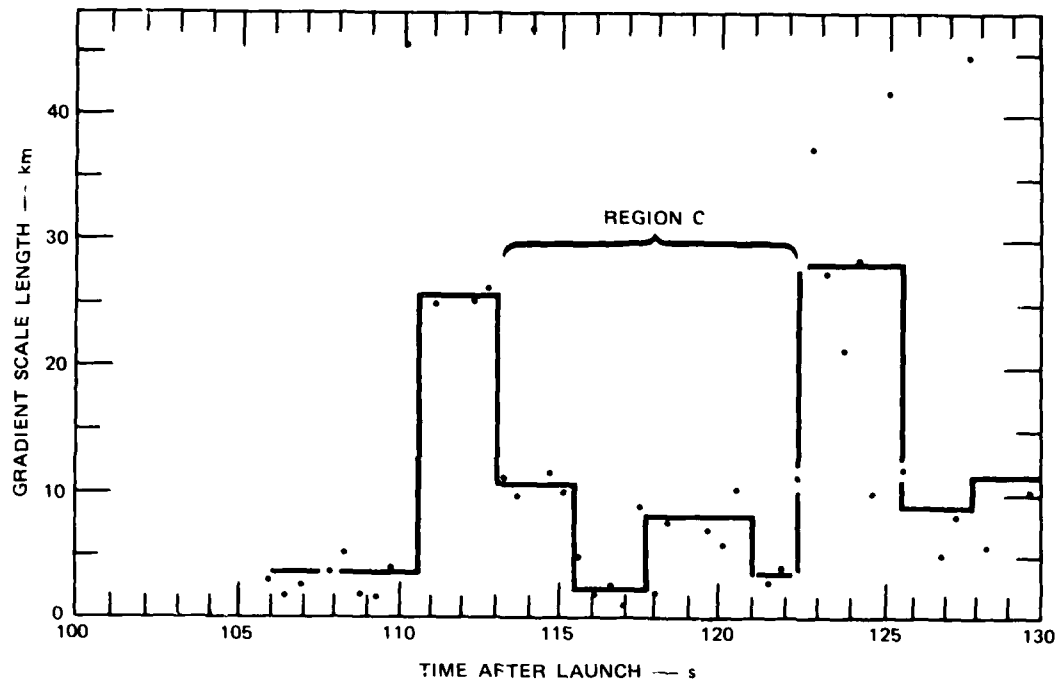


FIGURE 8 GRADIENT SCALE LENGTHS $\left(L = \left[\frac{1}{N_e^0} \frac{dN_e^0}{dy} \right]^{-1} \right)$ **ON THE BOTTOMSIDE**
GRADIENT OF THE F-REGION LAYER SHOWN IN FIGURES 5 AND 6.

shown that the bottomside gradient (encompassed in the 105- to 125-s period) is not characterized by a single value of L . In Region C ($114 s \leq t \leq 122 s$), L is seen to vary between 2 and 10 km, but in adjacent domains ($110 s < t < 113 s$ and $122 s \leq t < 126 s$) can be characterized by $L = 25$ km. We would suggest that the adjacent domains are representative of the zero-order gradient-scale length and that $L = 25$ would be a more appropriate value in the numerical simulation.

In any event, computer simulations¹¹ with $L = 5$, 10, and 15 km showed that linearly unstable modes saturate by nonlinear generation of vertical modes. The results yield one-dimensional power laws (horizontal and vertical) that vary with a spectral index ($\equiv n$ in $P_{N_e^0} \propto k^{-n}$) between 2.0 and 2.5. To explore this result within the context of Region C, power spectral analyses were conducted over sliding intervals of 2.4 km. The results, presented in Figure 9, show that the dominant behavior is $k^{-2.5}$ over the range $k = 2\pi/1000 m^{-1}$ to $k = 2\pi/25 m^{-1}$. The $k^{-1.85}$

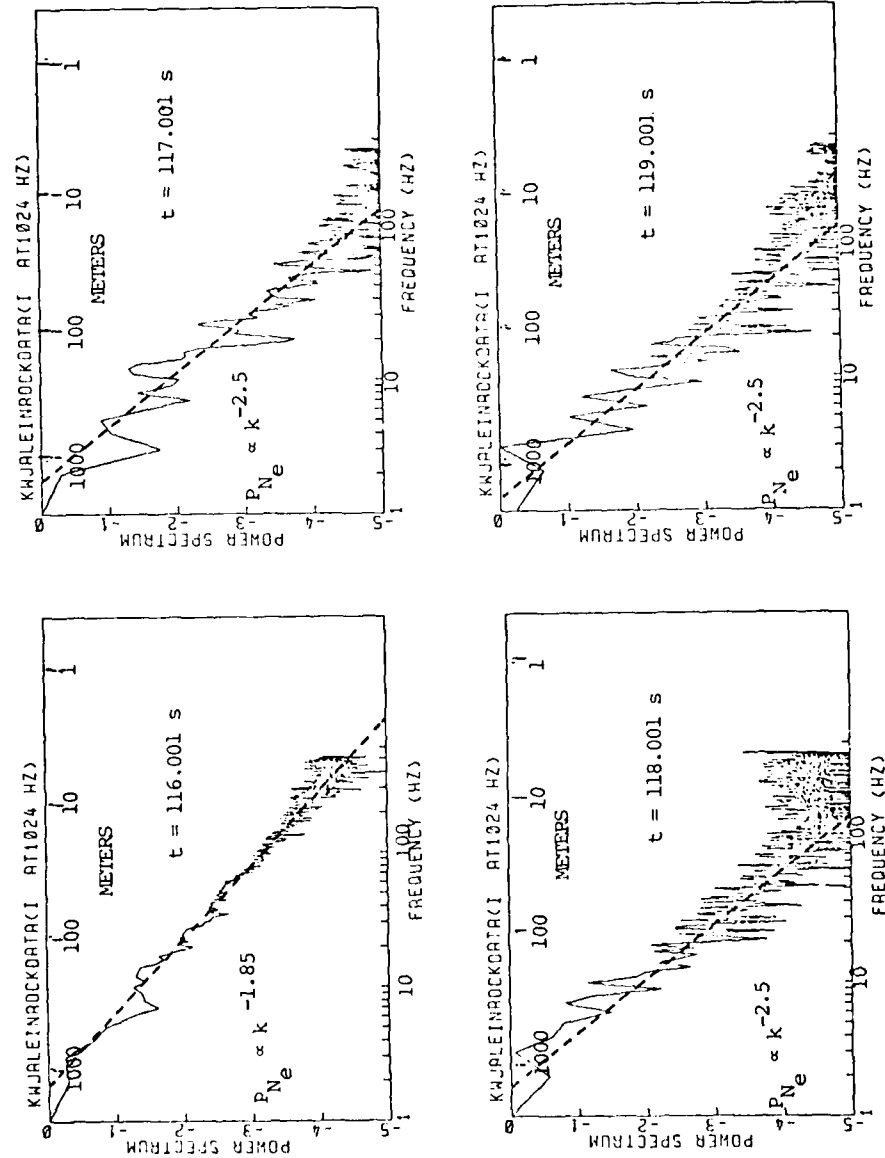


FIGURE 9 POWER SPECTRAL ANALYSES OF DENSITY FLUCTUATIONS IN REGION C
(FIGURE 5).

behavior at $t = 116.001$ s is a result of the very sharp density gradient (Region C, Figure 6) encompassed by the domain of the spectral analysis.

In general we would conclude that our results support the numerical simulations of Keskinen et al.¹¹ We point out, however, that a spectral index variation from 2 to 2.5 is a rather broad domain. Further testing of this support can be achieved with an $L = 25$ -km simulation and a downward drifting F-layer model that is more in keeping with the actual experimental conditions. The F-layer time history can be important because unstable modes appear to require times in excess of 4,000 s to saturate--a time during which the F layer encountered in PLUMEX I drifted downward in excess of 40 km.

IV SUMMARY

In each of the two rocket operations (PLUMEX I and II) conducted at the Kwajalein Atoll during July 1979, the NRL pulsed plasma probe performed flawlessly. General results concerning coordinated rocket and radar measurements of small- and large-scale irregularities have been discussed in companion papers.^{1,2} Complementary results developed here include:

- In PLUMEX I a number of major depletions ($\Delta N_e/N_e^0 \lesssim 0.9$) were distributed throughout the F region, from the bottom-side gradient centered near 260 km, through the F peak, to a topside altitude of 500 km. The most intense in-situ irregularities occurred on the bottomside ledge where gradient-scale lengths were found to vary between 2 and 25 km. The power-spectral density in this region of intense irregularities on the bottomside was dominated by a $k^{-2.5}$ power law over the intermediate wavelength domain, $k = 2/1000 \text{ m}^{-1}$ to $k = 2/25 \text{ m}^{-1}$. The experimental conditions were reasonably matched to the numerical simulations of Keskinen et al.,¹¹ and a comparison of the two resulted in general agreement.
- In PLUMEX I, the F peak was at 375 km, with $N_e^{\max} = 1.3 \times 10^{16} \text{ cm}^{-3}$ ($\pm 10\%$). The electron energy distribution was characterized by $T_e = (1350 \text{ K} \pm 250 \text{ K})$ with no obvious signatures of energy redistribution in and around the depletions.

ACKNOWLEDGMENTS

This work was supported by the Defense Nuclear Agency under Subtask Code I25AAXHX640, Communications Effects Experiments (Plasma Probes). We wish to thank L. Kegley for his dedication in every phase of instrument development from design through field operations. We also extend our thanks to Dr. C. S. Lin for his diligence and commitment to the task of data reduction and analysis.

REFERENCES

1. E. P. Szuszczewicz, R. T. Tsunoda, R. Narcisi, and J. C. Holmes, "PLUMEX I: Coincident Radar and Rocket Observations of Equatorial Spread F," Proceed. of the Summer Equatorial Experiment Data Review Meeting, 18 March 1980 (1980).
2. E. P. Szuszczewicz, R. T. Tsunoda, R. Narcisi, and J. C. Holmes, "PLUMEX II: Coincident Radar and Rocket Observations of Equatorial Spread F," Proceed. of the Summer Equatorial Experiment Data Review Meeting, 18 March 1980 (1980).
3. J. C. Holmes and E. P. Szuszczewicz, "Versatile Plasma Probe," Rev. Sci. Instr., Vol. 46, No. 5, pp. 592-598 (May 1975).
4. E. P. Szuszczewicz and J. C. Holmes, "Surface Contamination of Active Electrodes in Plasmas: Distortion of Conventional Langmuir Probe Measurements," J. Appl. Phys., Vol. 46, No. 12, pp. 5134-5139 (December 1975).
5. E. P. Szuszczewicz, J. C. Holmes, and D. N. Walker, "On the Probing of Ion and Electron Irregularity Spectra," EOS, Vol. 60, No. 18, p. 339 (May 1979).
6. M. Singh, E. P. Szuszczewicz, and J. C. Holmes, "High Resolution Measurements of Equatorial F-Region Irregularities," EOS, Vol. 61, No. 17, p. 314 (April 1980).
7. E. P. Szuszczewicz, J. C. Holmes, and D. N. Walker, "Plasma Diffusion in a Space-Simulation Beam-Plasma-Discharge," Geophys. Res. Lett., 6, No. 3, pp. 201-204 (March 1979).
8. E. P. Szuszczewicz and P. Z. Takacs, "Magnetosheath Effects on Cylindrical Langmuir Probes," Phys. Fluids, Vol. 22, No. 12, pp. 2424-2433 (December 1979).

9. F. F. Chen, "Electrical Probes," Plasma Diagnostic Techniques, R. H. Huddlestone and S. L. Leonard, eds., pp. 113-200 (Academic Press, New York, 1965).
10. E. P. Szuszczewicz and J. C. Holmes, "Observations of Electron Temperature Gradients in Mid-Latitude E_s Layers," J. Geophys. Res., Vol. 82, No. 32, pp. 5073-5080 (November 1977).
11. M. J. Keskinen, S. L. Ossakow, and P. K. Chaturvedi, "Preliminary Report on Numerical Simulations of Intermediate Wavelength Collisional Rayleigh-Taylor Instability in Equatorial Spread F," J. Geophys. Res., Vol. 85, No. A4, pp. 1775-1778 (April 1980).
12. P. K. Chaturvedi and S. L. Ossakow, "Nonlinear Theory of the Collisional Rayleigh-Taylor Instability in Equatorial Spread F," Geophys. Res. Lett., Vol. 4, No. 12, pp. 558-560 (December 1979).

ALTAIR RADAR MEASUREMENTS IN SUPPORT OF THE PLUMEX ROCKET CAMPAIGN

Roland T. Tsunoda
Radio Physics Laboratory
SRI International
Menlo Park, CA 94025

I INTRODUCTION

During July 1979, the Defense Nuclear Agency (DNA) conducted a coordinated rocket campaign, called PLUMEX, at Kwajalein Atoll, Marshall Islands, to study equatorial spread-F (ESF) phenomena--in particular, the formation and character of intense, scintillation-producing irregularities in the equatorial ionosphere. SRI International conducted a supporting experiment, using the ALTAIR radar located on Roi-Namur Island in the Kwajalein Atoll. The objectives of the ALTAIR experiment were to provide the key real-time diagnostics needed as rocket-launch criteria, and to establish a unique data base that would be extremely valuable for furthering our understanding of equatorial spread F.

ALTAIR was operated for eight nights, including 17 and 24 July 1979 (UT dates) when the two PLUMEX rockets were launched. A summary of the ALTAIR data base is given in Table 1. Except on the nights that the rockets were launched, typical operation was from 0730 to about 1100 UT. (Local solar time leads universal time by 11 hours and 10 min.) Segments of this data base have been analyzed and those results will be presented in future reports.

In this report, we present a summary of ALTAIR measurements made on the nights of the two rocket launches. These measurements are described and then discussed in the light of our current understanding of ESF phenomena.

Table 1
ALTAIR DATA SUMMARY

Date (UT)	Time (UT)	Description
13 July	0710 to 1030	Test night (limited amount of data) Quiet, some development of bottomside spread F
14 July	0725 to 1040	Countdown rehearsal Moderate activity, plumes
17 July	0740 to 1320	1st rocket Strong plume activity
18 July	0715 to 1040	Radar night Absolutely quiet
19 July	0730 to 1050	Radar night Spread-F activity, plumes
22 July	0715 to 1040	Radar night Spread-F activity, plumes
23 July	0730 to 1120	Rocket countdown, scrubbed Spread F
24 July	0720 to 1210	2nd Rocket Strong plume activity

II THE EXPERIMENT

ALTAIR was operated in a number of antenna beam-steering modes during the eight nights. Operational modes included (1) east-west scans made with the radar beam directed perpendicularly to the geomagnetic-field lines at F-region altitudes, (2) east-west scans at off-perpendicular angles, (3) latitude scans in the magnetic meridian, and (4) skintracks of east-west orbiting satellites. The magnetic perpendicular, east-west scan was the basic mode used to detect and track backscatter plumes from the west into the rocket-launch corridor. Latitude scans and east-west scans at off-perpendicular angles were used for incoherent-scatter measurements of the background F layer. In addition, the satellite tracks were used to spatially map the east-west variations in total electron content and scintillations. We are concerned here with

only the magnetically perpendicular east-west scans that detected and characterized the backscatter plumes toward which the two rockets were launched.

The basic radar parameters for ALTAIR are given in Table 2. ALTAIR operates at two frequencies simultaneously, and has power-aperture products at both frequencies that are large enough for incoherent-scatter measurements. The pulsedwidths of 30 μ s (VHF) and 40 μ s (UHF) correspond to range resolutions of 4.5 km and 6 km, respectively. Although both VHF and UHF data were recorded, only the VHF data are presented in this report. The VHF data are approximately 10 dB more sensitive to ESF irregularities than that obtained at UHF, and hence are useful for the descriptive purposes of this report. More detailed descriptions of ALTAIR system characteristics and the various modes of operation have been published previously by Tsunoda et al.^{1*} and Towle.²

Table 2
ALTAIR SYSTEM CHARACTERISTICS

PARAMETER	VHF	UHF
Frequency (MHz)	155.5	415.0
Peak Power (MW)	10.0	20.0
Pulsedwidth (μ s)	30.0	40.0
Antenna		
Diameter (m)	45.7	45.7
Beamwidth (deg)	2.8	1.1
Gain (dB)	34.7	42.4
Effective aperture (m^2)	870.0	720.0
Temperature (K)	975.0	785.0

* References are listed at the end of this paper.

The principal changes in the basic east-west scan used during the 1979 DNA campaign (as compared to those described by Tsunoda et al.¹ and Towle² are (1) the scan was continuous, with selectable scan rates, (2) the scan was reversible, allowing east-to-west scans as well as west-to-east scans, and (3) the largest sector that could be scanned was expanded nearly double to that used in past years. A continuous scan allowed improved angular resolution. The reversible scan with selectable scan rate allowed improved time resolution of backscatter plumes. In addition, the expanded sector coverage allowed the detection of backscatter plumes further to the west, and the tracking of time evolution over a longer period of time. For example, the mapping of wave structure in the bottomside F layer and the observation of plume development from this wave structure, made possible by the expanded sector coverage, are described by Tsunoda and White.³

III FIRST ROCKET NIGHT--17 July 1979

A. Ionospheric Conditions

A summary of the ionospheric conditions that prevailed during the first rocket night is presented in Figure 1. Using ionogram data that SRI collected nearby we have plotted $h'F$, the minimum virtual height of the F layer, as a function of time. (Note that Kwajalein Standard Time is 12 hours behind universal, and that local solar time leads universal time by 11 hours 10 min.) Prior to 0700 UT, the bottom of the F layer was situated below a 250-km altitude. A rapid lifting of the F layer followed, between 0730 and 0900 UT, coinciding approximately with E-region sunset. This postsunset rise of the F layer is a regular feature in the equatorial ionosphere, and associated with solar maximum conditions.⁴

Equatorial spread F, as seen on ionograms, commenced shortly after 0900 UT and developed very rapidly into strong range spread. By 0930 UT, the ionogram traces were completely spread. The period from 0930 UT to around 1300 UT was characterized by a gradual descent of the F layer, and a corresponding general decay in ESF activity. By 1330 UT, the ionogram traces were virtually without spread.

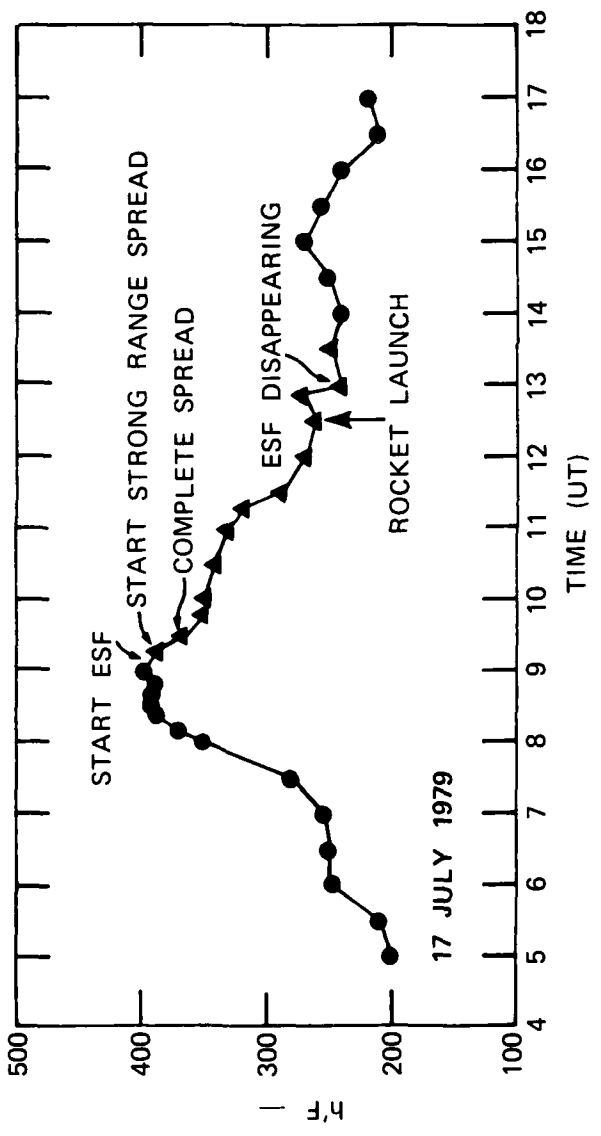


FIGURE 1
IONOSPHERIC CONDITIONS FOR THE FIRST ROCKET NIGHT
(17 JULY 1979) AS DEPICTED BY $h'F$, VIRTUAL HEIGHT OF THE
F LAYER, PLOTTED AS A FUNCTION OF TIME

The first rocket was launched at 1231:30 UT, as shown in Figure 1. Both rocket and ALTAIR data, therefore, correspond to measurements of decaying ESF irregularities.

B. ALTAIR Measurements

ALTAIR east-west scans commenced at 0740 UT. At that time there was no evidence of ESF backscatter (which is consistent with ionogram data), but after one scan radio-frequency (rf) silence was imposed. When rf silence was lifted, strong backscatter plume activity was in progress (~0942 UT). Backscatter plume activity continued through the time of the rocket launch up to the time of the last east-west scan by ALTAIR, around 1250 UT. Plume activity was definitely weakening at that time.

An east-west scan taken between 1119:38 and 1126:18 UT is shown in Figure 2. Strong backscatter plumes exist over ALTAIR and to the west. The backscatter plume through which the rocket was launched, more than an hour after this scan was made, is just entering the scanned sector--approximately 600 km west of ALTAIR. (An eastward drift of 600 km/hr corresponds to 167 m/s.) At this time, the plume already extended up to almost a 600-km altitude, and its backscatter strength was 50 dB above incoherent-scatter (IS) levels. The backscatter plumes were mapped continuously by ALTAIR and were tracked as they drifted eastward toward the rocket launch corridor.

The fully developed plume of interest, as it approached overhead of ALTAIR, is shown in Figure 3. The scan was made about 19.5 prior to rocket launch. The 30-dB contour is seen to extend in altitude from 300 km up to 750 km. The backscatter strength appears to be weakening, compared with that shown in Figure 2.

The geometric relationship between the rocket trajectory and the plane containing the ALTAIR scan sector is shown in Figure 4. The coordinates of the plot are geographic latitude and longitude. The location of the point directly beneath the rocket (subrocket point) as a function of time after launch is shown by a curve that begins at

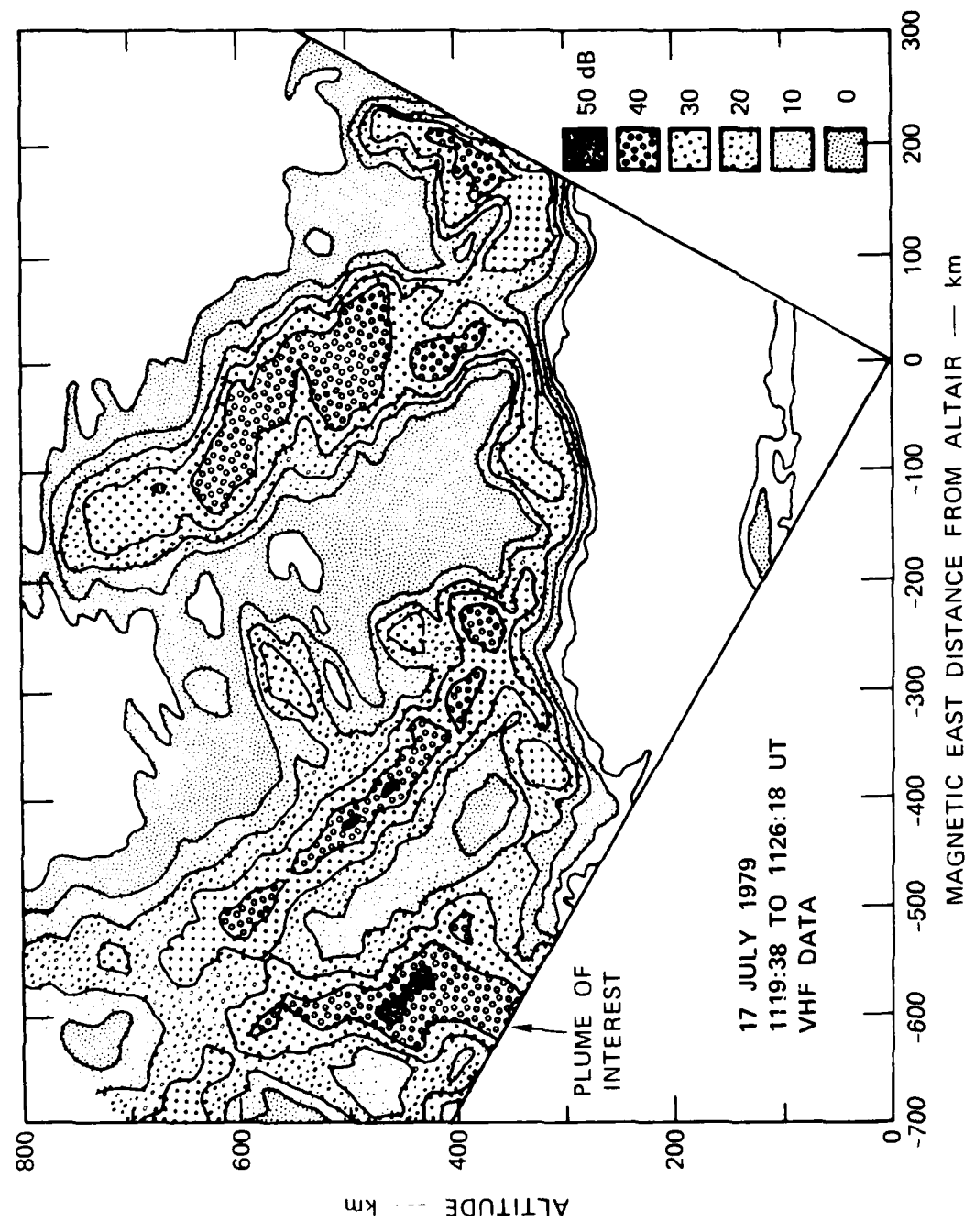


FIGURE 2 FIRST DETECTION OF THE BACKSCATTER PLUME OF INTEREST — 17 JULY 1979

1212:00-UT
17 JULY 1979

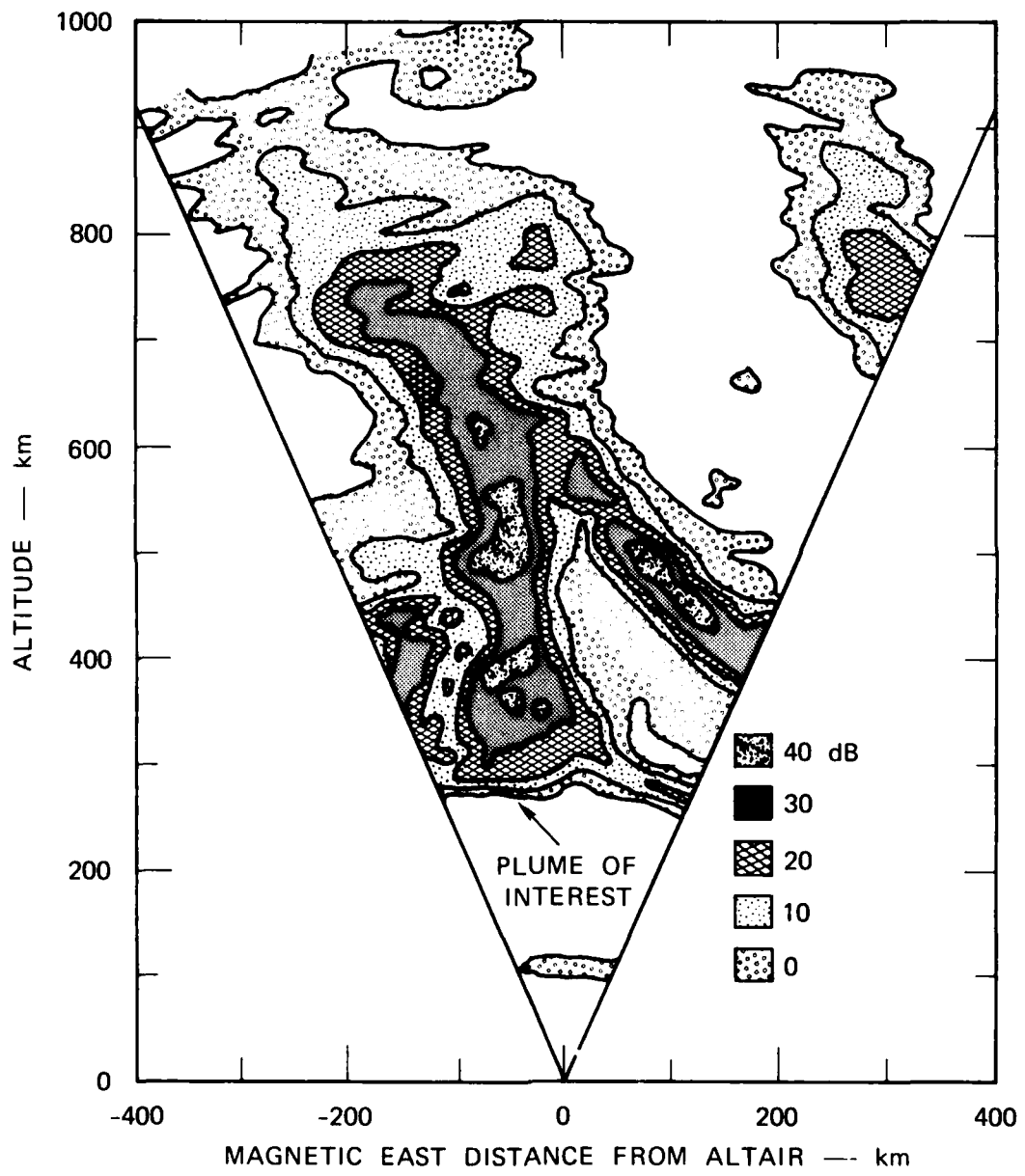


FIGURE 3 BACKSCATTER PLUME OF INTEREST AS IT APPROACHED THE ROCKET LAUNCH CORRIDOR — 17 JULY 1979

17 JULY 1979
T = 1231:30.5 UT

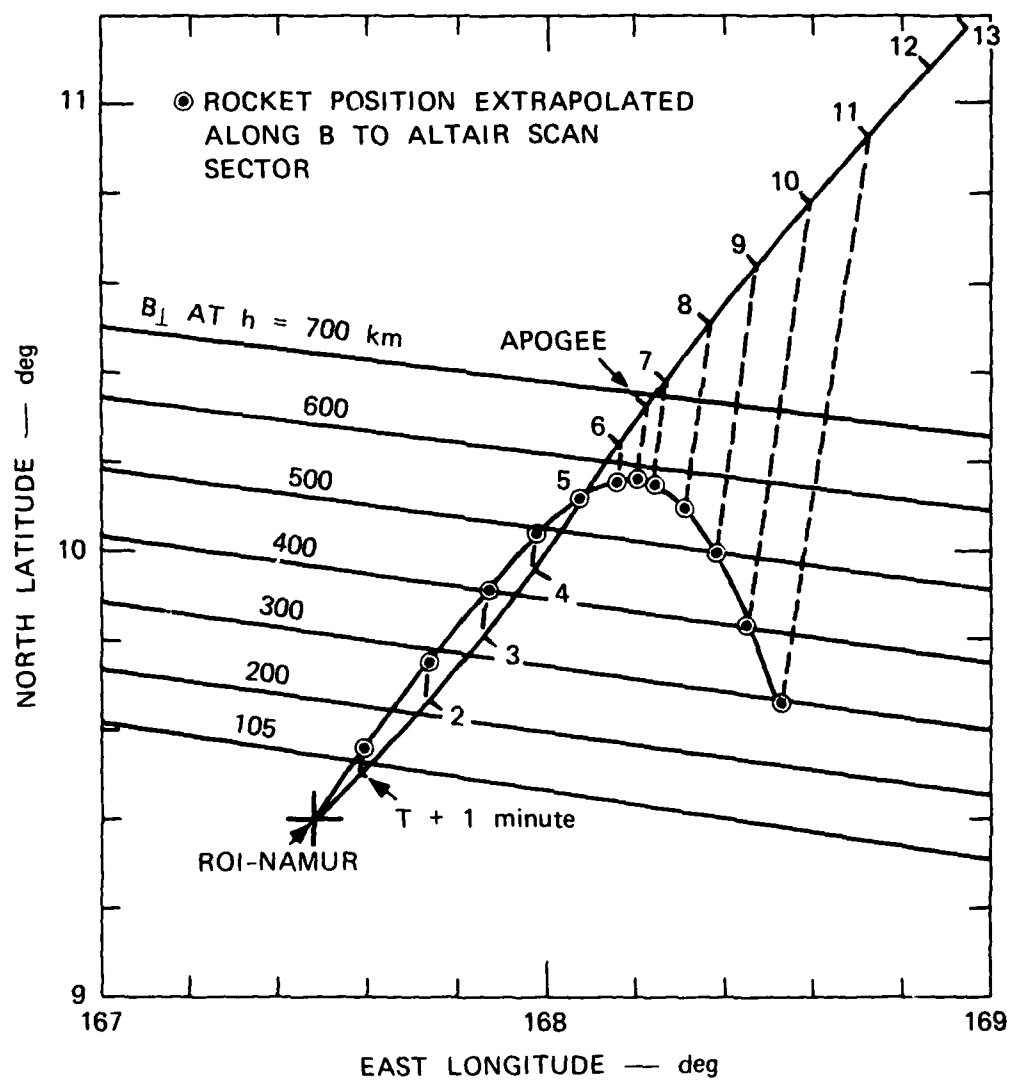


FIGURE 4 ROCKET TRAJECTORY AND ITS EXTRAPOLATION INTO THE EAST-WEST SECTOR SCANNED BY ALTAIR ---
17 JULY 1979 (T = 1231:30 UT)

Roi-Namur Island and extends into the northeast corner of the figure. The tick marks on the curve correspond to the subrocket position, and are shown at one-minute intervals from the time of launch, T. The trajectory data used for this plot was provided by William Millard (Sandia Corporation) from his model trajectory calculations. The plane containing the ALTAIR scan sector is shown schematically by the parallel lines that slope downward to the right of the figure. Each line represents the ground image of the loci of points at which the radar beam perpendicularly intersects the geomagnetic field, labeled B, at a given altitude. The actual plane that contains the zero magnetic aspect points is positioned perpendicularly to the magnetic meridian (9° E true azimuth) and titled at an angle of 9° N of vertical.

The rocket trajectory--as it would map along the geomagnetic-field lines, B, onto the ALTAIR scan sector--can, therefore, be schematically drawn, by extrapolating the subrocket positions along a constant magnetic declination, to the position (in latitude and longitude) on the schematic plane (zero magnetic aspect) that corresponds to the appropriate rocket altitude. In this figure, the trajectory (constructed as described above) is shown as circles connected by a smooth curve. The rocket trajectory has a velocity component in the magnetic east direction. We can estimate its value by measuring the eastward displacement for any given interval of time. For example, at an altitude of 500 km, the mean eastward rocket speed was about 150 m/s (using the T + 4-min and T + 9-min points). Later in this report, we show that this velocity value was comparable to the eastward plume drift of about 160 m/s.

At the time of the rocket flight, the spatial distribution of backscatter that was observed with ALTAIR at VHF 9 (155.5 MHz) is shown by the three backscatter contour maps in Figure 5. Each map is drawn using calibrated contours of constant backscatter strength--after correcting for the range-squared decrease in signal strength. The regions between contours have been shaded for greater clarity.

The strongest backscatter regions (shown near the right edge of the first map) is the backscatter plume of interest. The rocket trajectory is displayed by straight-line segments containing circles that correspond

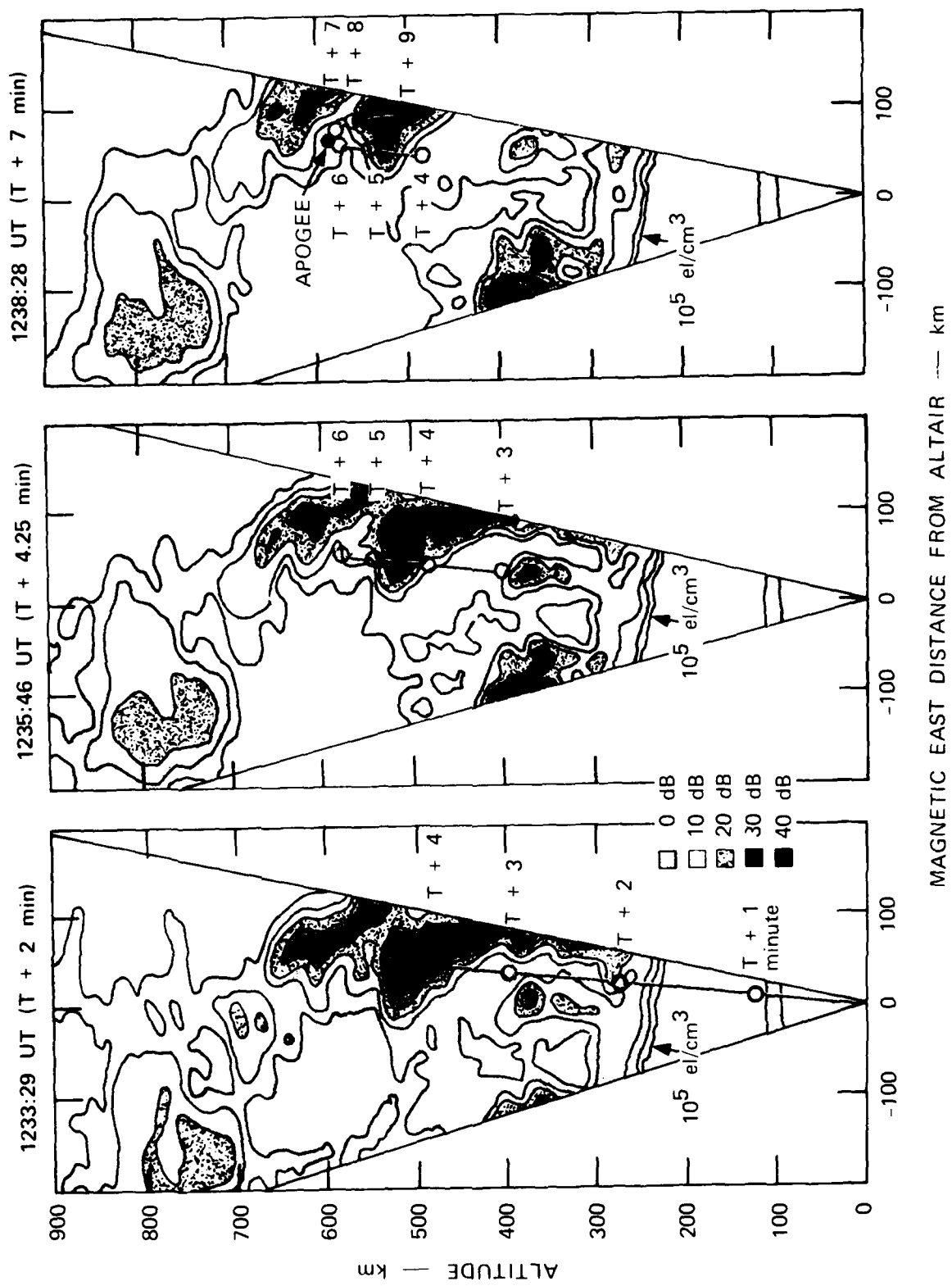


FIGURE 5 ALTAIR BACKSCATTER MAPS OBTAINED DURING THE FIRST ROCKET FLIGHT — 17 JULY 1979

to a one-minute interval. The rocket barely missed passing directly along the neck of the plume, i.e., the strong backscatter region that connects the plume to the bottomside backscatter region. Instead of this course, the rocket passed to the west of the plume until it penetrated the plume at an altitude of approximately 450 km (about $T + 200$ s).

That the plume is undergoing a process of decay is evident by comparing the maps in Figures 2 and 4. The plume had already extended up to a 600-km altitude by 1120 UT, with a peak backscatter strength of 50 dB (Figure 2). By 1233 UT, the plume has decreased in backscatter strength by 10 dB. A continued decay in backscatter strength is also evident in the three maps in Figure 4. The decrease in plume height from 600 to 550 km is the result of a descending F layer (~ 10 m/s).

The continued flight of the rocket is shown in the second (center) map. The rocket is seen to have penetrated through the most intense backscatter region of the plume (between $T + 4$ and $T + 5$ min). Shortly thereafter, at $T + 6$ minutes, the rocket reached apogee (see third map). As the rocket fell, it again passed through the plume of interest. Because of its slightly larger eastward velocity component, the rocket passed approximately 15 km to the east of its interception point during the upleg of the rocket trajectory. This near-synchronous flight of the rocket, with the eastward drift of the backscatter plume, accounts for the near identical electron density profiles that were obtained by in-situ rocket measurements during the upleg and downleg portions of the rocket flight.

The decay of plume backscatter strength is clearly shown in Figure 6. We have plotted the altitude extent of the 40-dB contour in the plume of interest, as a function of time. That contour is shown to extend in altitude from 475 km up to nearly 700 km, around 1200 UT. The decay is seen to occur from the top of the plume lowering the upper end of the plume down to 525 km by the time of the rocket launch. Backscatter-plume decay phase has been described by Tsunoda⁵.

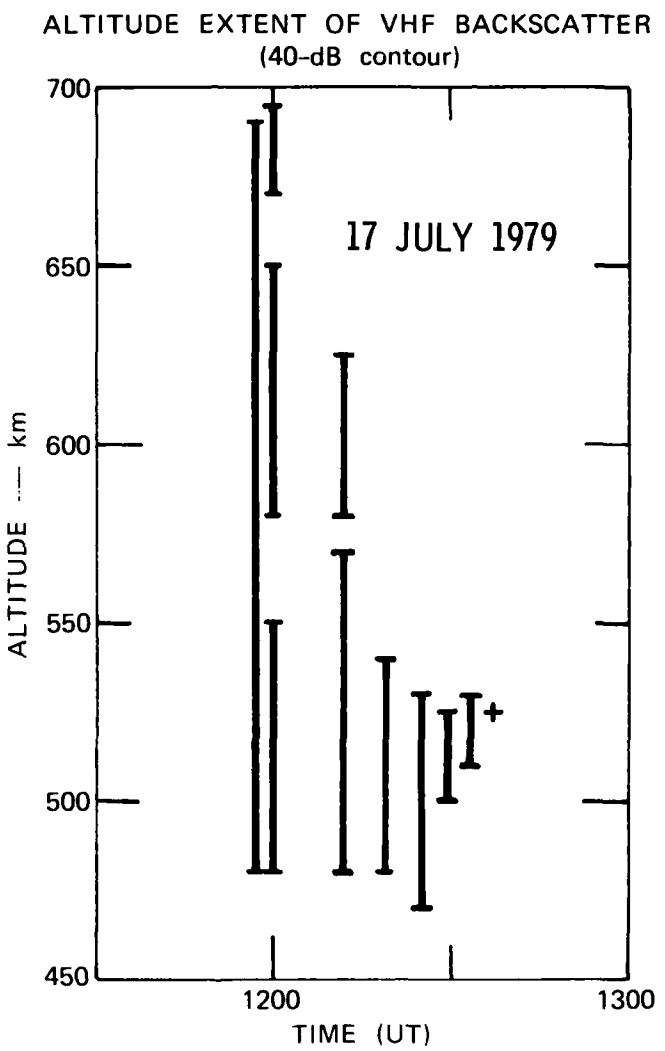


FIGURE 6 ALTITUDE EXTENT OF VHF BACK-
SCATTER (40-dB CONTOURS) IN
PLUME OF INTEREST, AS A FUNCTION
OF TIME --- 17 JULY 1979

IV SECOND ROCKET--24 July 1979

A. Ionospheric Conditions

The ionospheric conditions for the second rocket night are summarized in Figure 7, using a plot of $h'F$ versus time. The virtual height of the bottomside F layer is seen to increase monotonically starting around 0500 UT and continuing until 0800 UT when $h'F$ reached 350 km and the ionogram traces began to spread. Full range spread developed around 0830 UT; therefore, despite the fact that the base of the F layer did not reach as high an altitude as on the first rocket night, equatorial spread F started sooner.

The second rocket was launched at $T = 0957:30$ UT during a time when the F layer began to rise again. The second rocket launch differed from the first, in that general ESF activity was probably at its peak than in its decay phase.

B. ALTAIR Measurements

The first ALTAIR observations of the backscatter plume of interest were made between 0844 and 0925 UT. Two backscatter maps showing the development of the plume are presented in Figure 8. The backscatter region of interest at 0844 UT appears at the extreme west end of the map in the upper panel. What appears to be a plume with an eastward tilt (from vertical) is really bottomside backscatter associated with an upwelling of the bottomside F layer to altitudes around 550 km. Initial plume development is seen in the second map (lower panel) in Figure 8. The plume can be differentiated from bottomside backscatter by the abrupt change in tilt angle above a 650-km altitude. The plume extends up to an altitude of 900 km.

The geometry relating the second rocket trajectory to the sector scanned by ALTAIR is shown in Figure 9. The second rocket trajectory, when compared with that for the first rocket, is directed at a slightly more northerly azimuth. The rocket position at one-minute intervals has been extrapolated to the plane of the ALTAIR scan sector (circles). There is little difference in the trajectories of the two rockets.

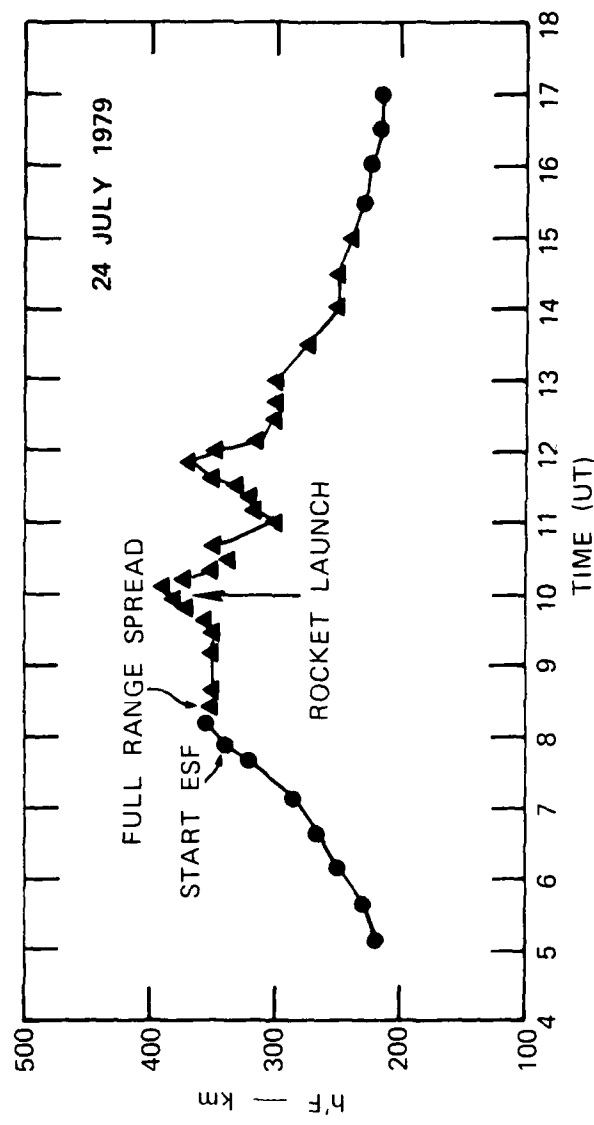


FIGURE 7 IONOSPHERIC CONDITIONS FOR THE SECOND ROCKET NIGHT (24 JULY 1979) AS DEPICTED BY $h'F$, THE VIRTUAL HEIGHT OF THE BOTTOM OF THE F LAYER, PLOTTED AS A FUNCTION OF TIME

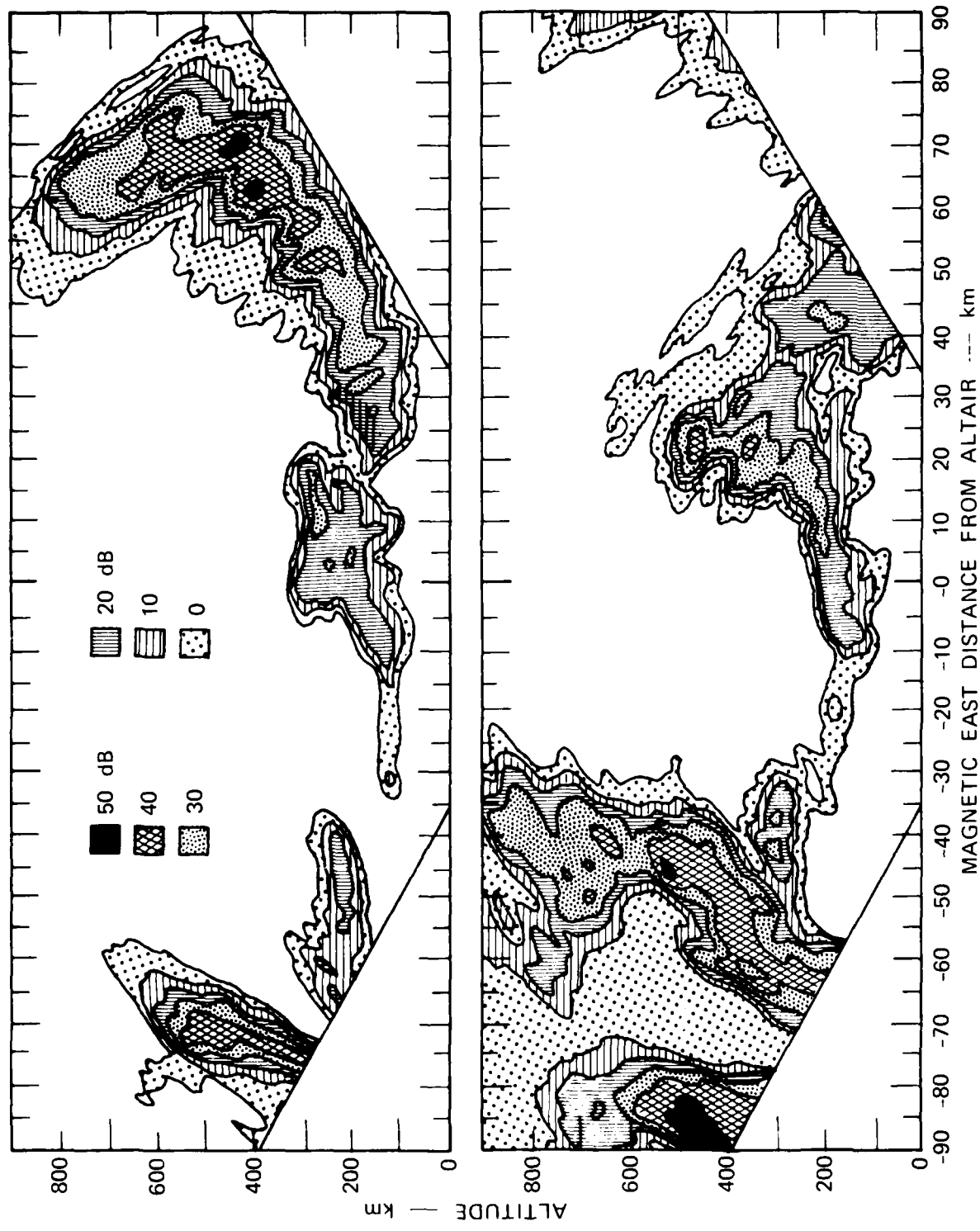


FIGURE 8 FIRST DETECTION OF BACKSCATTER PLUME OF INTEREST -- 24 JULY 1979

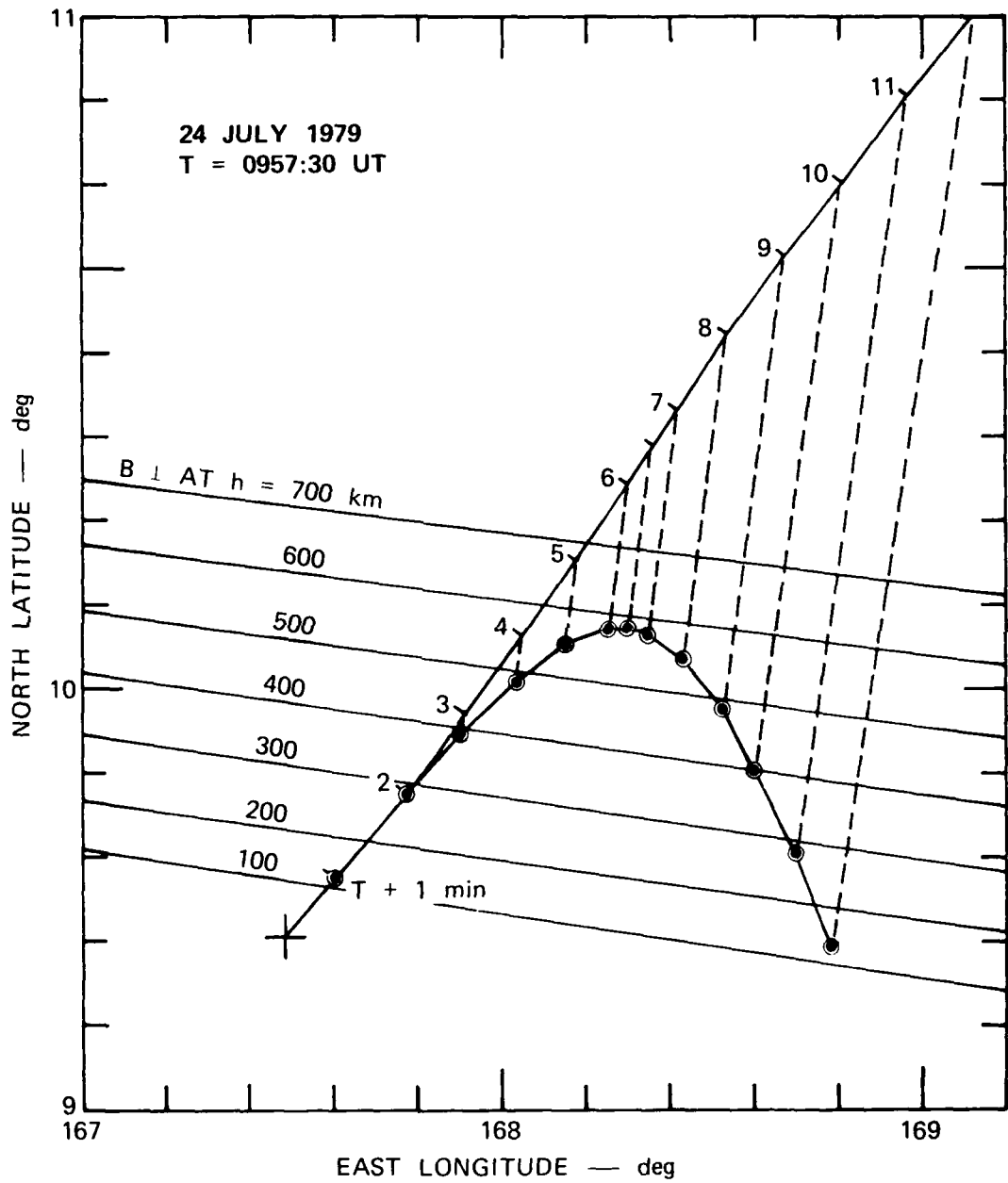
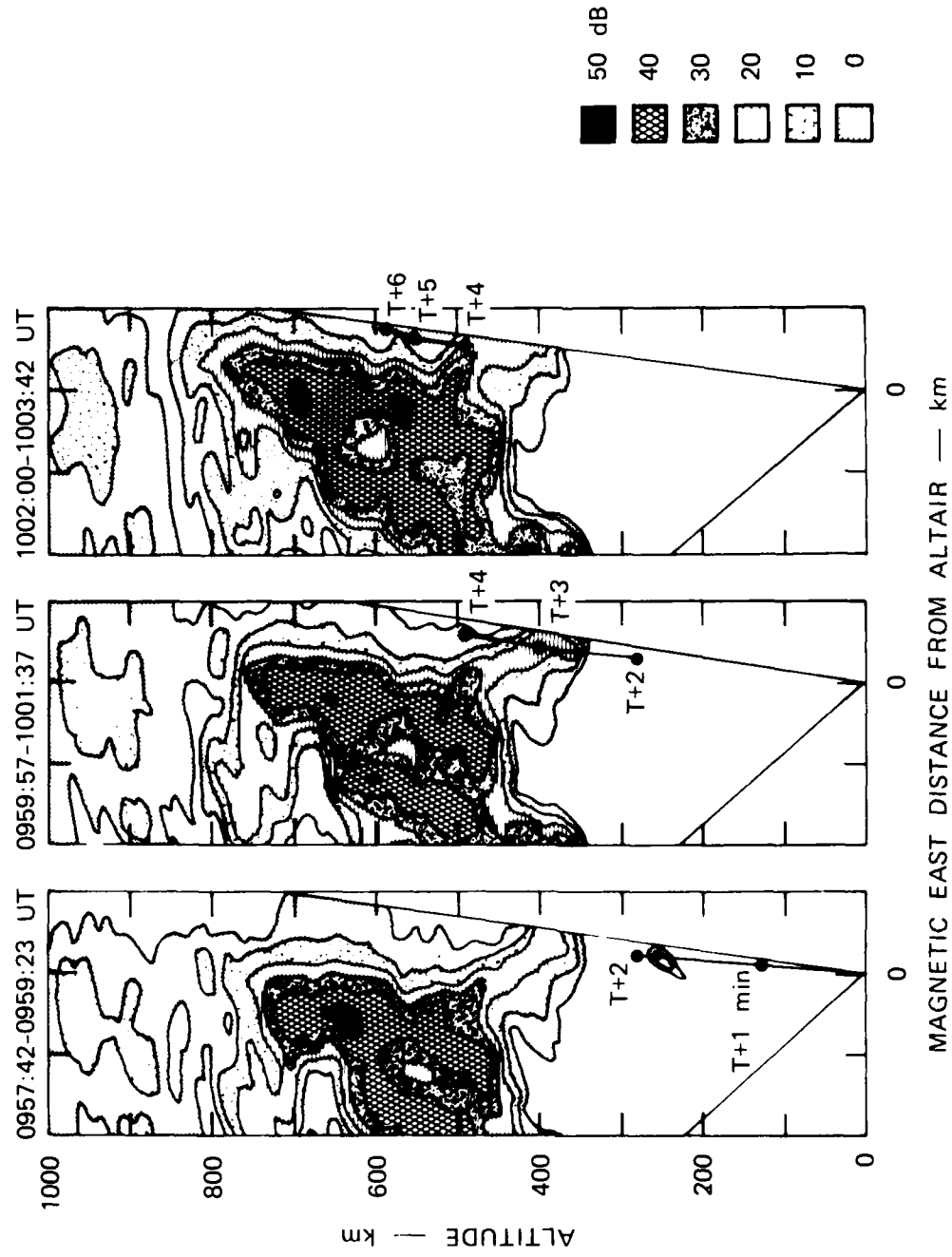


FIGURE 9 ROCKET TRAJECTORY AND ITS EXTRAPOLATION INTO THE EAST-WFST SECTOR SCANNED BY ALTAIR — 24 JULY 1979



Three ALTAIR backscatter maps taken during the flight of the second rocket are shown in Figure 10. The plume toward which the rocket was directed is centered in the first map, and drifts eastward in the following two maps. The strong backscatter region (\gtrsim 30 dB) extends up to about 750 km in altitude. The top part of the plume, however, that extended up to a 900 km altitude has decayed significantly, although remnants from that portion are still seen in the maps.

The location of the rocket as function of time is shown by solid circles connected by straight line segments. The first map covers the period between launch (0957:30 UT) and T + 2 min. The rocket trajectory is seen below the backscatter region, directed toward the right of the plume. The small backscatter at the 250-km altitude was produced by radar backscatter from the body of the rocket as it passed through the ALTAIR beam. The second map corresponds to the time T + 2.5 to T + 4 min. The rocket passed through bottomside backscatter (between T + 2.5 and T + 3.5 min). In the last map in Figure 10 (T + 4.5 to T + 6 min), the rocket is seen to pass along the east wall of the plume.

V DISCUSSION

In this report, we have summarized the ALTAIR operation during the PLUMEX rocket campaign and described the backscatter plume characteristics of the plumes toward which the two rockets were launched. Both plumes were in their decay phases⁵. The first plume however, occurred during a period of general decline in ESF activity (the midnight sector). The second plume occurred during a period of strong ESF activity (the pre-midnight sector).

The relationships of backscatter plumes to in-situ probe measurements have been described by Szuszczewicz et al^{6,7}. The results from the first PLUMEX rocket appear to be in good agreement with earlier findings obtained with ALTAIR^{8,9}. In both cases backscatter appears to be associated with plasma depletions and regions of positive electron-density gradients. The results from the second rocket are also in

agreement with past results--that is, the second rocket passed along the east wall of the backscatter plume and recorded very weak ESF irregularities.

The observations also support the east-west asymmetry model proposed by Tsunoda⁵. In this report, Tsunoda hypothesized that the west wall of plasma bubbles would be more structured than the east wall because the gradient-drift instability would be driven on the west wall by the eastward neutral wind. This model is supported by the discovery of scintillation-producing irregularities near the west wall of the first plume,¹⁰ and the near-absence of ESF irregularities along the east wall of the second plume⁷. This model is further supported by the demonstration that wave structure occurs in the bottomside F layer and that the wave structure leads to the development of plumes from the west walls⁸.

REFERENCES

1. R. T. Tsunoda, M. J. Baron, and J. Owen, "ALTAIR: An Incoherent Scatter Radar for Equatorial Spread-F Studies," Radio Sci., Vol. 14, No. 6, pp. 1111-1120 (November/December 1979).
2. D. M. Towle, "VHF and UHF Radar Observations of Equatorial F Region Ionospheric Irregularities and Background Densities," Radio Sci., Vol. 15, No. 1, pp. 71-86 (January/February 1980).
3. R. T. Tsunoda and B. R. White, "On the Generation and Growth of Equatorial Backscatter Plumes: Wave Structure in the Bottomside F Layer," Summer Equatorial Experiment Data Review Meeting, 18 March 1980 (1980).
4. B. G. Fejer, D. T. Farley, R. F. Woodman, and C. Calderon, "Dependence of Equatorial F-Region Vertical Drift on Season and Solar Cycle," J. Geophys. Res., Vol. 84, No. A10, pp. 5792-5796 (October 1979).
5. R. T. Tsunoda, "The Growth and Decay of Equatorial Backscatter Plumes," Topical Report, Contract DNA-001-79-C-0153, SRI Project 8164, SRI International, Menlo Park, California (February 1979).
6. E. P. Szuszczewicz, R. T. Tsunoda, R. Narcisi, and J. C. Holmes, "Coincident Radar and Rocket Observations of Equatorial Spread F," Proceed. of the Summer Equatorial Experiment Data Review Meeting, 18 March 1980 (1980).

7. E. P. Szuszczewicz, R. T. Tsunoda, R. Narcisi, and J. C. Holmes, "PLUMEX II: A Second Set of Coincident Radar and Rocket Observations of Equatorial Spread F," Summer Equatorial Experiment Data Review Meeting, 18 March 1980 (1980).
8. R. T. Tsunoda, "On the Spatial Relationship of l-m Equatorial Spread-F Irregularities and Plasma Bubbles, J. Geophys. Res., Vol. 85, No. A1, pp. 185-190 (January 1980).
9. R. T. Tsunoda, "Magnetic-Field-Aligned Characteristics of Plasma Bubbles in the Nighttime Equatorial Ionosphere," J. Atmos. Terr. Phys., (submitted for publication, 1980).
10. C. L. Rino, R. T. Tsunoda, J. Petriceks, and R. C. Livingston, "Simultaneous Rocket-Borne Beacon and In-Situ Measurements of Equatorial Spread F" (to be published).

**OPTICAL STUDIES IN SUPPORT OF THE JULY 1979 KWAJALEIN
EQUATORIAL SPREAD-F CAMPAIGN**

D. P. Sipler and M. A. Biondi

Department of Physics and Astronomy
University of Pittsburgh, Pittsburgh, PA 15260

and

R. D. Hake

SRI International
Menlo Park, CA 94025

I INTRODUCTION

During the July 1979 Kwajalein Equatorial Spread-F Campaign, under joint DNA and NSF sponsorship, two optical instruments were fielded at Roi-Namur, Marshall Islands, to provide real-time F-region neutral wind measurements^{1*} and mapping of 630.0-nm airglow depletions that are believed to be associated with the scintillation regions² (plasma depletions, plumes or plasma bubbles³). The wind-determining instrument was the 94-mm-aperture Fabry-Perot (FP) interferometer, with the multiple-aperture exit plate, that was fielded at Roi-Namur for the 1977 and 1978 Wideband Equatorial Measurements Program.¹ Before shipping the instrument to the Pacific in July 1979, improvements were made that increased its detection sensitivity by a factor of ~ 2 . This was a fortunate development in view of the substantially weaker 630.0-nm nightglow intensities in 1979, as compared to 1978 and 1977 (the result of an increase in the F-region's average altitude during this time period).

* References are listed at end of paper.

The other instrument fielded in July 1979 was a new 630.0-nm night-glow mapping instrument that had been completed just in time for the 1979 program. It consisted of a 3-channel filter photometer (630.0 nm, 631.0 nm, and 557.7 nm) with dual-axis pointing head. The weather was rather unfavorable for filter photometer operation (partly cloudy many of the nights), and the instrument did not become fully operational until late in the campaign. Fortunately, the instrument was operating during a clear-night period which coincided with the last of the ALTAIR incoherent-scatter observations of scintillation regions. It appears that the location of the observed 630.0-nm airglow depletion region corresponded to the scintillation region that was detected simultaneously by ALTAIR (R. Tsunoda, private communication).

In the following sections, we (1) describe the principles of the two measurements; (2) present the results of the neutral wind vector determinations for the 1979 campaign and, for comparison, for the 1978 and 1977 observation periods; (3) display the motion of the 630.0-nm airglow depletions via X versus t intensity contour maps for successive W → zenith → E zonal scans covering a four-hour period; and (4) give examples of all-sky intensity contour maps at the end of the period.

II PRINCIPLES OF THE EXPERIMENTS

A. Fabry-Perot Interferometer

The pressure-tuned 94-mm-aperture Fabry-Perot interferometer (employing a photomultiplier detector) has been described in some detail¹ and is a current version of our nightglow instrument design.^{4,5} The present instrument achieves a > 3-fold increase in sensitivity over "conventional" instruments by use of a multiple annular ring exit aperture in place of the usual central hole exit aperture. Added sensitivity over earlier instruments was obtained by use of the extended-red-sensitivity Varian VPM-192MB (or RCA 31034A10) photomultiplier in place of the earlier EMI 9558A and 9658A tubes.

Typically we pressure-scanned through a 630.0-nm line profile in ~ 25 seconds, coherently summing repetitive scans until a satisfactory line profile was obtained. At a 100-Rayleigh intensity of 630.0-nm nightglow, it was possible to obtain a line profile of sufficient quality to determine neutral winds to an accuracy of \pm 15 m/s in 3 to 4 minutes, while in weak nightglow periods we were able to obtain usable 630.0-nm profiles in ~ 20 minutes for intensities as low as ~ 7 Rayleighs. To determine the instrumental resolution of the FP and to provide a frequency reference and frequency scale, the FP was periodically made to scan through 1-1/2 order of the 632.8-nm line from a stabilized He-Ne laser. Such a scan typically requires ~ 50 seconds to complete.

The F-region neutral winds were determined on clear nights, by programming the pointing head of the instrument to "look" successively N, S, E, W, at 30° elevation (with occasional zenith-directed observations). From these observations, we determined the Doppler shifts of the profiles relative to a "zero" velocity reference (e.g., a vertical observation), to find the wind vector components along the various lines-of-sight. On partially cloudy nights, an observer using a boresighted telescope attached to the pointing head, directed the FP line-of-sight to suitable openings in the clouds. From a simple trigonometric program, these "odd" line-of-sight velocity components were translated into zonal and meridional wind components.

B. Sky-Mapping Filter Photometer

The all-sky-mapping, three-channel filter photometer was designed to provide flexibility in mapping the nightglow emission patterns. Three nightglow radiation regions were monitored by use of 2 1/2-in. diameter, multilayer interference filters ($\Delta\lambda = 0.3$ nm) that were centered at the appropriate wavelengths for the F-region OI 630.0-nm nightglow, the adjacent continuum background (at 631.0 nm), and the E-region OI 557.7-nm nightglow.

The radiation was detected by three Varian VPM-192 MB phototubes (see Figure 1) that were mounted in a compact equilateral triangle

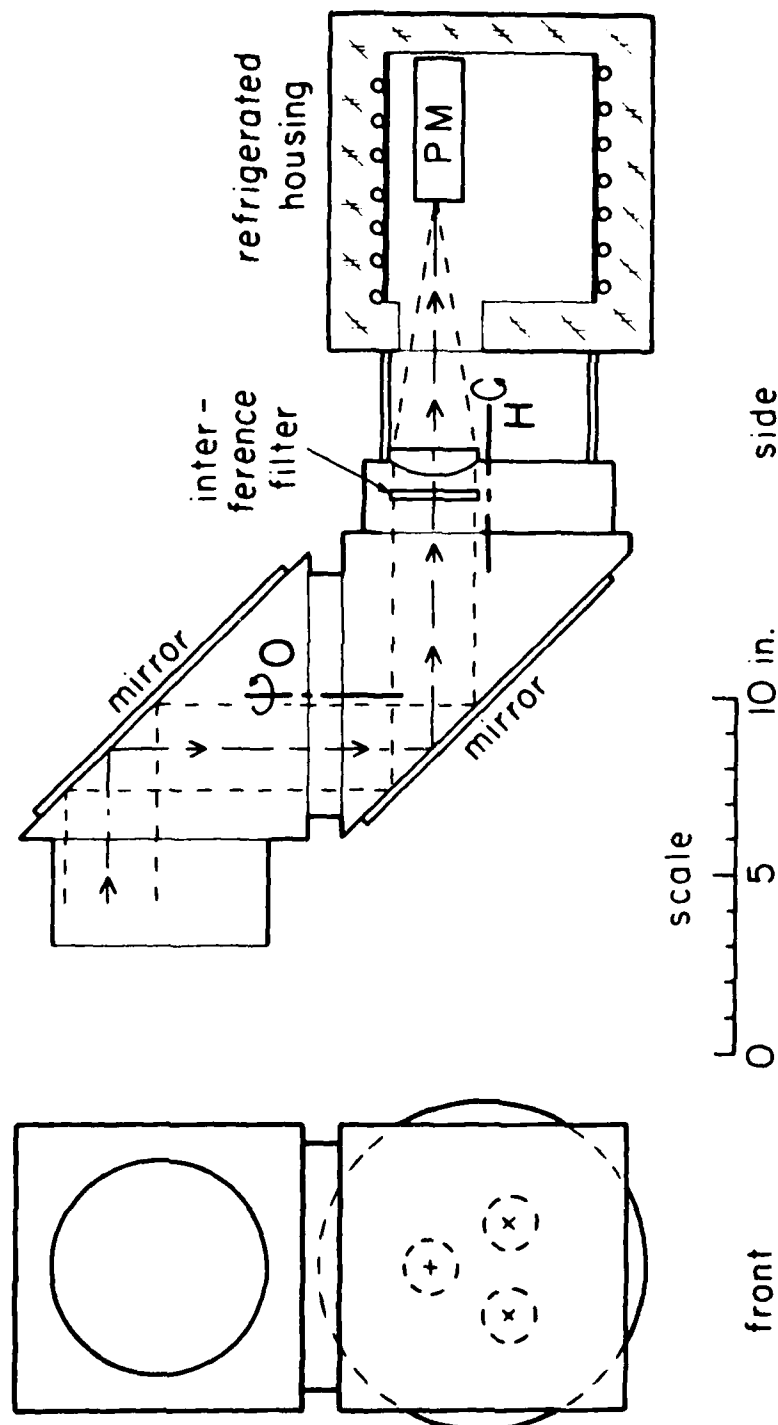


FIGURE 1 SIMPLIFIED DIAGRAM OF THE 3-CHANNEL, SKY-MAPPING FILTER PHOTOMETER SHOWING THE OPTICAL PATH FOR ONE CHANNEL AND THE TWO-AXIS POINTING HEAD (H = HORIZONTAL AXIS, O = ORTHOGONAL AXIS)

configuration within a freon-cooled thermal housing (operating temperature $\sim -30^{\circ}\text{C}$). The three parallel optical axes of the photomultiplier channels, after passing through the interference filters, impinged at 45° angle of incidence on a mirror pivoted about a horizontal axis (indicated by H in Figure 1), and were thereby redirected at 45° angle of incidence onto a second mirror pivoted about an axis (0 in Figure 1) orthogonal to the horizontal axis.

With this mirror system it was possible to make all-sky maps, by holding the horizontally pivoted mirror fixed at successive positions, while the orthogonally pivoted mirror was swept back and forth through 180° . This leads to a hemispherical sweep pattern akin to the longitude lines on a globe whose North-South axis is oriented horizontally. Since the airglow intensity patterns often exhibit substantial N-S extents, we oriented our instrument with its horizontal mirror axis H aligned E-W.

The horizontal mirror axis position shown in Figure 1 yields a sweep of half of the horizon (i.e., at 0° elevation) when the orthogonal mirror turns from 0° (the position shown) to 180° . For a horizontal mirror position that is 90° from that shown, the motion of the orthogonal mirror gives a zonal sweep (W at 0° elevation \rightarrow zenith \rightarrow E at 0° elevation). In practice, more limited sweeps were used--typically from 20° elevation to 20° elevation. For all-sky maps, a 39×39 element "rectangular" array was swept, with a dwell-time of 0.5 s at each position in the sweep; thus one all-sky map was made each ~ 13 minutes. To trace the movements of the airglow depletions as a function of time, a 39-step zonal sweep (20°W elevation \rightarrow zenith \rightarrow 20°E elevation and the reverse) was employed, requiring 20 seconds per sweep.

The photomultipliers were operated in a pulse-counting mode; the resulting nightglow intensity data (along with subsidiary information such as look-angles) were processed by means of a microcomputer and stored on magnetic discs and/or magnetic tape. Real-time imaging of the sky-maps was provided by the microcomputer and a color video monitor, using chromatic gradations to indicate intensity differences.

III NEUTRAL WIND DETERMINATIONS

The July 1979 weather was rather rainy; cloud cover presented a problem for our optical measurements on a number of nights. By working through clear-sky openings in the partially cloudy sky, however, we were able to obtain useful F-region wind measurements on many nights--including both nights that the instrumented rockets were launched. An additional problem was that, within \sim 45 minutes after astronomical twilight (sunset at \sim 300 km), the lower edge of the F_2 region moved up to rather high altitudes ($>$ 350 km), causing a very rapid decrease in intensity of the 630.0-nm radiation [whose origin is the dissociative recombination reaction $e^- + O_2^+ \rightarrow O^*(^1D) + O$] to rather low values, $<$ 10 Rayleigh. The intensity recovered just before midnight, when the sinking of the F_2 region into a region of greater O_2 density restored the recombination (via increased molecular ion production through the $O^+ + O_2 \rightarrow O + O_2^+$ charge transfer reaction), typically to values of \sim 100 Rayleigh.

The measured F-region winds for the nights on which we have extensive data are shown in two series--as separate zonal and meridional wind components as a function of time (Figures 2 through 6), and as polar plots of the position of the tip of the wind vector as a function of time (Figures 7 through 11). Rather different wind patterns were observed on each of the nights, with the winds at astronomical twilight (\sim 8 hr UT) ranging from near-zero in value to \gtrsim 100 m/s, and directed between SE and S. In all cases, the peak neutral winds seemed to occur just before local midnight (\sim 11 hr UT), and had values ranging from 160 m/s to $>$ 300 m/s. The zonal wind component usually decreased toward zero or reversed sign in the late night.

On the night of the first rocket launch (17 July 1979), very large zonal winds were observed, with a neutral wind of \sim 260 m/s at \sim 108° azimuth (20% below the peak value) at the time of rocket launch (1231 UT). On the night of the second rocket launch (24 July 1979), the winds at launch (0957 UT) were near the maximum value for the night, i.e., 170 m/s at 120° azimuth. The geomagnetic activity on 17 July was moderate ($\Sigma K_p = 23-$), while 24 July was a geomagnetically quite night ($\Sigma K_p = 11+$).

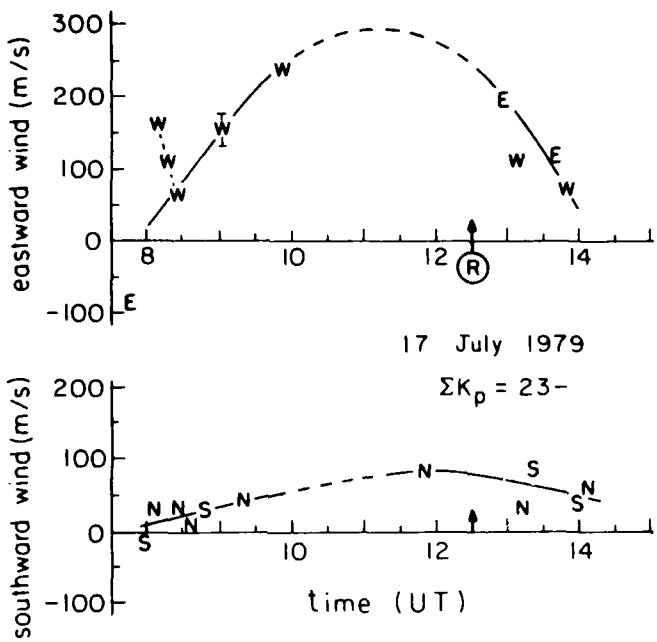


FIGURE 2 EQUATORIAL F-REGION ZONAL AND MERIDIONAL WIND COMPONENTS MEASURED ON 17 JULY 1979. The symbols E, W, N, S, refer to the line-of-sight azimuth for the Fabry Perot. The (R) symbol indicates the time of launch (1231 UT) of the instrumented rocket.

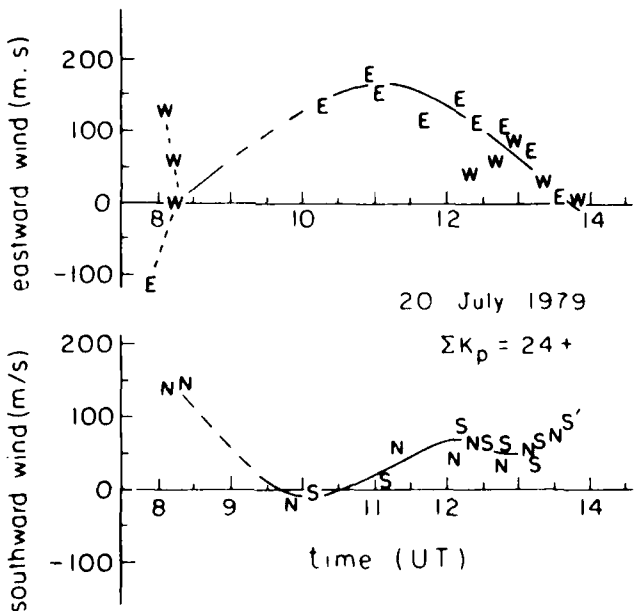


FIGURE 3 ZONAL AND MERIDIONAL WIND COMPONENTS ON 20 JULY 1979.

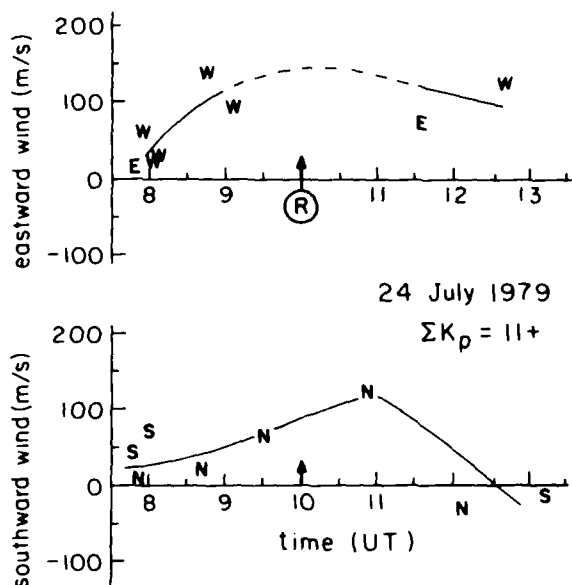


FIGURE 4 ZONAL AND MERIDIONAL WIND COMPONENTS ON 24 JULY 1979.
The rocket launch time (0957 UT) is indicated by the symbol (R).

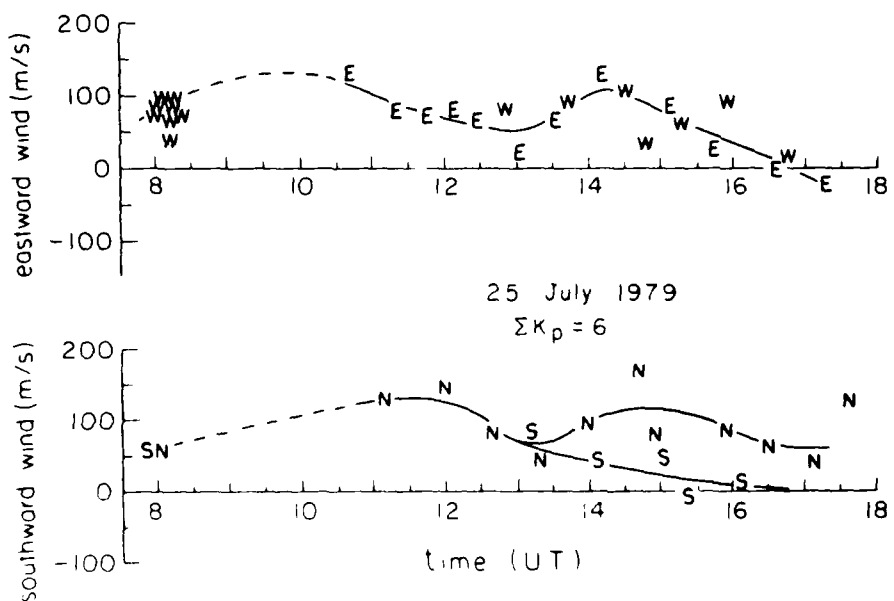


FIGURE 5 ZONAL AND MERIDIONAL WIND COMPONENTS ON 25 JULY 1979.
Note the difference in meridional winds observed north and south of Kwajalein starting at 1315 UT.

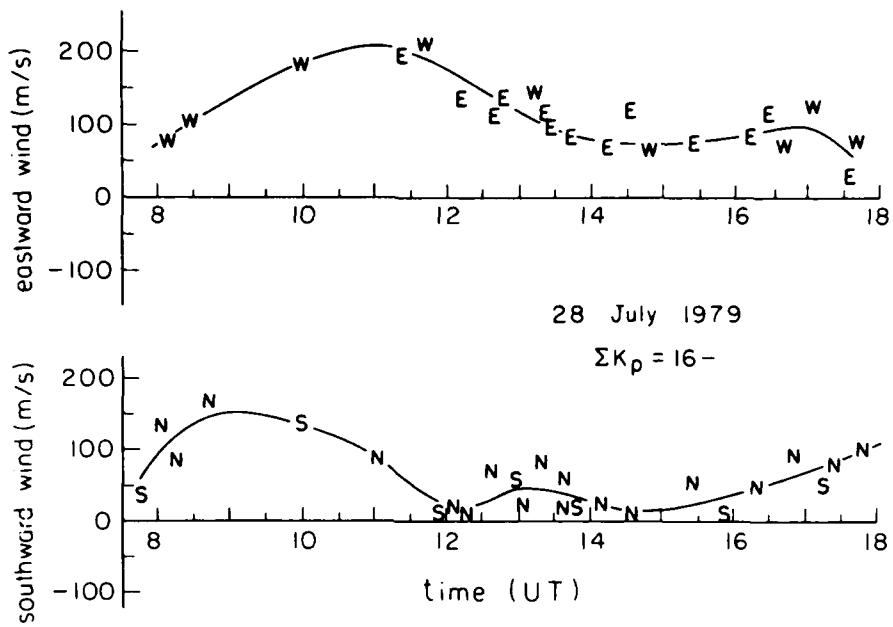


FIGURE 6 ZONAL AND MERIDIONAL WIND COMPONENTS ON 28 JULY 1979

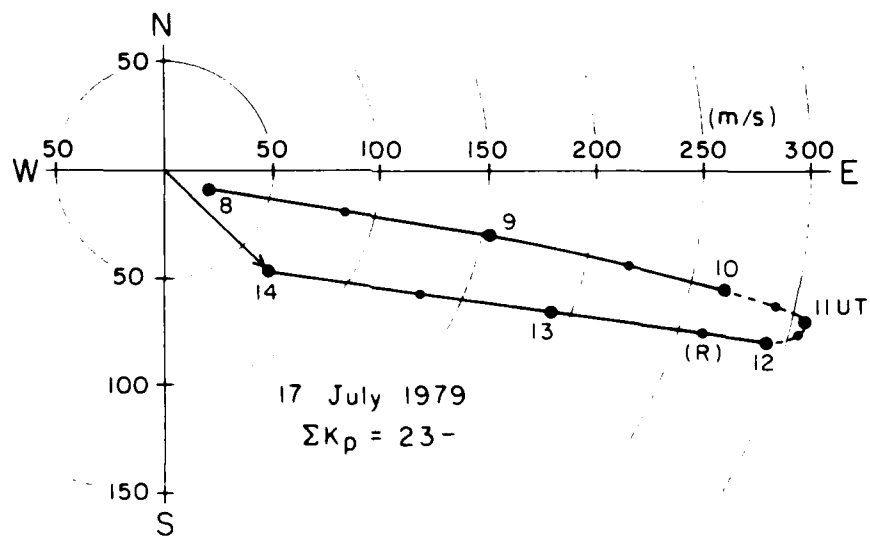


FIGURE 7 POLAR DIAGRAM OF THE POSITION OF THE TIP OF THE WIND VECTOR AS A FUNCTION OF TIME ON 17 JULY 1979, INFERRED FROM THE SMOOTH CURVES DRAWN THROUGH THE DATA POINTS OF FIGURE 2. (An example of the wind vector is drawn at 1400 UT.) The symbol (R) indicates the time of launch of the instrumented rocket.

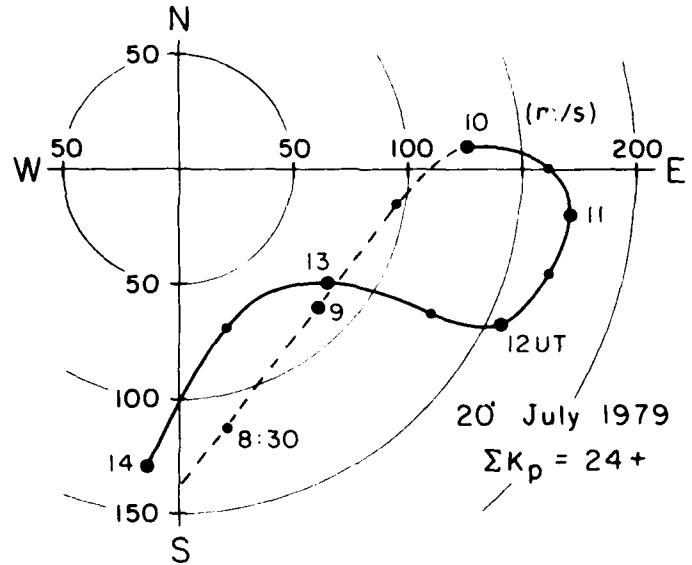


FIGURE 8 POSITION OF THE TIP OF THE WIND VECTOR ON 20 JULY 1979

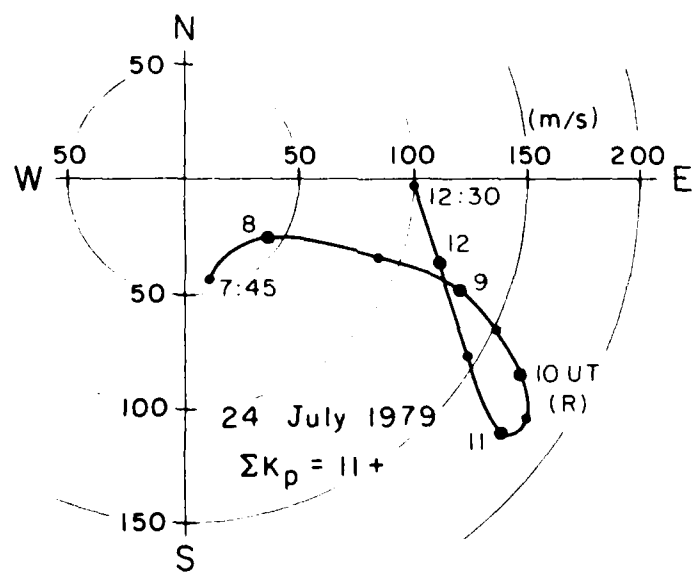


FIGURE 9 POSITION OF THE TIP OF THE WIND VECTOR ON 24 JULY 1979. The symbol (R) indicates the rocket-launch time.

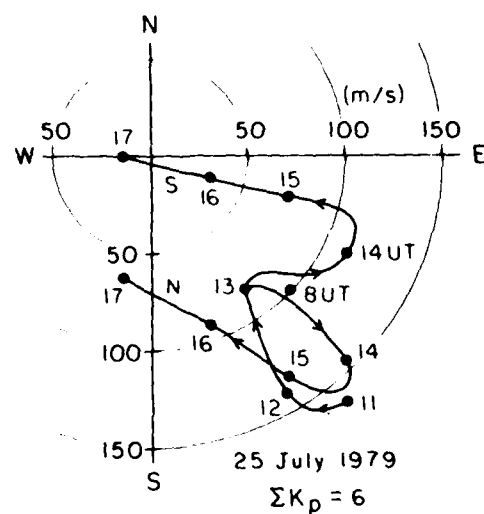


FIGURE 10 POSITION OF THE TIP OF THE WIND VECTOR ON
25 JULY 1979, SHOWING DIFFERENT WIND VECTORS
OBSERVED NORTH AND SOUTH OF KWAJALEIN

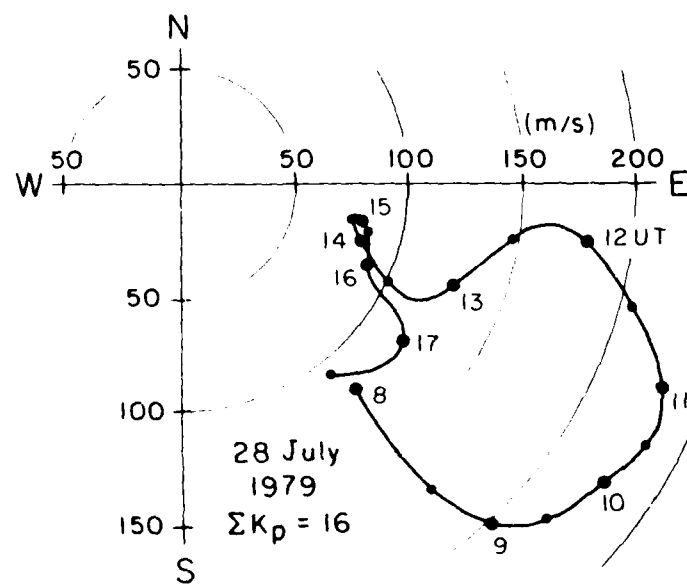


FIGURE 11 POSITION OF THE TIP OF THE WIND VECTOR ON 28 JULY 1979

Another unusual feature of the neutral winds may be seen in Figures 5 and 10, which show the data for 25 July 1979. Somewhat after local midnight, at 1330 UT, the meridional wind components, that were obtained in north-looking and south-looking observations, diverged in value. Because, for a 630.0-nm emission height of 300 km and an instrument line-of-sight at 30° elevation, we are observing regions of the ionosphere that are separated by ~ 1000 km, this difference in meridional wind (with a smaller value south of Kwajalein), may be evidence for flow convergence in the circulation of the upper atmosphere as it approaches the equator (e.g., a vertical circulation cell). However, because 25 July was a very quite night geomagnetically ($\Sigma K_p = 6$), it is not clear why unusual flow patterns were set up.

To permit comparison with neutral wind measurements from previous years, we have included data from 1978 in Figures 12 through 14 (only zonal winds were obtained on 19 August 1978), and from 1977 in Figures 15 and 16. While the patterns differ in detail, even on successive nights, there are qualitative similarities. For example, in both the 1977 and the 1979 data, the peak neutral winds occurred just before local midnight (~ 11 hr UT)--we cannot make a similar comment for 1978, because the data shown do not extend to early enough times. With the exception of the somewhat fragmentary 24 July 1979 data, all measurements indicate a dying-away of the eastward zonal wind component late at night, with an actual reversal to a westward-directed component before dawn on three of the nights.

IV 630.0-nm NIGHTGLOW INTENSITY MAPPING

As noted in Section II, the sky-mapping photometer can be operated in a variety of modes--two of which are all-sky mapping (covering the sky down to ~ 20° elevation, where atmospheric extinction becomes a problem) and zonal scanning through the zenith to provide rapid monitoring of the movement of airglow depletions (which are known to exhibit a N-S alignment, often with a large extent in that direction). Thus, we

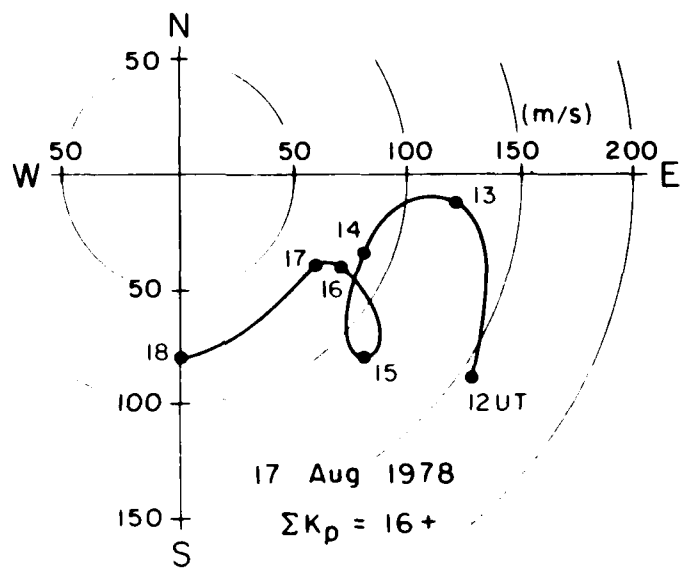


FIGURE 12 POSITION OF THE TIP OF THE WIND VECTOR ON 17 AUGUST 1978

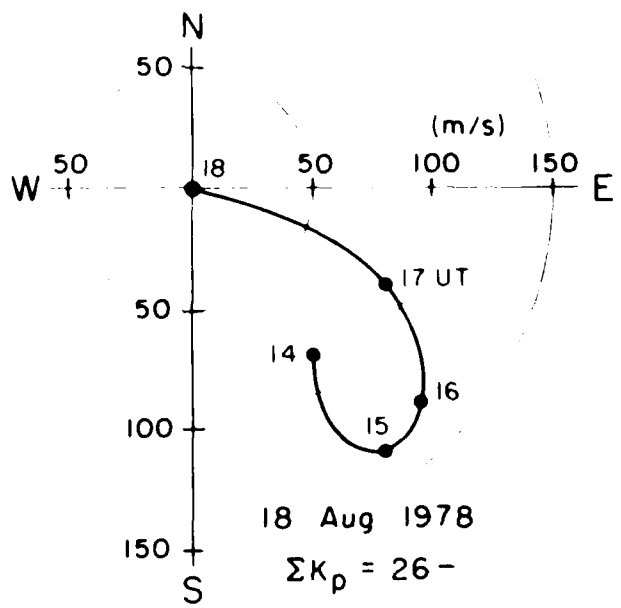


FIGURE 13 POSITION OF THE TIP OF THE WIND VECTOR ON 18 AUGUST 1978

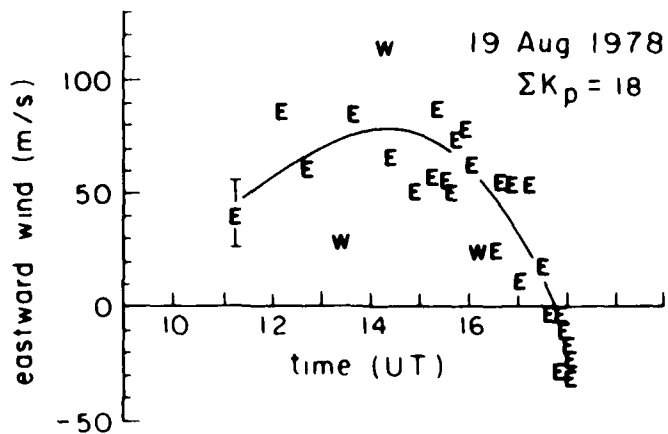


FIGURE 14 ZONAL WIND COMPONENT OBSERVED ON 19 AUGUST 1978 (NO MERIDIONAL COMPONENTS WERE OBTAINED)

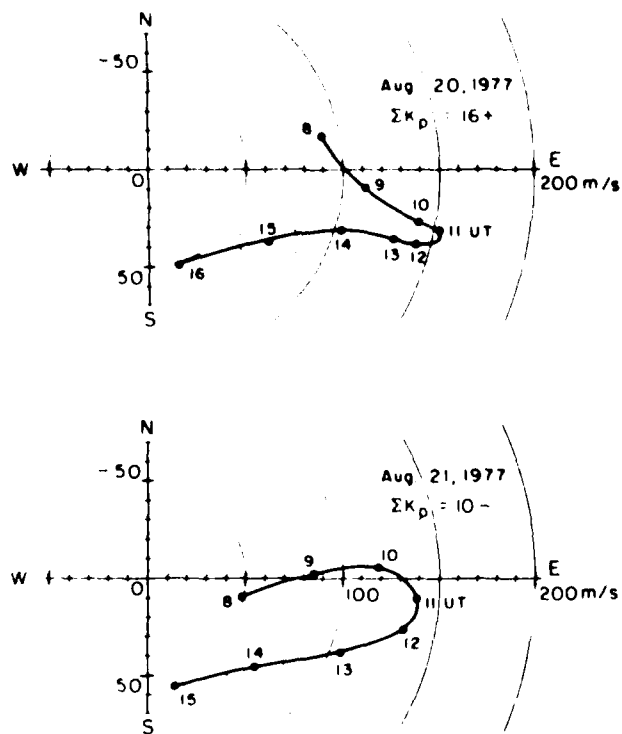


FIGURE 15 POSITION OF THE TIP OF THE WIND VECTOR ON 20 AND 21 AUGUST 1977

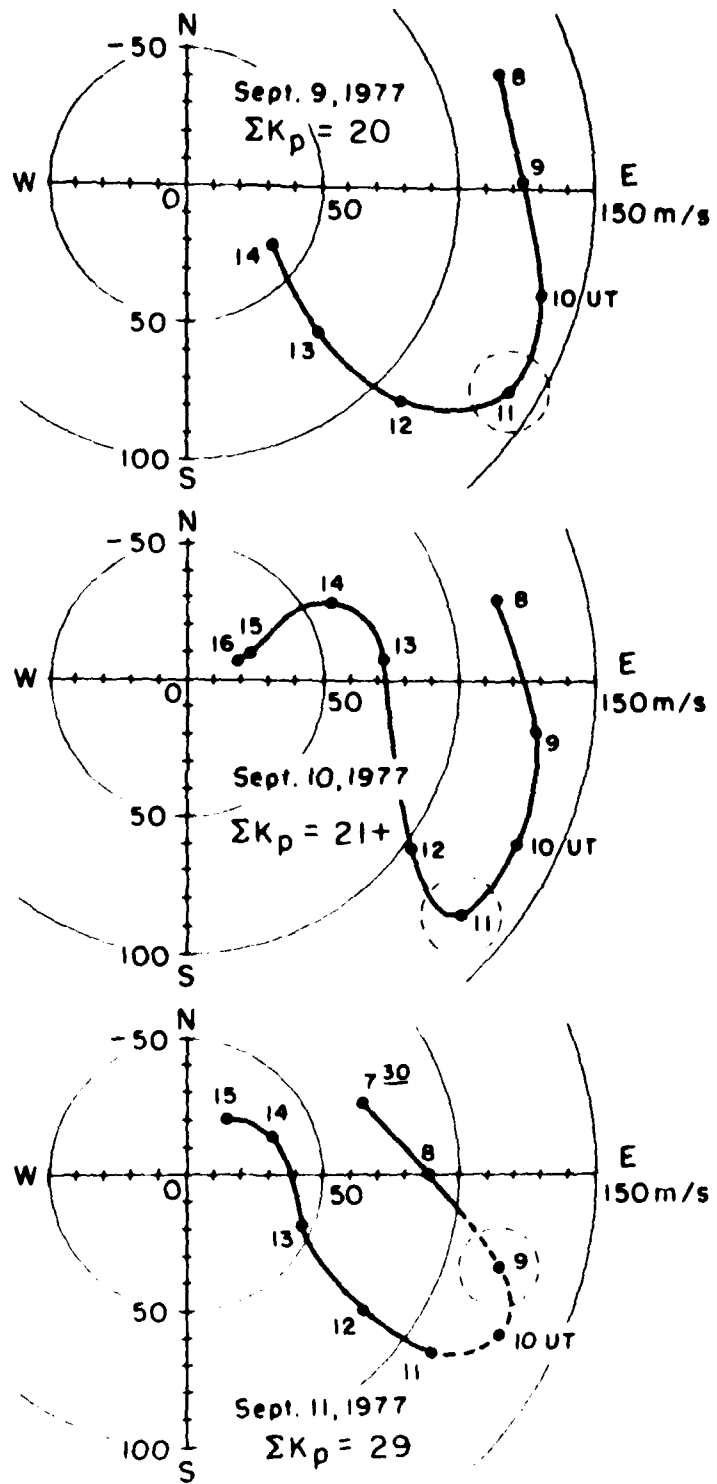


FIGURE 16 POSITION OF THE TIP OF THE WIND VECTOR
 ON 9, 10, AND 11 SEPTEMBER 1977

present our data either as X versus t plots of intensity contours (Figures 17 through 21) or as X versus Y intensity contour "sky-maps," each requiring 12 to 13 minutes to obtain (see Figures 22 and 23).

The nights of the rocket launches (17 and 24 July 1979) were not sufficiently cloud-free to permit satisfactory airglow intensity contour mapping. However, after local midnight (\sim 12 hr UT) on 25 July 1979, the sky cleared sufficiently so that we could obtain the nightglow maps shown in Figures 17 through 23. A continuous set of zonal sweeps ($W \rightarrow Z \rightarrow E$ and return) provided an X versus t record of the 630.0-nm intensity distribution for the period 1215 to 1600 UT--this record has been divided into Figures 17 through 21. The intensity contours are labelled in terms of counting rates (in hundreds of counts/0.5 s; a rough calibration: 1 contour unit \sim 5 R). At the bottom of each figure is a distance scale based on a 300-km emission height.

The dashed lines in the figures trace the motion of the centers of the airglow depletions. The slope of the dashed line yields the zonal component of the drift velocities of the depletion. Values ranging from > 200 m/s at 1220 UT, to very small (~ 0 m/s) at 1355 UT are obtained from the figures. It is interesting to note from Figure 5 or Figure 10, that at 1220 UT, the zonal component of the neutral wind was only ~ 70 m/s, while at 1355 UT it was ~ 100 m/s; i.e., the airglow depletions, at times, drift eastward both faster than and slower than the neutral atmosphere in which they originate. Because these airglow depletions have been associated with the bottomside of the "plumes" (plasma depletions or unstable plasma regions), which give rise to the scintillation regions in the ionosphere, these simultaneous determinations of the drift velocity of the airglow depletion plus the F-region neutral wind velocity, provide valuable data for comparison with the theoretical predictions of the plume formation, growth, and motion.

For completeness, in Figures 22 and 23 we have shown two examples of all-sky maps that were taken shortly after the completion of the X versus t scans on 25 July 1979. (The vertical and horizontal distance scales are unequal as the result of an artifact in the video plotting

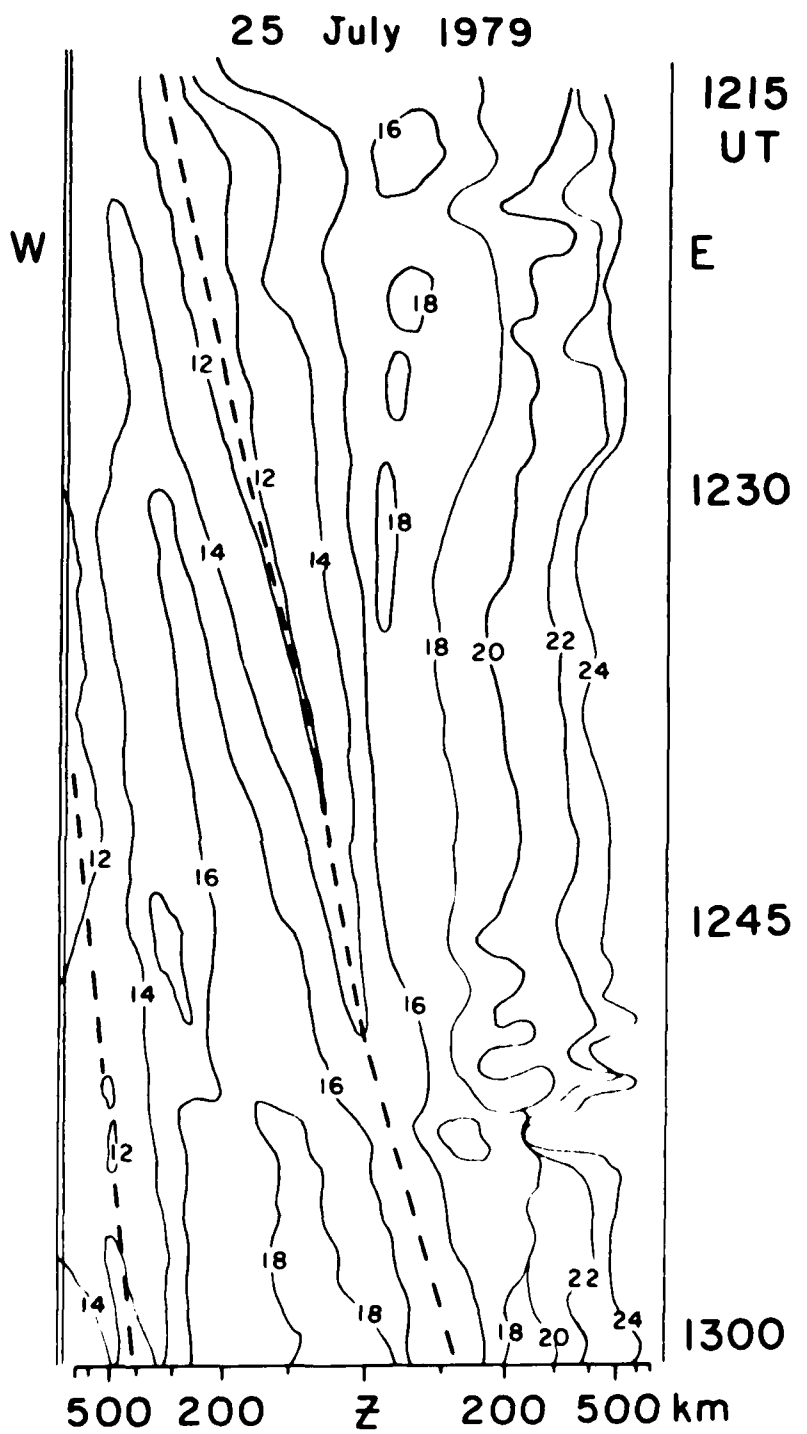


FIGURE 17 NIGHTGLOW 630.0-nm INTENSITY CONTOURS OBSERVED ON 25 JULY 1979 IN X vs t PRESENTATION FOR THE PERIOD ~ 1215 TO ~ 1300 UT. The contour numbers refer to hundreds of counts/0.5 s (approximate calibration: 1 contour unit ~ 5 R). A distance scale based on a 300-km emission height is given at the bottom of the figure.

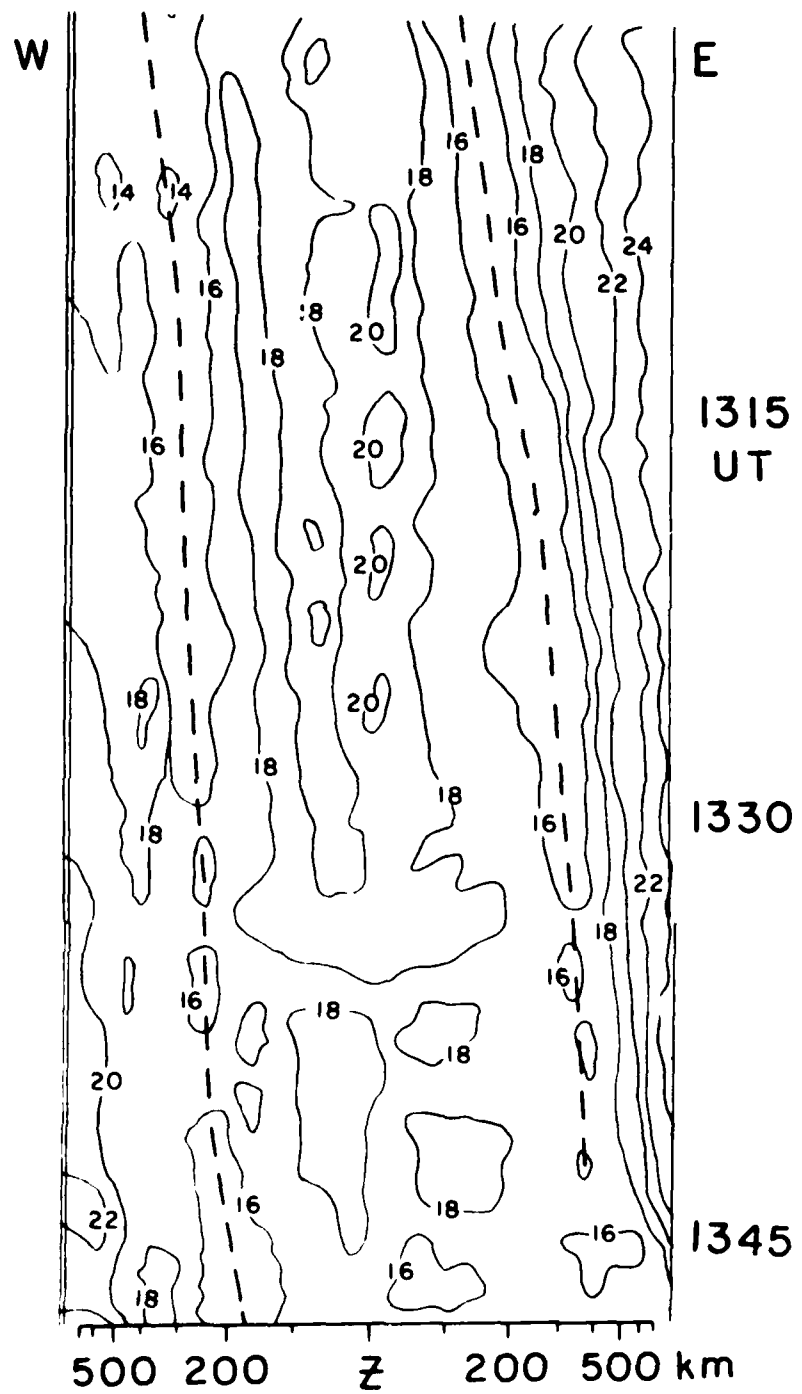


FIGURE 18 NIGHTGLOW 630.0-nm INTENSITY CONTOURS OBSERVED ON 25 JULY 1979 IN X vs t PRESENTATION FOR THE PERIOD ~ 1300 TO ~ 1348 UT. The contour numbers refer to hundreds of counts/0.5 s (approximate calibration: 1 contour unit ~ 5 R). A distance scale based on a 300-km emission height is given at the bottom of the figure.

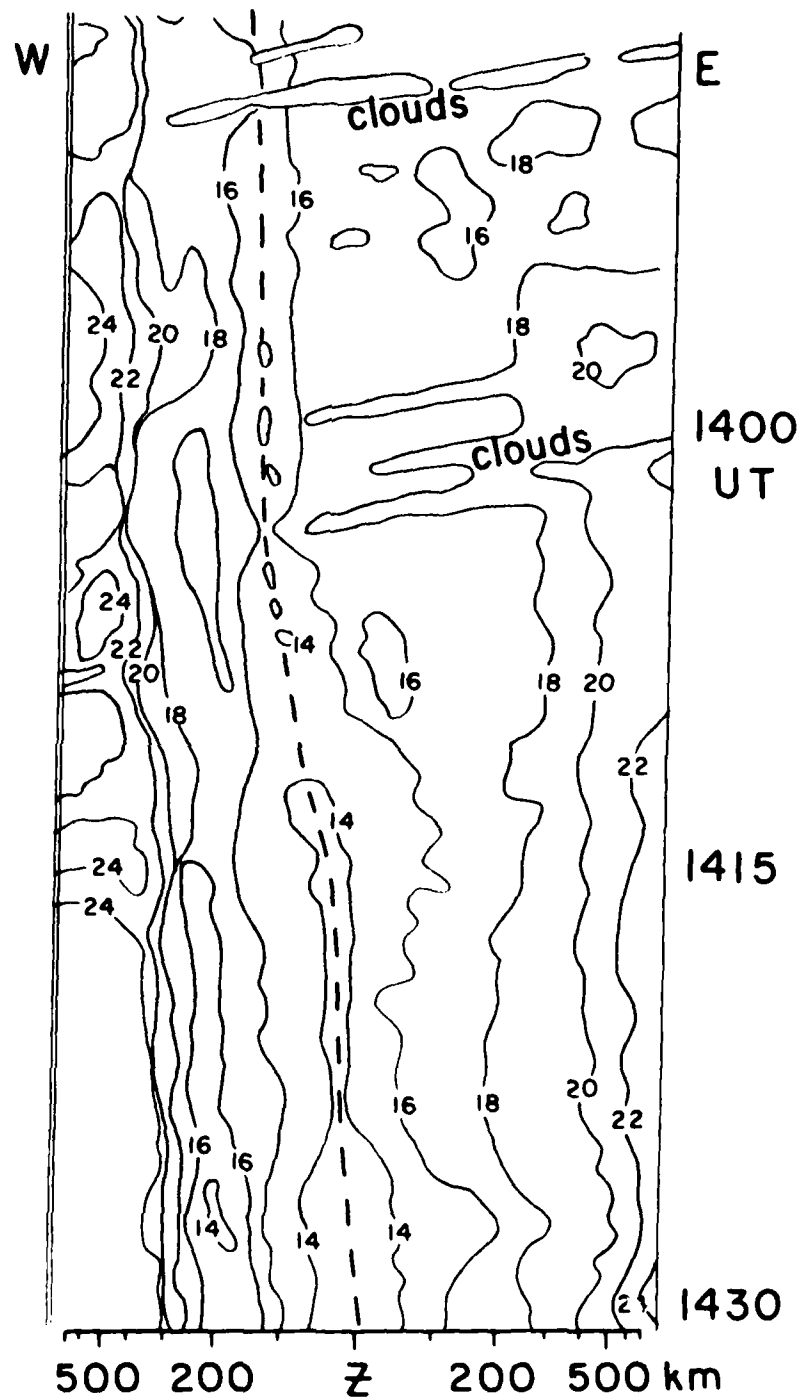


FIGURE 19 NIGHTGLOW 630.0-nm INTENSITY CONTOURS OBSERVED ON 25 JULY 1979 IN X vs t PRESENTATION FOR THE PERIOD ~ 1348 TO ~ 1431 UT. The contour numbers refer to hundreds of counts/0.5 s (approximate calibration: 1 contour unit ~ 5 R). A distance scale based on a 300-km emission height is given at the bottom of the figure.

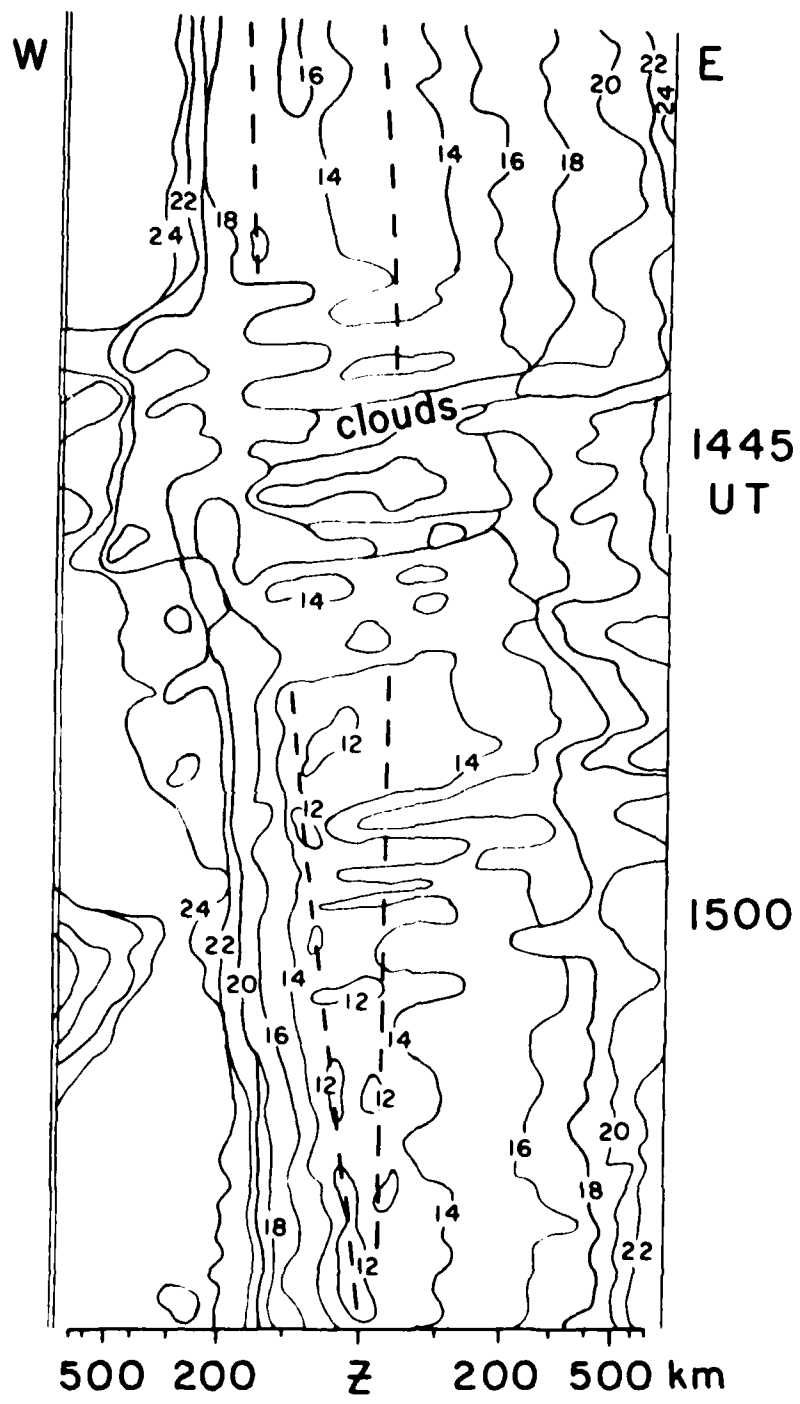


FIGURE 20 NIGHTGLOW 630.0-nm INTENSITY CONTOURS OBSERVED ON 25 JULY 1979 IN X vs t PRESENTATION FOR THE PERIOD ~ 1431 TO ~ 1514 UT. The contour numbers refer to hundreds of counts/0.5 s (approximate calibration: 1 contour unit ~ 5 R). A distance scale based on a 300-km emission height is given at the bottom of the figure.

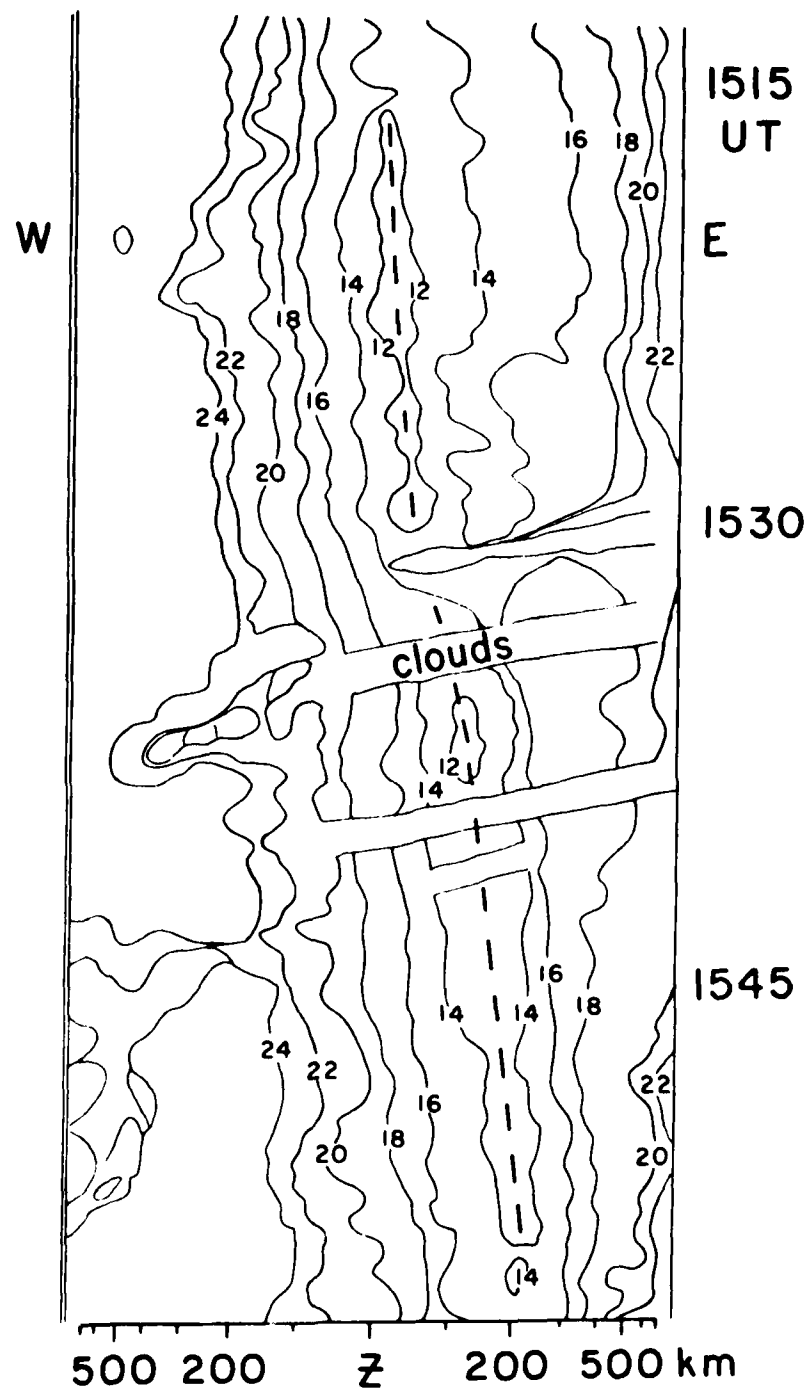


FIGURE 21 NIGHTGLOW 630.0-nm INTENSITY CONTOURS OBSERVED ON 25 JULY 1979 IN X vs t PRESENTATION FOR THE PERIOD ~ 1514 TO ~ 1555 UT. The contour numbers refer to hundreds of counts/0.5 s (approximate calibration: 1 contour unit ~ 5 R). A distance scale based on a 300-km emission height is given at the bottom of the figure.

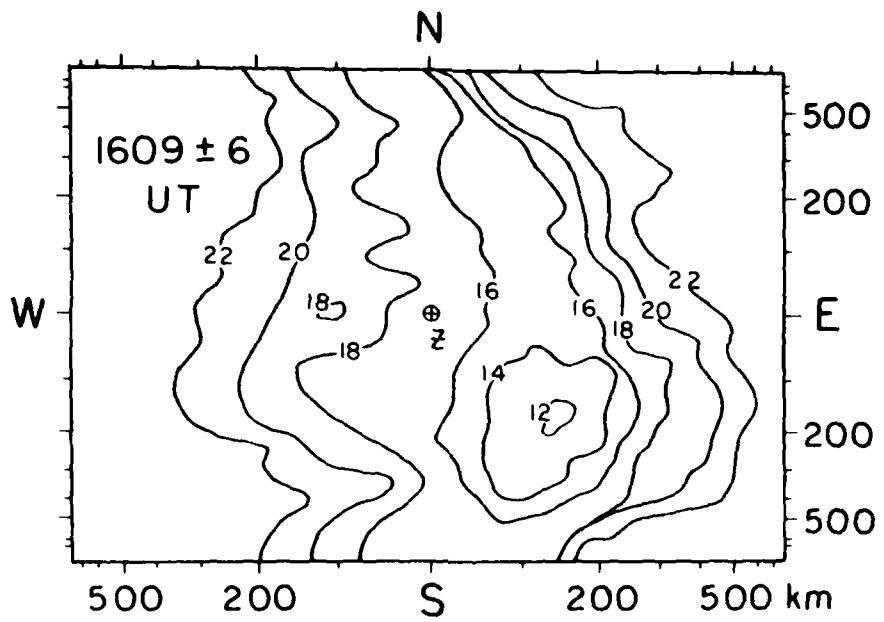


FIGURE 22 ALL-SKY 630.0-nm INTENSITY CONTOUR MAP IN X-Y PRESENTATION FOR 1609 ± 6 UT ON 25 JULY 1979. Same intensity scale as in Figure 17. The symbol, Z, indicates the local zenith. Note that the N-S and E-W distance scales are not the same.

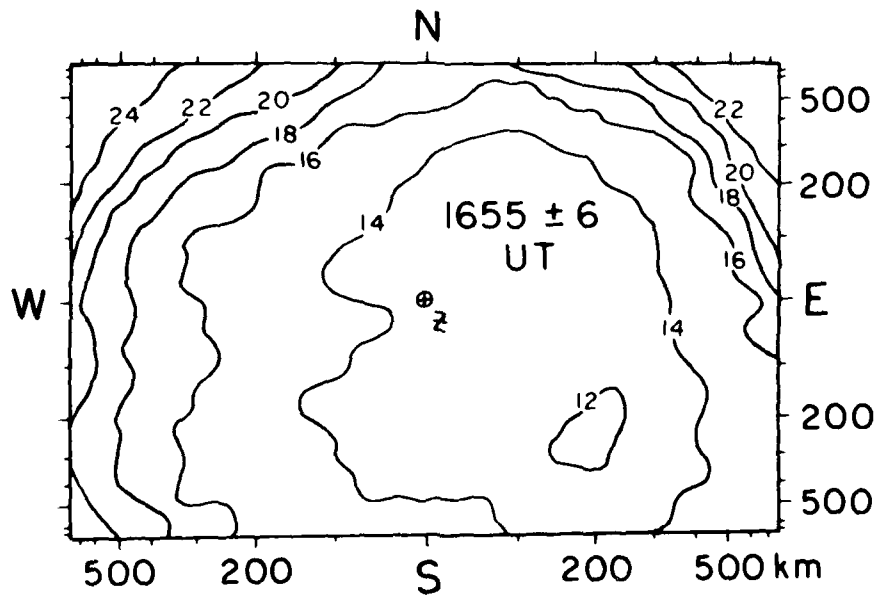


FIGURE 23 ALL-SKY MAP FOR 1655 ± 6 UT ON 25 JULY 1979. SAME INTENSITY SCALE AS IN FIGURE 17.

program.) At 1609 ± 6 UT the remnant of the N-S-aligned airglow depletion is still visible; while 3/4 hour later, at 1655 ± 6 UT, the pattern is approaching the smooth concentric-ring form of a spatially uniform 630.0-nm airglow, with the van Rijn brightening apparent toward the lower elevations (the symbol Z in the figures indicates the local zenith).

V SUMMARY

Detailed intercomparison of the present results on F-region neutral wind vectors, and 630.0-nm airglow depletion morphology, with the results of the other investigators who were involved in the July 1979 Kwajalein Equatorial Spread-F Campaign, awaits the presentations at the March 18-19 Final Data Review Meeting. For example, in view of the substantial difference in the magnitudes of the zonal winds at the times of the two rocket launches, it will be interesting to determine just how the structure and behavior of the plumes compare on the two nights. A number of general conclusions, however, can be drawn:

- (1) The equatorial neutral wind patterns, that were obtained only during geomagnetically quiet or unsettled periods ($K_p \leq 5$; $\Delta K_p < 30$), in most instances show peak neutral winds of $\lesssim 180$ m/s, attained at ~ 11 hr UT.
- (2) The nighttime zonal winds are almost always directed eastward and die away late at night, sometimes reversing to westward near dawn.
- (3) The wind vector patterns exhibit qualitative features that are consistent with an upper atmosphere circulation driven by solar EUV heating (the principal energy source under nonstorm conditions).
- (4) The 300 m/s F-region winds during the rocket-launch night of 17 July 1979 appear anomalously large for a non-storm period (K_p values $\leq 3+$ were noted up to 24 hours before and during the measuring period).
- (5) The 630.0-nm airglow depletions are readily mapped and, to the extent that they result directly from the plasma depletions associated with the bottomside of the plumes, they provide a simple and inexpensive means of observing plume development, subsequent motion, and decay.

REFERENCES

1. D. P. Sipler and M. A. Biondi, "Equatorial F-Region Neutral Winds from Nightglow OI 630.0 nm Doppler Shifts," Geophys. Res. Letts., Vol. 5, No. 5, pp. 373-376 (May 1978).
2. E. J. Weber, J. Buchau, R. H. Eather, and S. B. Mende, "North-South Aligned Equatorial Airglow Depletions," J. Geophys. Res., Vol. 83, No. A2, pp. 712-716 (February 1978).
3. J. P. McClure, W. B. Hanson, and J. H. Hoffman, "Plasma Bubbles and Irregularities in the Equatorial Ionosphere," J. Geophys. Res., Vol. 82, No. 19, pp. 2650-2664 (July 1971).
4. M. A. Biondi and W. A. Feibelman, "Twilight and Nightglow Spectral Line Shapes of Oxygen $\lambda 6300$ and $\lambda 5577$ Radiation," Planet. Space Sci., Vol. 16, No. 4, pp. 431-444 (April 1968).
5. W. A. Feibelman, R. D. Hake, D. P. Sipler, and M. A. Biondi, "Twilight and Nighttime Ionospheric Temperatures from Oxygen $\lambda 6300$ and $\lambda 5577$ Spectral-Line Profiles," J. Geophys. Res., Vol. 77, No. 10, pp. 1869-1877 (April 1972).

AD-A099 998

SRI INTERNATIONAL MENLO PARK CA
PROCEEDINGS OF THE SUMMER EQUATORIAL EXPERIMENT DATA REVIEW MEE--ETC(U)
NOV 80 D R MC DANIEL

F/G 22/2

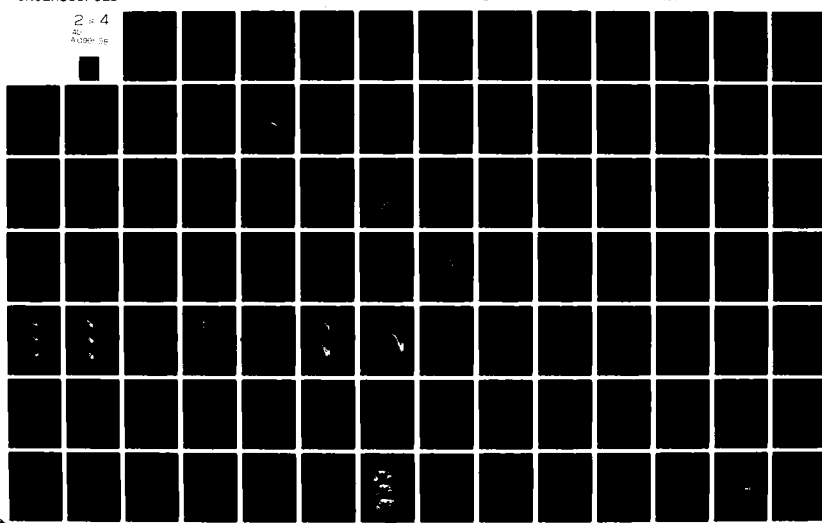
DNA001-78-C-0379

NL

UNCLASSIFIED

DNA-5528P

2 x 4
A100M 5B



**A COMPARATIVE ANALYSIS OF EQUATORIAL
IRREGULARITY STRUCTURES AS MEASURED BY WIDEBAND,
AE-E, AND IN-SITU ROCKET PROBES**

C. L. Rino, R. C. Livingston, and J. Petriceks

Radio Physics Laboratory
SRI International
Menlo Park, CA 94025

I INTRODUCTION

Wideband satellite observations of equatorial scintillation at Kwajalein were made on a regular schedule from the fall of 1976 until the fall of 1979. Complementary measurements were made at Ancon, Peru over a somewhat longer period. Scintillation, as it is observed at each station, occurs with a pronounced seasonal variation. Enhanced scintillation occurs only over a seven- to eight-month period centered on local summer--July at Kwajalein; December at Ancon.^{1*}

The most intense equatorial scintillation develops shortly after sunset.^{2,3} Severe scintillation, however, persists through midnight. Because of the sun-synchronous Wideband satellite orbit, only the midnight local time sector is sampled. Nonetheless, scintillation at L band with $S_4 \geq 0.4$ is observed in 2 to 4 percent of the passes. There is, moreover, a close association between equatorial scintillation and spread F in general and gigahertz scintillation and radar backscatter "plumes" in particular.

Gigahertz scintillation has received considerable attention because it only occurs near the geomagnetic equator. To explain it using the conventional theory requires rms electron density variations

*References are listed at the end of this paper.

in excess of 40 to 50 percent of the background. Many researchers have been reluctant to accept the existence of such large perturbations.⁴ Special scattering mechanisms have, therefore, been invoked to explain it.^{5,6,7}

In-situ equatorial electron density measurements from the Atmospheric Explorer-E (AE-E) satellite, however, clearly demonstrate the existence of extensive regions of extremely large electron-density variations. Moreover, the very large total electron content (TEC) variations in the Wideband satellite data can only be explained by the presence of such electron-density structures.

A major objective of the Wideband satellite has been the quantitative demonstration of the relationship between the in-situ irregularity structure and the observed scintillation. To this end, a large data base of AE-E satellite data has been processed carefully so that direct quantitative comparisons between the in-situ data and Wideband scintillation data can be made. The results of this effort are described in Sections II and III as an introduction to the similar analysis that has been applied to the data from the DNA 1979 Kwajalein rocket campaign.

A quantitative characterization of disturbed propagation environments generally proceeds from the spectral density function (SDF)--formally the (ensemble) average of the intensity of the Fourier transform of the random process of interest. The three-dimensional electron density is ultimately the desired quantity, but only one-dimensional scans can be measured and the full three-dimensional structure must be inferred indirectly or through modeling.

In Figure 1 a schematic representation of the one-dimensional spatial SDF, $\Phi_1(k)$ is shown. The figure was constructed by W. G. Chesnut, SRI International. A similar representation has been used by Workman⁸ who used a slightly different nomenclature for the various spectral domains. The very large scale-size range of the power-law continuum and the large dynamic range are the most conspicuous features of the spectrum. This creates practical problems both for modeling and data analysis.

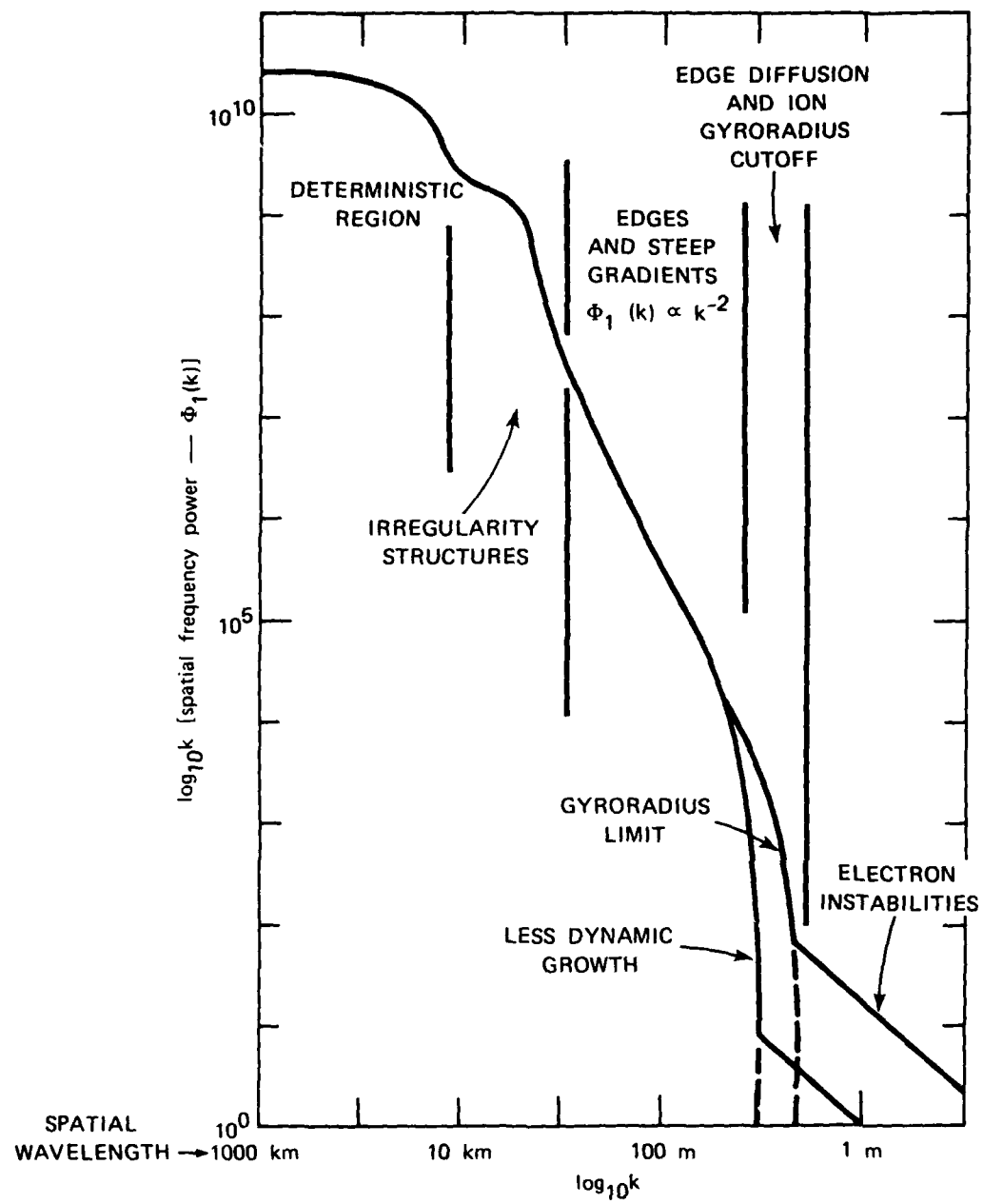


FIGURE 1 SCHEMATIC REPRESENTATION OF ONE-DIMENSIONAL SPECTRAL DENSITY FUNCTION

In this respect, the AE-E satellite is ideally suited for sampling the large-scale structures because it is in a nearly geomagnetic east-west orbit. This insures that the scan trajectory relative to the magnetic field remains nearly constant over a large interval. The Wideband satellite, by comparison is in a north-south orbit such that the propagation geometry relative to the magnetic field changes continually. Moreover, there are a number of assumptions that must be made to relate the phase SDF to the in-situ SDF.

The combined RF-beacon and in- situ electron-density measurements made during the 1979 Kwajalein rocket campaign eliminate these difficulties because, at least on the up-leg, the scan direction and the propagation path are nearly coaligned at a constant angle relative to the magnetic field. Thus, all geometrical factors are complementary and unchanging so that direct comparison can be made. The measurement itself is, however, unique and its interpretation does not follow directly from the scintillation theory as it is normally applied. This is discussed in Section IV in which the RF-beacon spectral data are presented.

II IN-SITU ELECTRON DENSITY MEASUREMENTS USING AE-E

This section summarized the results of a detailed analysis of 13 disturbed AE-E satellite passes over Kwajalein during late July and early August 1978. A more detailed account can be found in Livingston et al.⁹ An example of the measured electron density is shown in the upper frame of Figure 2. To isolate the background electron density, a low-pass filter with a sharp cutoff at 0.02 Hz which corresponds to a spatial wavelength of ~ 400 km was used.

The lower frame of Figure 2 shows the residual electron density, which admits scale sizes between 400 km and 2.6 km, (the spatial interval corresponding to the 3-Hz sampling rate used in the low-resolution AE-E data-taking mode). Because of the occasional very abrupt transitions from low to high, but nearly constant electron density, the settling time of the filter is apparent in the data (arrows).

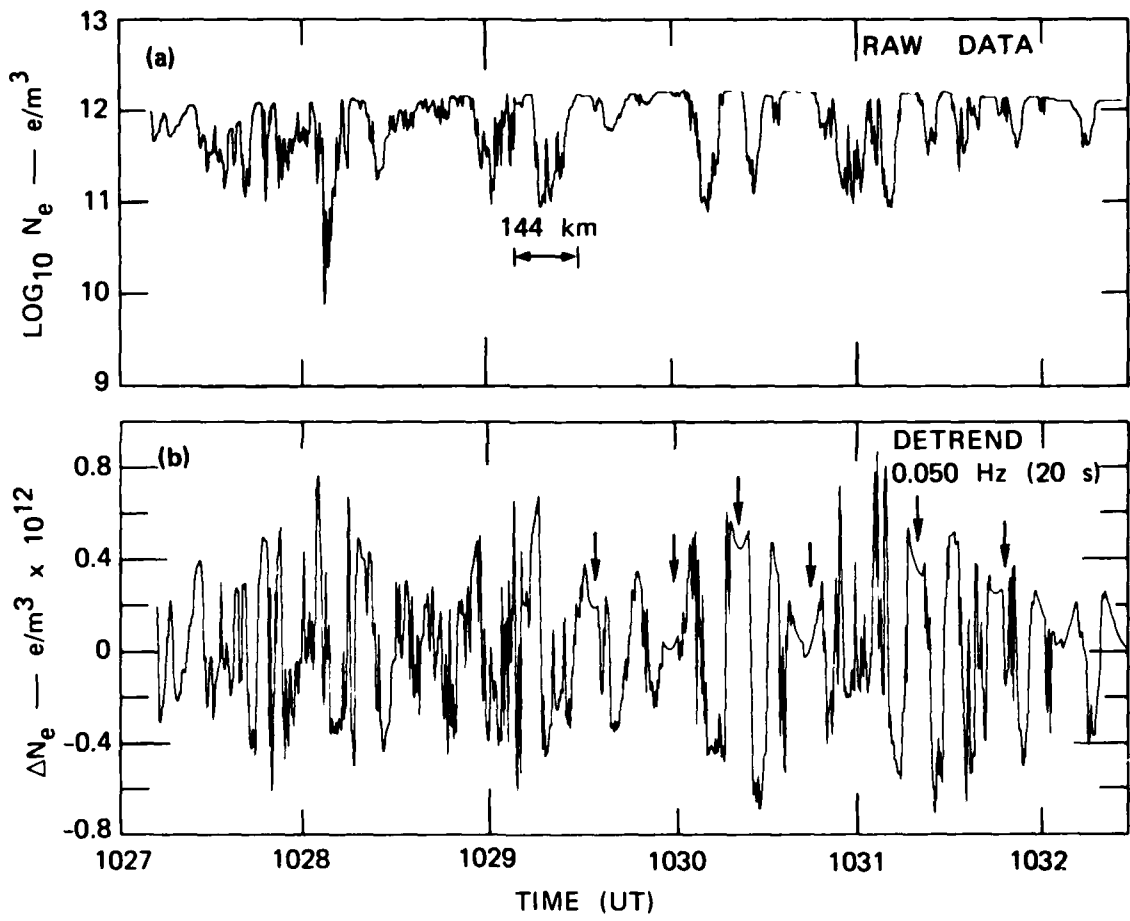


FIGURE 2 EXAMPLE OF RAW AND DETRENDED DATA FROM AE-E AT 372 km NEAR KWAJALEIN

Considerable care was taken in the data reduction to insure that such features do not affect the spectral characterization of the data. Spectral analysis was performed on overlapping 85-s (~ 600 km) data spans. Spectral fits to the function form

$$\varphi_1(f) = T_1 f^{-p_1} \quad (1)$$

were made by calculating the least-squares fit to the smoothed log-log SDF between 0.1 and 0.7 Hz. This frequency interval was chosen to minimize noise contamination at the high-frequency end and detrend effects at the low-frequency end. This is illustrated in Figure 3 in which a comparison of two detrends for a typical SDF is shown. The two spectra give essentially the same results for T_1 and p_1 . We also note that there is no evidence of a systematic outer-scale cutoff up to spatial scales approaching 300 km.

To further test the consistency of the estimates of T_1 and p_1 as well as the overall conformity to the power-law model, the calculated rms electron density

$$\begin{aligned} \langle \Delta N_e^2 \rangle &= \int_{f_c}^{\infty} T_1 f^{-p_1} df \\ &= \frac{2T_1}{p_1 - 1} f_c^{-(p_1 - 1)} \end{aligned} \quad (2)$$

was compared with the directly measured value. The results were correlated without bias, indicating general conformity to the power-law model and no systematic outer-scale cutoff within the spatial frequencies admitted by the detrend filter.

The upper frame of Figure 4 shows a plot of T_1 against the universal time of the pass (local midnight at Kwajalein where the AE-E satellite was activated occurs at 1200 UT). A clear decreasing trend in perturbation strength from premidnight to postmidnight is evident. To cast the

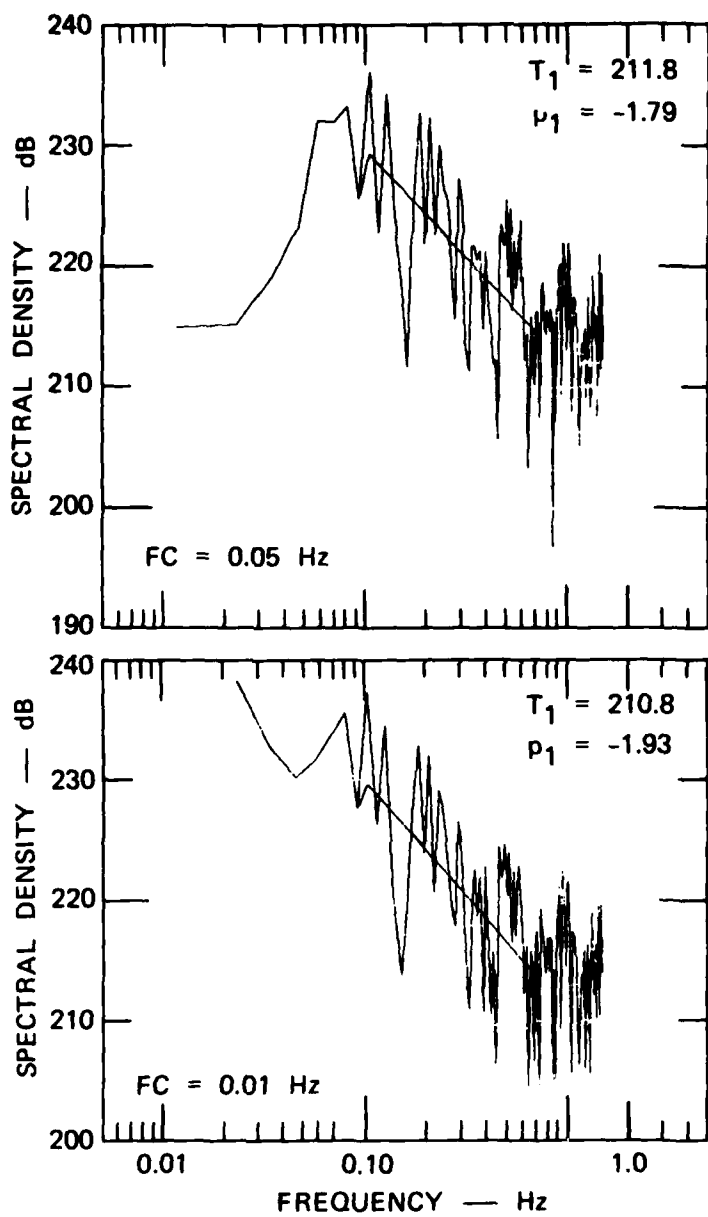


FIGURE 3 AE-E DENSITY SPECTRA FOR TWO DIFFERENT DETREND CUTOFF FREQUENCIES

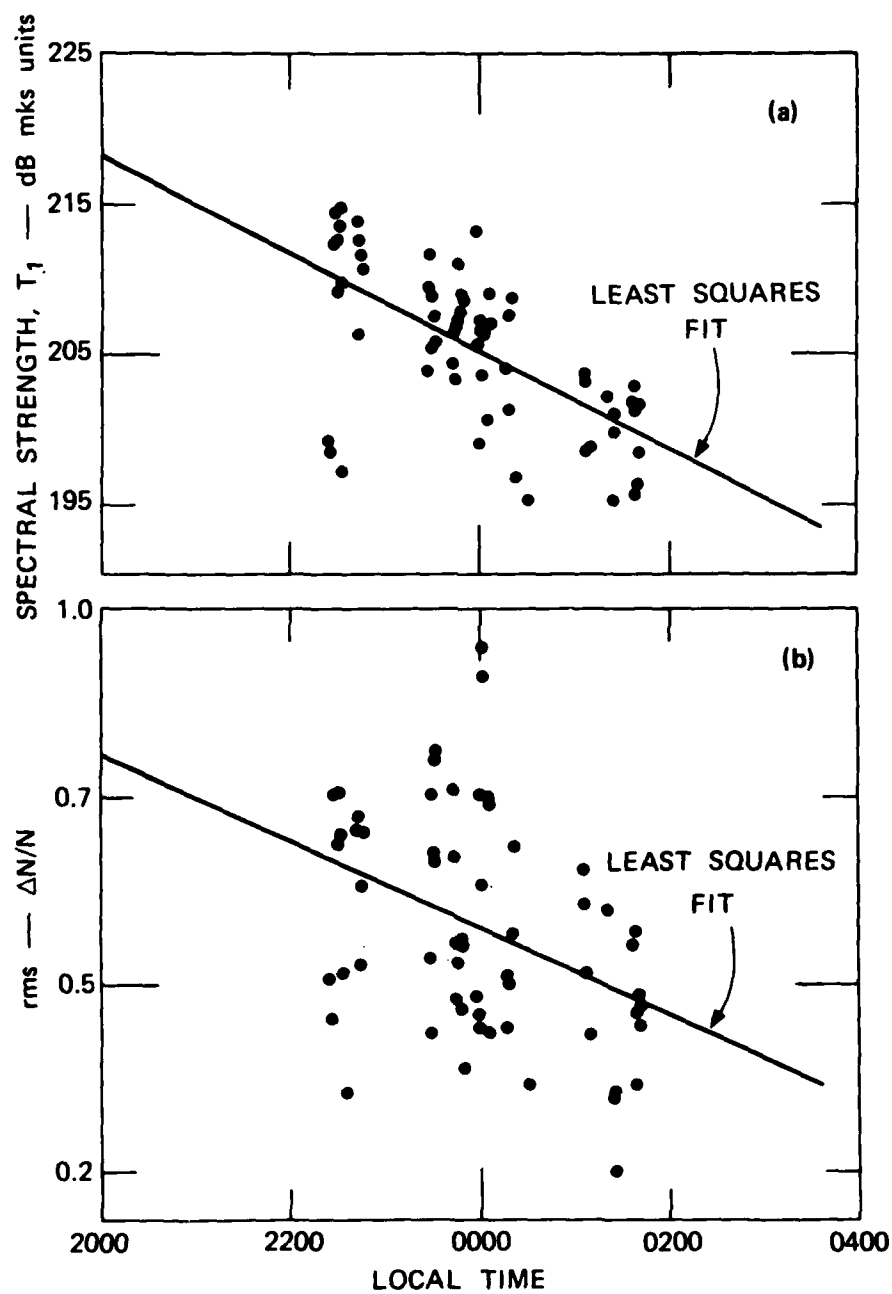


FIGURE 4 LOCAL TIME VARIATION OF EQUATORIAL SPREAD F

result in more familiar terms, in the lower frame $\langle \Delta N_e^2 \rangle^{1/2} / \bar{N}_e$ is shown plotted against universal time. Keep in mind that both \bar{N}_e and $\langle \Delta N_e^2 \rangle^{1/2}$, particularly the latter, are sensitive to the detrend filter cutoff. Indeed, the scatter about the linear least-squares fit is larger for the fractional density than it is for T_1 . In any case, it is clear that the average perturbation level, however quantified, is extremely large.

In such measurements, however, most attention has been given the spectral index, p_1 . Figure 5 shows a histogram of the measured p_1 values. The median value 1.87 is essentially identical to the value (1.84 ± 0.1) reported by Dyson et al.¹² The small skew in the distribution toward the smaller p_1 values, however, merits further consideration.

Thus, in Figure 6 the measured p_1 values are plotted against T_1 . Here we see a systematic decrease in p_1 with increasing perturbation strength. It is obvious from this behavior that we are not sampling structures dominated by steep gradients. That is, the k^{-2} portion of the one-dimensional SDF (Figure 1) does not extend to spatial scales larger than a few kilometers. Moreover, the spectral index varies systematically with perturbation strength.

To make direct quantitative comparison to scintillation data or other in-situ data we calculate the equivalent isotropic turbulent strength. That is, we assume that the three-dimensional electron density SDF has the form

$$\hat{\Delta N}_e(\vec{k}, k_z) = \frac{ab C_s}{[q_o^2 + q^2]^{v+0.5}} \quad (3)$$

where $q^2 = (\vec{k}, k_z)^T C (\vec{k}, k_z)$ is a quadratic form defined in Rino and Fremouw,¹¹ a and b are axial ratios along and transverse to the magnetic field, and q_o is the outer-scale wave number. As long as $q \gg q_o$ $\hat{\Delta N}_e(q) \sim ab C_s q^{-(2v+1)}$. The parameter, C_s , is the equivalent isotropic turbulent strength.

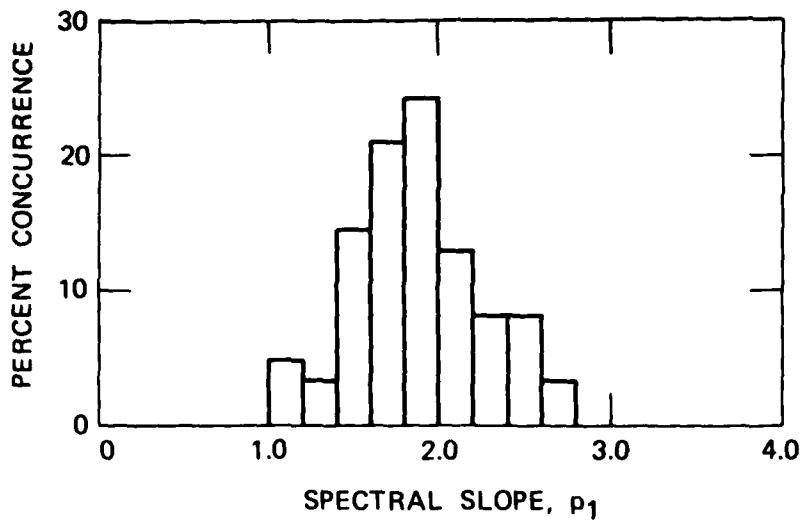


FIGURE 5 DISTRIBUTION OF AE-E SPECTRAL INDICES

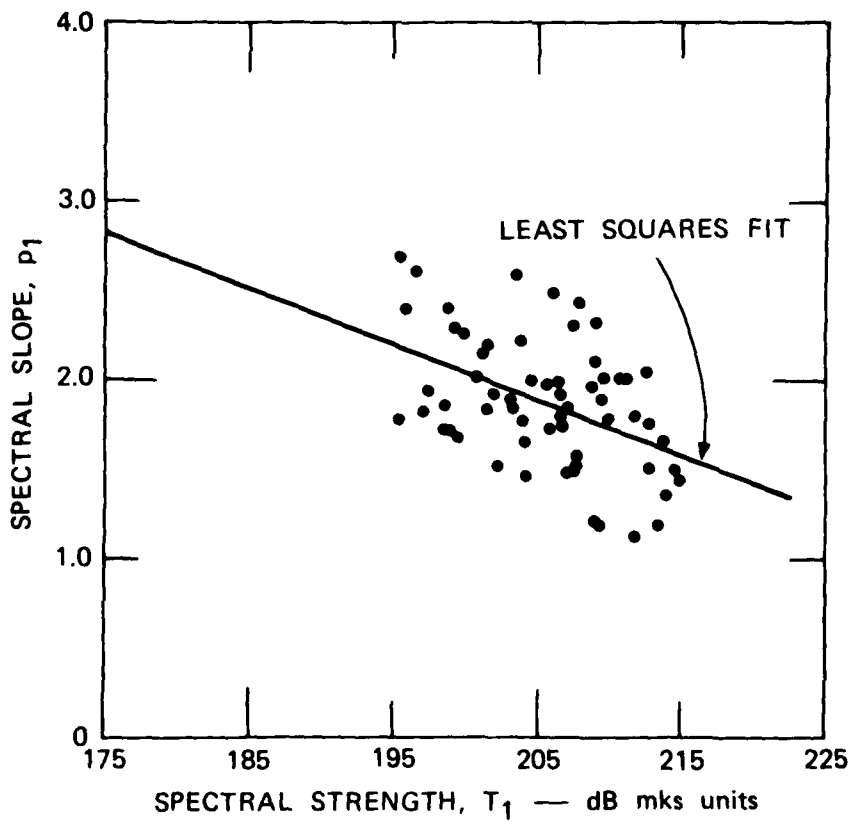


FIGURE 6 VARIATION OF p_1 WITH TURBULENT STRENGTH

One can calculate the rms electron density by integrating Eq. (3) over κ_x , κ_y , and κ_z . The result is

$$C_s = 8\pi^{3/2} \langle \Delta N_e^2 \rangle q_o^{2v-2} \frac{\Gamma(v+1/2)}{\Gamma(v-1)} \quad (4)$$

To provide some feeling for the magnitude of C_s , in Figure 7 $\langle \Delta N_e^2 \rangle^{1/2}$ is plotted against C_s for several different outer-scale values $\lambda_o = 2\pi/q_o$. T_1 can be calculated straightforwardly from Eq. (3). The result is

$$T_1 = \frac{C_s \Gamma(v-0.5)}{4\pi^2 \Gamma(v+0.5)} \frac{1}{v_p (2\pi/v_p)^{2v-1}} \quad (5)$$

and

$$p_1 = 2v - 1 \quad (6)$$

where $v_p = \vec{v}^T C \vec{v}$ is the effective probe velocity.¹² If the irregularities are isotropic, then v_p is simply the magnitude of the relative probe velocity, \vec{v} . If the irregularities are highly elongated, as is the case at the equator, then v_p is very nearly equal to the component of \vec{v} normal to the magnetic field direction.

For AE-E the satellite scan velocity is known and nearly constant over the pass. Moreover, even the largest irregularity drifts are small when compared to the satellite velocity (~ 7 km/s). Thus, the relationship between C_s and T_1 is essentially unique. Rather than use the measures value of p_1 , however, we used the median value as determined from the least squares fit shown in Figure 6.

The results are shown in Figure 8. For C_s values beyond 10^{20} , one expects significant levels of gigahertz scintillation.¹² Thus, the disturbed AE-E passes summarized here can easily account for all the observed gigahertz scintillation at Kwajalein. The fact that the spectral index varies systematically with perturbation strength is, however, a new result that has not previously been reported.

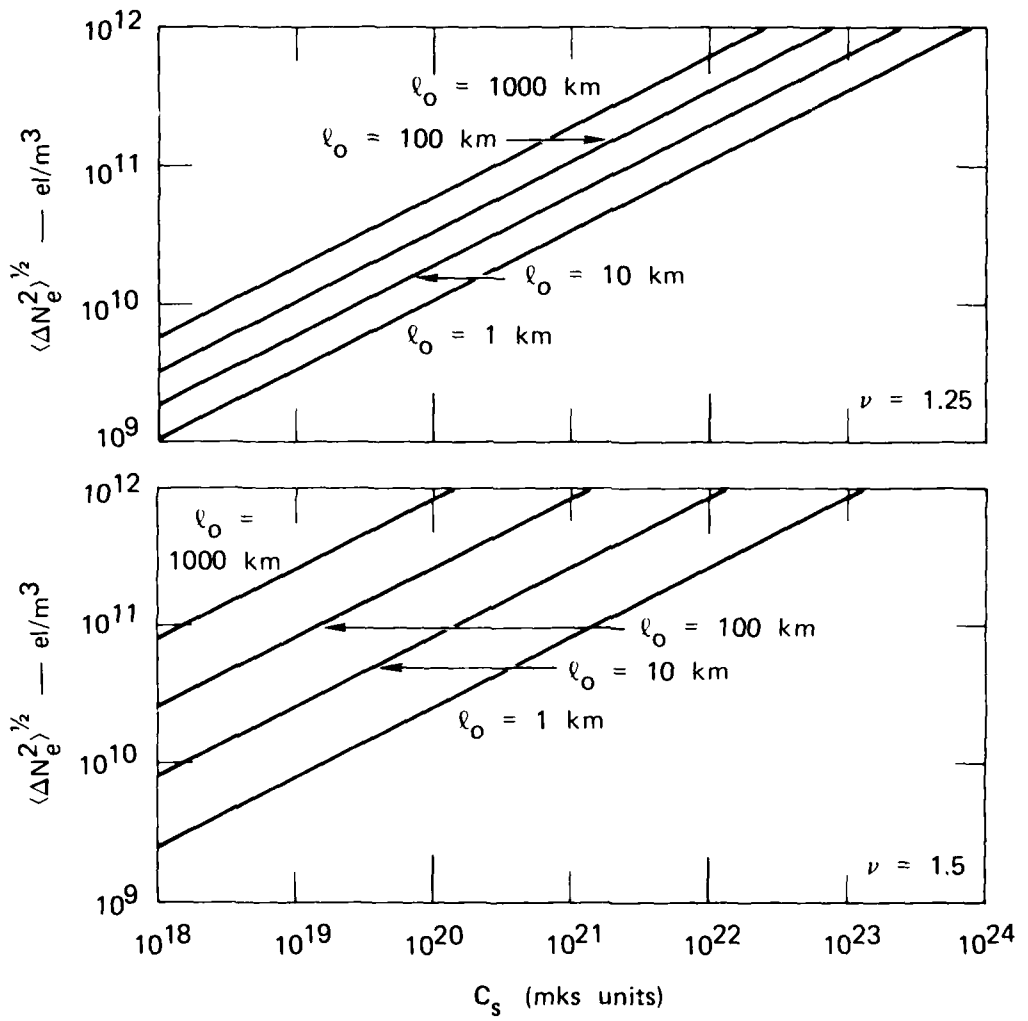


FIGURE 7 rms ELECTRON DENSITY vs C_s

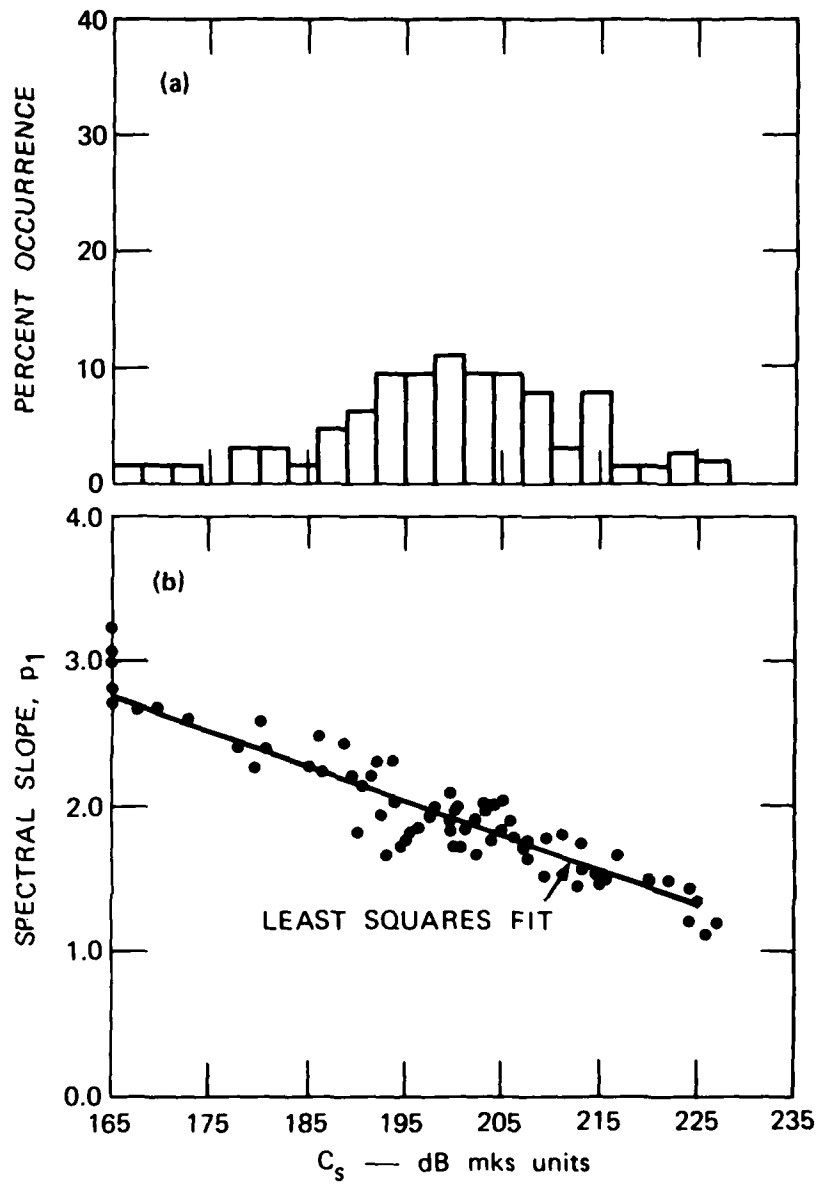


FIGURE 8 DISTRIBUTION OF C_s FOR AE-E (July 1978)

III WIDEBAND EQUATORIAL SCINTILLATION DATA

The first order in terms that depend on the Fresnel radius, the phase scintillation is directly proportional to the integral of the electron density along the propagation path. It can be shown¹² that the one-dimensional phase SDF $\varphi(f)$ has the form Tf^{-p} where

$$T = C_p G \frac{\sqrt{\pi} \Gamma(\gamma)}{\Gamma(\gamma + 1/2)} v_{\text{eff}}^{2\gamma - 1} \quad (7)$$

and

$$p = 2\gamma \quad (8)$$

In Eq. (7)

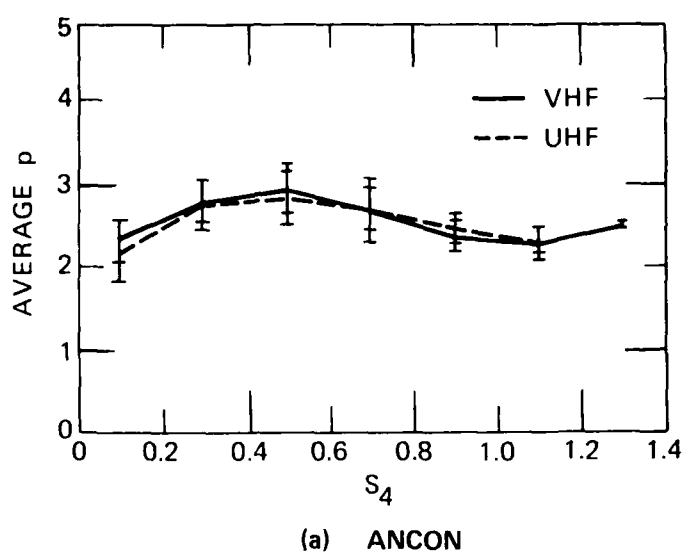
$$C_p = r_e^2 \lambda^2 \ell_p C_s \quad (9)$$

is the phase turbulence level, r_e is the classical electron radius, λ is the wavelength, and ℓ_p is the length of the propagation path.

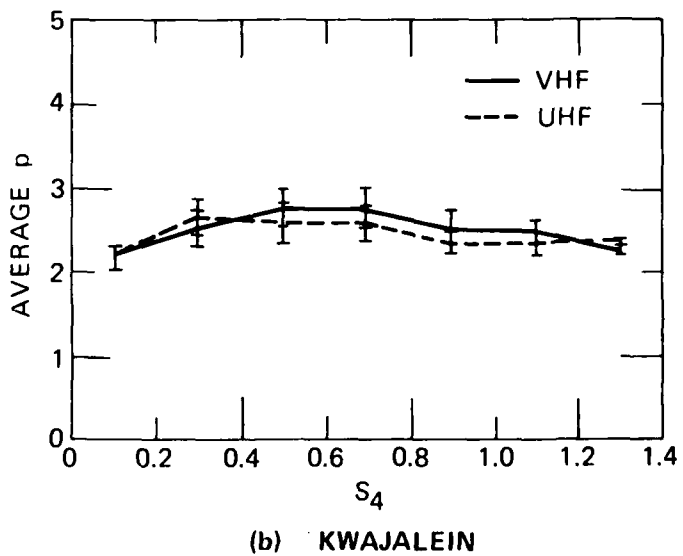
The parameter, G , is the geometrical enhancement factor. It varies from unity for cross-field propagation to a for field-aligned propagation. The parameter v_{eff} behaves similarly to v_p . For example, in an isotropic medium v_p is nearly equal to the component of the scan velocity perpendicular to the line of sight. In general, however, v_{eff} is much smaller than the perpendicular component of the line-of-sight velocity; moreover, it depends critically on the irregularity height.

The phase spectral index, p , however, is simply related to γ . Indeed, if $p_1 = 2$, then $p = 3$. One of the earliest findings in the Wideband satellite data was that the spectral index is systematically less than 3. This is illustrated in Figure 9.¹²

Eqs. (7) and (8) have been applied using the measured values of T and p , and ionospheric parameters appropriate to the nighttime equatorial F region: a 100-km thick scattering layer centered at 400 km, and an



(a) ANCON



(b) KWAJALEIN

FIGURE 9 VARIATION OF WIDEBAND PHASE SPECTRAL INDEX WITH S_4

irregularity axial ratio of 100:1. Figure 10(a) shows the resulting C_s distribution, which is similar in shape, but shifted upward from the C_s distribution derived from the in-situ data [Figure 8(a)]. In Figure 10(b) the phase slope, p , has been plotted as a function of C_s , for comparison to the in-situ p_1 versus C_s [Figure 8(b)]. The most important feature in the comparison of Figures 8(b) and 10(b) is, perhaps, that both experiments show nearly identical trends in the decrease of spectral slope with increased turbulence. The slope of the least-squares-fit line in Figure 10(b) is slightly steeper; we attribute this to the data points above the $C_s = 215$ -dB level, which show an accelerated shallowing of spectral slope. This effect is caused most likely by diffraction.

When we compare the separation of the p_1 and p indices at low values of C_s , we find the unity separation dictated by Eqs. (6) and (8). At higher values of C_s , this separation narrows, probably because of diffraction effects in the phase spectrum. In general, however, care must be used in interpreting this slope separation; although the in-situ-implied C_s values are essentially unambiguous, the phase-implied values depend highly on the model. Indeed, an upward shift of 5 dB in the C_s values in Figure 10 would bring the average slope separation to unity.

As for absolute turbulence levels, we believe that the difference between the C_s distributions in Figures 8 and 10 is real and can be explained. We argue that for the data sets used here, the Wideband satellite sampled, on average, much more intense irregularities than AE-E. Consider first that phase scintillation is the integrated effect of all the contributions along the propagation path, whereas the in-situ data come from a single narrow range of altitudes. If that range of altitudes does not include the strongest F-layer turbulence, the in-situ C_s will generally fall below the values deduced from the scintillation data. Second consider that for this particular data set the strongest scintillation arises from penetration locations well north of Kwajalein (coincident with the equatorial anomaly). The flux tubes intersecting this region are well above the AE-E altitude at the latitudes sampled.

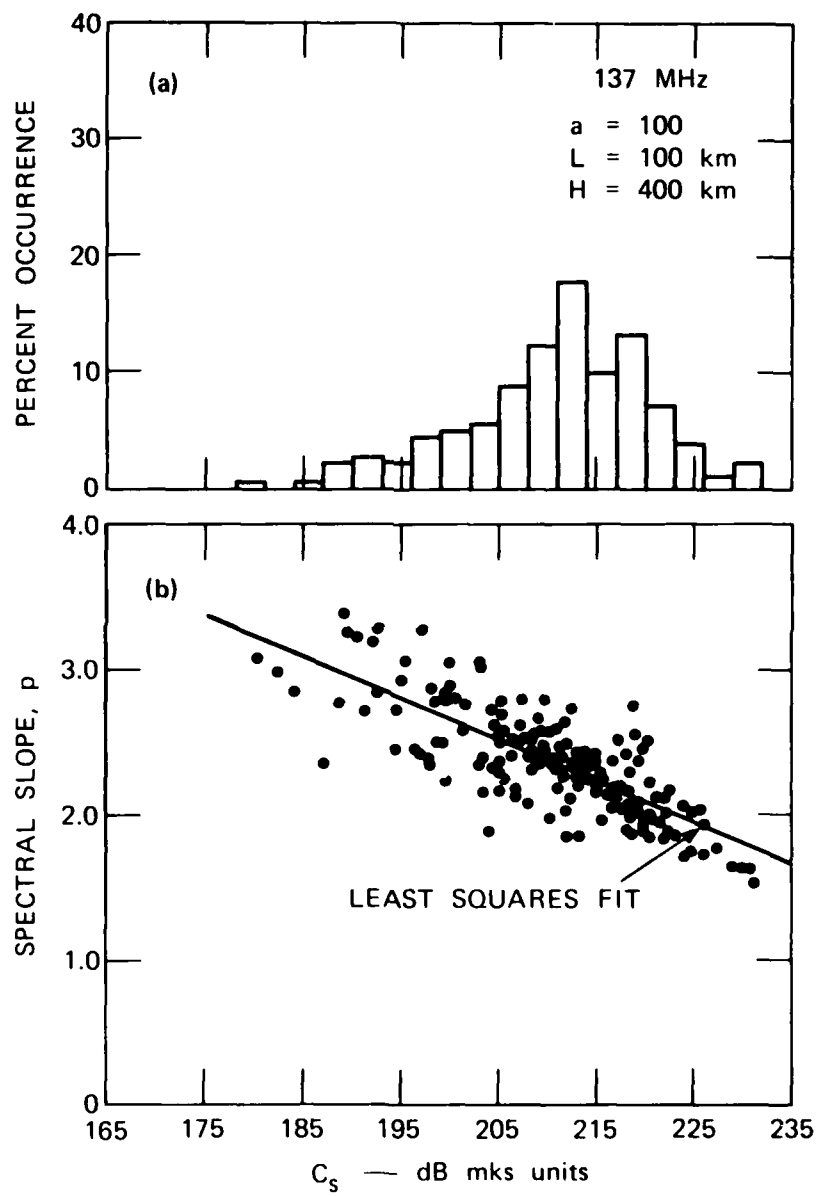


FIGURE 10 DISTRIBUTION OF C_s COMPUTED FROM WIDEBAND DATA (July 1978)

We conclude that a completely unambiguous direct comparison of in-situ and phase-scintillation turbulence levels is not feasible with the small data set at hand. The differences, however, can be explained and would most likely disappear in a true global comparison of in-situ and phase scintillation turbulence levels. The most important result, however, is that a decreasing spectral slope with increasing turbulence level is observed, and that the trend matches the trend observed in the in-situ spectral index almost exactly. The p-index values are plotted against the corresponding S_4 scintillation index to reveal any systematic variation that might indicate contamination of the measurement caused by diffraction effects.

The systematic flattening of the spectra at the very low S_4 values is due to noise contamination. For S_4 greater than 0.4, however, there is a tendency for p to decrease with increasing S_4 . Initially, we attributed this trend to diffraction effects and chose the largest p value as a representative median. There was, however, no basis for choosing p larger than 2.5 to 2.6 for Kwajalein and 2.6 to 2.7 for Ancon. That is, even allowing for a bias caused by diffraction, the spectral index remains less than 3.

To perform a detailed comparison between the AE-E and Wideband data a set of 9 disturbed passes taken during the July-August-1978 period were selected for comparison. To eliminate the noise-contaminated p values, only data with $S_4 \geq 0.4$ were used.

We now turn to the spectral analysis of the rocket beacon and Langmuir probe data obtained during the DNA 1979 Kwajalein Campaign.

IV ROCKET BEACON SCINTILLATION ANALYSIS

A. Introduction

Petriceks¹³ describes the rocket beacon experiment in detail. In this section we shall discuss the scintillation data. To extract the scintillation from the slower trend-like data variations, we have used a

detrend filter with a 50-km cutoff. That is, in the scintillation data we preserve all Fourier components with spatial wavelengths shorter than 50 km. As discussed in Petriceks,¹³ the raw data have been interpolated onto a uniformly sampled spatial grid to simplify the data interpretation.

For reference, Figure 11 shows the upleg electron-density profile derived from the Langmuir probe data. Also in the figure is the background profile that was obtained by using a 10-km detrend filter. The shorter detrend interval was used to provide better definition of the large-scale features in the profile, particularly the well-defined depletion at 500 km.

We shall be concerned mainly with the phase data because it is most simply related to the in-situ data. Neglecting diffraction effects, the phase perturbation is given by the integral

$$\delta\varphi(z) = r_e \lambda \int_0^z \Delta N_e(\vec{p}, \eta) d\eta \quad (10)$$

where z is the distance along the propagation path, which is essentially coincident with the upleg rocket trajectory.

If $\Delta N_e(\vec{p}, z)$ remains stationary and time invariant over the interval that the phase data are being accumulated, it follows from Eq. (10) that

$$\dot{\delta}\varphi(\kappa_z) = r_e^2 \lambda^2 \Phi_1(\kappa_z) / \kappa_z^2 \quad (11)$$

where $\Phi_{\delta\varphi}(\kappa_z)$ is the one-dimensional spectral density function of the beacon phase data. Thus if

$$\Phi_1(\kappa_z) = T'_1 \kappa_z^{-p_1} \quad (12)$$

then

$$\dot{\delta}\varphi(\kappa_z) = T'_z \kappa_z^{-p_z} \quad (13)$$

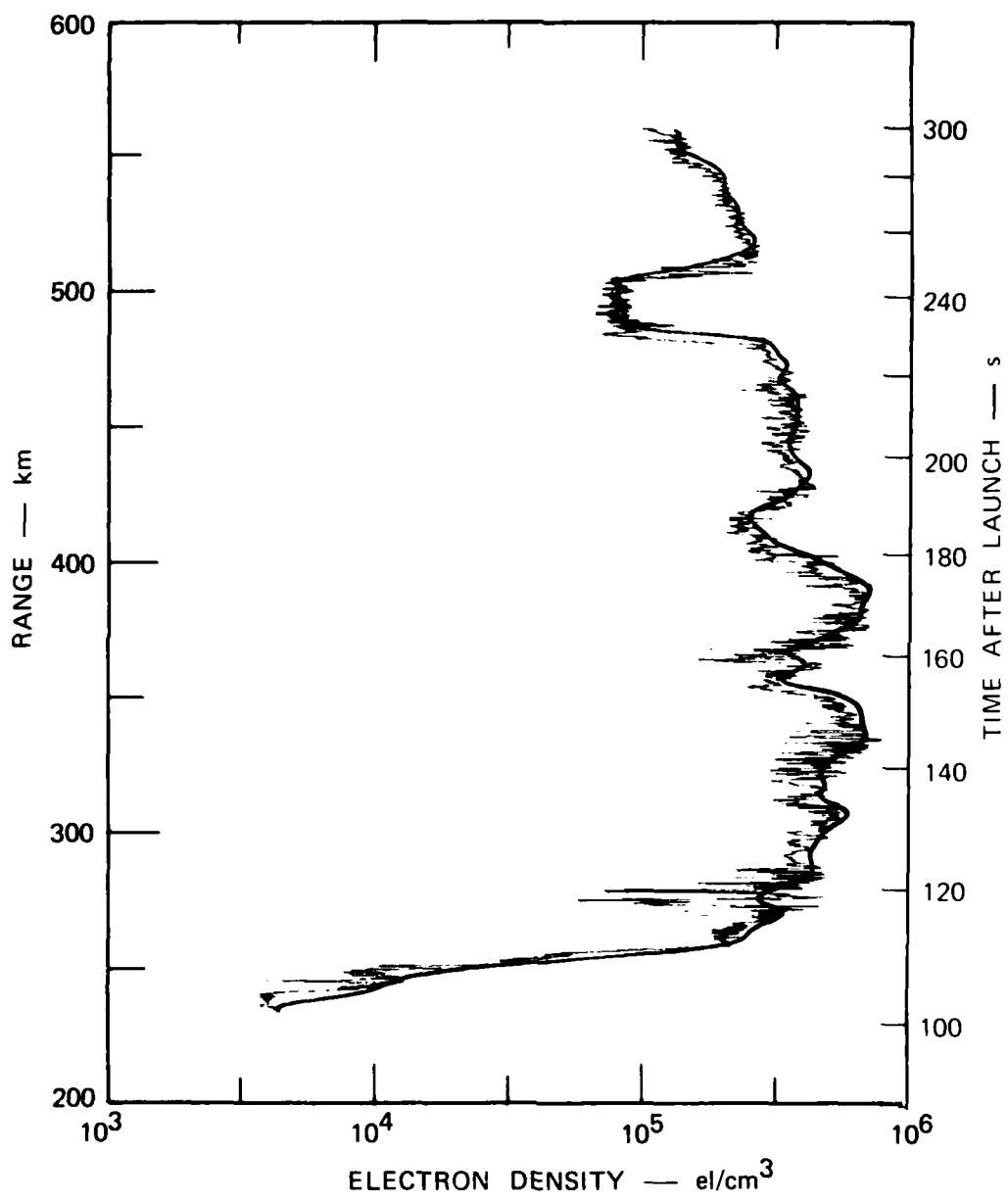


FIGURE 11 UPLEG ELECTRON-DENSITY PROFILE DERIVED FROM THE LANGMUIR PROBE DATA

where

$$T'_z = r_e^2 \lambda^2 T'_1 \quad (14)$$

and

$$p_z = p_1 + 2 \quad (15)$$

We note that the relationship between T'_z and T'_1 does not depend on geometrical factors [cf. Eq. (5)]. The primes are used to indicate that the turbulent strength refers to spatial wave number rather than temporal frequency as do T_1 and T , as defined by Eq. (5) and Eq. (7), respectively. For convenience, we shall measure spatial wave number in units of reciprocal length, that is with no 2π factor.

B. S_4 and σ_φ

A good test of the stationarity of $\Delta N_e(\vec{r}, z)$ is the behavior of S_4 and σ_φ as a function of z . Because these summary parameters depend on the integrated effects along the propagation path, we expect a monotonic increase in both S_4 and σ_φ as a function of z . Figure 12 shows the upleg S_4 values measured over 40-km overlapping data intervals. The very large 145-MHz S_4 values at ~ 350 km are due to deep, persistent fades (Petriceks¹³, Figure 3), and are probably not reliable measures. It is clear, however, that S_4 increases monotonically only to ~ 350 km. This behavior is more clearly seen in the σ_φ data shown in Figure 13. Before plotting the 291-MHz σ_φ data, it was scaled by the wavelength ratio of the 291-MHz and 437-MHz signals to verify the expected linear dependence of σ_φ in wavelength. The discrepancy beyond 500 km is caused by "cycle slipping" at 291 MHz caused by the severe fading. Beyond 350 km, the scintillation structure shows both increases and decreases that suggest that the propagation environment was very dynamic indeed.

The ALTAIR backscatter data described in Tsunoda¹⁴ confirms the dramatic short-term changes that were occurring on the lower portion of the upleg. It appears that the decrease in scintillation at 350 km is

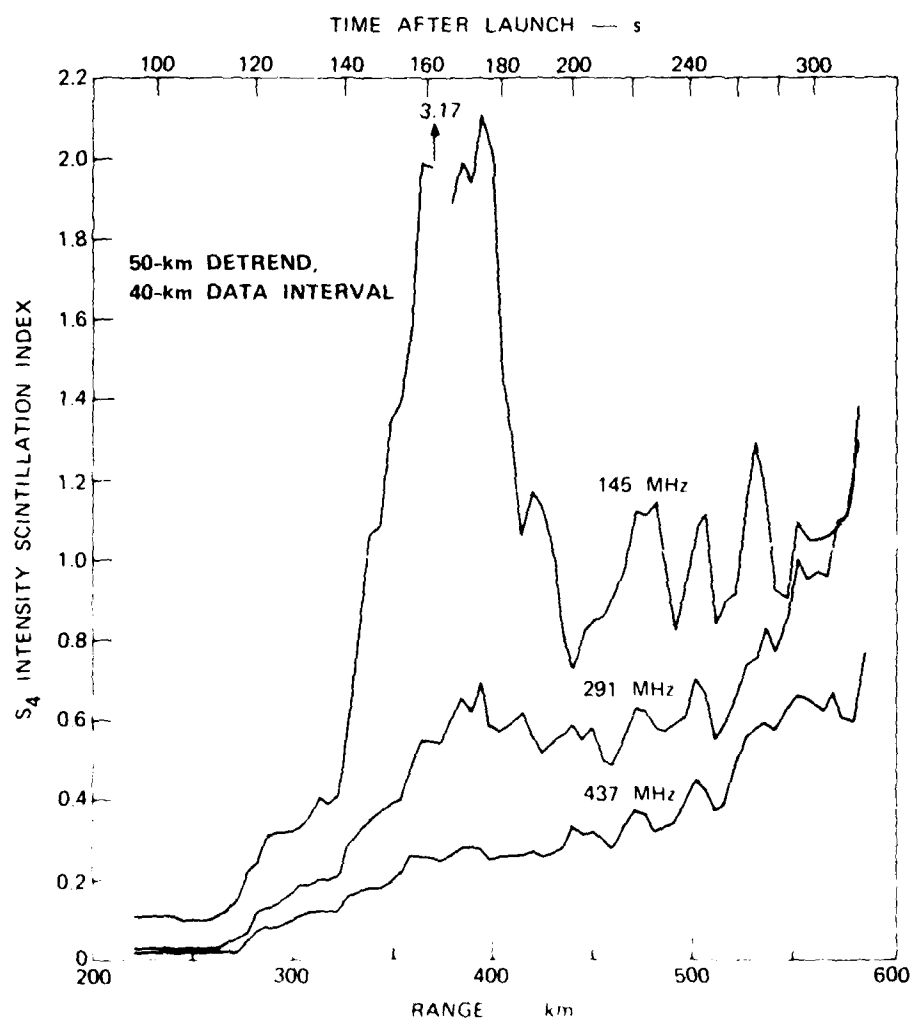


FIGURE 12 INTENSITY SCINTILLATION INDEX FOR ROCKET UPLEG

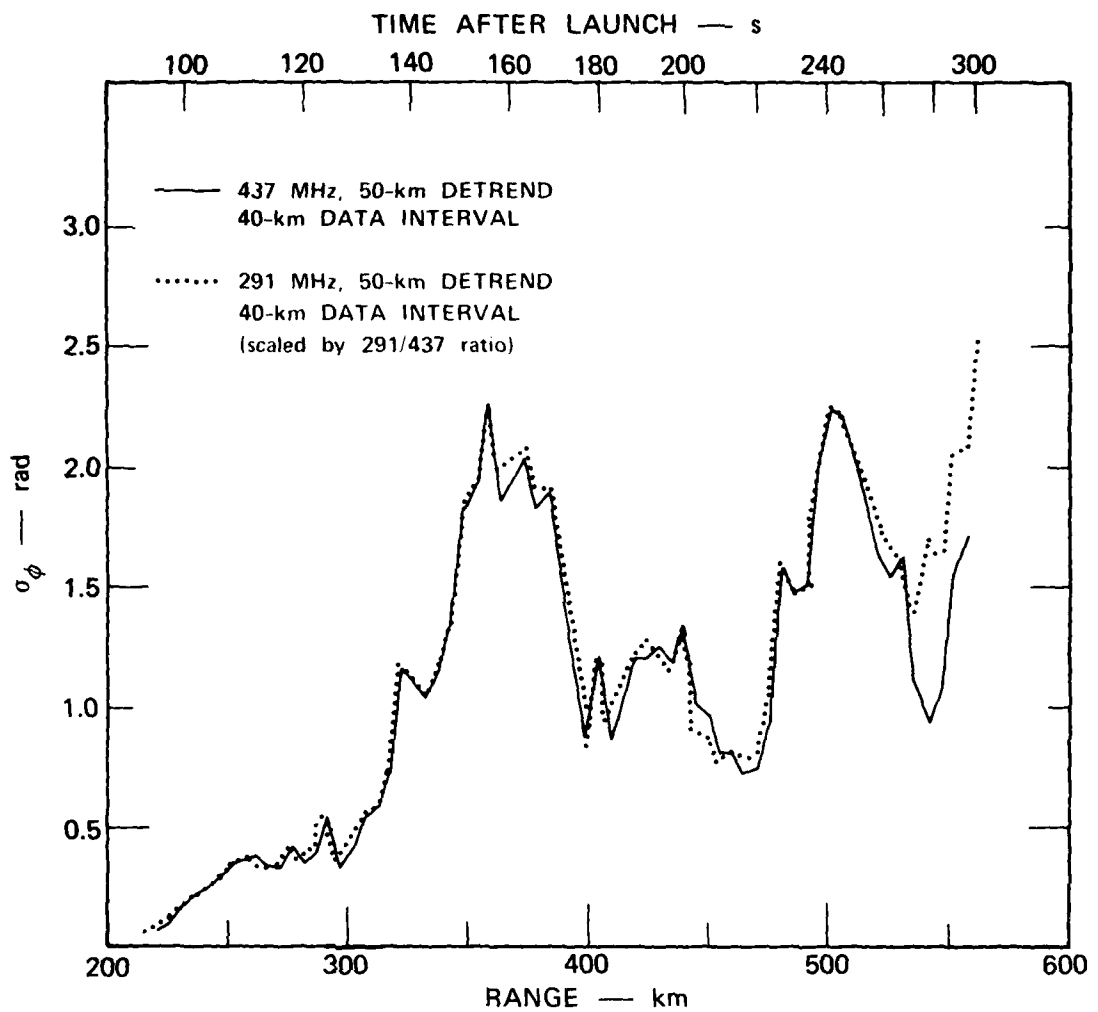


FIGURE 13 PHASE SCINTILLATION DATA FOR ROCKET UPLEG

caused by the passage of a depleted-density region into the propagation path. This is, of course, not reflected in the probe density profile (Figure 11) because the probe was already above the altitude at which ALTAIR showed the enhanced backscatter signature that has been associated with depletions.

It is also significant that the most intense scintillation occurred on the lower portion of the upleg where the background densities were highest. In fact, we shall see that the enhanced scintillation at 500 km cannot be attributed to the depletion there. The enhancement is most likely caused by an enhanced structure near the electron-density maximum of the same type that we unambiguously associate with the scintillation enhancement at 350 km.

C. Spectral Analysis

We now turn to the spectral analysis of the beacon phase-scintillation data. Extreme care was taken in performing the spectral analysis to ensure that the processing itself did not influence the final T_z and P_z parameters. Because there is only a short data segment means that contamination owing to invariable end-point mismatch is always a possibility, particularly in an environment characterized by a steeply sloped spectral density function.

To test for end-point effects we have processed the data using several different detrend intervals. We found that the results did indeed vary. We applied a second linear detrend to ensure that the end points matched prior to the actual spectral analysis. We also tried data windowing, but the results were less satisfactory. As an aside, standard windowing is effective when isolated spectral features are present. Where low-frequency spectral content is important, windowing can and does cause spurious results.

In Figure 14 we show the spectral indices, p_z , derived by using three different detrend intervals. The p_z index was derived by performing a log-linear least-squares fit to the measured spectral density function over the spatial wave-number range 0.2 to 2.0 km^{-1} . This is well

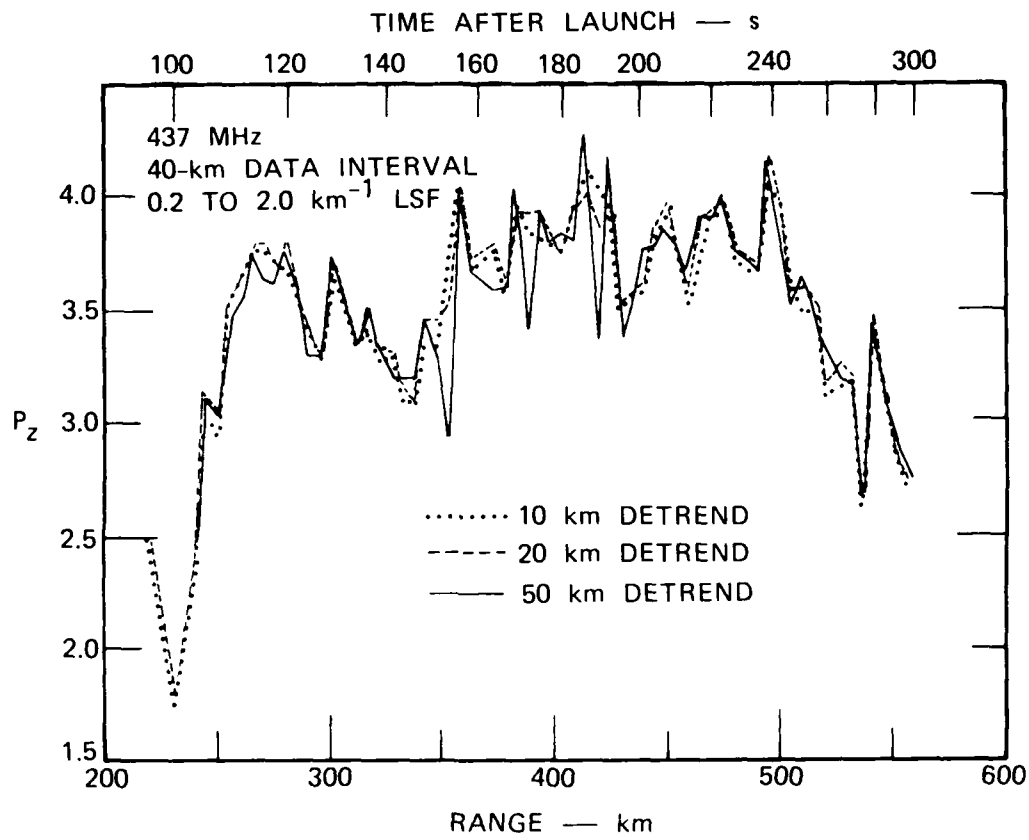


FIGURE 14 PHASE SPECTRAL INDEX p_z FOR ROCKET UPLEG

below the detrend-filter cutoff (0.02 km^{-1}). The logarithmical spacing of the contributing data points in the least-squares fit does not significantly affect the result. The results consistently indicate that there is no contamination because of end-point mismatch.

The first point to note is that the p_z index varies systematically after the abrupt onset of scintillation. As the rocket-payload penetrates the bottom of the F layer, p_z decreases from ~ 3.65 to ~ 3.1 . Around $\sim 350 \text{ km}$, p_z abruptly increases and then fluctuates about ~ 3.8 until $\sim 500 \text{ km}$, at which p_z again systematically decreases. The regions in which the systematic decreases in p_z occur are precisely the regions in which pronounced scintillation enhancement occur, which is the same effect that was observed in the Wideband satellite data (Section III).

The second point to note is that, except for the region between ~ 360 and $\sim 500 \text{ km}$, p_z is well below 4, which corresponds to a κ^{-2} one-dimensional in-situ spectral density function. This is also consistent with the Wideband satellite data. It is, however, more interesting to consider the in-situ probe data. For this purpose Utah State University kindly made the Langmuir-probe data available to us. The Langmuir probe does not give an absolute electron-density measurement, but this is not important for our purposes here.

D. Langmuir-Probe Spectra

A density calibration for the Langmuir-probe data was obtained by comparing it to incoherent scatter data from the ALTAIR radar. The density data were then processed in exactly the same manner as the beacon phase data. The consistency of the estimated p_1 values for different detrend intervals was better than that obtained from the scintillation data. This was expected because the more intense low-frequency content of the phase data caused by its steeper spectral index [Eq. (5)] exaggerates the end-point mismatch contamination.

Figure 15 shows the measured p_1 values obtained by fitting over the spatial wave-number range $0.2 - 2.0 \text{ km}^{-1}$. Superimposed on the plot is κ^{-2} from the beacon data. The agreement is very good through 340 km.

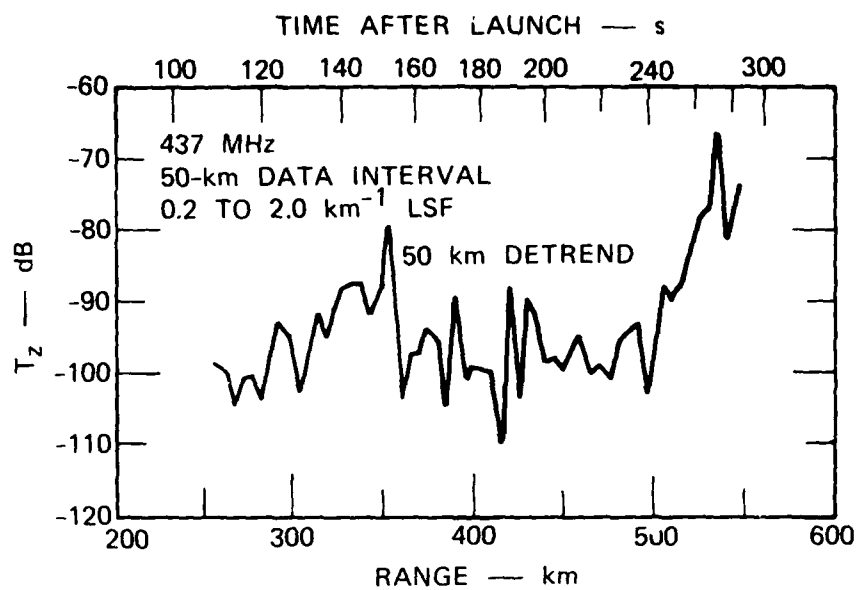


**FIGURE 15 SPECTRAL INDEX FOR LANGMUIR PROBE
LARGE SCALE STRUCTURE**

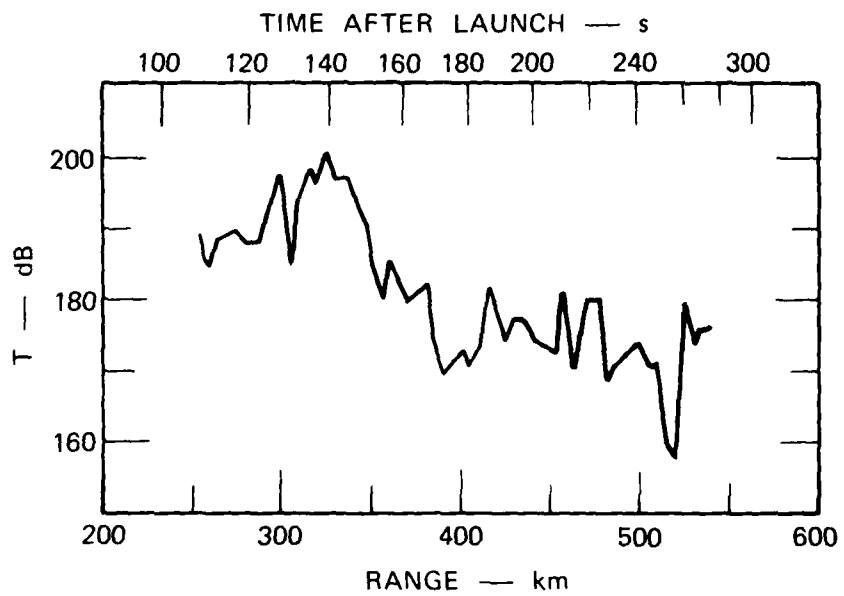


**FIGURE 16 COMPARISON OF SPECTRAL INDEX FOR LARGE-
AND SMALL-SCALE STRUCTURE**

From that point on the beacon data imply generally smaller values than the in-situ probe shows particularly through the large depletion at 500 km. We believe the discrepancy is due to the strong influence on the beacon data by structure at lower altitudes, which follows the variable, more shallowly sloped spectra.

This is also evident in the behavior of the T'_1 parameter for the probe data shown in Figure 16. The T'_1 parameter is large through 350 km at which it begins a decline throughout the rest of the upleg portion of the flight. It is instructive to compare the T'_1 parameter to the rms electron density and

$$\langle \Delta N_e^2 \rangle^{1/2} / N_e .$$

These are shown in Figures 17 and 18, respectively.

The rms electron density gives essentially the same picture as does T'_1 . Keep in mind, however, that $\langle \Delta N_e^2 \rangle$ depends on p_1 as well as the detailed structure of the dominant low-frequency portion of the spectral density function. It is a good approximation to take [c.f. Eq. (2)]

$$\begin{aligned} \langle \Delta N_e^2 \rangle &= 2 \int_{\lambda_o^{-1}}^{\infty} T'_1 q^{-p_1} dq \\ &= \frac{2T'_1}{p_1 - 1} \lambda_o^{p_1 - 1} \end{aligned} \quad (16)$$

Here $\lambda_o \sim 40$ km because the data interval is shorter than the detrend interval. Because of the large variations in \bar{N}_e , however, the fractional variation shown in Figure 18 can be very misleading.

As a final comparison of the upleg probe and beacon data, we have used Eq. (14) and

$$(2\pi)^{p_1+1} T'_1 = \frac{C_s \Gamma(v - 0.5)}{2\pi \Gamma(v + 0.5)} \quad (17)$$

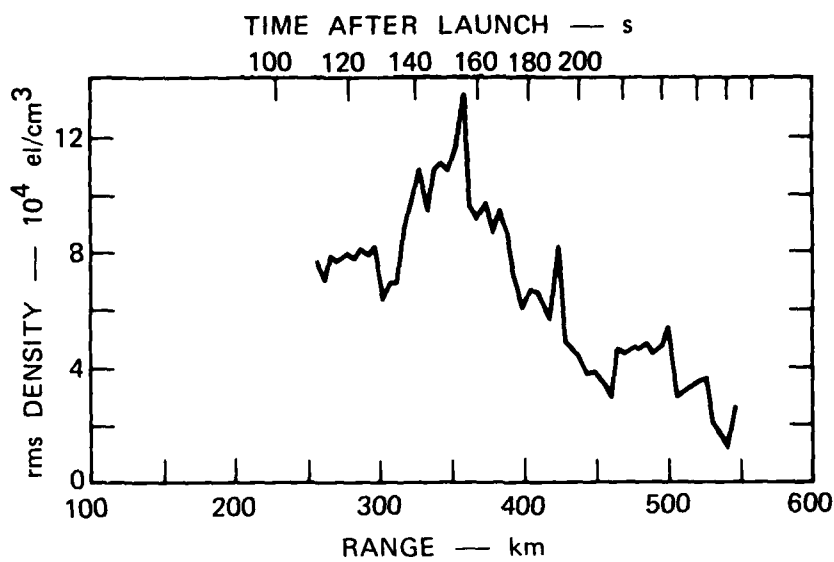


FIGURE 17 rms ELECTRON DENSITY FROM LANGMUIR PROBE DATA

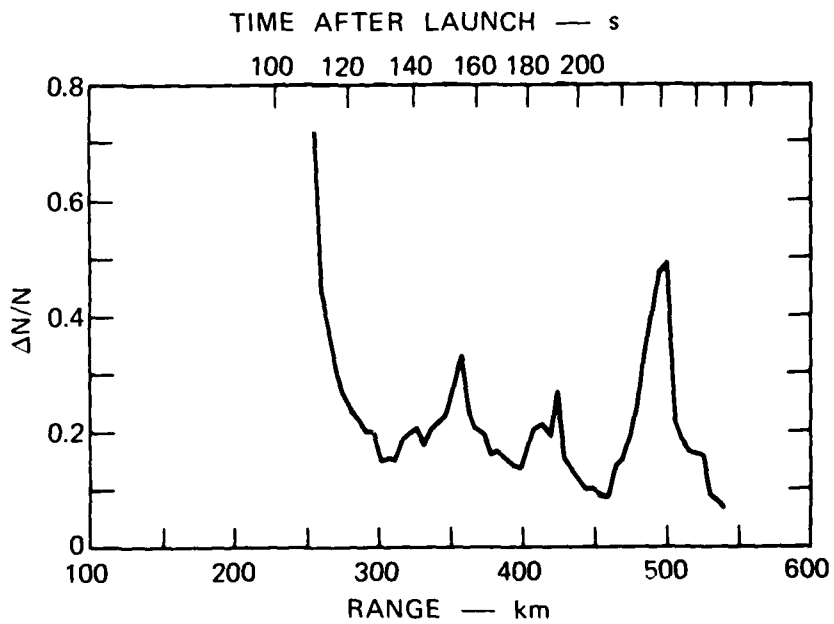


FIGURE 18 FRACTIONAL rms ELECTRON DENSITY FROM LANGMUIR PROBE DATA

from Eq. (5) to compute the three-dimensional isotropic turbulent strength C_s from the beacon and Langmuir probe data. The $(2\pi)^{p_1+1}$ factor allows for the fact that C_s is computed in terms of the usual spatial wavelength units which include the 2π factor.

The results are shown in Figure 19. The beacon and probe C_s values track feature for feature through 350 km. The beacon C_s values are, however, approximately a factor of four higher, which possibly indicates the Langmuir probe calibration is a factor of 2 too low. Recent results from the pulsed plasma probe have verified this result. In any case, the interpretation of the structure derived from the beacon and probe data agree completely from the lower F region through the F-region peak. Beyond that, the probe is clearly sampling very different structures (both in intensity and spectral distribution) than are dominating the beacon data.

E. Downleg Data

On the downleg portion of the rocket flight, the interpretation of the beacon data is complicated by the fact that the rocket velocity vector develops a component perpendicular to the line of sight. This is illustrated in Figure 20 in which the ratio of the rocket velocity vector components perpendicular to parallel are plotted. Only near apogee does the perpendicular component actually dominate.

The downleg density profile is shown in Figure 21. Both the raw data and the 10-km detrend are shown. The rocket evidently penetrated the large depletion on the downleg near 450 km. Here, however, the plot is against height rather than range. (On the upleg the differences between height and range are small.) The downleg data were actually interpolated against height rather than range.

Figure 22 shows the downleg S_4 data. Figure 23 shows the corresponding σ_ϕ data. As with the upleg data, there are large variations in scintillation structure. Similarly, the downleg p_z data that Figure 24 shows admit large systematic variations. The tendency to smaller p_z values

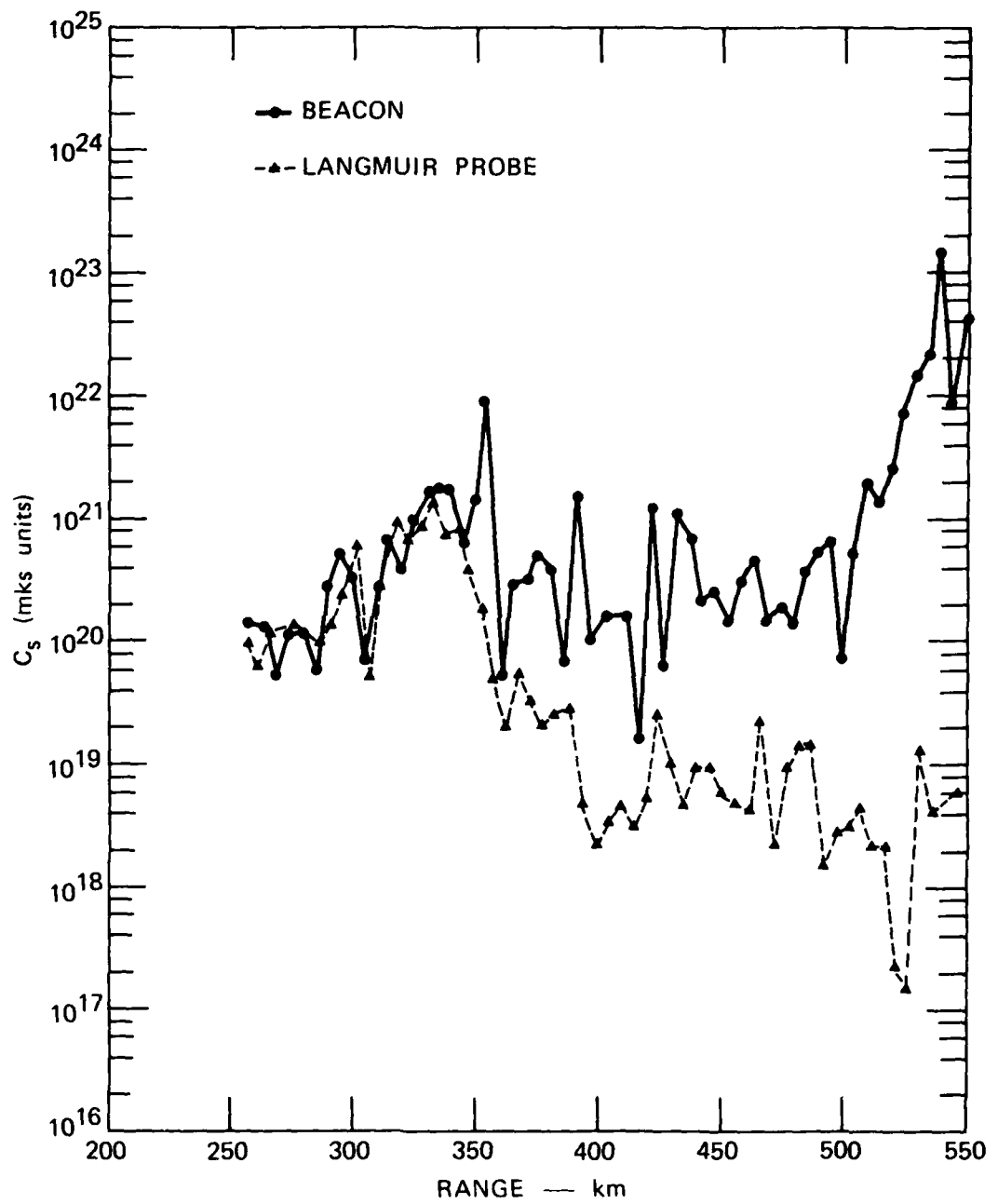


FIGURE 19 COMPARISON OF TURBULENT STRENGTH AS MEASURED BY IN-SITU PROBE AND BEACON PHASE DATA

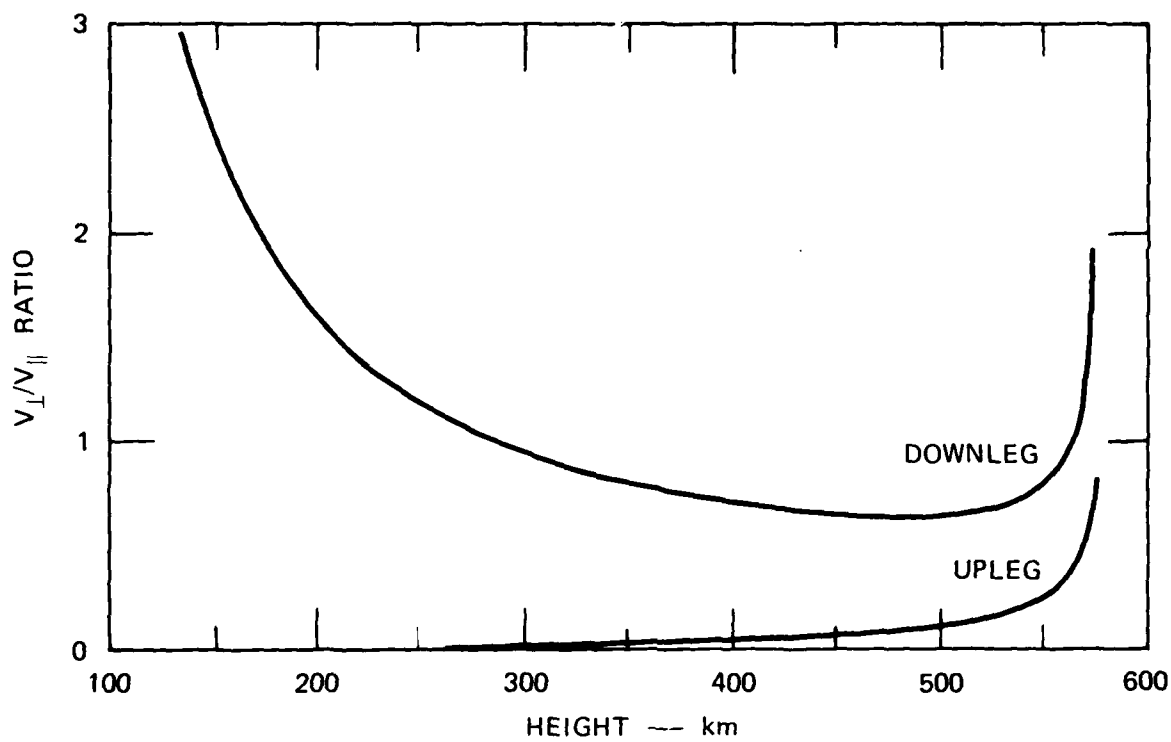


FIGURE 20 RATIO OF ROCKET VELOCITY COMPONENTS ALONG AND TRANSVERSE TO THE LINE OF SIGHT

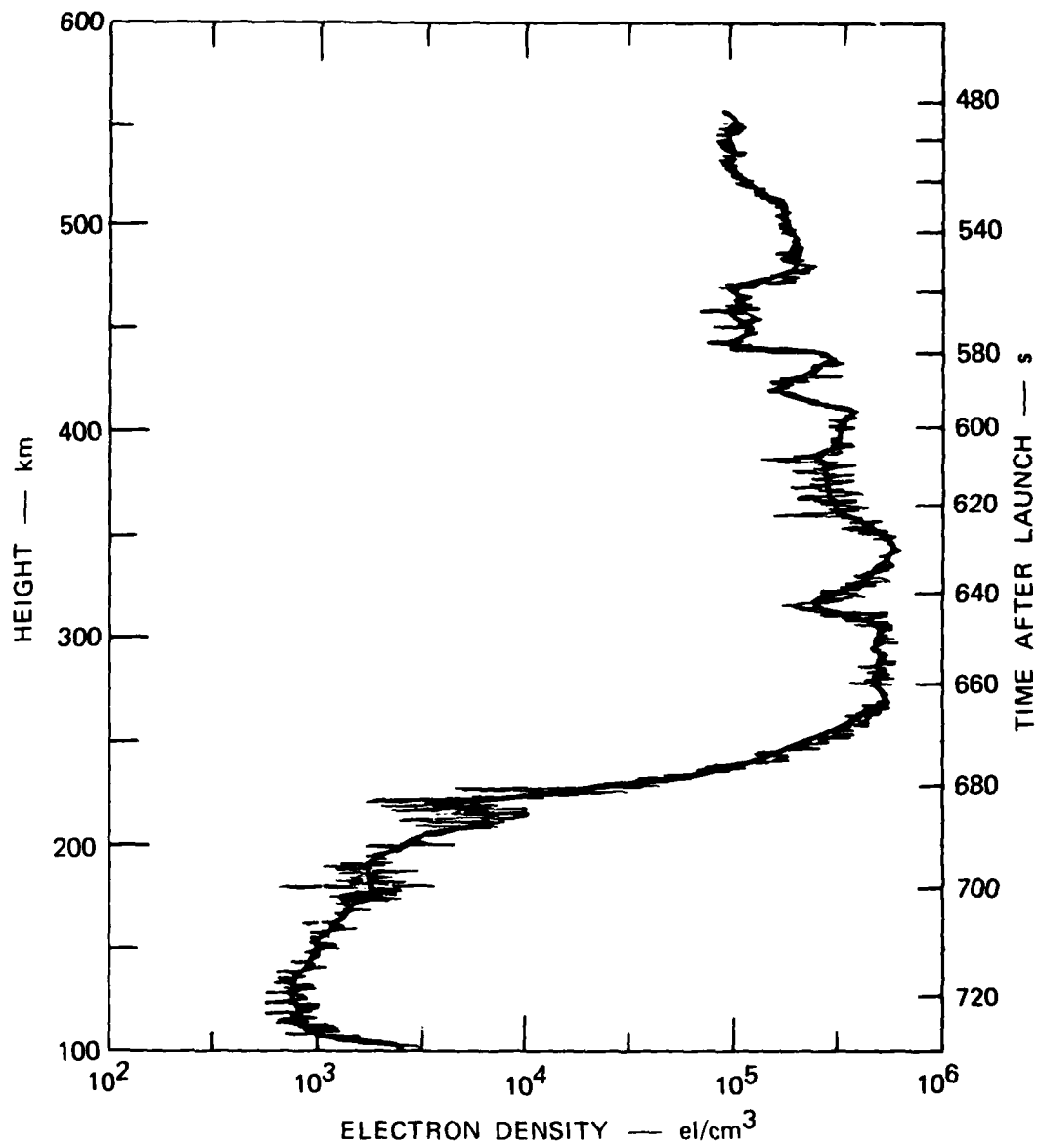


FIGURE 21 DOWNLEG ELECTRON-DENSITY PROFILE FROM LANGMUIR PROBE

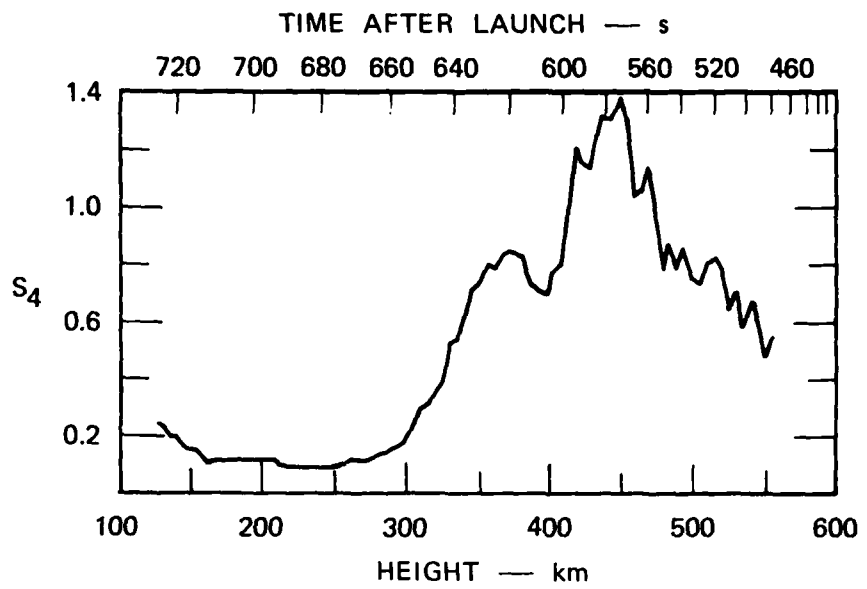


FIGURE 22 INTENSITY SCINTILLATION INDEX AT 291 MHz
FOR DOWNLEG

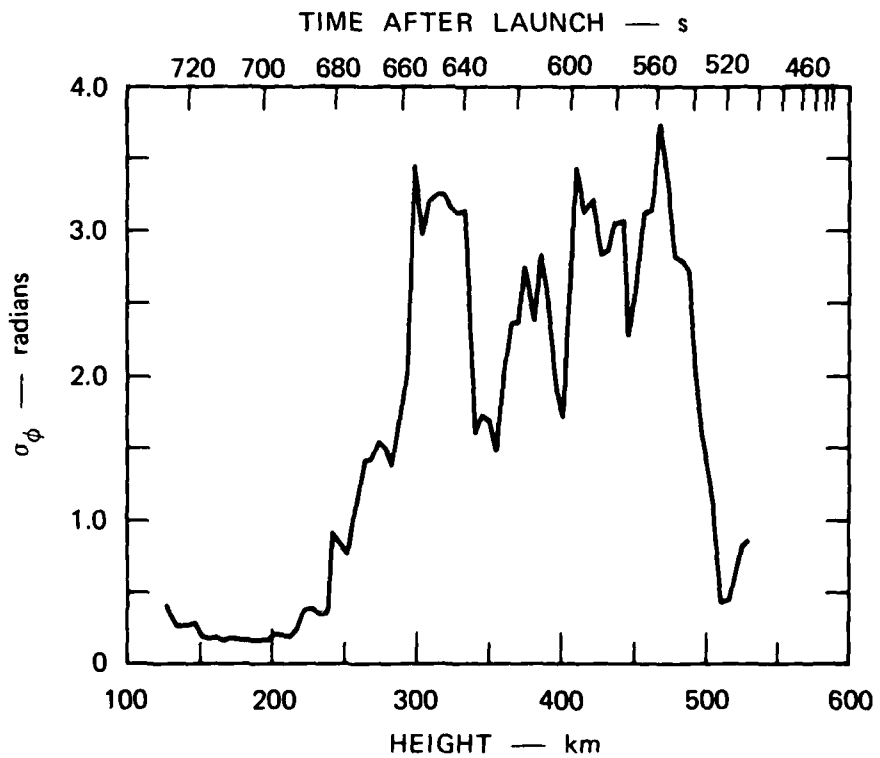


FIGURE 23 rms PHASE AT 437 MHz FOR DOWNLEG

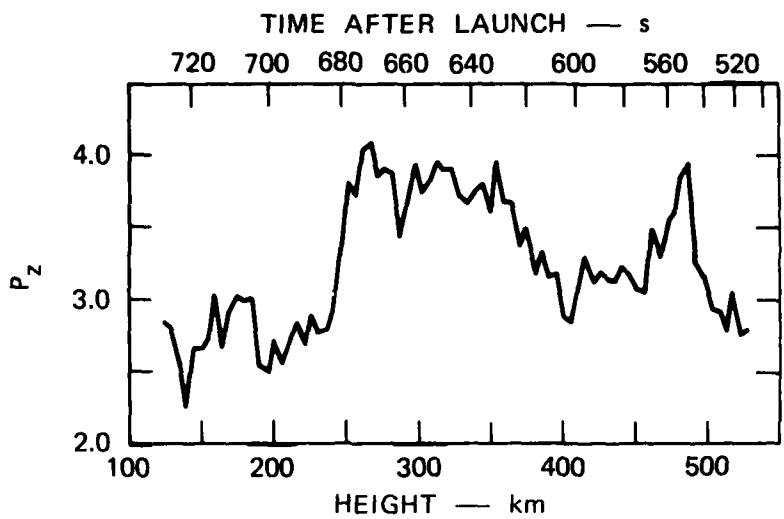


FIGURE 24 PHASE SPECTRAL INDEX FOR DOWNLEG

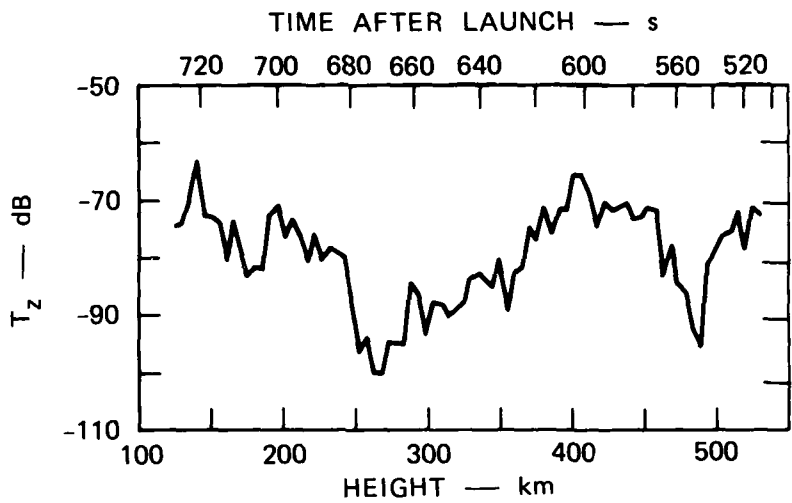


FIGURE 25 TURBULENT STRENGTH T_z FOR DOWNLEG

where the most intense scintillation is occurring can be seen from Figure 25 in which T_z for the downleg is plotted.

Figures 26 and 27 show the downleg p_1 and T_1' values from the Langmuir probe data, respectively. The general variation of T_1' is very similar to the corresponding data for the upleg (Figure 16). The p_1 values are consistently less than 2 below 400 km as was the case for the upleg. Moreover, the lowest p_1 values occur between 250 and 350 km at which the T_1' values are the largest.

The consistent result in all the data is that p_1 (and p_z) vary systematically depending on the perturbation strength. Correlations of p_z with p_1 and T_z' and T_1' are not particularly meaningful on the downleg because of the differences between the rocket trajectory and the propagation path. The general pattern is, however, quite similar to that of the upleg.

V SUMMARY AND CONCLUSIONS

In this report we have presented the results of the spectral analysis of large-scale equatorial spread-F structures from in-situ AE-E satellite measurements, from Wideband satellite phase scintillation data, and from rocket-beacon and Langmuir data obtained during the DNA 1979 Kwajalein Campaign. The large-scale regime to which we refer here encompasses spatial wavelength from greater than 50 km to less than 500 m. This structure regime causes essentially all scintillation effects from VHF to L band.

The results that have emerged from these analyses were quite unexpected. Indeed, they show that the structures that are responsible for the most intense equatorial scintillation are not associated with the prominent equatorial backscatter plumes. Moreover, the spectral structure verifies that steep gradients are not the dominant mechanism that produces these very intense structures.

The most consistent feature in all the data is that the power-law spectral index that characterizes these structures systematically decreases

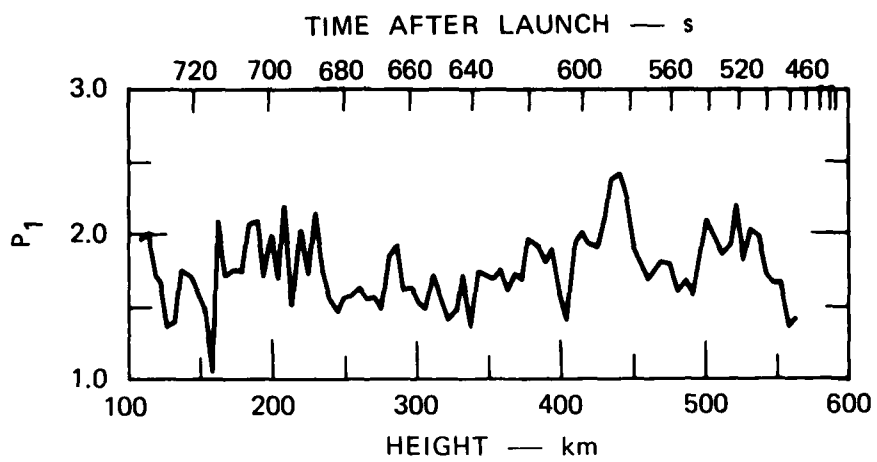


FIGURE 26 IN-SITU SPECTRAL INDEX FOR DOWNLEG

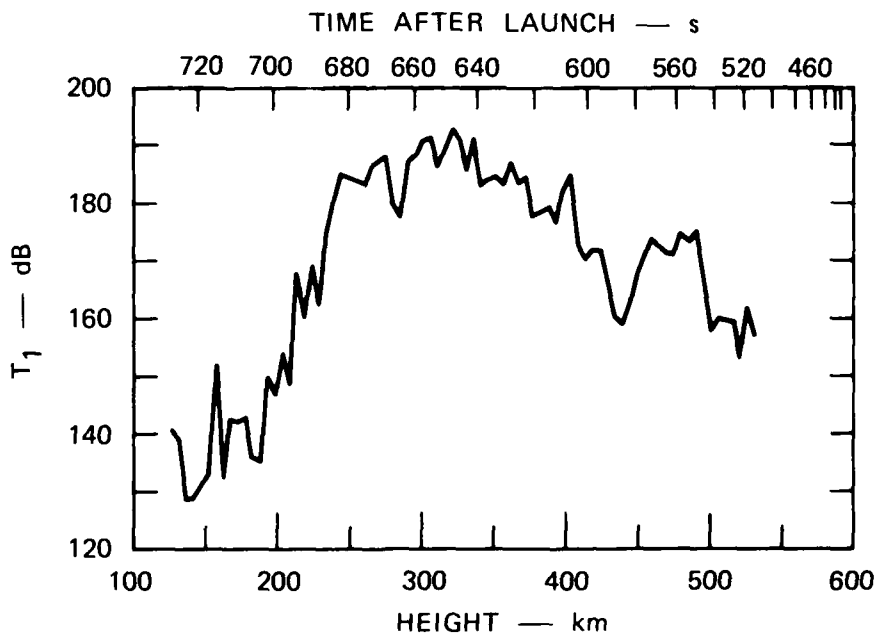


FIGURE 27 IN-SITU TURBULENT STRENGTH FOR DOWNLEG

as the turbulent strength increases. In all cases the one-dimensional in-situ power-law index is less than the steep-gradient-driven value 2. This effect has been apparent in the Wideband satellite phase scintillation data for some time, but it was attributed to diffraction effects. By using the empirically derived relation

$$p = 2.15 - 0.025 T(\text{dB}) , \quad (17)$$

a substantially improved fit to theoretical predictions of the intensity coherence time was obtained.¹⁶ Moreover, the effect of a varying spectral index is clearly present in the Wideband frequency coherence measurements.¹⁷

The variable spectral index is confirmed in both the rocket beacon data and the Langmuir probe data. In the lower portion of the rocket upleg in which direct comparisons are most meaningful, the beacon data and the Langmuir probe data give virtually identical results. The beacon data show, moreover, the very dynamic behavior of propagation environment, which may be a clue to the causal mechanism of the irregularities. In any case, the most intense scintillation producing irregularities occur through the F-region peak (upleg and downleg) in high-density regions adjacent to the backscatter plumes.

To make quantitative intercomparisons of the different data sets, we have used the isotropic turbulent strength C_s . In mks units, C_s values exceeding 10^{20} are required to produce gigahertz scintillation with reasonable layer heights and thicknesses. Values in this range were measured in all the data sets. Thus, there is no difficulty in explaining the scintillation levels using the conventional theory.

Considerable work remains to be done in establishing the interrelationships among the depletions, scintillation structures, and 1-m irregularities. The spectral characterization of the large-scale structures, however, is now well established.

REFERENCES

1. R. C. Livingston, "Comparison of Multifrequency Equatorial Scintillation: American and Pacific Sectors," Radio Sci. (in press, 1980).
2. J. Aarons, J. Buchau, S. Basu, and J. P. Mullen, "The Localized Origin of Equatorial F Region Irregularity Patches," J. Geophys. Res., Vol. 83, No. A4, pp. 1659-1664 (April 1978).
3. S. Basu and M. C. Kelley, "A Review of Recent Observations of Equatorial Scintillations and Their Relationship to Current Theories of F-Region Irregularity Generation," Radio Sci., Vol. 14, No. 3, pp. 471-486 (May-June 1979).
4. H. G. Booker and D. C. Miller, "Weak Scattering Theory Applied to Equatorial Ionospheric Scintillation for a Wide Range of Parametric Values," J. Atmos. Terr. Phys., Vol. 42, No. 3, pp. 189-204 (March 1980).
5. C. H. Liu and K. C. Yeh, "Model Computations of Power Spectra for Ionospheric Scintillations at GHz Frequencies," J. Atmos. Terr. Phys., Vol. 39, No. 2, pp. 149-156 (February 1977).
6. C. M. Crain, H. G. Booker, and J. A. Ferguson, "Use of Refractive Scattering to Explain SHF Scintillations," Radio Sci., Vol. 14, No. 1, pp. 125-134 (January-February 1979).
7. A. W. Wernik, "Extinction Effects in the Single Scattering Scintillation Theory," Pub. Inst. Geoph. Pol. Acad. Sci., Vol. E-1, p. 43. 1976.
8. J. B. Workman, "The Relevance of Barium Releases to Problems of the Nuclear Environment," DNA 4514T, Topical Report for Period 1 November 1975 to 31 December 1977, Berkeley Research Associates, Inc., Berkeley, CA (December 1977).
9. R. C. Livingston, C. L. Rino, J. P. McClure, and W. B. Hanson, "Spectral Characteristics of Medium-Scale Equatorial F-Region Irregularities," J. Geophys. Res., submitted for publication, 1980.
10. P. L. Dyson, J. P. McClure, and W. B. Hanson, "In Situ Measurements of the Spectral Characteristics of F Region Ionospheric Irregularities," J. Geophys. Res., Vol. 79, No. 10, pp. 1497-1502 (April 1974).
11. C. L. Rino and E. J. Fremouw, "The Angle Dependence of Singly Scattered Wavefields," J. Atmos. Terr. Phys., Vol. 39, No. 8, pp. 859-868 (August 1977).

12. C. L. Rino, "A Power-Law Phase Screen Model for Ionospheric Scintillation 1. Weak Scatter," Radio Sci., Vol. 14, No. 6, pp. 1135-1146 (November-December 1979).
13. J. Petriceks, "Rocket RF Beacon Experiment for the Summer 1979 Kwajalein Campaign," Proceed. of the Summer Equatorial Experiment Data Review Meeting, 18 March 1980 (1980).
14. R. T. Tsunoda, "ALTAIR Radar Measurements in Support of the PLUMEX Rocket Campaign," Proceed. of the Summer Equatorial Experiment Data Review Meeting, 18 March 1980 (1980).
15. E. P. Szuszczewicz, R. T. Tsunoda, R. Narcisi, and J. C. Holmes, "PLUMEX I: Coincident Radar and Rocket Observations of Equatorial Spread F, Proceed. of the Summer 1979 Kwajalein Experiment Data Review Meeting, 18 March 1980 (1980).
16. C. L. Rino and J Owen, "On the Temporal Coherence Loss of Strongly Scintillating Signals," Radio Sci., submitted for publication (1980).
17. C. L. Rino, V. H. Gonzales, and A. R. Hessing, "Coherence Bandwidth Loss in Transitionospheric Radio Propagation," Radio Sci., submitted for publication (1980)..

PLASMA-DENSITY AND ELECTRIC-FIELD MEASUREMENTS MADE DURING THE PLUMEX I ROCKET FLIGHT

K. Baker, J. C. Ulwick and L. Jensen

Space Measurements Laboratory
Utah State University
Logan, UT 84322

M. C. Kelley and R. Pfaff

School of Electrical Engineering
Cornell University
Ithaca, NY 14853

J. Petriceks

Radio Physics Laboratory
SRI International
Menlo Park, CA 94025

ABSTRACT

For the PLUMEX I rockets, Utah State University supplied a relative plasma density measurement instrument, a Langmuir probe operated in the electron saturation regime, and a vector electric-field probe. Both instruments worked exceptionally well and obtained an excellent data set with which to study and characterize equatorial spread F. The usefulness of the data set is particularly enhanced by the simultaneous measurements made by the SRI beacon experiment, the ALTAIR and TRADEX radars and, of course, the onboard instrumentation. A short initial report emphasizing the unique features of the rocket/radar experiment and presenting results from some of the onboard instrumentation has already been published. It will take several years to analyze fully and report the data obtained to the scientific community. The purpose of this report is to present the most important and relevant of the experimental data to the Defense Nuclear Agency in a timely and usable manner.

We have concentrated on characterizing the structure in the medium over the widest range of spatial scales possible. To achieve this goal the full capability of the plasma-density and electric-field design was necessary, because of the

enormous range of spatial scale (>5 orders of magnitude) and signal intensity ($\gtrsim 11$ orders of magnitude) that the spread-F phenomenon exhibited and that the instruments supplied by USU detected. Four different telemetry channels were used to achieve this range, each with different sensitivities, and each with different wavelength response.

A second goal was to compare the observed in-situ electron density structure with the SRI International beacon experiment, which measured directly the phase scintillation created by the variations in medium along the rocket path. The excellent comparison not only has supported the results of both instruments, but has built confidence in the theory as applied to the propagation of signals through disturbed media.

A third goal was to learn as much as possible about the plasma instabilities and nonlinear processes operating in equatorial spread F. An important tool in determining wave modes is simultaneous measurement of the wave-number spectrum of the electric-field and plasma-density fluctuations.

The most important results to date are summarized as follows:

- (1) The wave-number spectrum of topside equatorial-spread-F density irregularities has been determined simultaneously from tens of kilometers to 0.6 m. These data can be used directly by the communications channel modeler and may yield new and important results for the construction of nuclear codes.
- (2) The accepted k^{-2} power law spectrum at the kilometer scale was found not to characterize the most highly turbulent and most intensity disturbed regions near and above the F peak. This report is confirmed by the beacon experiment and is in agreement with studies using Wideband and AE satellite data. The k^{-2} spectrum slope is systematically shallower than k^{-2} in the most intensity disturbed regions. Kelley and Ott (1978) predicted such a decrease in slope when velocity turbulence acts on zero-order density gradients in spread F. Further analysis of the electric-field data from PLUMEX I, measuring as it does the velocity field, may prove or disprove the importance of velocity turbulence in the natural case and perhaps by analogy in the nuclear case.
- (3) The simultaneous electric-field and plasma-density measurements have verified experimentally that a plasma instability, other than the pure Rayleigh-Taylor process, operates at the shorter scales. This has long been conjectured and various modes have

been suggested as part of a "hierarchy of instabilities." The PLUMEX I data show that a type of drift mode is the most likely; furthermore, data show that the spectral form steepens at wavelengths below 100 m to near k^{-5} , then becomes less steep again below a few meters. These results agree with radar results at 3 m, 1.45 m, and 0.36 m. The electric-field data were essential in determining this spectrum.

I INTRODUCTION

In this report we present results from the plasma-density fluctuation and electric-field experiments provided by Utah State University (USU) on the PLUMEX I payload. Both experiments worked exceptionally well on Flight I and we concentrate here entirely upon that data. The separation failure on Flight II precluded lower-boom deployment and the subsequent attitude deterioration adversely effected the upper-boom electric-field data.

There were two aspects of the system. A dc-probe experiment yielded a relative electron-density-profile measurement that spans the wavelength regime from 10 cm to several hundred kilometers. This was done with a fixed-bias Langmuir Probe to collect saturation electron current. Either the ALTAIR radar or the pulsed plasma probe yields absolute density data with which we can normalize the profile obtained from the dc probe. We have used the ALTAIR data provided by SRI International to normalize the data in this report. Because the electric-field can be used to identify spurious effects owing to changes in vehicle potential, this total system provides an inexpensive and effective irregularity detector. In addition the high-frequency, $\delta n/n$ measurement is optimized to produce a good power spectrum at short wavelengths using instruments and techniques for wave experiments in space plasma.

The second thrust of this USU experiment involved measurements of the vector electric field from dc to 10,000 Hz. This corresponds to scale sizes from many hundred kilometers down to fractions of a meter. The electric fields are an essential feature of equatorial spread F because without the velocity field created by the $\vec{E} \times \vec{B}$ drifts, density

gradients would not be mixed, and no irregularities would occur. These fields are necessary to drive the bubbles out of their low-altitude region high into the topside. Furthermore, the short-wavelength backscatter is almost certainly caused by an electrostatic instability in which electric fields also are of essential importance.

Our analysis thus far has taken three main thrusts:

- (1) The long-wavelength dc-probe data was severely affected by the attitude control pulses, as were many other instruments. The times when this occurred were identified and removed from the data set. A new data tape was then identified and removed from the data set. A new data tape was then constructed and used to study the density profiles, irregularity spectra, and steep density gradients. This study was performed in conjunction with SRI and their beacon experiment which yields a similar, although not identical, data set in the presence of irregularities. We joined our analysis so that differences in detrending technique by the two groups would not affect the interpretation. Some overlap occurs between the two reports submitted at this time.
- (2) The high-frequency electric-field, δE , and plasma-density, $\delta n/n$, fluctuation data are in analog form and each has an automatic gain control system that acts to maximize the signal-to-noise ratio in discrete steps. Sonograms (frequency-time spectrograms), which allow a quick, qualitative survey of the important wave emission events, were first produced at Stanford University. The data were then digitized and FFT routines used to study the wave phenomena.
- (3) The dc electric-field data correspond to a vector sum of the ambient electric field and the $v \times \vec{B}$ field of the moving vehicle. An attitude solution using the gyro data has been produced and the $v \times \vec{B}$ field subtracted. There has not yet been enough time to optimize the analysis programs and to remove all the adverse effects of the attitude control pulses; hence, the results are still somewhat preliminary. We anticipate that these data will give new insights into the electrical structure of discrete bubbles and of velocity turbulence near the F peak.

II DATA PRESENTATION

A. Density Profiles

The current measured by the fixed-bias Langmuir probe is plotted in Figures 1 and 2 as a function of altitude. These plots yield locally

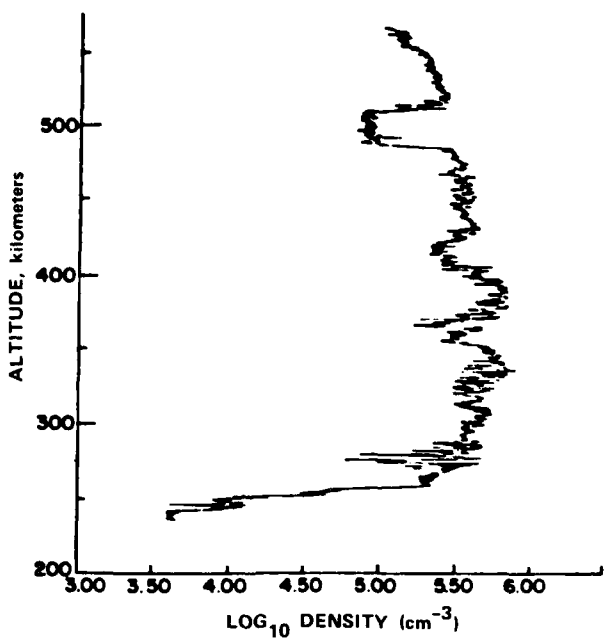


FIGURE 1 UPLEG PLASMA DENSITY PROFILE FROM PLUMEX I NORMALIZED TO THE ALTAIR INCOHERENT SCATTER DATA

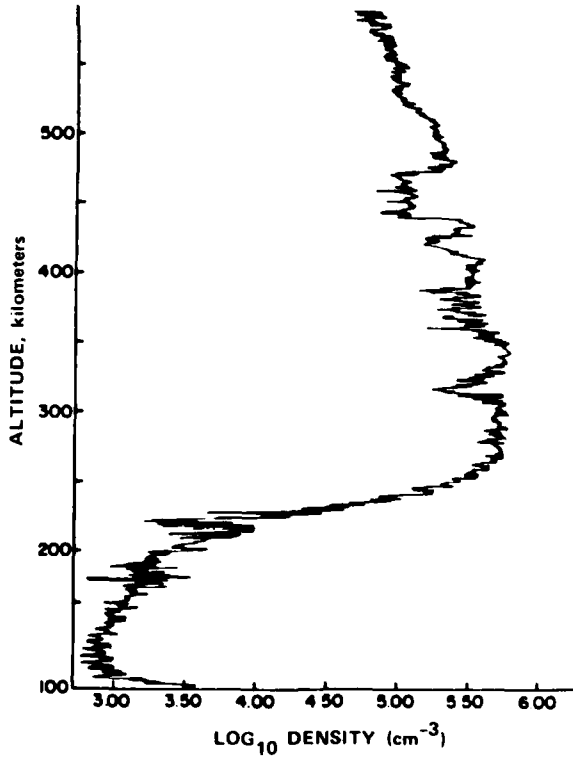


FIGURE 2 DOWNLEG PLASMA DENSITY PROFILE FROM PLUMEX I NORMALIZED TO THE ALTAIR INCOHERENT SCATTER DATA

valid, relative plasma-density profiles and, when normalized at several points, reasonably accurate absolute density values. These plots were normalized to the value measured nearly simultaneously by the incoherent scatter radar at two altitudes separated by over 100 km. The normalization factor was the same for both altitudes, which lends further validity to the plotted profile. The postsunset electron temperature rapidly converges to the neutral temperature, which in turn admits only a small dependence on altitude in the F region. Thus the weak dependence of the electron current on temperature should not change the results significantly at high altitudes where we concentrate our study.

Several features of the profile are immediately apparent. The very dense portion of the profile near and above the F peak is extremely turbulent and displays variations in the plasma density from 25 to 90 percent every few kilometers. Above the F peak, three large-scale highly structured regions of low plasma density were penetrated. The highest of these, near 500 km, was collocated with a region of intense small-scale irregularities (0.16 m and 0.36 m) detected by the ALTAIR radar.¹ These data^{1,2} thus verify the conjectures by Kelley et al.³ and Woodman and La Hoz⁴ that holes or bubbles are the seat of range-limited, intense, short-wavelength radar backscatter above the F peak.

The remarkably structured nature of the upleg data is emphasized in the presentation of Figure 3 in which the normalized density is plotted with a linear scale. Here it can be seen that the profile is not uniformly disturbed. Several quieting periods are evident. Also, the shorter-scale irregularities tend to be more intense in regions where the local density gradient is directed upward (this has been noted also by Szuszczewicz et al.²). The bars indicate regions where short wavelength waves were detected in the range 5 to 100 m.

The upleg data were detrended using a 50-km detrend interval and power spectra computed in 40-km intervals during the upleg. One example is presented in Figure 4 and the whole set reproduced in Appendix A. Some of the features of these data are discussed in the companion report by Rino et al.,⁵ particularly with respect to the simultaneous beacon

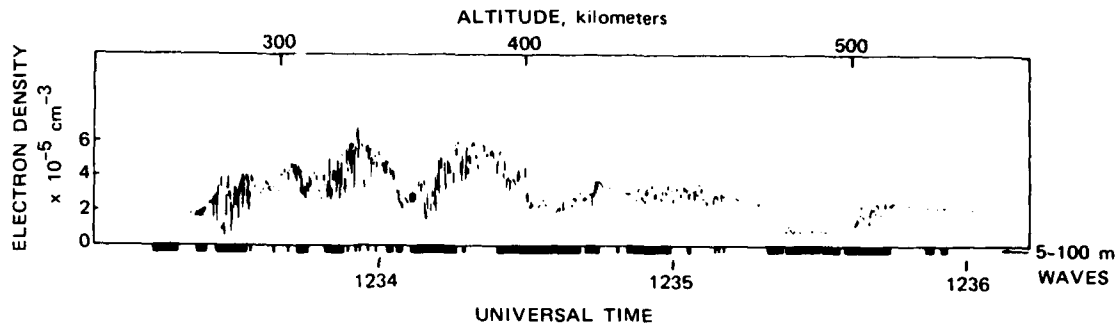


FIGURE 3 PLUMEX I UPLEG PLASMA DENSITY MEASUREMENTS ON A LINEAR SCALE. Regions of intermediate wavelength irregularities are shown with the dark bars.

data. Some features are evident from Figure 4. Unlike previous power spectra in bottomside equatorial spread F^{3,6} and barium cloud structures⁷ a single power law cannot be used to characterize the spectrum above the "deterministic" region. In Figure 4, two distinct power laws are apparent with the break at about 0.5 km. The long-wavelength region had a slope varying as $k^{-1.5}$ while below 3 km the slope was $k^{-3.2}$. A plot of the slope between 0.2 km^{-1} and 2 km^{-1} plotted in Figure 5 with 5-km resolution. Below the 360-km altitude the spectral index was well below the value 2 often reported for ionospheric irregularities. The beacon results are in excellent agreement with the probe results. These data thus cast into doubt the use of k^{-2} spectra in all ionospheric modeling cases.

A plot proportional to the integrated power in the range 0.2 to 2 km^{-1} is presented in Figure 6. Comparison with Figure 5 shows that regions of high turbulence coincide with the shallower spectral slope. This result also agrees with the study of AE data done by Rino et al.⁵

The picture emerging is that highly driven plasma instabilities in the ionosphere need not be dominated by sharp gradients on the dominant structures. Other factors must, therefore, play a role in determining the spectrum and result in a more "turbulent" waveform. Kelley and Ott⁸ suggested that velocity turbulence acting alone on the zero-order

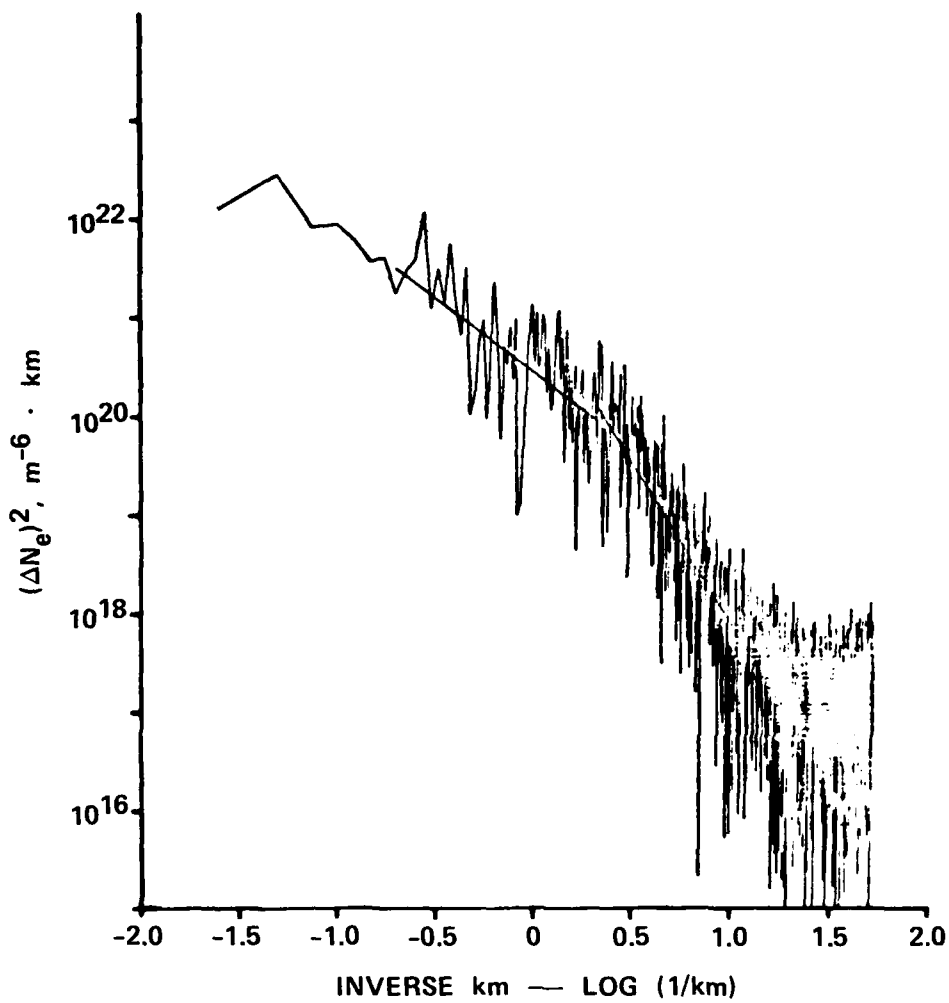


FIGURE 4 PLUMEX I UPLEG--295.5 km. An example of the long-wavelength power spectral analysis for a 40-km interval centered at 295.5 km. Note the distinct break in the spectral form. Many more examples are in Appendix A.

vertical density gradient in equatorial spread F would result in a k^{-1} spectrum. The combination of velocity turbulence and the primary process may in fact cause the observed $k^{-1.5}$ spectrum.

B. Intermediate-Wavelength Regime

At wave numbers above 2 km^{-1} , the spectral slope tends to be steeper than k^{-2} in the most turbulent regions. To study this further a number

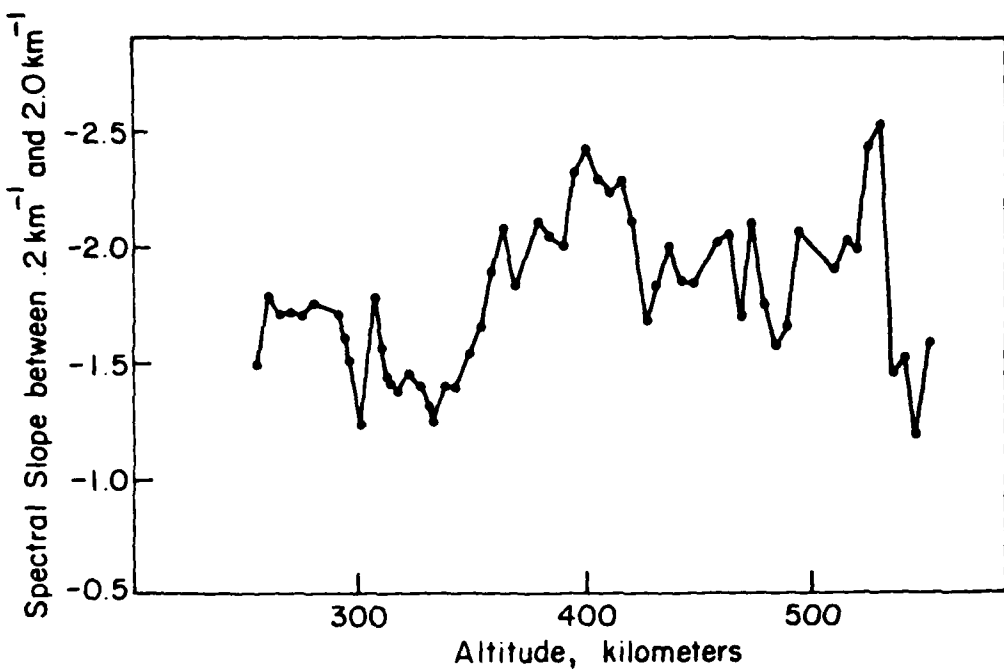


FIGURE 5 PLUMEX I SPECTRAL INDEX--UPLEG. The spectral index in the long-wavelength regime plotted vs altitude. Note the shallow slopes in the most turbulent regions.

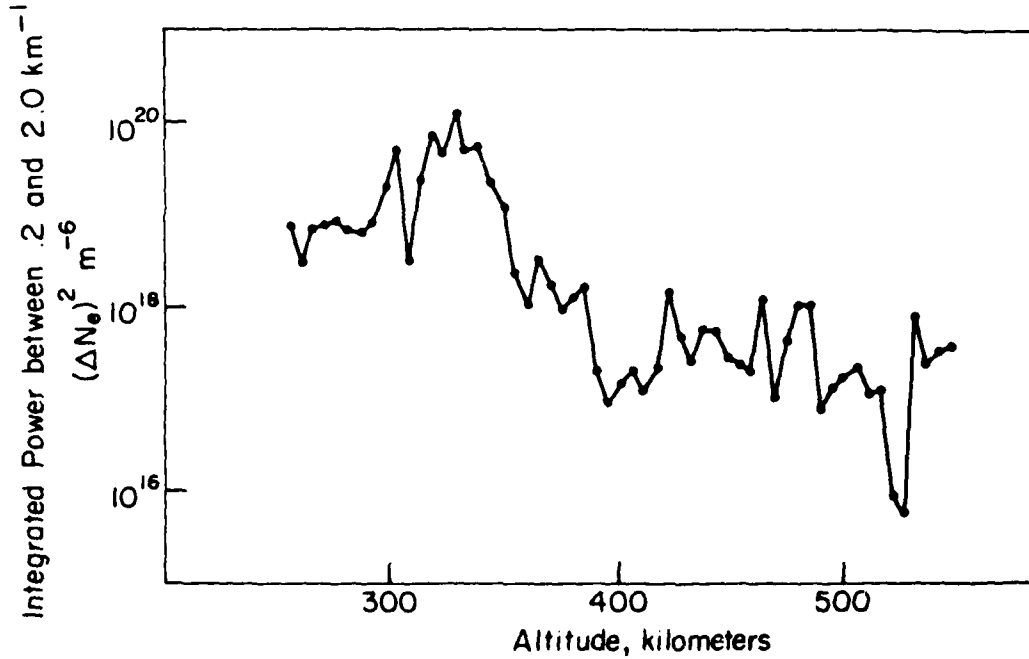


FIGURE 6 INTEGRATED POWER IN THE LONG-WAVELENGTH REGIME PLOTTED vs ALTITUDE FOR PLUMEX I UPLEG. Note the anticorrelation between turbulence level and slope.

of 4-s intervals were studied in the region of the highest topside bubble as was a 40-s interval including the whole region. The full interval spectrum is plotted in Figure 7 and selected spectra in Figures 8 (a through f). Unlike the earlier spectra, the data have been analyzed in the time domain. Because the velocity only changes by 3 percent in a 4-s interval, constant velocity can be assumed (~ 1200 m/s in the interval discussed). There is clearly a tendency for higher intensity to be associated with steeper slopes in the range (4.9 to 49 Hz) fit by the straight line in the plots. This is shown more clearly in Figure 9 in which the straight lines have been replotted and labeled by numbers corresponding to those in Figure 8. This is also shown in Figure 10 in which the slope and signal intensity (log scale) are plotted. Large signal strengths correspond to steep slopes just the opposite of the data in Figures 5 and 6. Notice also that the strongest signals are on the upper edge of the bubble.

The picture emerging is that the most turbulent regions are characterized by shallower spectral slopes, below 2 km^{-1} , and steeper spectral slopes, above 2 km^{-1} , than the edge-dominated k^{-2} spectrum. This result may have important implications for modeling of the nuclear case, which certainly should be very turbulent.

C. Short-Wavelength Waves

Data plotted thus far have come from the dc-coupled electron Langmuir probe. This detector output is sampled every millisecond, but the detectable level corresponds to one telemetry bit and is not sufficiently sensitive to cover the enormous dynamic range of the phenomenon. This problem is not unique to this instrument, but is inherent in any dc-coupled, absolute or relative, density measurement system presently available. The Utah instrumentation includes a channel dedicated to short-wavelength waves. The intense, long-wavelength (low frequency in reference to the rocket) waves are electronically suppressed and the short-wavelength signals are enhanced. Because the waves are electrostatic, the electric-field instrument can detect them and it also has the electronic features necessary to enhance the short-wavelength waves.

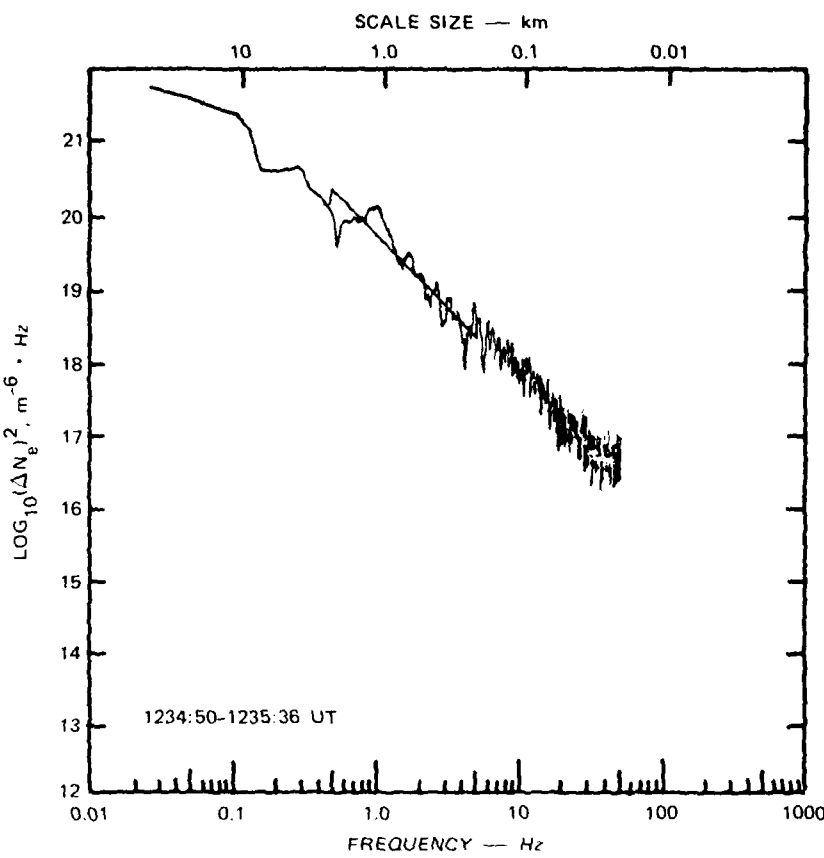


FIGURE 7 POWER SPECTRUM FOR A 40-s INTERVAL INCLUDING THE BUBBLE NEAR 500-km ALTITUDE

The electric-field sensor was more susceptible to interference from the pulsed plasma probe. For reasons not completely understood, this interference was suppressed inside the topside bubble near 500-m altitude. Our most interesting results, therefore, come from this altitude. Before presenting these data let us comment on the short-wavelength waves during the rest of the upleg.

Referring back to Figure 3, the dark bars show regions at which density fluctuations in the frequency range 10 Hz to 200 Hz (~ 100 m to 5 m) were found. Comparison with the density profile above shows that the quietest of regions was bereft of these waves. Typical spectra are plotted in Figures 11(a-c) for several altitude ranges. For reference a

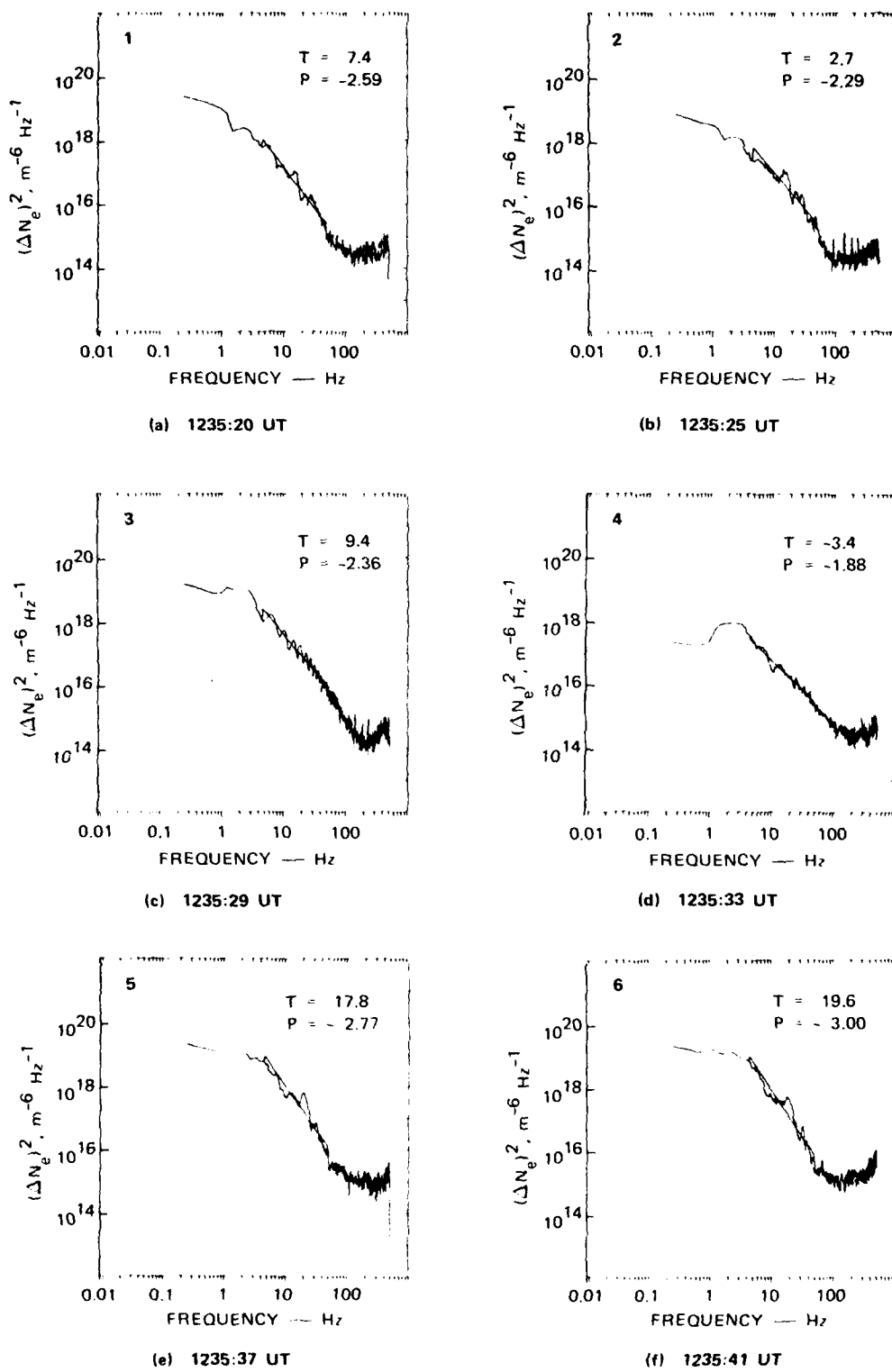


FIGURE 8 POWER SPECTRA FOR 4-s INTERVALS

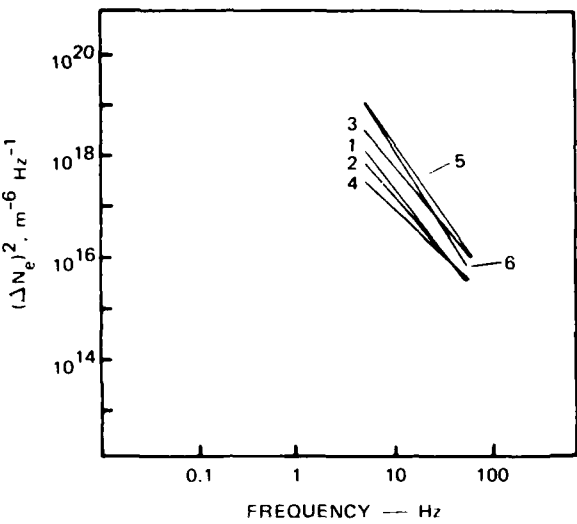


FIGURE 9 STRAIGHT-LINE FITS TO THE SPECTRA IN THE INTERMEDIATE-WAVELENGTH REGIME FOR THE SPECTRA IN FIGURE 8. The numbers correspond to the numbers in that set of figures.

line with slope k^{-5} is plotted in Figure 11(a). The spectral index is quite steep and shows that an extension of the k^{-2} spectrum is not a valid estimator. In fact, once the break in spectral slope occurs from the long-wavelength regime, it is not possible to characterize the spectrum with a single power law. We discuss this point more fully below. Note that the turnover at long wavelengths (low frequency) is due to a high pass filter and the leveling out at short wavelengths (high frequency) is the noise level of the instrument.

Comparison between electric-field spectra and a density spectra are presented in Figure 12(a-c). The electric spectrum is clearly less steep than the density fluctuation spectrum. The following argument explains the difference in the spectral slopes. For some electrostatic waves, such as the drift wave, electrons stream along the magnetic field lines in response to the wave electric fields and obey a Boltzmann distribution in the potential.² This implies that the potential, ξ , and the density perturbation are related by

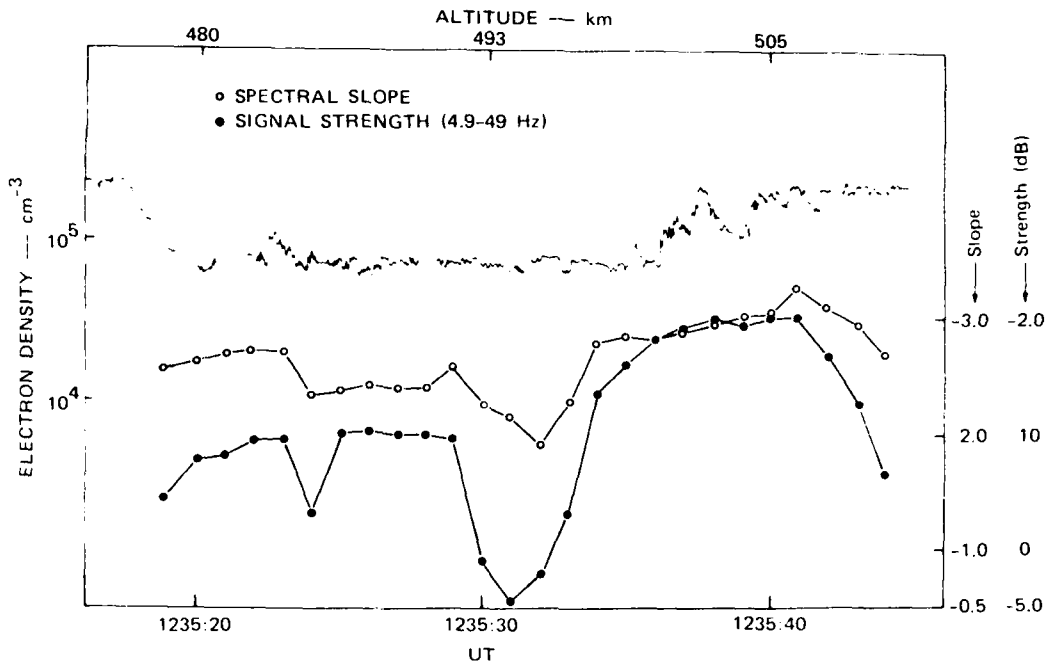


FIGURE 10 PLUMEX I UPLEG PLASMA DENSITY, SPECTRAL SLOPE AND SIGNAL STRENGTH DURING PASSAGE THROUGH THE BUBBLE NEAR 500-km ALTITUDE. (c.f. Figures 8 and 9.)

$$\delta\phi = \frac{KT}{e} \left(\frac{\delta n}{n} \right)$$

where T is the electron temperature, K is Boltzman's constant, and e is the electron charge. Because the electric field is the negative gradient of the potential, we have

$$\delta E = -\bar{V}(\delta\phi)$$

$$\delta E = -i \bar{k} \delta\phi$$

$$\delta \bar{E} = -i \left(\frac{KT}{e} \right) \frac{\delta n}{n} \bar{k}$$

Thus the power spectrum $(\delta E)^2$, should be two powers of k less steep than that of $(\delta n/n)^2$. The PLUMEX I data bear out this prediction.

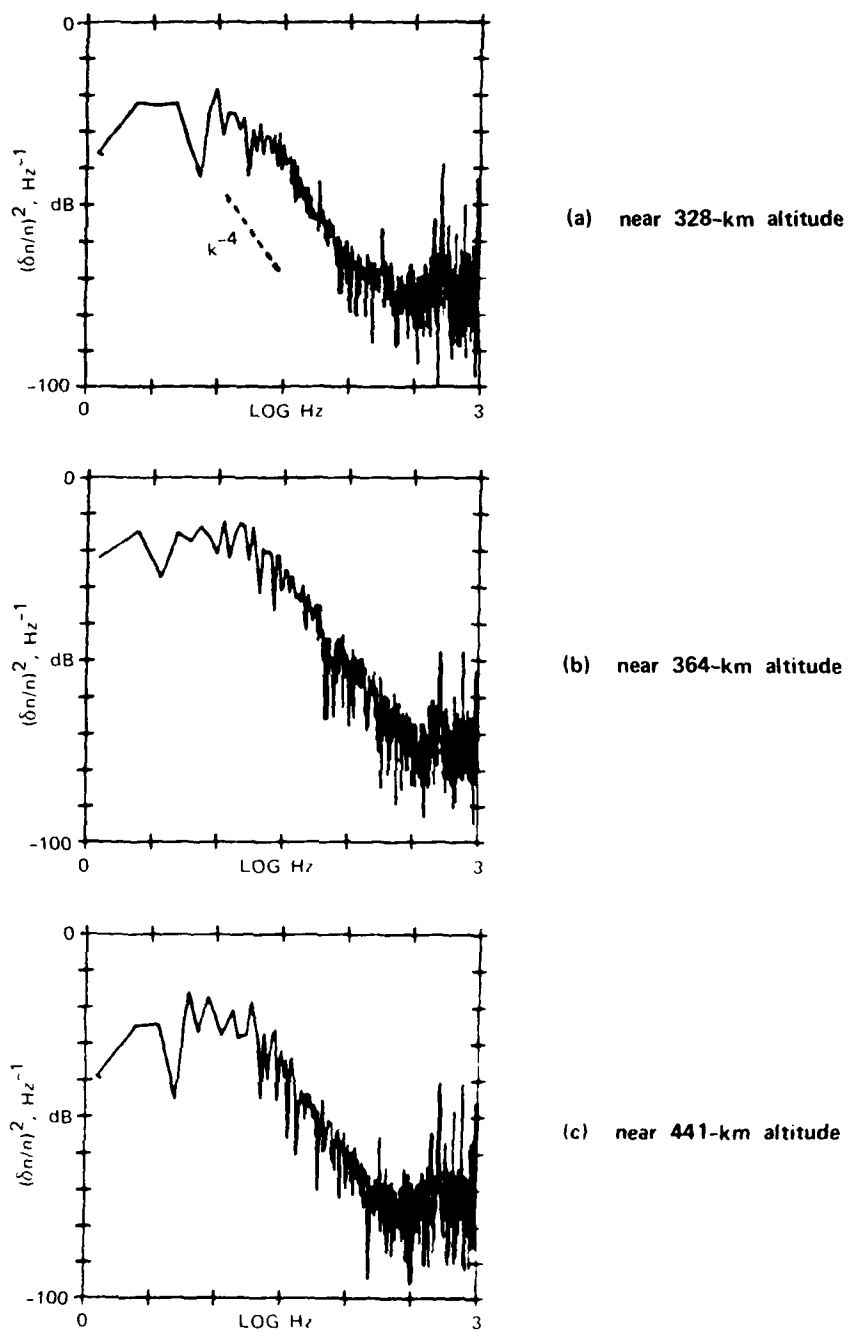


FIGURE 11 UPLEG, SHORT-WAVELENGTH PLASMA-DENSITY FLUCTUATION SPECTRA

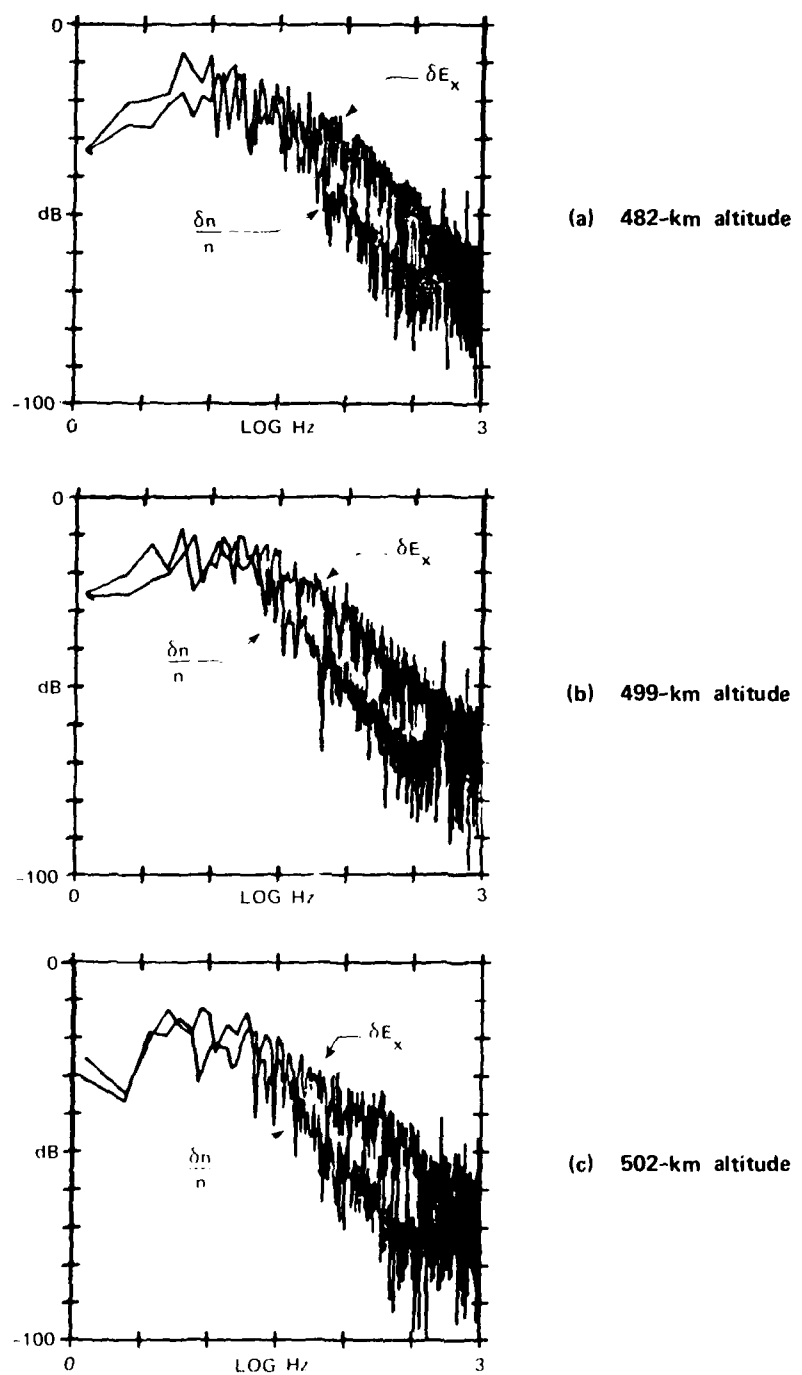


FIGURE 12 SIMULTANEOUS MEASUREMENTS OF ELECTRIC-FIELD AND DENSITY-FLUCTUATION SPECTRA IN THE BUBBLE. Note the difference in spectral slope.

These data in turn strongly argue for the importance of this type of electrostatic wave in equatorial spread F for wavelengths below 100 m. The source of free energy for drift waves are sharp density gradients. (Note that the electric-field and plasma-density fluctuation spectra in the long-wavelength Rayleigh-Taylor should both have the same spectral form.¹⁰) Hudson and Kennel¹¹ first suggested the collisional drift mode and Costa and Kelley¹² made some additional calculations based upon sharp density gradients detected on the bottomside and assumed to exist also on the topside during the intense spread F.

As mentioned above, we have concentrated our analysis thus far on the bubble near the 500-km altitude that was penetrated during both the upleg and downleg of the rocket flight. Backscatter maps made by R. Tsunoda¹ of SRI International show that the bubble was collocated with the most intense backscatter.

Because gradients are important for drift waves of all types we have studied all sharp changes in plasma density exceeding 5 percent and calculated the inverse gradient scale length $L = \frac{1}{2} \frac{dn}{dx}$. These results are plotted in Figures 13 and 14 for both passes through the highest bubble. The length of the bars at the left are equal to L^{-1} . On the upleg, two regions of small L were detected, one on the upper edge of the bubble and one interval. Seven examples with $L < 100$ m were found and 23 more with 100 m $< L < 200$ m. During the downleg only three gradients were detected with $L < 100$ m and seven with 100 m $< L < 200$ m. Tsunoda¹ found that the backscatter had decayed by 9 dB between the time the rocket entered the region on the upleg and its later reentry. These data are, therefore, consistent with a gradient driven process. Furthermore, the instability will act to destroy the sharp gradients eventually resulting in less backscatter and few sharp gradients, as observed in the experiment.

Huba et al.¹³ pointed out that ion-ion collisions will damp the pure drift waves suggested by Costa and Kelley.^{10,11} They suggested drift cyclotron and lower hybrid drift waves and presented detailed calculations in a more recent paper.¹⁴

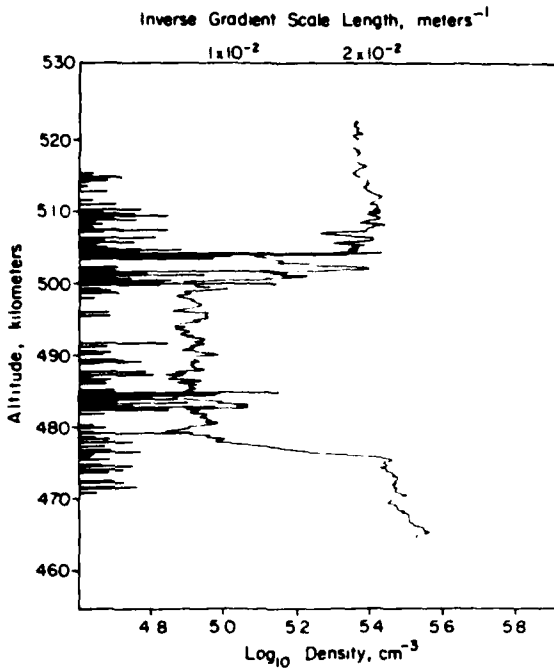


FIGURE 13 UPLEG PLASMA DENSITY PROFILE IN THE HIGHEST ALTITUDE BUBBLE ALONG WITH THE MEASUREMENTS OF THE DENSITY GRADIENTS

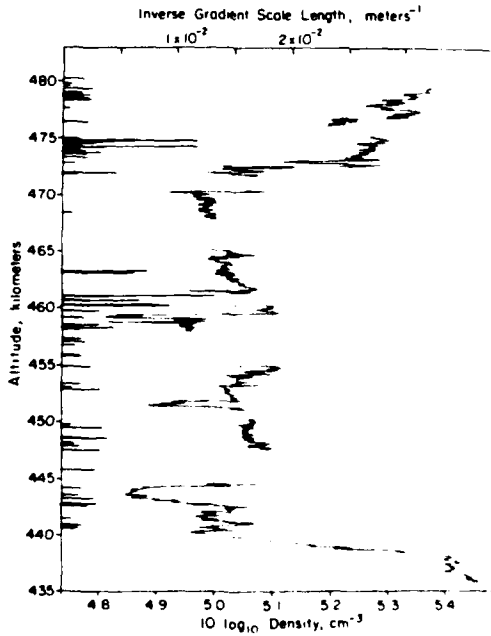


FIGURE 14 DOWNLEG PLASMA DENSITY PROFILE IN THE HIGHEST ALTITUDE BUBBLE ALONG WITH THE MEASUREMENTS OF THE DENSITY GRADIENTS

One mystery of topside spread-F radar measurements is that the extrapolation of 3-m scattering levels to the ALTAIR (0.93 m and 0.36 m) and TRADEX (0.11 m) wavelengths were not internally consistent with prior probe data. On the one hand, the Jicamarca data (3 m) seemed to require a steepening of the spectrum from k^{-2} to some higher index.¹⁵ The shorter wavelength data were not consistent with a continuation of the steep slope, however.¹⁷ The steep slopes at intermediate scales reported here seem consistent with the suggestion by Woodman and Basu.¹⁸

To extend our present study to the shorter scales, we must rely on the electric-field data because the sensitivity of the density instrument was lower because of the steeper spectrum. A $(\delta E)^2$ spectrum obtained at the top edge of the bubble near 500 km is plotted in Figure 15 and a composite of $(\delta E)^2$ and $(\delta n/n)^2$ in Figure 16. The density detector is at the noise level above 200 Hz (6 m), but the electric-field spectrum is valid up to 2000 Hz (0.6 m). Close inspection shows that the electric-field spectrum becomes less steep at wavelengths less than about 2 m. This suggests that a source of free energy exists at very short wavelengths. The arguments above indicate that the lower hybrid drift wave may be the mode operating between the ion and electron gyro radii.

III A COMPOSITE SPREAD-F SPECTRUM

We have taken our best information concerning the spectrum from the density detectors and the electric field sensor and produced the composite spectrum in Figure 17. Figure 17 covers 5 orders of magnitude in spatial scale and eleven orders of magnitude in signal strength. The form agrees amazingly well with the schematic diagram put together by Chesnut⁶ and reproduced in Figure 18. Note that the full spectrum including the shortest scales is only valid in and around the bubble at the highest altitude because only there was the electric-field detector free from interference by the pulsed probe. The steep density spectrum between 6 m and 60 m is common throughout the flight, however. Deviation from a steep spectral form for δn probably occurs in regions of the "electron

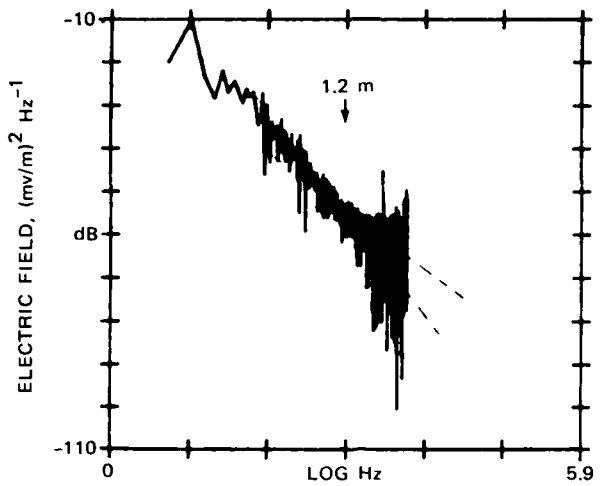


FIGURE 15 ELECTRIC-FIELD POWER SPECTRUM PLOTTED TO 5000 Hz. Note that the noise level is not reached until about 2000 Hz which corresponds to 0.6 m.

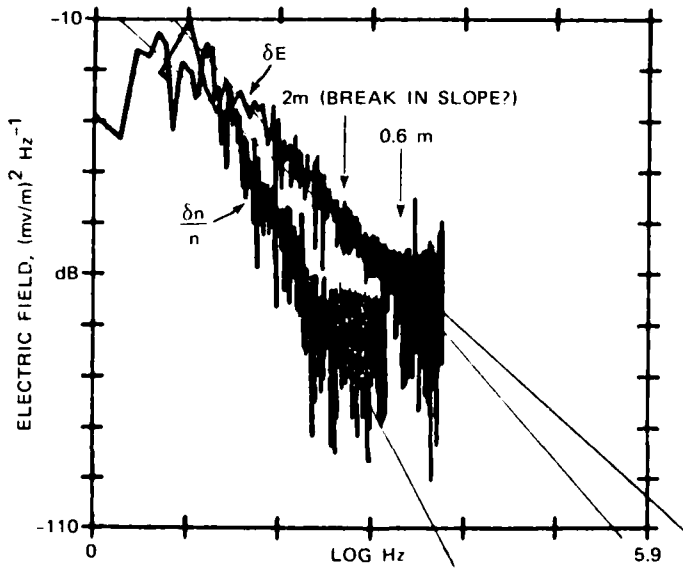


FIGURE 16 COMPARISON OF ELECTRIC-FIELD AND DENSITY SPECTRA FOR THE SAME INTERVAL AS FIGURE 15

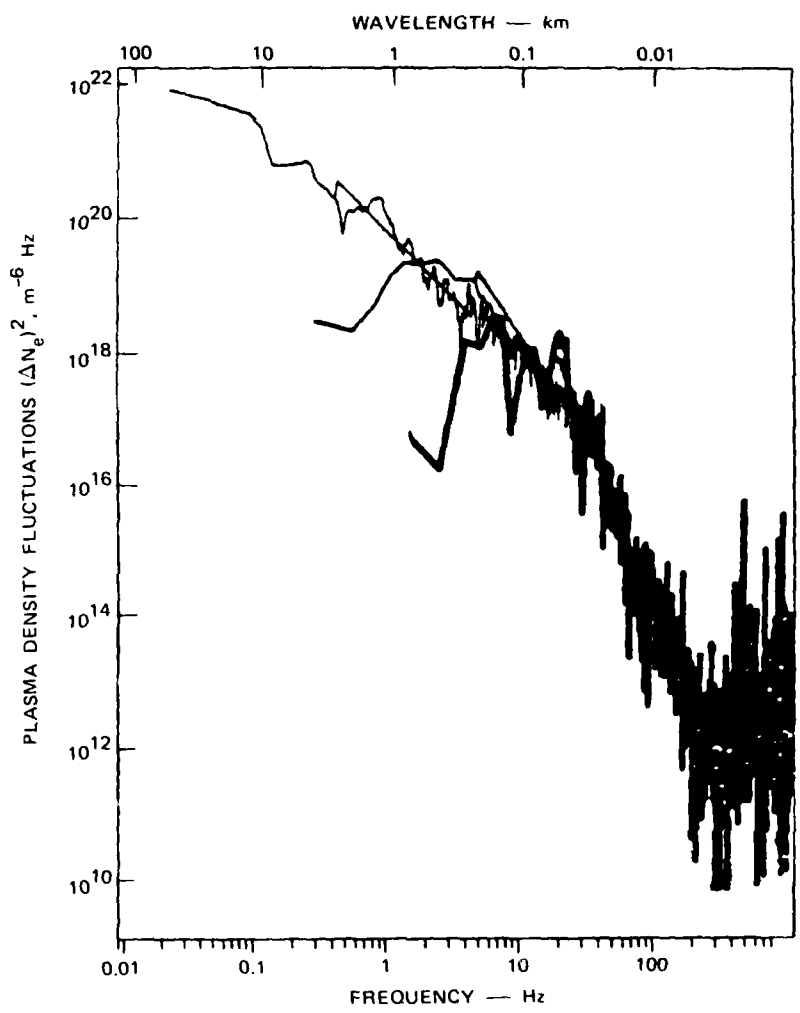


FIGURE 17 COMPOSITE PLASMA DENSITY FLUCTUATION SPECTRA. This can be extended by one order of magnitude using the electric-field data of Figures 15 and 16.

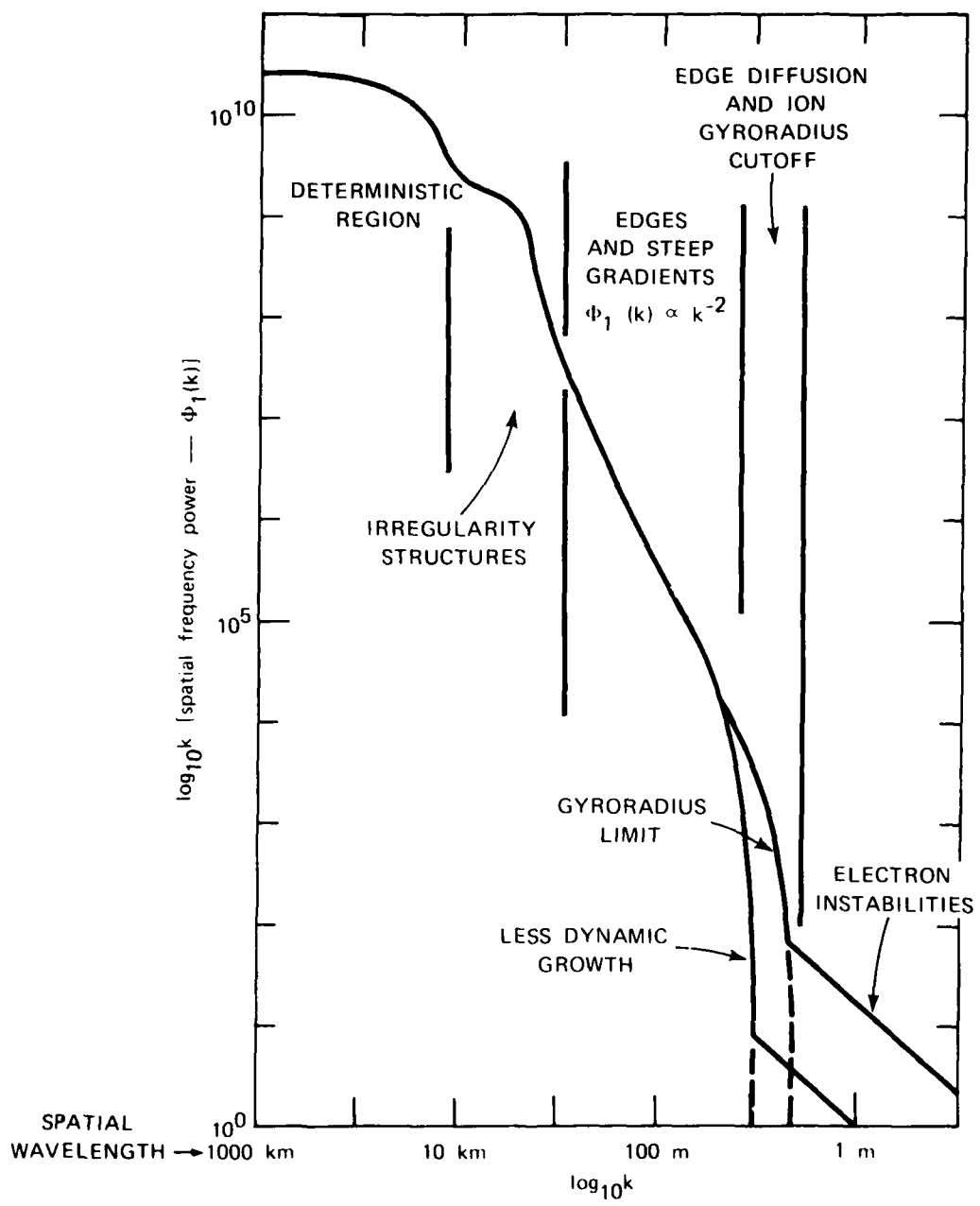


FIGURE 18 HYPOTHEZIZED DENSITY FLUCTUATION SPECTRUM SUGGESTED BY CHESNUT

"instabilities" that are traced by the ALTAIR and TRADEX radars. In the PLUMEX I flight the most intense backscatter of this type occurred in the highest bubble.

One important difference between Figure 18 and the PLUMEX I results is that the k^{-2} spectrum becomes less steep in form (e.g., $k^{-1.5}$) in the most turbulent regions.

ACKNOWLEDGMENTS

We acknowledge the help given by SRI International in the analysis of the long-wavelength data. It seemed advisable to use the same analysis technique on the beacon and probe data because spectral determinations depend so much upon detrending techniques. Also, the experience which SRI International has had in dealing with the DNA-sponsored Wideband analysis was of great value. Such cooperation made possible the considerable progress evidenced by this and other reports submitted at this time.

Appendix A
SPATIAL SPECTRA DURING THE UPLEG

Each of the following spectra correspond to an approximately 40-m altitude range that changes by about 10 km for each of the consecutive plots.

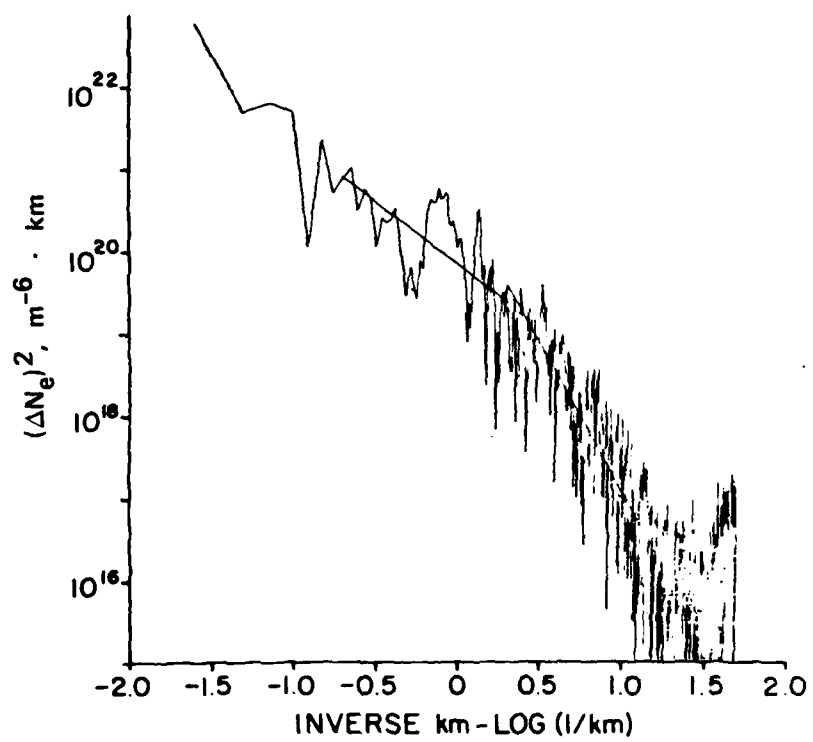


FIGURE A-1 PLUMEX I UPLEG — 254.5 km

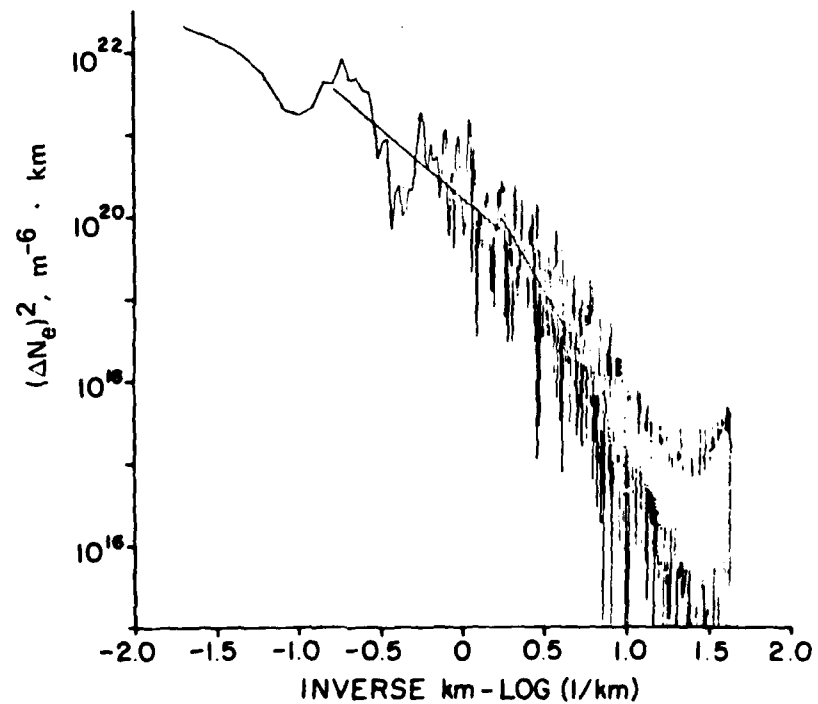


FIGURE A-2 PLUMEX I UPLEG — 264.5 km

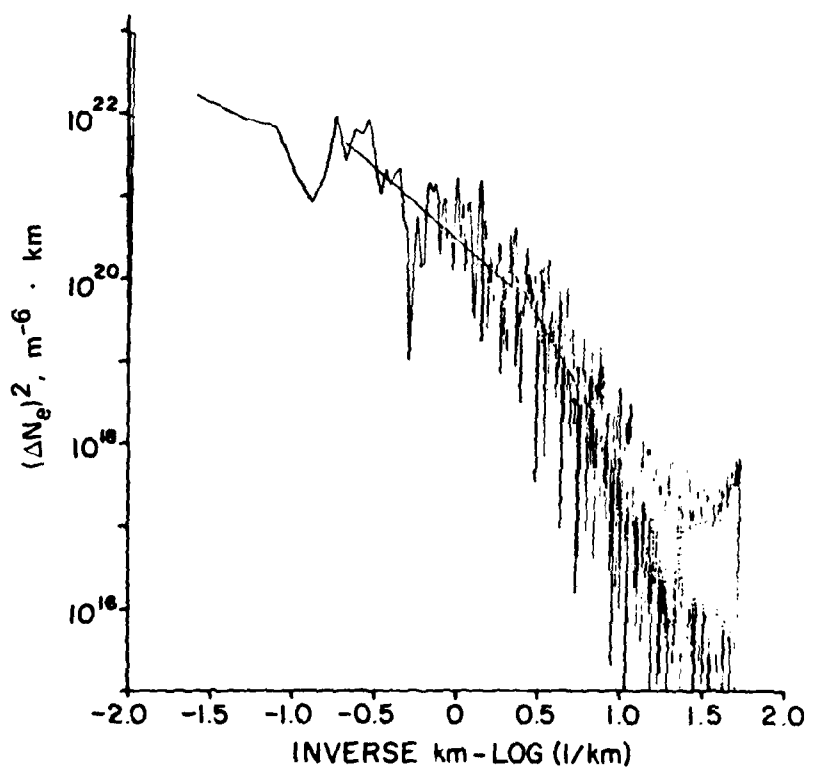


FIGURE A-3 PLUMEX 1 UPLEG — 274.5 km

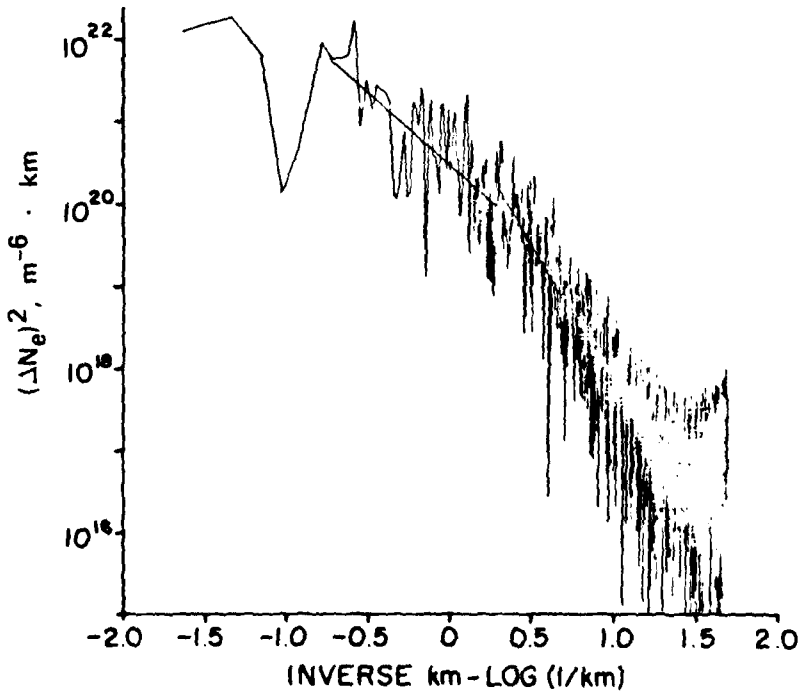


FIGURE A-4 PLUMEX 1 UPLEG — 285.5 km

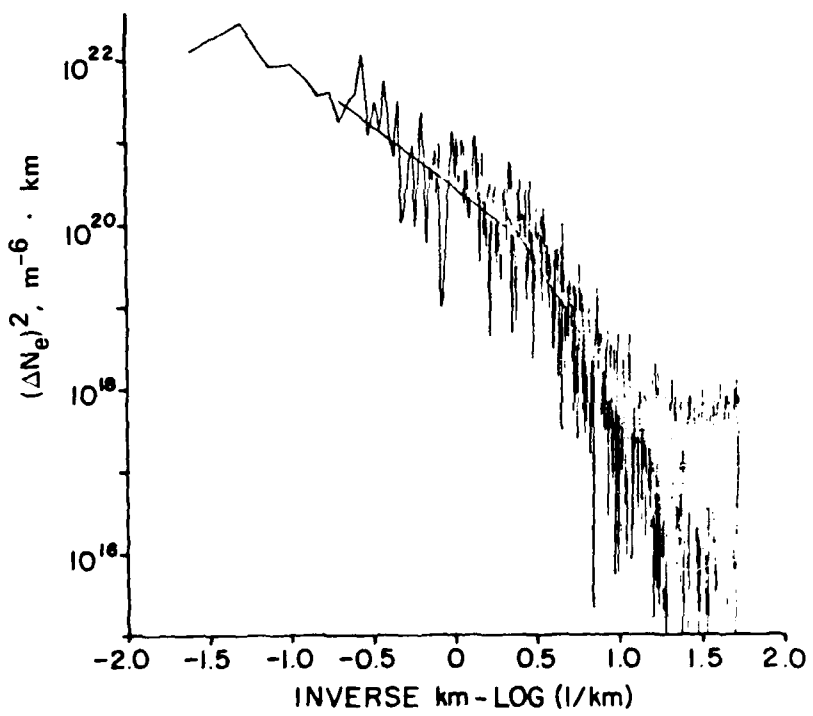


FIGURE A-5 PLUMEX I UPLEG — 295.5 km

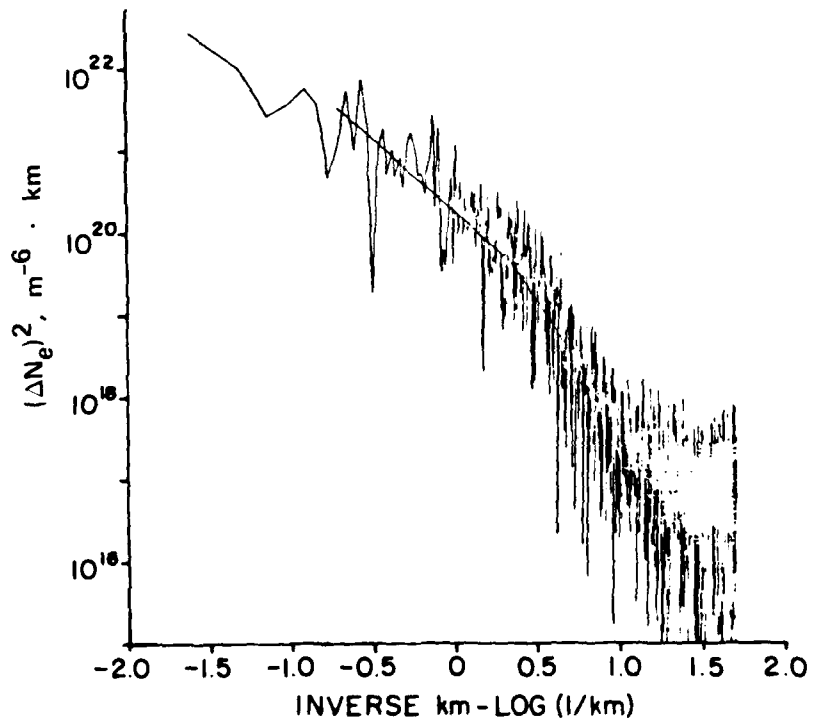


FIGURE A-6 PLUMEX I UPLEG — 305.5 km

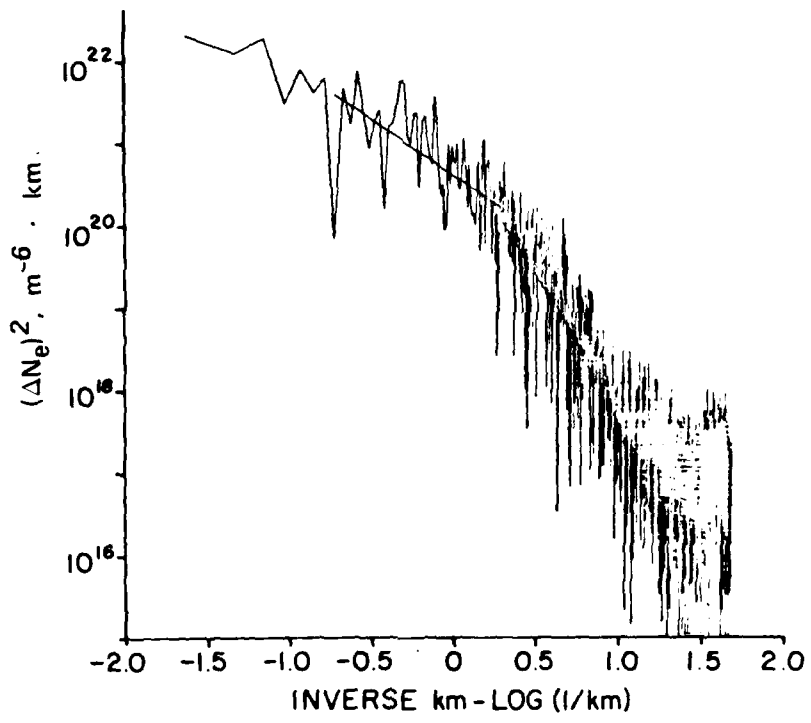


FIGURE A-7 PLUMEX I UPLEG — 315.5 km

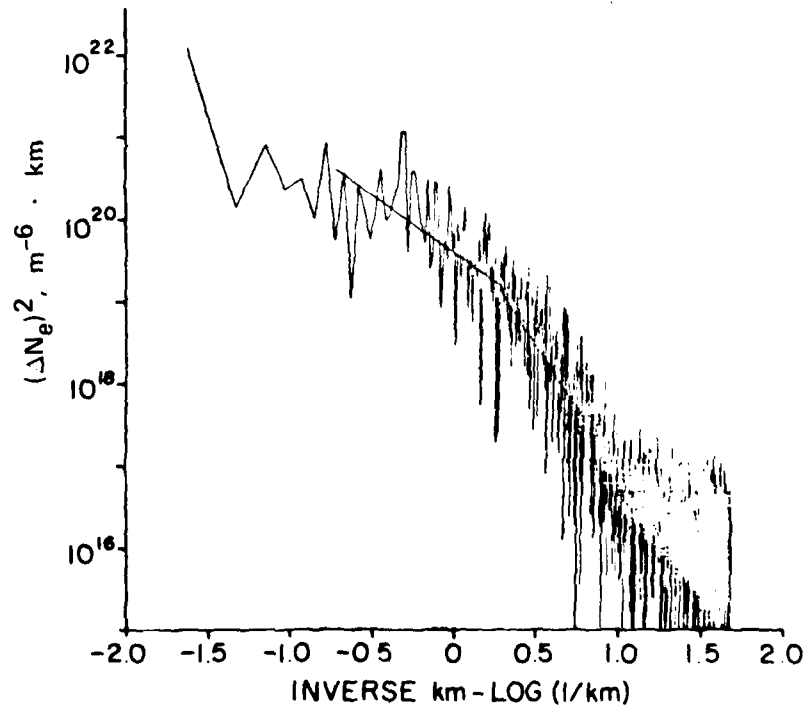


FIGURE A-8 PLUMEX I UPLEG — 326.5 km

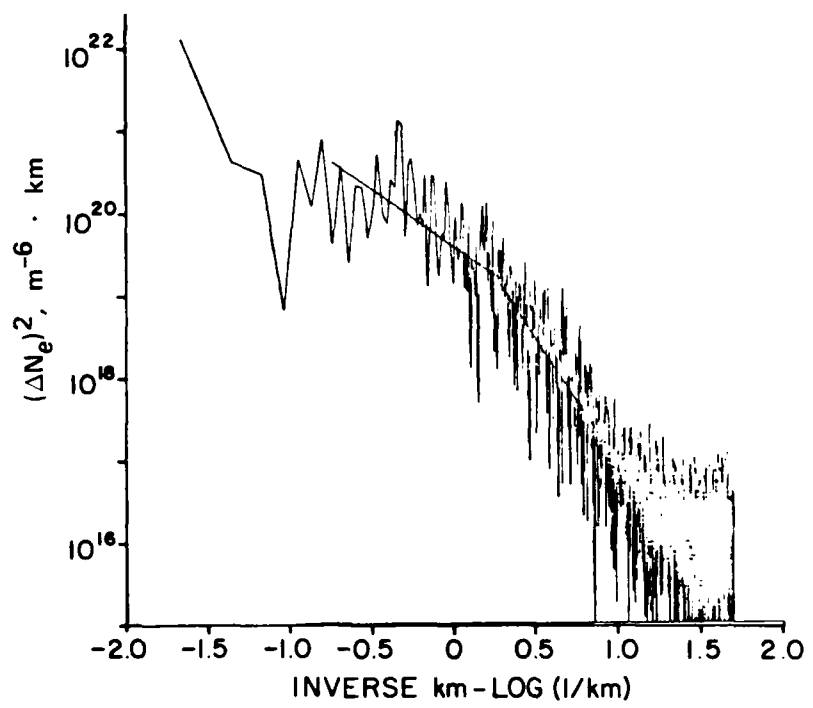


FIGURE A-9 PLUMEX I UPLEG — 336.5 km

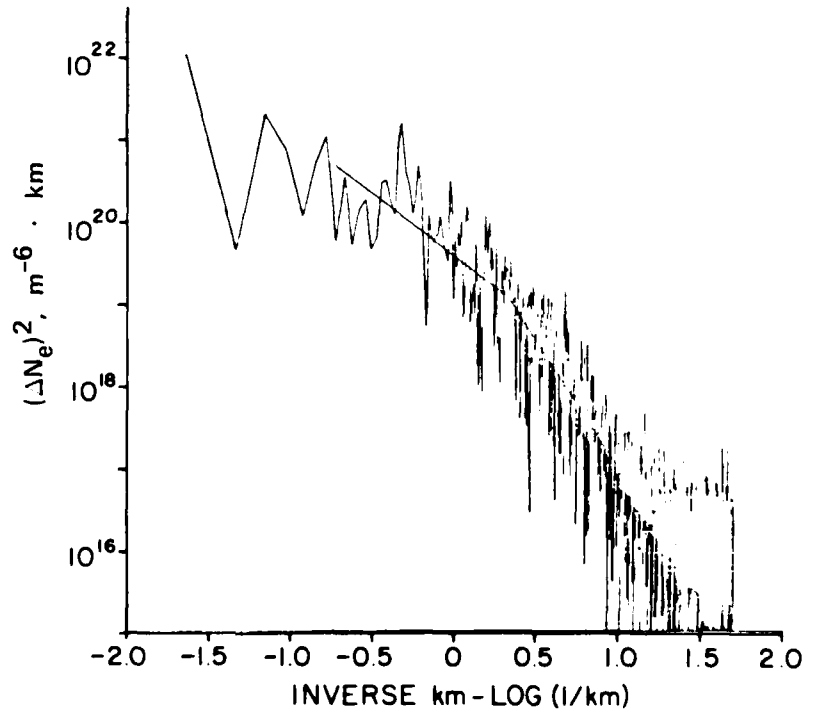


FIGURE A-10 PLUMEX I UPLEG — 346.5 km

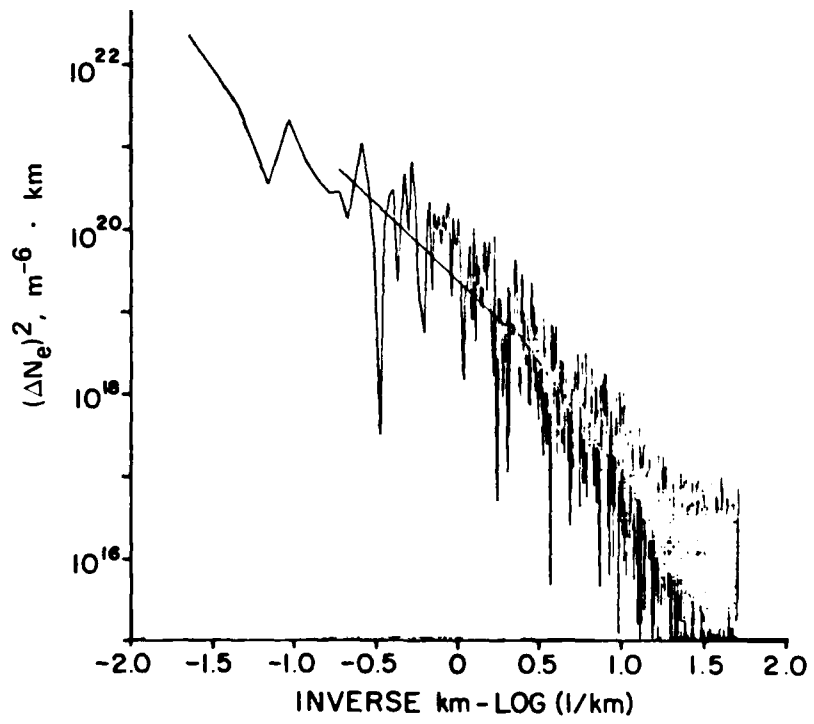


FIGURE A-11 PLUMEX I UPLEG — 356.5 km

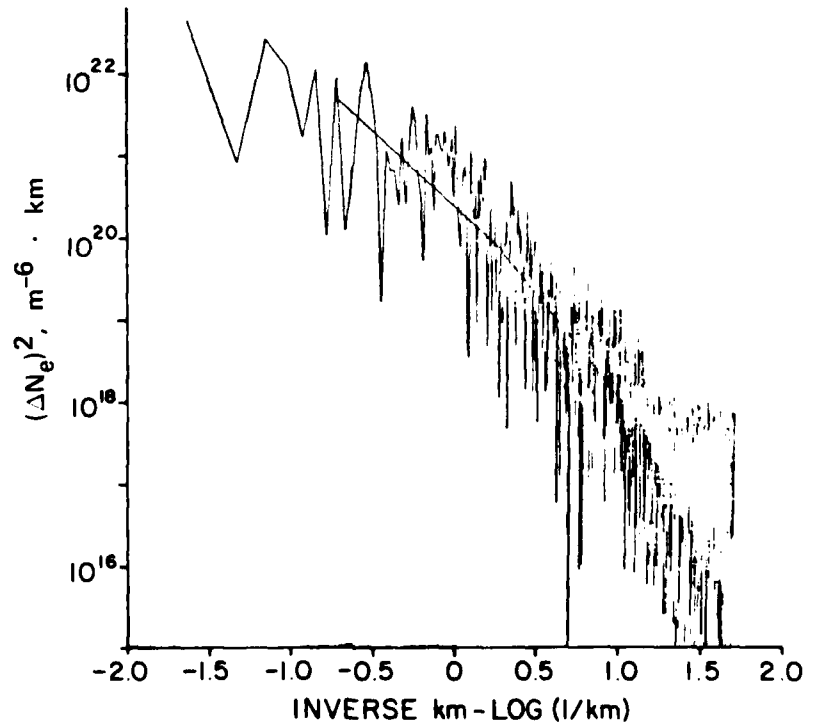


FIGURE A-12 PLUMEX I UPLEG — 366.5 km

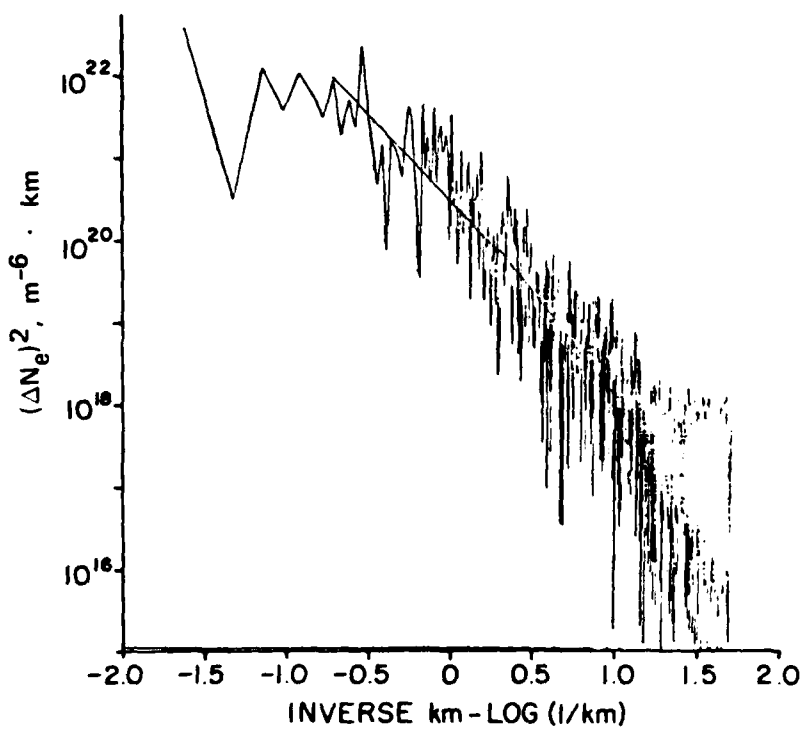


FIGURE A-13 PLUMEX I UPLEG — 377.5 km

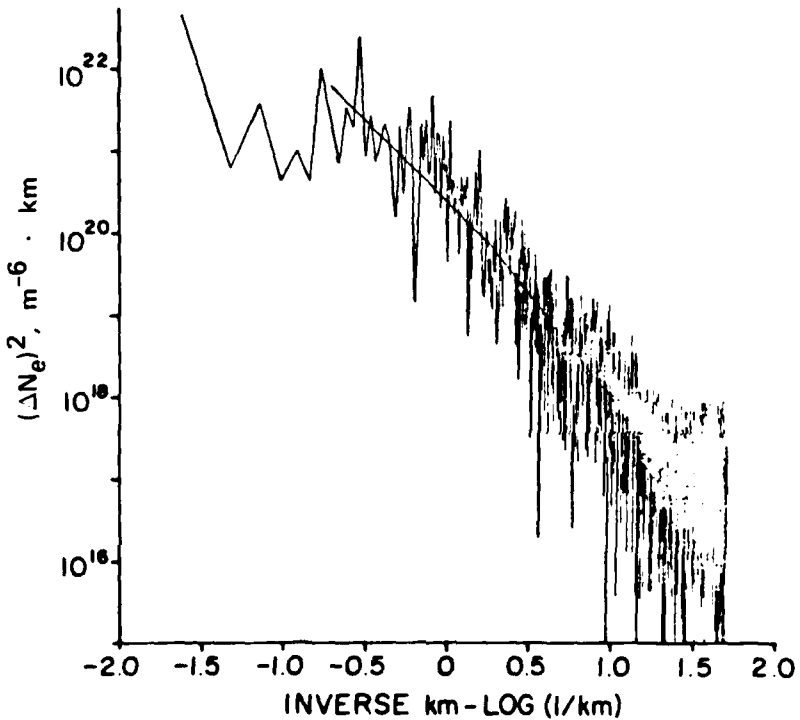


FIGURE A-14 PLUMEX I UPLEG — 387.5 km

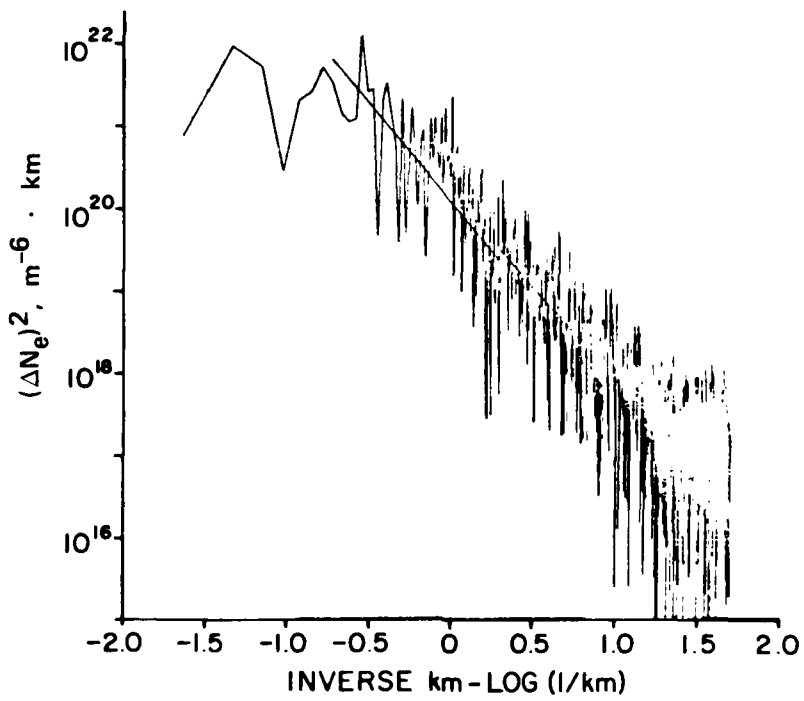


FIGURE A-15 PLUMEX I UPLEG — 397.5 km

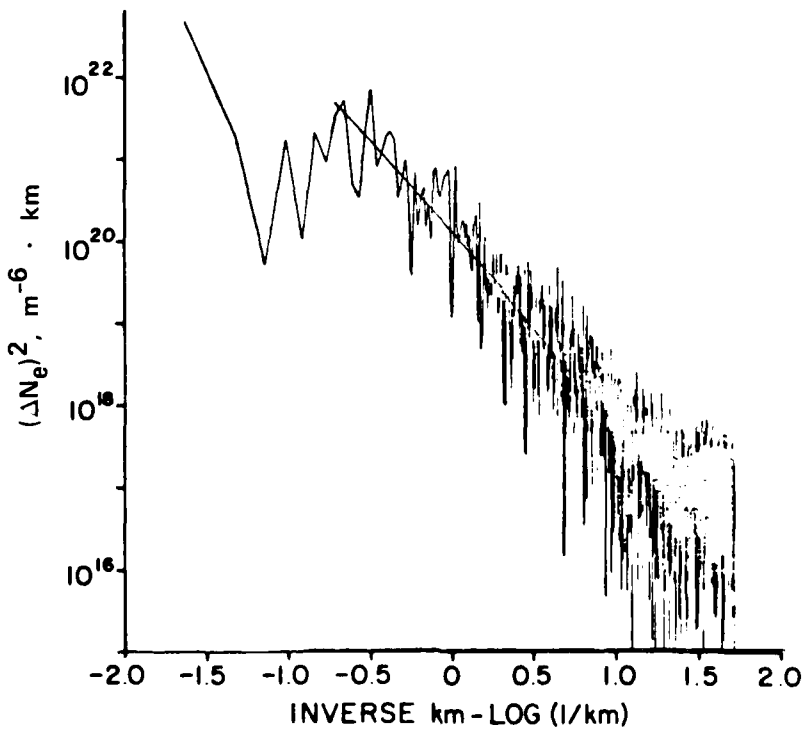


FIGURE A-16 PLUMEX I UPLEG — 407.5 km

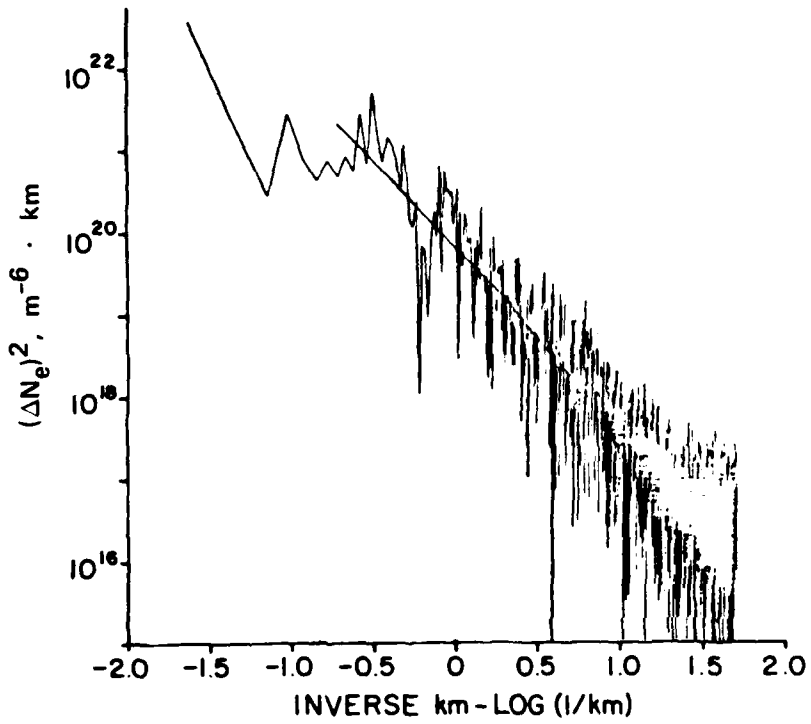


FIGURE A-17 PLUMEX I UPLEG — 417.5 km

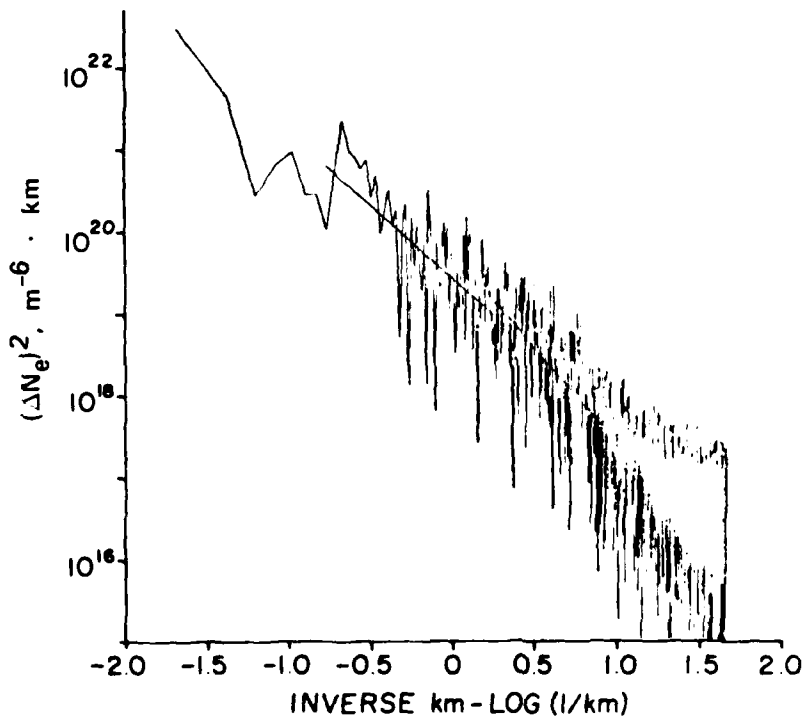


FIGURE A-18 PLUMEX I UPLEG — 427.5 km

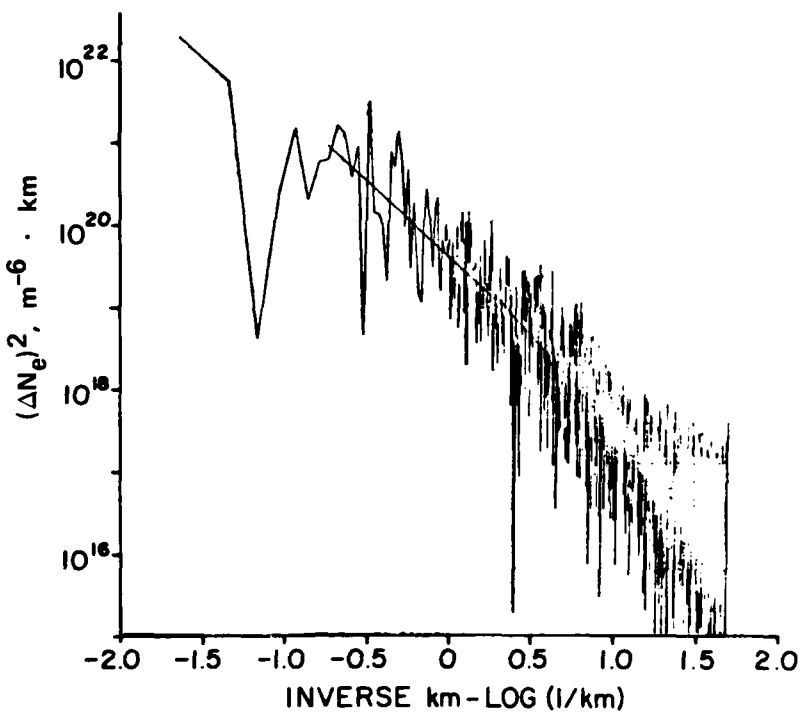


FIGURE A-19 PLUMEX I UPLEG — 438.5 km

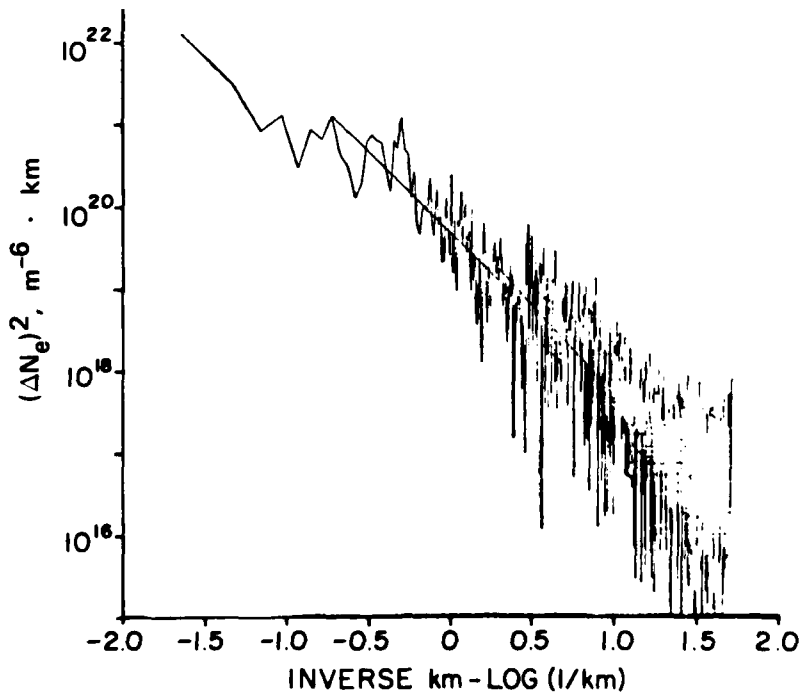


FIGURE A-20 PLUMEX I UPLEG — 448.5 km

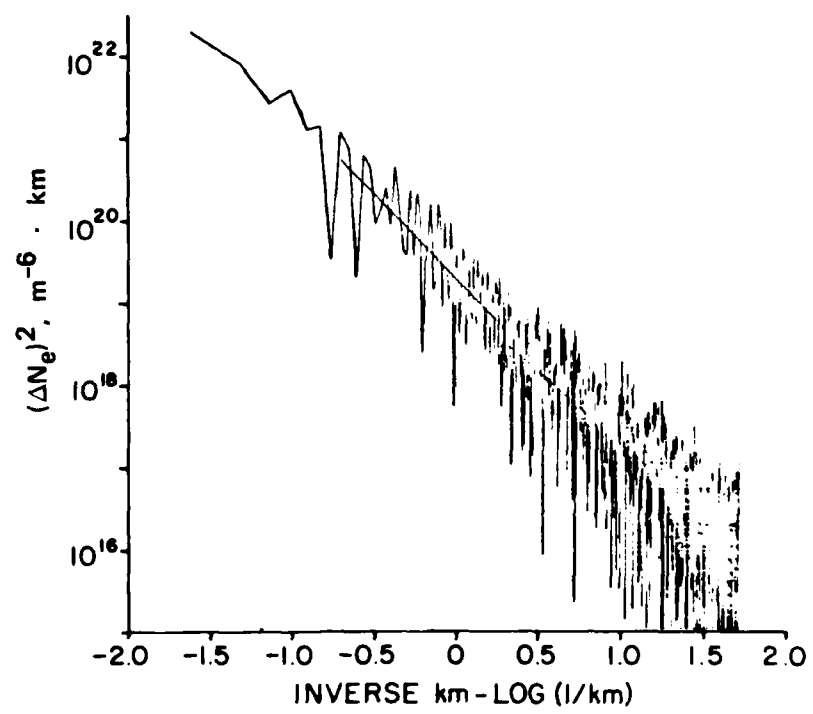


FIGURE A-21 PLUMEX I UPLEG — 458.5 km

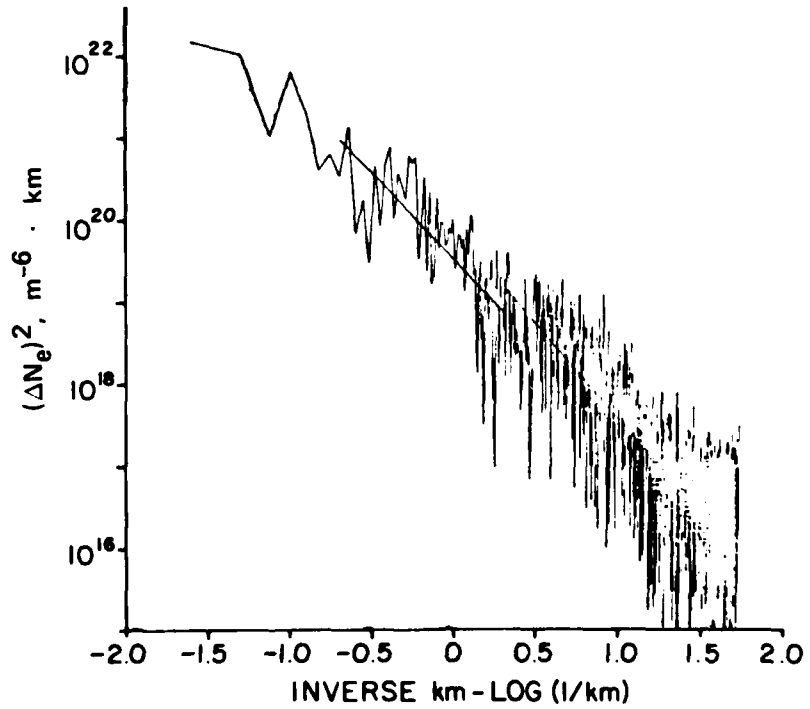


FIGURE A-22 PLUMEX I UPLEG — 468.5 km

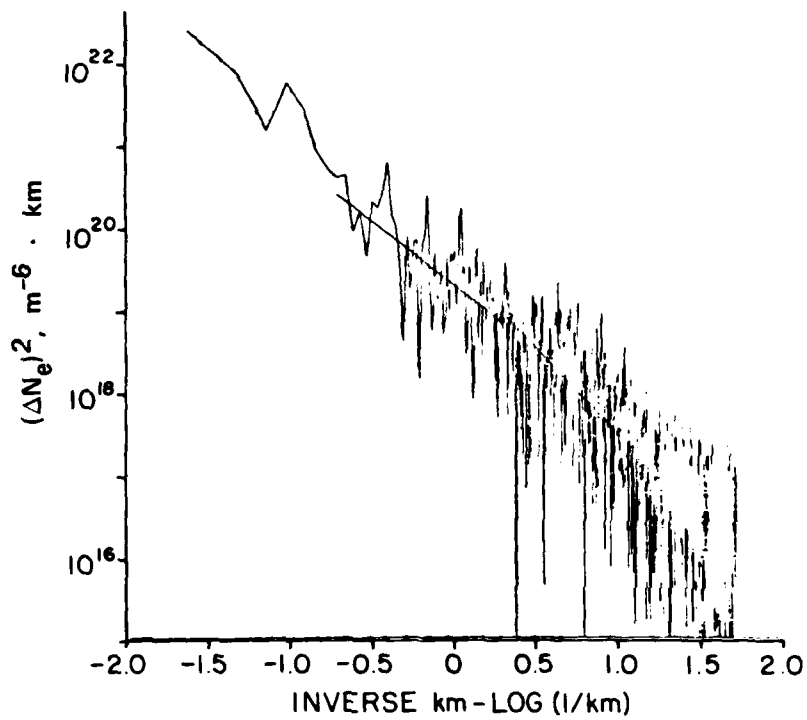


FIGURE A-23 PLUMEX I UPLEG — 478.5 km

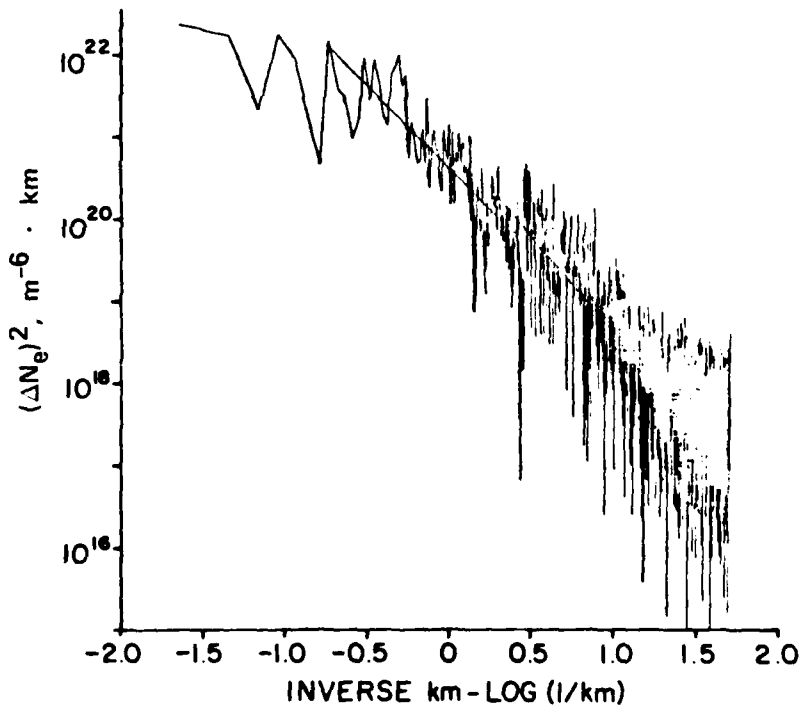


FIGURE A-24 PLUMEX I UPLEG — 489.5 km

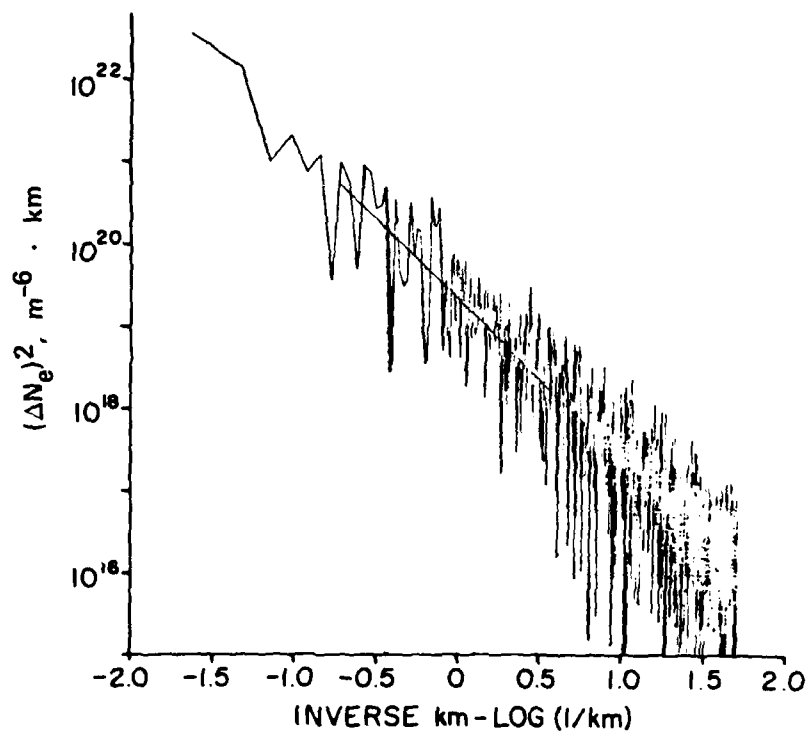


FIGURE A-25 PLUMEX I UPLEG — 499.5 km

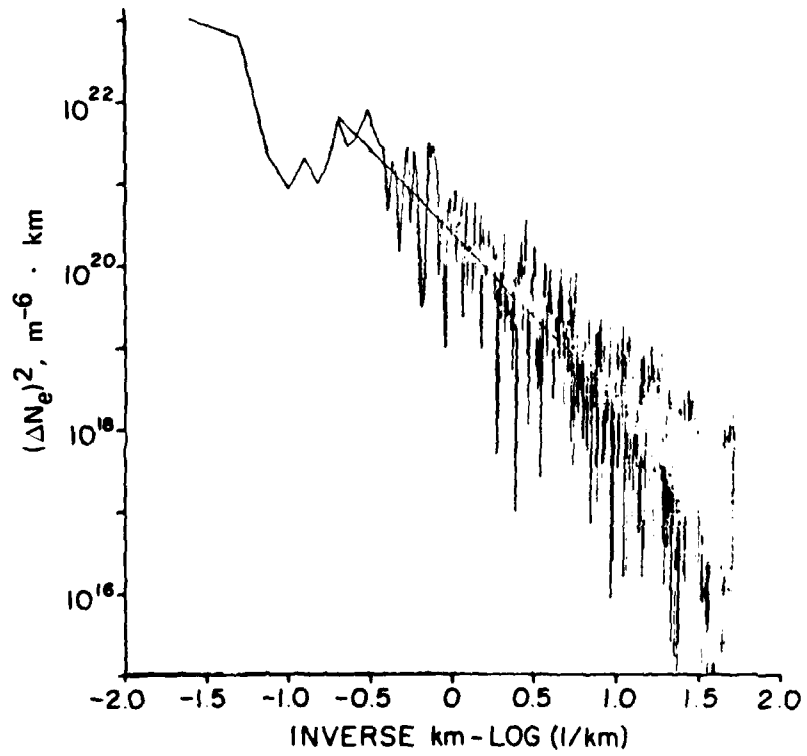


FIGURE A-26 PLUMEX I UPLEG — 509.5 km

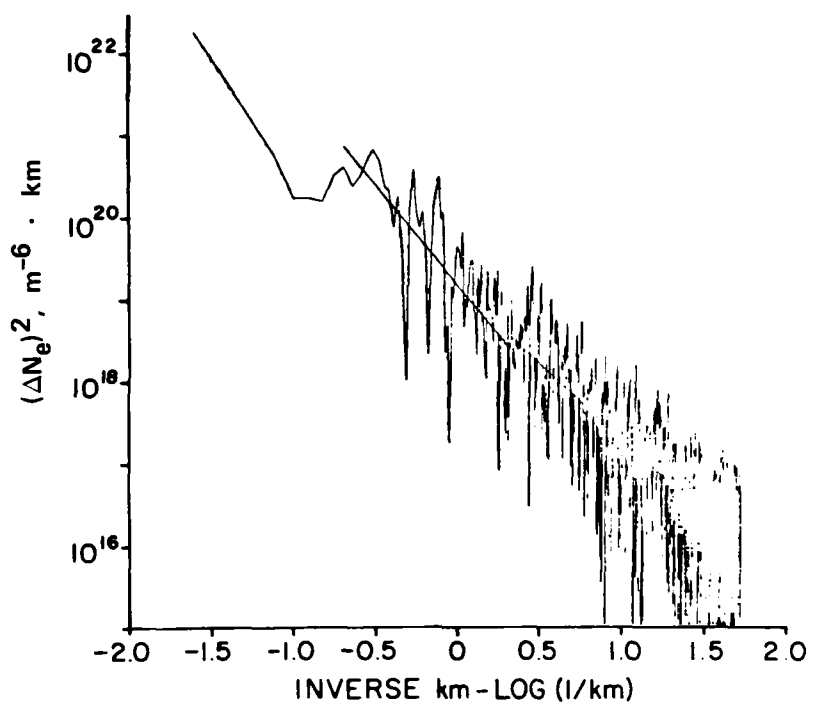


FIGURE A-27 PLUMEX I UPLEG — 519.5 km

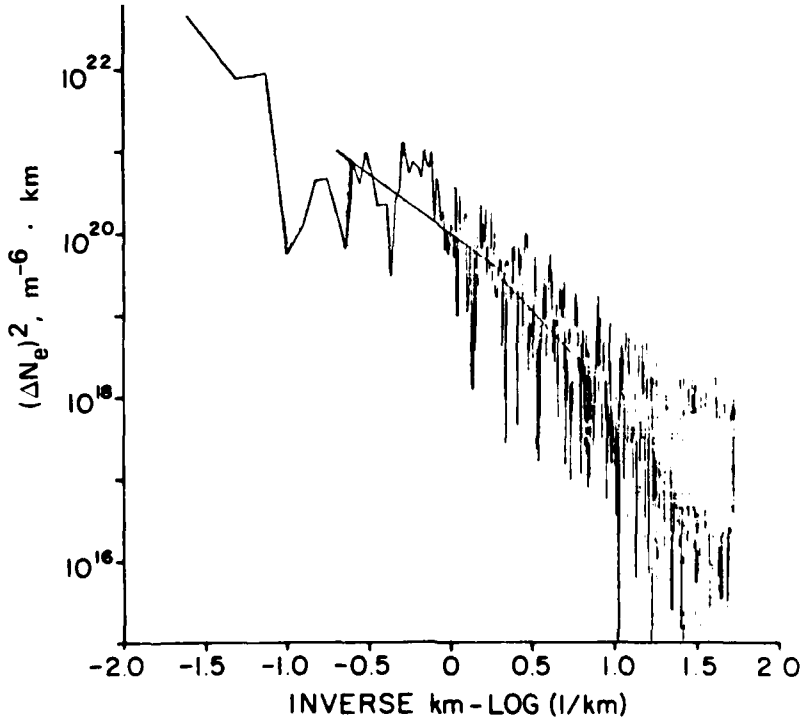


FIGURE A-28 PLUMEX I UPLEG — 529.5 km

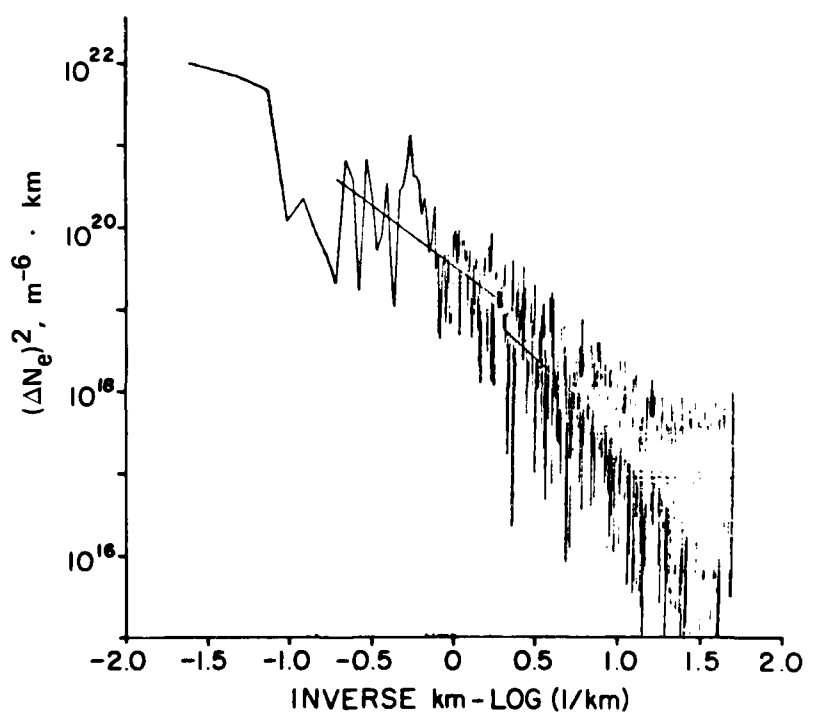


FIGURE A-29 PLUMEX I UPLEG — 549.5 km

Appendix B
DC ELECTRIC-FIELD DATA

This analysis is more complicated since the measured electric field is the vector sum of the ambient field and the $\vec{V} \times \vec{B}$ field induced by the rocket motion. A full attitude solution is thus necessary. This is complicated by the facts that the vehicle was not immediately tracked and that the altitude control system operated nearly continuously.

The data are of high quality and we have confidence that ambient fields will eventually be determined. For example, 20 s of raw, but calibrated electric-field data are plotted in Figure B-1. The data are from the upper boom pair and are spin-modulated because of the vehicle rotation. In Figure B-2 we have plotted the dot produce of $\vec{V} \times \vec{B}$ with the same antenna. Except for a phase difference, which has now been removed, the two figures are nearly identical.

An example of a strong, bubble-related, electric-field perturbation is presented in Figure B-3. Clearly, the smoothly varying sine wave because of $\vec{E} + (\vec{V} \times \vec{B})$, where \vec{E} is the unperturbed, ambient field, underwent a major change inside the bubble. Velocities of several hundred m/s are indicated. We plan to compare the structure of such small bubbles with the NRL code which now routinely includes electric-field calculations.

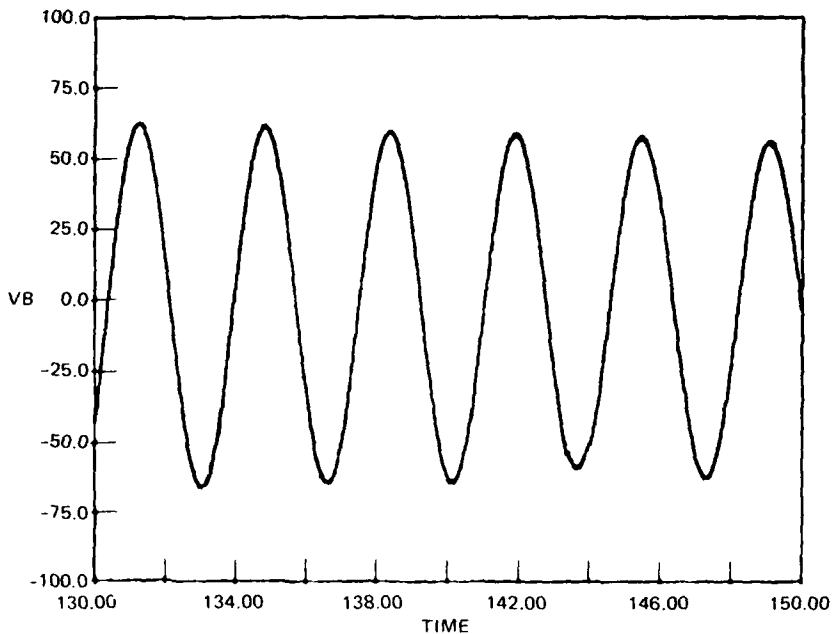


FIGURE B-1 MEASURED DC ELECTRIC-FIELD SIGNAL IN THE SPIN PLANE

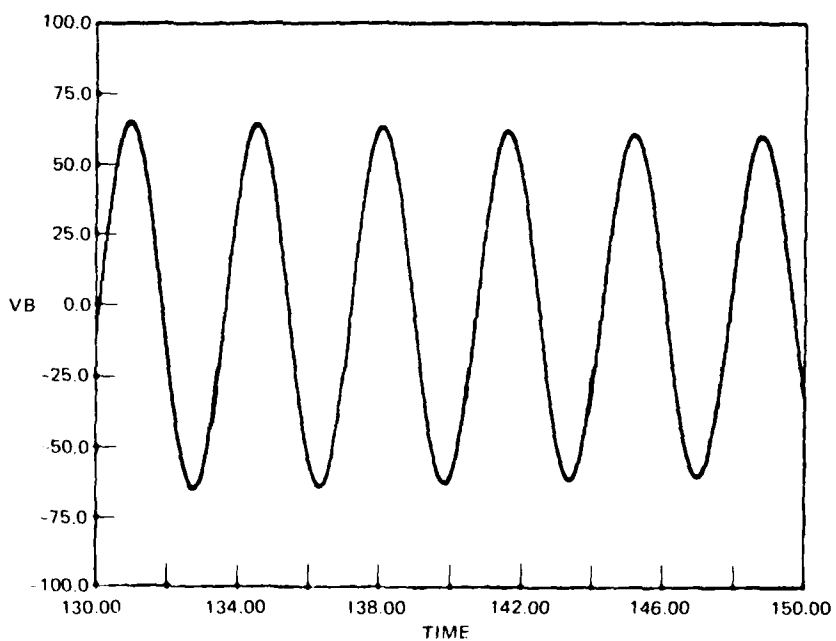


FIGURE B-2 CALCULATED $V \times B$ SIGNAL IN THE ROCKET SPIN PLANE
FOR THE SAME PERIOD AS FIGURE B-1

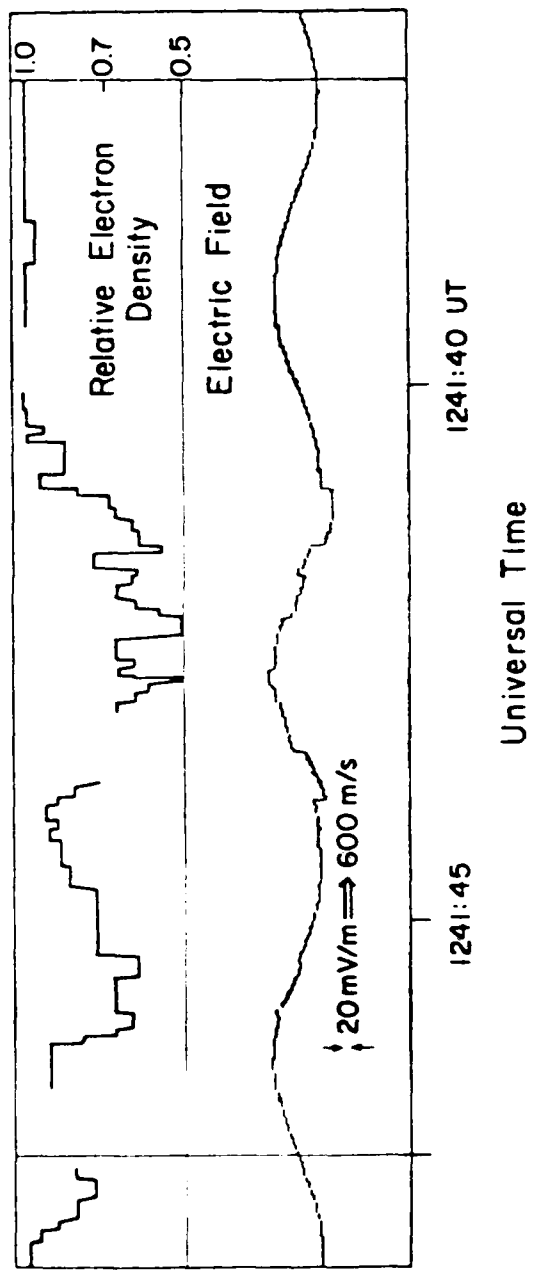


FIGURE B-3 PLUMEX I DOWNLEG — 385 km. Electron density and perturbation E field for a small bubble.

REFERENCES

1. R. Tsunoda, "ALTAIR Radar Measurements in Support of the PLUMEX Rocket Campaign," Proceed. of the Summer Equatorial Experiment Data Review Meeting, 18 March 1980 (1980).
2. E. P. Szuszczewicz, R. T. Tsunoda, R. Narcisi, and J. C. Holmes, "PLUMEX I: Coincident Radar and Rocket Observations of Equatorial Spread F," NRL Memorandum Report 4201, NRL, Washington, D.C., 1980.
3. M. C. Kelley, G. Haerendel, H. Kappler, A. Valenzuela, B. B. Balsley, D. A. Carter, W. L. Ecklund, C. W. Carlson, B. Hausler, and R. Torbert, "Evidence for a Rayleigh-Taylor-Type Instability and Upwelling of Depleted Density Regions During Equatorial Spread F," Geophys. Res. Lett., Vol. 3, No. 8, pp. 448-450 (August 1976).
4. R. F. Woodman and C. La Hoz, "Radar Observations of F-region Equatorial Irregularities," J. Geophys. Res., Vol. 81, No. 31, pp. 5447-5466 (November 1976).
5. C. L. Rino, R. C. Livingston, and J. Petriceks, "A Comparative Analysis of Equatorial Irregularity Structures as Measured by Wideband, AE-E, and In-Situ Rocket Probes," Proceed. of the Summer Equatorial Experiment Data Review Meeting, 18 March 1980 (1980).
6. F. A. Morse, B. C. Edgar, H. C. Koons, C. J. Rice, W. J. Heikkila, J. H. Hoffman, B. A. Tinsley, J. D. Winningham, A. B. Christensen, R. F. Woodman, J. Pomalaza, and R. N. Teixeira, "Equion, an Equatorial Ionospheric Irregularity Experiment," J. Geophys. Res., Vol. 82, No. 4, pp. 578-592 (February 1977).
7. M. C. Kelley, K. D. Baker, and J. C. Ulwick, "Late Time Barium Cloud Striations and Their Relationships to Equatorial Spread F," J. Geophys. Res., Vol. 84, No. A5, pp. 1898-1904 (May 1979).
8. M. C. Kelley and E. Ott, "Two-Dimensional Turbulence in the Equatorial Spread F," J. Geophys. Res., Vol. 83, No. A9, pp. 4369-4372 (September 1978).
9. M. C. Kelley and F. S. Mozer, "A Technique for Making Dispersion Relation Measurements of Electrostatic Waves," J. Geophys. Res., Vol. 77, No. 34, pp. 6900-6903 (December 1972).
10. E. Costa and M. C. Kelley, "Linear Theory for the Collisionless Drift Wave Instability with Wavelengths Near the Ion Gyroradius," J. Geophys. Res., Vol. 83, No. A9, pp. 4365-4368, (September 1978).

11. M. K. Hudson and C. F. Kennel, "Linear Theory of Equatorial Spread F," J. Geophys. Res., Vol. 80, No. 34, pp. 4581-4590 (December 1975).
12. E. Costa and M. C. Kelley, "On the Role of Steepened Structures and Drift Waves in Equatorial Spread F," J. Geophys. Res., Vol. 83, No. A9, pp. 4359-4364 (September 1978).
13. J. D. Huba, P. K. Chaturvedi, S. L. Ossakow, and D. M. Towle, "High Frequency Drift Waves with Wavelengths Below the Ion Gyroradius in Equatorial Spread F," Geophys. Res. Lett., Vol. 5, No. 8, pp. 695-698 (August 1978).
14. J. D. Huba and S. L. Ossakow, "On the Generation of 3-Meter Irregularities During Equatorial Spread F by Low Frequency Drift Waves," in press, J. Geophys. Res. (1980).
15. R. F. Woodman and S. Basu, "Comparison Between In-Situ Spectral Measurements of the F-Region Irregularities and Backscatter Observations at 3-m Wavelength," Geophys. Res. Lett., Vol. 5, No. 10, pp. 869-872 (October 1978).
16. R. Tsunoda, SRI International (Private Communication, 1980).

PLUMEX I

COINCIDENT RADAR AND ROCKET OBSERVATIONS OF EQUATORIAL SPREAD F

E. P. Szuszczewicz,^{*} R. T. Tsunoda,[†] R. Narcisi,[‡] and J. C. Holmes^{*}

ABSTRACT

Coordinated measurements of equatorial spread F that were conducted during July 1979 at the Kwajalein Atoll have yielded the first definitive space- and time-coincident radar and rocket observations of small-scale irregularities and large-scale plasma depletions. The results have shown that:

- During conditions of well-developed equatorial spread F, the most intense in-situ irregularities occurred on the bottomside F-layer gradient.
- Within a large-scale topside F-layer depletion, radar backscatter and in-situ irregularity strengths maximized near the upper wall of the depletion.
- Ion composition within a topside depletion provided signatures of its bottomside source domain and estimates of average maximum vertical drift velocity. For long-lived depletions, it was found that molecular-ion signatures (NO^+ and O_2^+) can be lost while bottomside levels of N^+ can be maintained when $[\text{O}^+] \approx N_e \gg [\text{NO}^+] + [\text{O}_2^+]$; and finally,
- Large-scale fluctuations of O^+ accompanied by a near-constant level of NO^+ and O_2^+ on the bottomside F-layer gradient suggests that neutral atmospheric turbulence is not a major source for bottomside ionospheric plasma irregularities and the associated triggering of equatorial spread F.

^{*}E. O. Hulbert Center for Space Research, Naval Research Laboratory, Washington, DC 20375.

[†]SRI International, Menlo Park, CA 94025.

[‡]Hanscom Air Force Base, Bedford, MA 01731.

I INTRODUCTION

Accumulated information about equatorial spread F points toward a definite causal relationship between the large-scale depletions (also referred to as holes, bite-outs, or bubbles) and observations of large ionospheric domains with strong radar backscatter returns from the much smaller (meter-size) irregularities (called plumes). Woodman and La Hoz¹* and Kelley et al.² have suggested that a plume was caused by a rising bubble leaving behind a wake of short wavelength irregularities. Another proposal by Szuszczewicz,³ arising from considerations of chemistry and transport, suggested that radar returns originate across density gradients at the boundaries of large-scale depletions. This concept is supported by Ossakow et al.,⁴ who inferred that a rising bubble will bifurcate on its topside and produce shorter and shorter wavelength irregularities, either by a cascade or two-step mechanism. Experimental evidence supporting this position was presented by Tsunoda,⁵ who showed that radar backscatter maxima tend to occur at altitudes corresponding to the electron density minimum or to the upper wall of a plasma depletion. More recently, Tsunoda⁶ has concluded that during the decay phase of meter-scale backscatter plumes, the radar returns were maximum on the upper walls of the plasma depletions.

Efforts to examine the exact relationship between radar plumes and ionospheric depletions by performing simultaneous in-situ and ground-based radar observations^{2,7} have been limited to conditions of bottom-side spread F and required extrapolations in space and time to establish correlations. As expected for bottomside spread F, the in situ probes only observed plasma fluctuations along the portion of the trajectory below the F-layer peak density while the ionosphere above the peak was quite smooth.

*References are listed at the end of this paper.

The ion composition within the depletions has also been the subject of a number of investigations. Typically, satellite mass-spectrometric observations^{3,8,9} have shown that the ion composition can differ vastly inside and outside the bite-outs. Fe^+ ions may be enhanced or depleted, with molecular ions usually more abundant inside the bite-out. Brinton et al.⁸ and McClure et al.⁹ have found O^+ depleted by as much as a factor of 10^3 to a concentration below that of NO^+ . The molecular ion NO^+ was found dominant in the O^+ depleted region; and the bite-outs varied from a few kilometers to tens of kilometers in width. An analysis of the Atmosphere Explorer-C data³ suggested that a given chemical volume on the bottomside F layer ($[\text{NO}^+]$, $[\text{O}_2^+] > [\text{O}^+]$) could move upward through a stationary neutral atmosphere and appear at higher altitudes as a bite-out in the local plasma density. As the bottomside F-region plasma cell moved upward, the relative magnitudes of its ionic components would depend on the transit time and on the altitude through the height distribution of the neutral gases. This model was consistent with the satellite observations as well as the computational work of Scannapieco and Ossakow.¹⁰

To understand further the detailed relationships that involve large-scale plasma depletions, meter-size irregularities, and associated ion-chemical signatures, a rocket payload that was instrumented with a plasma diagnostics complement (plasma probes, electric-field sensors, mass spectrometer and a four-frequency beacon experiment) was launched into the topside F-region ionosphere above Roi-Namur in the Kwajalein Atoll (4.3° N dip latitude). The investigation was part of a major effort to coordinate the rocket and ALTAIR radar observations with the bottomside soundings and ground-based photometric measurements of F-region winds. We present the initial coordinated observations of the radar plumes and the in-situ measurements of the rocket-borne plasma probes and mass spectrometer.

II EXPERIMENTAL RESULTS

A. Ionospheric Conditions and Radar Maps

By 2100 LT on the night of the rocket launch, ionograms showed that the nominal bottomside of the F layer had risen to an altitude of 400 km. At that point, the F layer began to drift downward with an almost immediate occurrence of spread F. The F layer continues to drift downward (as did the spread F) at an approximate average velocity of 10 m/s. The bottomside F layer had descended to an altitude near 270 km when the rocket was launched (1231:30 UT on day 198; 0031:30 LT, 17 July 1979).

Operating at 155.5 MHz (radar backscatter from 1-m field-aligned irregularities) the ALTAIR radar executed consecutive east-west scans in a plane that included the penetration of the rocket upleg trajectory. Figure 1 presents the contours of constant backscatter strength plotted in 10 dB increments. (For details see Tsunoda et al.¹¹). The first panel in Figure 1 shows a backscatter plume near the radar's eastern-most field of view. That plume, with its highest and most intense backscatter region near 510 km, is connected to backscatter domains that extend down to the bottomside of the F layer. The second panel, with a center scan time 137 s later than the first, shows the intense backscatter region further to the east, indicating an eastward velocity of 160 m/s. In the third panel the plume has moved almost completely out of the field of view of the radar and the intense region near 510 km has decayed.

B. Rocket Profile and Comparison with Radar

The rocket payload that was launched into the spread-F conditions which are depicted in Figure 1 carried, among other instruments, a quadrupole ion mass-spectrometer (from the Air Force Geophysics Laboratory) and a pair of pulsed plasma probes (from the Naval Research Laboratory). The pair of pulsed probes simultaneously tracked ion- and electron-saturation currents while generating conventional Langmuir probe characteristics.¹²

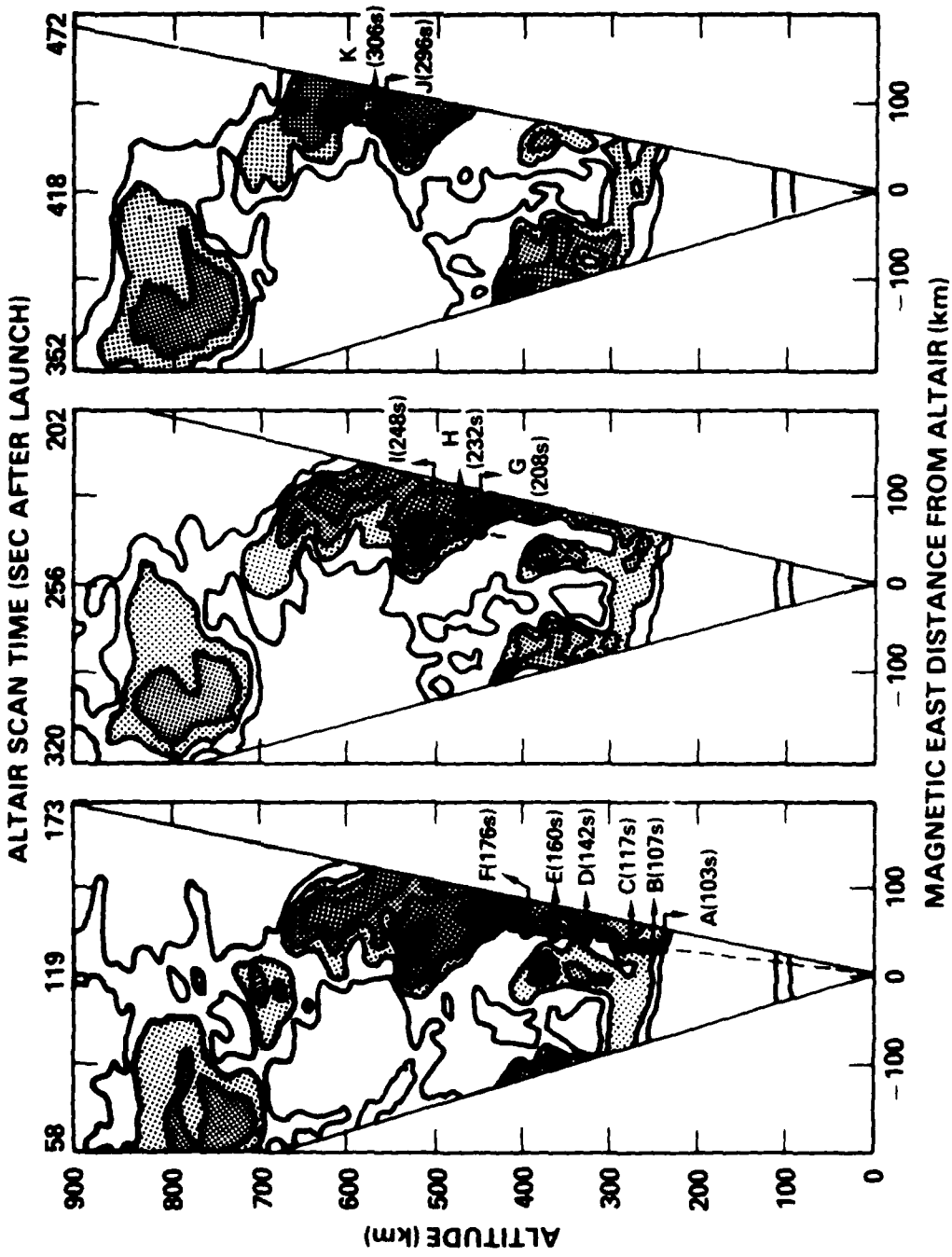


FIGURE 1 BACKSCATTER INTENSITY CONTOUR MAPS WITH THE ROCKET TRAJECTORY SUPERIMPOSED.
 Contours are in 10-dB increments, dark gray \equiv 0 dB. The times identified with Observations A through K are included for a more complete representation of temporal correlation with successive radar scans.

Figure 2 displays the upleg measurements of relative electron density as presented by electron-saturation currents. The ordinate has a linear scale for time-after-launch with altitude superimposed at 50-s increments. (Because ion- and electron-saturation currents have significantly different sensitivities to velocity, sheath, and magnetic-field effects¹³ variations in electron data not corroborated by ion saturation currents were attributed to the various aspect sensitivities and excluded from Figure 2. This approach facilitates quick-look analysis and establishes credibility in the interpretation of the curves as relative electron density profiles.)

The profile shows that the payload entered the very bottom of the F layer at $t \geq 103$ s ($Z \geq 240$ km). From that point, to an apogee near 590 km the in-situ measurements revealed a number of plasma depletions depicted in the figure as Regions C, D-E, F-G, H-I, and J-K. The largest depletion was in Region H-I where $\Delta N_e / N_e^0 = 0.85$ with a half-minimum vertical extent approximately equal to 23 km. (The density ratio was scaled directly from the electron currents, with the superscript "zero" identifying an undisturbed value extrapolated from regions outside the hole.)

In the regions of the large-scale depletions, the in-situ probe measurements (temporal resolution as great as 2 kHz) revealed much smaller scale irregularities. The central plot of "irregularity intensity" in Figure 2 identifies the regions of smaller irregularities and attempts to establish a preliminary quantification for their intensity. The "irregularity intensities" were scaled directly from analog records of probe-current fluctuations about an estimated mean. As an illustration, the -4.0 to +4.0 irregularity intensity within Region C approximately represents a ± 80 -percent peak-to-peak fluctuation level measured in that region of the bottomside F-layer gradient. (If vehicle potential, plasma temperature, and mean ion mass were constant during the irregularity measurements, then $I \propto N_e$. More quantitative analyses along with power spectral densities will be determined for future publication.) The results show that the most intense irregularities occurred on the bottomside gradient (Region C) with corresponding measurements at all other altitudes at a much lower level. We note that the fluctuations in the largest depletion (Region H-I) are smaller than those at Region C.

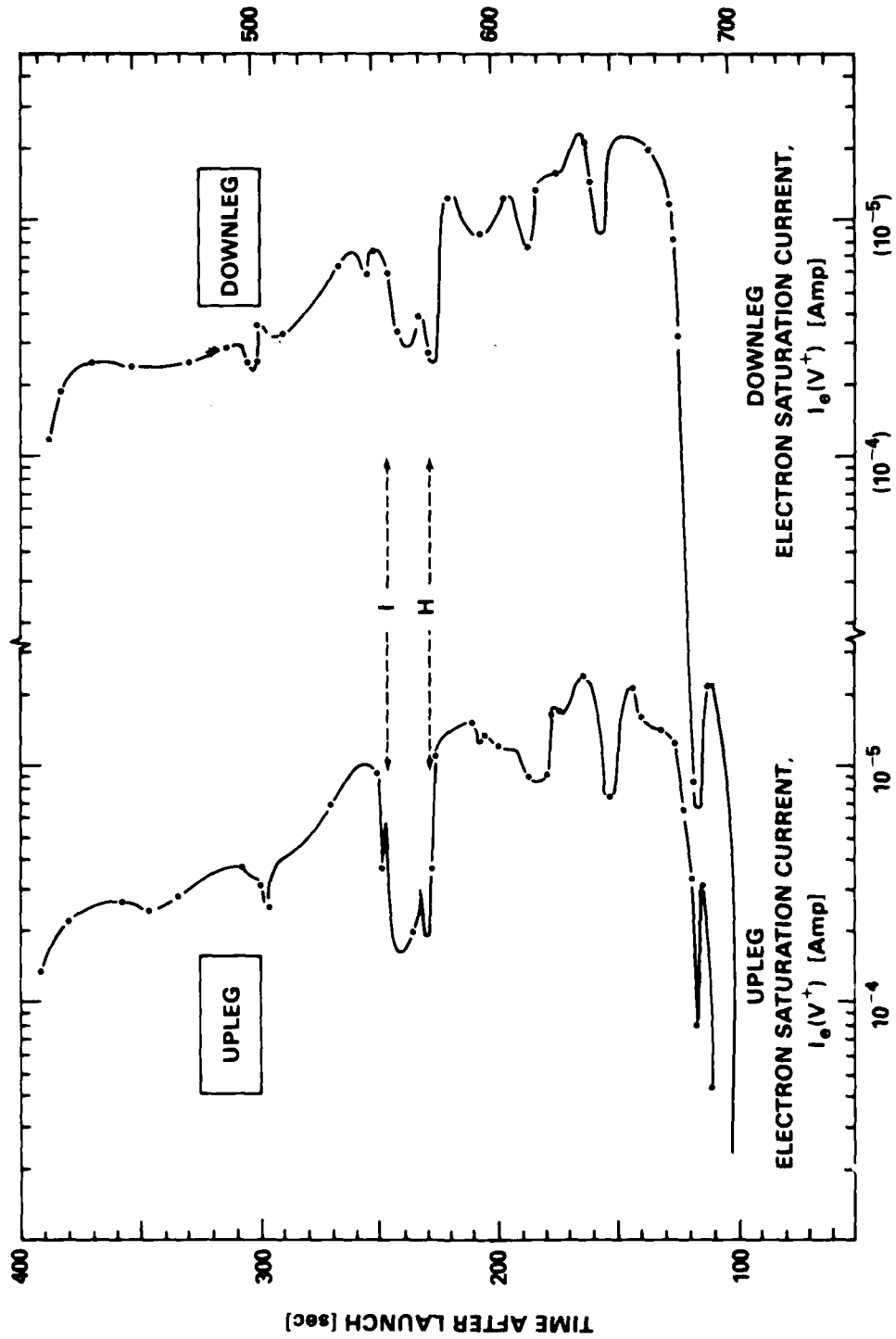


FIGURE 2 RELATIVE ELECTRON DENSITY PROFILE AS MEASURED BY ELECTRON-SATURATION PROBE CURRENTS COLLECTED ON THE UPLEG TRAJECTORY. The "irregularity intensity" provides an approximate measure of smaller-scale structure as scaled from analog strip-chart records of probe current fluctuations. The inset is ion-mass-spectrometer data which expands Region C and clarifies the discussions on chemistry and turbulence.

Furthermore, the fluctuations at Regions C, D, E, and I are more intense than at all other locations; and C, D, E, and I are collocated with positive density gradients of larger scale features. We note, with reference to the mass-spectrometer aperture plate current in the inset to Figure 2, that Region C is not one narrow bite-out as the macroscale plot would suggest, but rather a region of intense irregularities on the bottomside gradient. (The chemical features will be discussed later.)

The upleg trajectory of the payload has been superimposed on the radar maps in Figure 1 with domains A through K (and their associated times of observation) identified on the panel best matched for time coincidence with the radar results. A step-wise comparison of in-situ irregularity observations (Figure 2) with the radar maps reveals some interesting correlations:

Region A corresponds to the lowest position of the bottomside F-layer, while Region B is midway up the steep bottomside and very near the point of maximum positive density gradient. Region C is at the boundary of the third highest backscatter level (30 dB), and appears to represent the midphase development of large-scale Rayleigh-Taylor turbulence (i.e., an intermediate stage in the cascading process). Observations at Region D, E, F, and G occur along the western "wall" of the plume, and encompass an altitude domain identified with the F-layer peak. Region G represents the entry of the payload into the large-scale depletion centered near 240 s (490 km) on the upleg trajectory. The payload's transit from Region G to Region I is marked by a positive gradient in backscatter radar energy, with the maximum return occurring on the topside (Region I and above) of the H-I depletion. Above the large-scale depletion, observations "J" and "K" begin to track the western "wall" of the plume in the topside F region.

C. Ion Composition

Throughout the entire F-region domain shown in Figure 2, O^+ was observed to be the dominant ion with metallics through mass 56 always being less than 1 part in 10^5 . From points of view focused on turbulence and transport the chemical constituency of two regions are worthy of note:

In the H-I depletion on the topside F-layer the major observed ion components were $[O^+] \approx 0.998 N_e$, $[N^+] \approx 0.002 N_e$ and $([NO^+] + [O_2^+]) < 10^{-4} N_e$. In the adjacent domains the distribution of ions was different, i.e., outside the depletion we found $[O^+] \approx 0.992 N_e$, $[N^+] \approx 0.007 N_e$ and $([NO^+] + [O_2^+]) < (2 \times 10^{-5}) N_e$, a distribution typical of the quiescent ionosphere at those altitudes. While we observed a change in the overall ion composition, there were no major differences in the absolute levels of molecular ions within and outside the depletion.

The ion composition within the H-I depletion suggests that its origin may have been at or near the bottomside F region where $[O^+] \approx [O^+]_{H-I}$. Such a region exists at 112 s ($Z = 262$ km) on the upleg trajectory where it was observed that $[NO^+]$ and $[O_2^+]$ were 1 to 2 percent of N_e . That the source region levels of NO^+ and O_2^+ have not been preserved in the topside hole results from their losses by dissociative recombination and by a simultaneous decrease in production by ion-atom interchange and charge exchange reactions because $[N_2]$ and $[O_2]$ decrease markedly with altitude. The longer it takes a bottomside depletion to move upward into the topside F-layer, the more likely the elimination of molecular ion signatures when $[O^+] \approx N_e \gg ([NO^+] + [O_2^+])$. In the case of the H-I depletion, a vertical transport time greater than 360 s would account for the molecular ion deficiency. (To arrive at this estimate we assumed an instantaneous displacement of the bottomside ion composition to the H-I altitude and calculated that in about 6 min the molecular ions would decrease to concentrations typically found on the topside.) This time estimate suggests an upper limit of about 600 m/s for the depletion's average vertical drift velocity, a value which is consistent with the wide range in predicted bubble rise velocities.^{14,4,15}

Additional information pinpointing source domains comes from the $[O^+]/[N^+]$ ratio. Our measurements show that the ratio in the H-I depletion was different from that in adjacent domains and somewhat smaller than that observed at the 262-km level where the N^+ lifetime is about 1 min. This suggests that the initial bubble formed on the bottomside gradient when it was at a higher altitude where N^+ has a longer lifetime, a result consistent with the F-peak time history leading up to launch operations.

The second region of special note is C where the Figure 2 inset shows that N^+ and O^+ followed the intense plasma density fluctuations (indicated by aperture plate current) while the molecular ions NO^+ and O_2^+ did not. A possible explanation rests in an assumption that requires steady state chemical equilibrium in an O^+ dominant domain. (Molecular ions in Region C can achieve equilibrium concentrations in less than 10 min). Under this condition, molecular ion concentrations are independent of O^+ and vary only with the scale height of the neutral atmospheric constituents N_2 and O_2 . The observations conform to this model with a standard zero-order atmospheric distribution, suggesting that neutral atmospheric turbulence is not a major source for the observed plasma fluctuations on the bottomside F region.

D. Horizontal Extent and Depletion Decay

Figure 3 presents the up- and downleg profiles of relative electron density as measured by in-situ probe electron-saturation currents. (The integrity of the downleg profile was established by the same procedure used in Figure 2.) A comparison of the profiles shows very good agreement in the two observations of plasma depletions. The H-I observations were separated along the flux tube by 112 km, while the C Region observations were separated by 168 km. These results support the generally accepted concept of plasma depletion flux-tube alignment.

A difference in the two profiles worth noting is the softening of the upper wall in the downleg observation of the H-I depletion. This result correlates very well with the decay of the most intense radar returns in the 510-km region of Figure 1.

III COMMENTS AND CONCLUSIONS

Space- and time-coincident measurements of equatorial spread F conducted during July 1979 at the Kwajalein Atoll have yielded the first definitive relationships of small-scale irregularities (at 1 m) and large-scale plasma depletions, measured independently throughout the

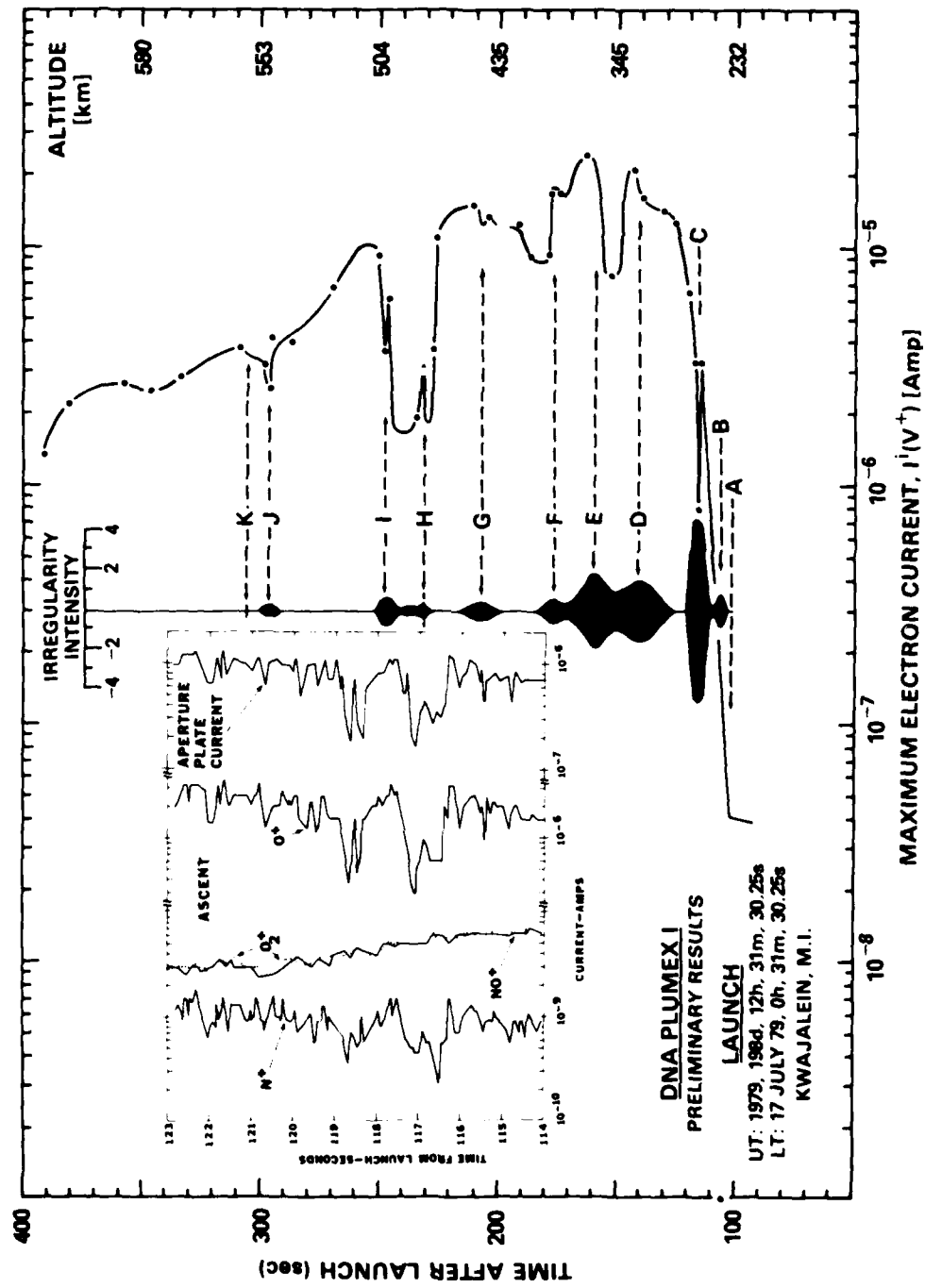


FIGURE 3 COMPARISON OF UPLEG AND DOWNLEG PLASMA PROFILES

F region by ground-based radar and in-situ plasma instrumentation. Preliminary analysis of the results leads to the following comments and conclusions:

- (a) Within a large-scale, decay-phase, topside F-layer depletion in which in-situ irregularities were reduced (compared with the topside wall of the depletion), the radar backscatter energy was also reduced (compared with the topside wall). This result suggests the collocation of maximum radar returns with the upper regions of a depletion (its topside wall and above) and not with the depletion minimum or bottomside wall.
- (b) The in-situ measurements established field alignment of large scale depletions to distances at least as great as 168 km. This result supports the topside sounder data of Dyson and Benson,¹⁶ the airglow observations of Weber et al.,¹⁷ the recent radar measurements of Tsunoda,^{5,6} and the assumption of depleted flux tubes in the theoretical considerations of Anderson and Haerendel.¹⁸
- (c) Ion-composition measurements within a topside depletion showed little evidence of bottomside molecular tracer ions (i.e., NO^+ and O_2^+). This result points to the requirement for rapid bubble-rise velocities and/or low-plasma densities within the hole if the bottomside molecular ion composition is to be maintained as bubbles drift upward through the F region.³ However, measurements of the N^+/O^+ ratio, found to be different inside and outside the depletion, helped identify the lower altitude domain as the source region for the topside bubble.
- (d) Strong irregularities on the bottomside F-region gradient showed that N^+ and O^+ followed large-scale density fluctuations while the molecular ions NO^+ and O_2^+ were relatively constant. Preliminary analysis of this result suggests chemical equilibrium and eliminates neutral atmospheric turbulence as a major source of the bottomside plasma irregularities.
- (e) Bubble-rise velocity was estimated by preliminary chemical analysis of ion composition within the hole. The analysis suggests an upper limit of 600 m/s for the average vertical velocity of an 85-percent depleted domain (85 percent on the topside, 100 percent at the F peak) as it drifted upward from its bottomside source region near 260 km to the topside F layer at 490 km. This upper limit (generally large compared with observations)^{14,4,15} is consistent with the wide range in predicted values.^{14,4,15}

AD-A099 998

SRI INTERNATIONAL MENLO PARK CA
PROCEEDINGS OF THE SUMMER EQUATORIAL EXPERIMENT DATA REVIEW MEE--ETC(U)
NOV 80 D R McDANIEL

F/G 22/2

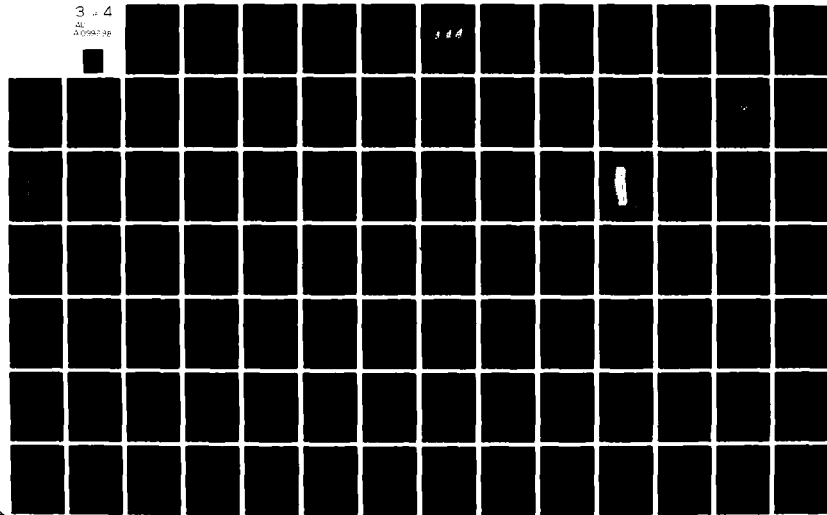
DNA001-78-C-0379

NL

UNCLASSIFIED

DNA-5528P

3 x 4
M
DNA-5528P



ACKNOWLEDGMENTS

Support for the plasma probe analysis was provided by the Defense Nuclear Agency (DNA) under Subtask Code I25AAXHX640, Communications Effects Experiments. The ALTAIR radar analysis was also supported by DNA under contract DNA 001-C-0153. Support for the ion-composition measurements was supplied mostly by the Air Force Office of Scientific Research under Task 2310-G3 and partially by DNA under Subtask I25AAXHX640, Work Unit 06. We also wish to acknowledge the dedicated technical support of E. Trzcinski, G. Federico, L. Wlodyka, L. Kegley and D. Walker, who independently and as a team contributed significantly to the successful execution of the rocket-borne plasma probe and mass-spectrometer experiments. Development of the plasma probe technique was provided by the Office of Naval Research under Work Unit A02-11.11 (71-0949-0-0), Ionospheric and Stratospheric Interactions, Task Area RR 043-02-44.

REFERENCES

1. R. F. Woodman and C. La Hoz, "Radar Observations of F-Region Equatorial Irregularities," J. Geophys. Res., Vol. 18, No. 31, pp. 5447-5466 (November 1976).
2. M. C. Kelly, G. Haerendel, H. Kappler, A. Valenzuela, B. B. Balsley, D. A. Carter, W. L. Ecklund, C. W. Carson, B. Hausler, and R. Torbert, "Evidence for a Rayleigh-Taylor-Type Instability and Upwelling of Depleted Density Regions during Equatorial Spread F," Geophys. Res. Lett., Vol. 3, No. 8, pp. 448-450 (August 1976).
3. E. P. Szuszczewicz, "Ionospheric Holes and Equatorial Spread-F: Chemistry and Transport," J. Geophys. Res., Vol. 83, No. A6, pp. 2665-2669 (June 1978).
4. S. L. Ossakow, S. T. Zalesak, B. E. McDonald, and P. K. Chaturvedi, "Nonlinear Equatorial Spread F: Dependence on Altitude of the F Peak and Bottomside Background Electron Density Gradient Scale Length," J. Geophys. Res., Vol. 84, No. A1, pp. 17-29 (January 1979).

5. R. T. Tsunoda, "On the Spatial Relationship of 1-m Equatorial Spread-F Irregularities and Plasma Bubbles," J. Geophys. Res., 85 (in press, 1980).
6. R. T. Tsunoda, "Magnetic-Field-Aligned Characteristics of Plasma Bubbles in the Nighttime Equatorial Ionosphere," J. Atmos. Terr. Phys. (submitted, January 1980).
7. F. A. Morse, B. C. Edgar, H. C. Koons, C. J. Rice, W. J. Heikkila, J. H. Hoffman, B. A. Tinsley, J. D. Winningham, A. B. Christensen, R. F. Woodman, J. Pomalaza, and N. R. Teixeira, "Equion, an Equatorial Ionospheric Irregularity Experiment," J. Geophys. Res., Vol. 82, No. 4, pp. 578-592 (February 1977).
8. H. C. Brinton, H. G. Mayr, and G. P. Newton, "Ion Composition in the Nighttime Equatorial F-Region: Implications for Chemistry and Dynamics" (abstract), Eos Trans. AGU, Vol. 52, No. 12, p. 1038 (December 1975).
9. J. P. McClure, W. B. Hanson, and J. H. Hoffman, "Plasma Bubbles and Irregularities in the Equatorial Ionosphere," J. Geophys. Res., Vol. 82, No. 19, pp. 2650-2656 (July 1977).
10. A. J. Scannapieco and S. L. Ossakow, "Nonlinear Equatorial Spread F," Geophys. Res. Lett., Vol. 3, No. 8, pp. 451-454 (August 1976).
11. E. P. Szuszczewicz and P. Z. Takacs, "Magnetsheath Effects on Cylindrical Langmuir Probes," Phys. Fluids, Vol. 22, No. 12, pp. 2424-2429 (December 1979).
12. E. P. Szuszczewicz and J. C. Holmes, "Observations of Electron Temperature Gradients in Mid-Latitude E_s Layers," J. Geophys. Res., Vol. 82, No. 32, pp. 5073-5080 (November 1977).
13. E. P. Szuszczewicz and P. Z. Takacs, "Magnetsheath Effects on Cylindrical Langmuir Probes," Phys. Fluids, Vol. 22, No. 12, pp. 2424-2429 (December 1979).
14. S. L. Ossakow and P. K. Chaturvedi, "Morphological Studies of Rising Equatorial Spread-F Bubbles," J. Geophys. Res., Vol. 83, No. A5, pp. 2084-2090 (May 1978).
15. D. N. Anderson and G. Haerendel, "The Motion of Depleted Plasma Regions in the Equatorial Ionosphere," J. Geophys. Res., Vol. 84, No. A8, pp. 4251-4256 (August 1979).
16. P. L. Dyson and R. F. Benson, "Topside Sounder Observations of Equatorial Bubbles," Geophys. Res. Lett., Vol. 5, No. 9, pp. 795-802 (September 1978).
17. E. J. Weber, J. Buchau, R. H. Eather, and S. B. Mende, "North-South Aligned Equatorial Airglow Depletions," J. Geophys. Res., Vol. 83, No. A2, pp. 712-716 (February 1978).

PLUMEX II

A SECOND SET OF COINCIDENT RADAR AND ROCKET OBSERVATIONS OF EQUATORIAL SPREAD F

E. P. Szuszczewicz,* R. T. Tsunoda,[†] R. S. Narcisi,[‡] and J. C. Holmes*

ABSTRACT

PLUMEX II was the second in a two-rocket operation that successfully recorded space- and time-coincident measurements of equatorial spread F. The first launch operation (PLUMEX I) was conducted during the late phase in the development and decay of spread F: major radar plume features were relatively stable with respect to vertical drifts, and the most intense regions of radar backscatter were beginning to decay. The PLUMEX II conditions were substantially different from PLUMEX I. The rocket was launched into the midphase of well-developed spread F: a ground-based ionosonde showed full-range spread while ALTAIR radar maps of meter-size irregularities displayed backscatter plumes that penetrated to the topside F layer and continued rising with time. Current analysis of PLUMEX II results show that a number of ionospheric depletions ($\Delta N_e^0/N_e^0 \lesssim 0.75$) were distributed throughout the F region with $F_2 h_{\max}$ at 510 km and $N_e^{\max} \approx 6 (10^5) \text{ cm}^{-3}$. Smaller-scale irregularities (i.e., small-scale structure imbedded in larger-scale features) appear less intense than corresponding observations in PLUMEX I. If substantiated by more quantitative analyses, this result could support current interpretations of east-west plume asymmetry, which suggests that the western wall of a plume (the PLUMEX I case) is more unstable than its eastern counterpart (the PLUMEX II case). NO^+ was the dominant positive-charge ion at altitudes below the F-region ledge. Across the ledge and throughout the F layer up to an apogee of 580 km, O^+ dominated. The ion results support a model of a Rayleigh-Taylor mode that assumes relatively small depletions originating on the F ledge with

*E. O. Hulbert Center for Space Research, Naval Research Laboratory, Washington, DC 20375.

[†]Radio Physics Laboratory, SRI International, Menlo Park, CA 94025.

[‡]Hanscom Air Force Base, Bedford, MA 01731.

initially small horizontal extent. In this model, the local ion composition will be transported to higher altitudes, but molecular ions will not be the dominant positive species.

I INTRODUCTION

The coordinated measurements of equatorial spread F that were conducted during July 1979 at the Kwajalein Atoll involved the launch of two instrumented rocket payloads that were designed to probe the detailed in-situ structure of the turbulent ionospheric plasma. The first launch operation (PLUMEX I; 17 July 1979, 0031:30.25 LT*) was conducted during the late phase in the development and decay of spread F. The associated results and discussions of ground-based and rocket-borne diagnostics have been presented in companion papers.^{1,2†} The second rocket (PLUMEX II: 23 July 1979, 2157:30 LT) was launched into the midphase of well-developed spread F, i.e., a ground-based ionosonde showed full-frequency and range spread while the ALTAIR radar maps of meter-size irregularity contours displayed backscatter plumes that penetrated to the topside F layer and continued rising with time. We present here the initial PLUMEX II observations of radar plumes and the in-situ measurements of the rocket-borne plasma probes and mass spectrometer. The results are then compared with PLUMEX I.

II EXPERIMENTAL RESULTS

A. Ionospheric Conditions and Radar Maps

By 2000 LT on the night of the PLUMEX II launch, ionograms showed that the virtual height ($h'F$) of the F layer had risen at an average rate of 12 m/s to an altitude of 350 km. At that point vertical drifting ceased and shortly thereafter full-range spread F was observed. The

* Local Time (LT).

† References are listed at the end of the paper.

virtual height remained constant until 2130 LT, when upward drifting again commenced at an average rate of 18 m/s. With full-range spread F still in effect and with the F layer still drifting at an upward rate of almost 18 m/s, the PLUMEX II rocket was launched (0957:30 UT on day 205; 2157:30 LT, 23 July 1979).

Operating at 155.5 MHz (radar backscatter from 1-m field-aligned irregularities) the ALTAIR radar executed consecutive magnetic east-west scans in a plane that included the upleg penetration of the rocket trajectory. Figure 1 presents the contours of constant backscatter strength³ plotted in 10-dB increments that range from 0 dB (domain of small dots) to 50 dB (solid black). The first panel in Figure 1 shows backscatter returns extending from 350 to 1000 km, with the most intense region (50-dB level) centered at 635 km. A measure of horizontal and vertical drift velocity can be achieved by focusing on α (the 50-dB region at 635 km) and β (the 20-dB region at an altitude of 550 km, and 125 km west of ALTAIR in the first panel). In the 135-s time lapse between the radar measurements in panels 1 and 2, the observations showed that V_{α}^{α} (hor), V_{α}^{α} (vert) \approx 290 m/s, 170 m/s and V_{β}^{β} (hor), V_{β}^{β} (vert) \approx 300 m/s, 150 m/s. The results can be interpreted as an average magnetic west-to-east plume drift velocity of 295 m/s (about 130 m/s faster than corresponding observations in PLUMEX I) with a corresponding average upward vertical drift velocity equal to 160 m/s. (Note that ionograms showed h'F moving upward at an average rate of 18 m/s throughout most of the time encompassed by the radar maps in Figure 1. Therefore, one concludes that the plume was drifting upward at a rate of 142 m/s relative to the F-layer bottomside.) In the 124-s interval between Panels 2 and 3 the average magnetic west-to-east drift velocity was considerably slower, with a rate of 100 m/s. During this same interval the average vertical drift velocity increased to 270 m/s (252 m/s relative to the bottomside F-region).

B. Rocket Profile and Comparison with Radar

The rocket payload that was launched into the spread-F conditions depicted in Figure 1 carried, among other instruments, a quadrupole

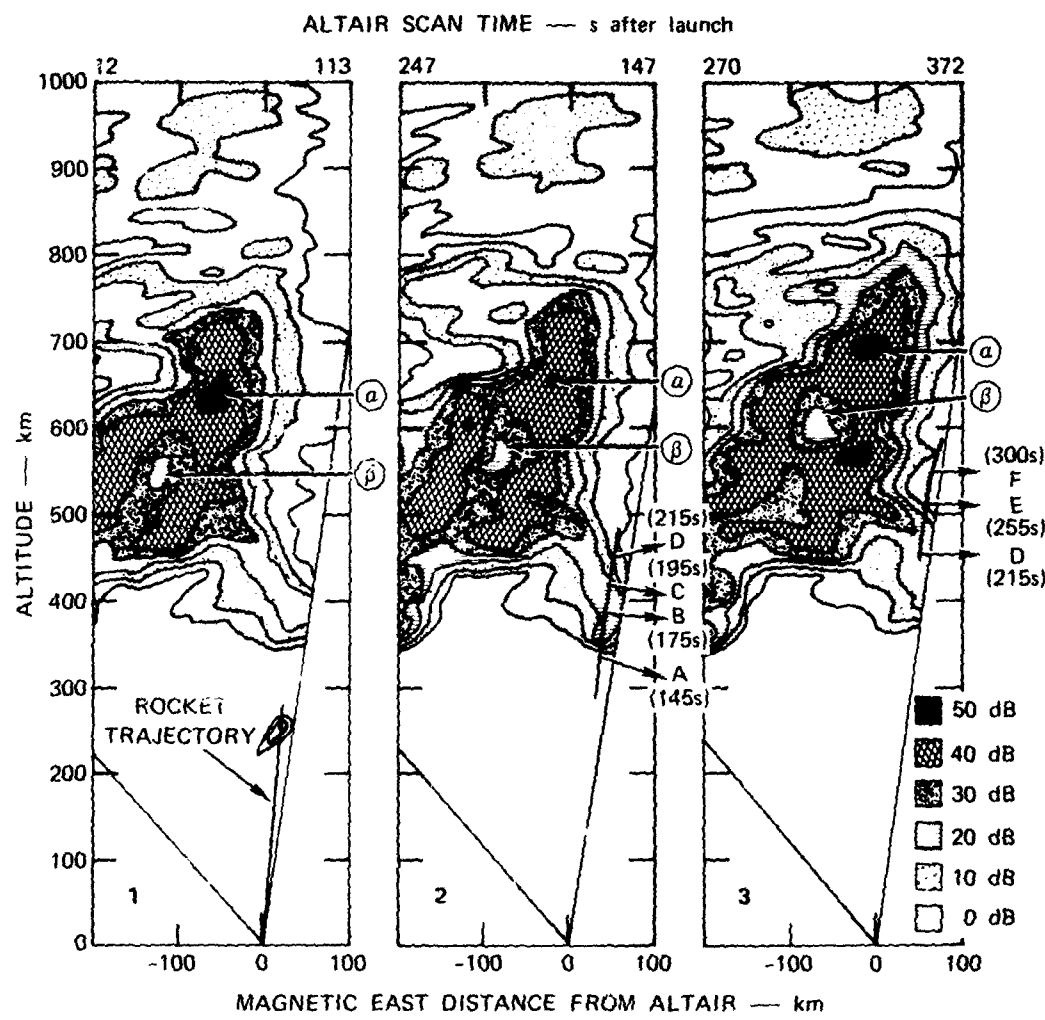


FIGURE 1 CONTOURS OF CONSTANT BACKSCATTER STRENGTH

ion-mass spectrometer and a pair of pulsed-plasma probes (see Szuszczewic and Holmes² and Narcisi et al. for instrumentation details and the payload configuration). The pair of pulsed probes simultaneously tracked ion and electron saturation currents while generating conventional Langmuir probe characteristics.² Figure 2 displays the upleg measurements of relative electron density as observed simultaneously by electron I_B^e and ion $I^e(V^-)$ saturation currents. Because ion and electron saturation currents have significantly different sensitivities to velocity, sheath, and magnetic-field effects, variations in one polarity current, not corroborated by the other, were attributed to the various aspect sensitivities and were excluded from Figure 2. This approach facilitates quick-look analysis and establishes credibility in the interpretation of the curves as relative electron-density profiles. It also proves to be a valuable technique for eliminating the otherwise degrading effects of uncontrolled payload tumble and ACS jet firings that resulted from the failure of payload separation from the rocket motor in PLUMEX II. The ordinate in Figure 2 has a linear scale for time-after-launch with altitude superimposed at 50-s increments.

The profile shows that the payload entered the very bottom of the F layer at $t \approx 145$ s ($Z \approx 340$ km), Point A in Figure 2. From there to an apogee near 581 km ($t = 390$ s) the in-situ probe measurements revealed a number of irregular structures that represented significant departures from an assumed zero-order (i.e., undisturbed) ionospheric profile. Local maxima in relative electron density are identified in Figure 2 by the letters B through F.

The upleg trajectory of the payload has been superimposed on the radar maps in Figure 1, with Regions A through F (and their associated times of observation) identified on the panel best matched for time coincidence. A step-wise comparison of in-situ observations (Figure 2) with the radar maps shows the following correlations:

- (1) Region A in Figures 1 and 2 corresponds to the lowest position of the bottomside F layer, a result which collocates the very bottom of the F-region radar returns with the very bottom of the F-region ledge. Before PLUMEX I and II (an

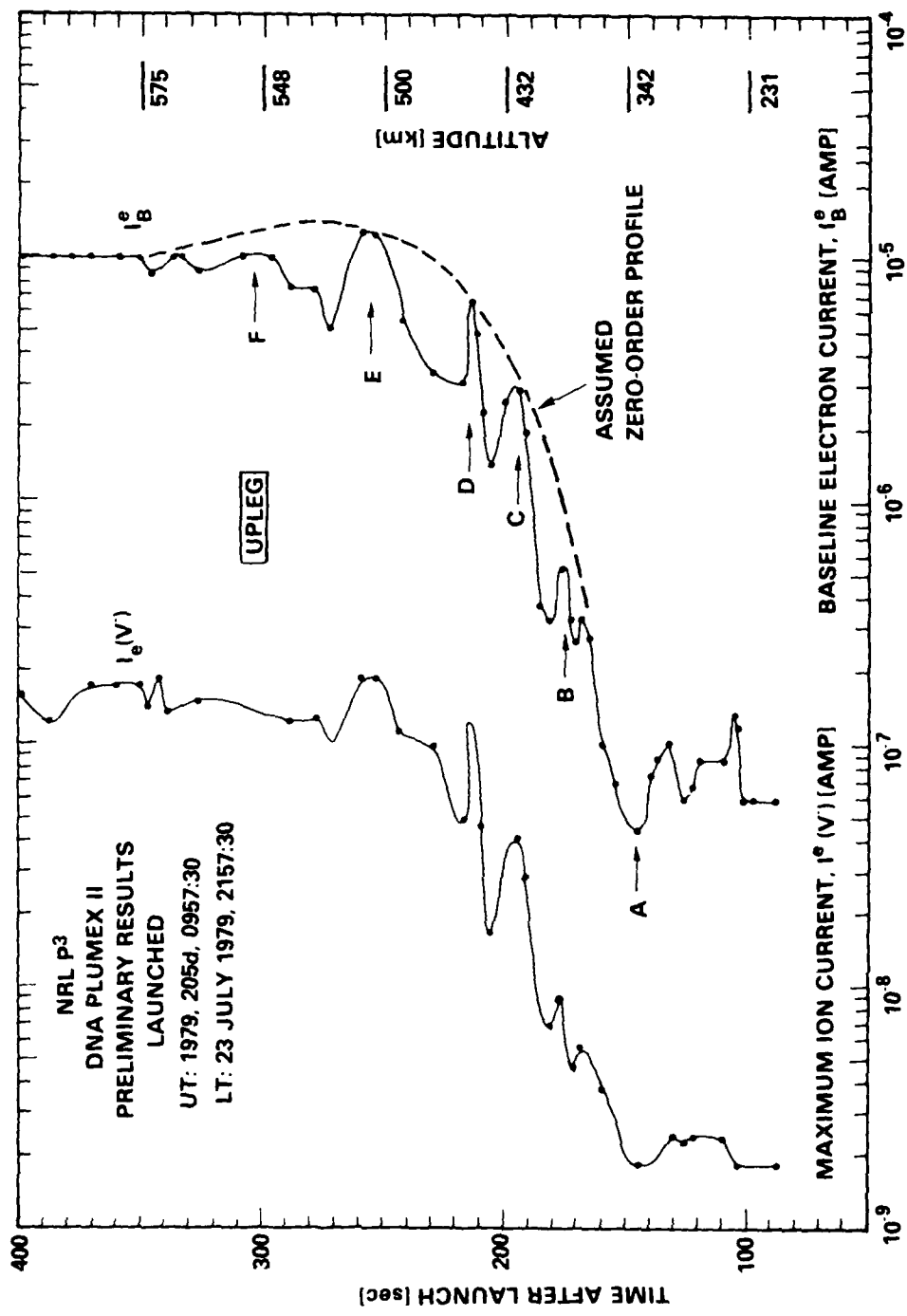


FIGURE 2 UPLEG MEASUREMENTS OF RELATIVE ELECTRON DENSITY

identical correlation was found in PLUMEX I), there were no data to determine their collocation or lack thereof.

- (2) The transition from Region A to B is marked by a 20-dB increase in radar backscatter energy, while Region B to C is marked by a relatively constant domain of backscatter energy.
- (3) Observations at Regions D, E, and F occur along the eastern wall of the plume, and encompass an altitude domain approximately identified with the F-layer peak.

Figure 3 presents the up- and down-leg profiles of relative electron density as measured by in-situ probe baseline electron saturation currents. (The integrity of the downleg profile was established by the same procedure used in Figure 2.) A comparison of the profiles shows the downleg results more representative of an undisturbed F region, a result consistent with the west-to-east movement of the rocket relative to the radar plume. This relative motion (approximately 160 m/s) carried the rocket payload into the undisturbed F region just to the east of the observed radar plume (i.e., into the white region on the eastern edge of the first panel in Figure 1). We note that the downleg profile is not significantly different from the assumed zero-order profile superimposed on Figure 2.

A comment is in order about the up- and down-leg altitudes that have been superimposed at 50-s intervals in Figure 3. In particular, attention is directed to the locations of the very bottom of the two F-region ledge observations, 340-km upleg and 305-km downleg. Because of the 9° dip in the local geomagnetic field, the downleg observation at 650 s corresponds to 338 km when projected along the magnetic-field line to the payload position at 145-s upleg, a result showing virtually no net movement of the ledge between the up and downleg observations. (We note that at the time of launch ionograms showed $h'F$ rising at an approximate rate of 18 m/s. This vertical drift then reversed near the middle of the flight, establishing consistency in rocket and ionogram results.)

With regard to ion composition, we note that the molecular ion NO^+ was the dominant positive-charge component at altitudes up to 340 km, the very bottom of the F-region ledge (A in Figure 2). At all altitudes

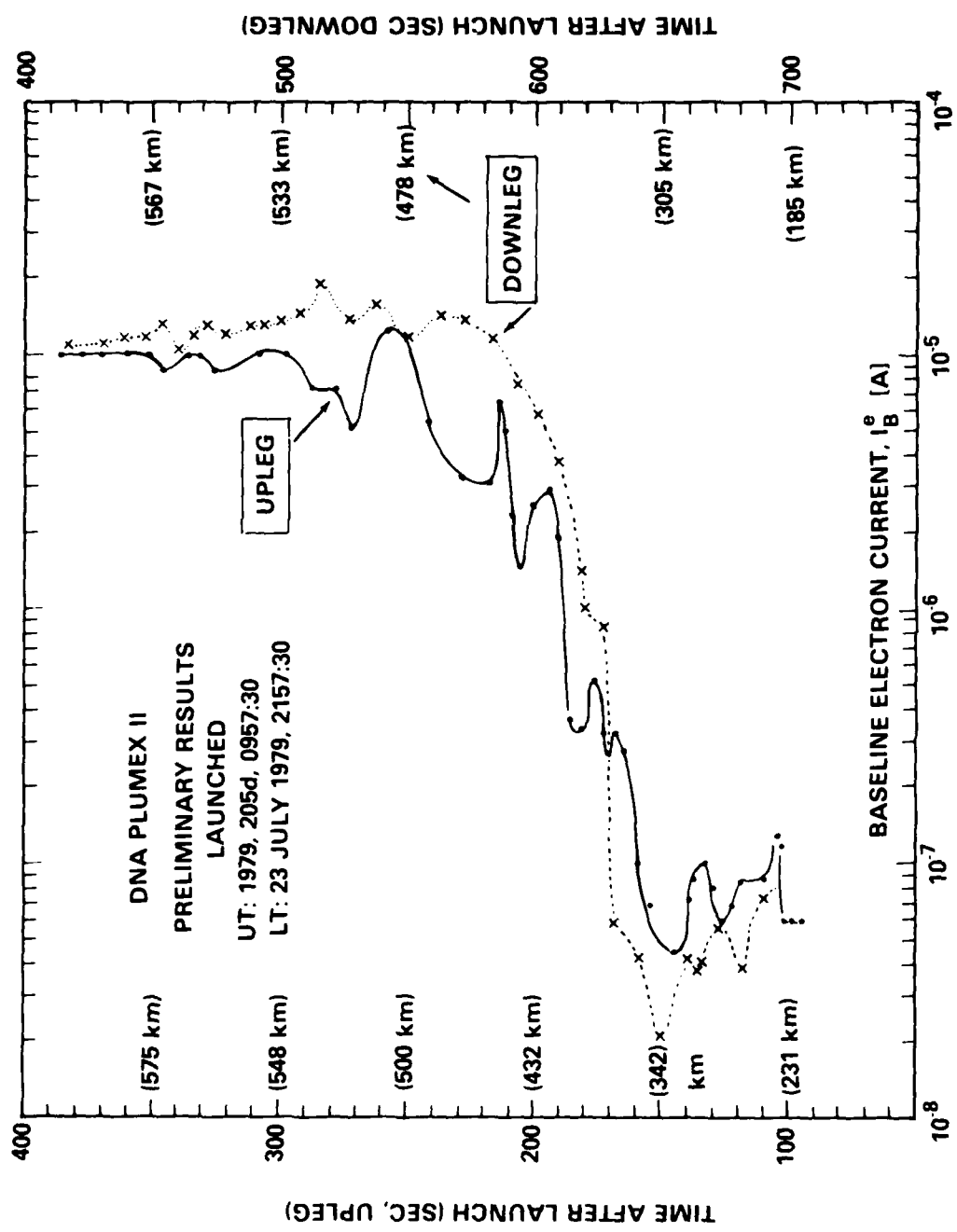


FIGURE 3 UPLEG AND DOWNLEG PROFILES OF RELATIVE ELECTRON DENSITY

above 340 km, O^+ was observed to be the dominant ion. (See Narcisi et al.⁴ for detailed ion profiles).

III CONCLUSIONS AND COMPARISONS WITH PLUMEX I

PLUMEX II was the second in a two-rocket operation that successfully performed space- and time-coincident measurements of equatorial spread F. Comparison of results and focus on differences in prevailing ionospheric conditions can be achieved by an analysis of the upleg electron density profiles observed in the two operations (PLUMEX I and II). These profiles are presented in Figure 4 with the specific features and conditions of the observation listed in Table 1.

- Spread-F conditions. PLUMEX I was conducted during the late phase in the development and decay of spread F. Specifically, the rocket was launched at 0031:30.25 (LT), a full 3 hrs after the occurrence of full range spread and only 30 min before its disappearance from ground-based ionograms. Major plume features were relatively stable with respect to vertical drifts, and the most intense regions of radar backscatter were beginning to decay.

The PLUMEX II conditions were substantially different, with the rocket having been launched into the midphase of well-developed spread F, i.e., a ground-based ionosonde showed full frequency and range spread while the ALTAIR radar maps of meter-size irregularity contours displayed backscatter plumes that penetrated to the topside F layer and continued rising with time. The payload was launched 1-1/2 hrs after the onset of full range spread and an estimated 2 hrs before decay.

- F-region profiles and in-situ irregularities. In the PLUMEX I operation, a number of major depletions ($\Delta N_e^o/N_e \lesssim 0.90$) were distributed throughout the F region with the F peak ($F_{2h\max}^o$) at 375 km and $N_e^{\max} = 1.3 \times 10^6 \text{ cm}^{-3} \pm 10\%$. The very bottom of the F layer (F bottom) was at 240 km and the macroscopic gradient scale length $L^{-1} = (N_e^o)^{-1} dN_e^o/dz$ of the bottomside ledge was 4 km. (The macroscopic L was calculated from a zero-order fit to the bottomside ledge between 10^{-2} and $10^{-1} N_e^{\max}$.) The electron energy distribution was characterized by $T_e = 1350 \text{ K} (\pm 250 \text{ K})$ with no obvious signatures of energy redistribution in and around the depletions. The most intense in-situ irregularities (i.e., smaller-scale structure imbedded in the larger-scale

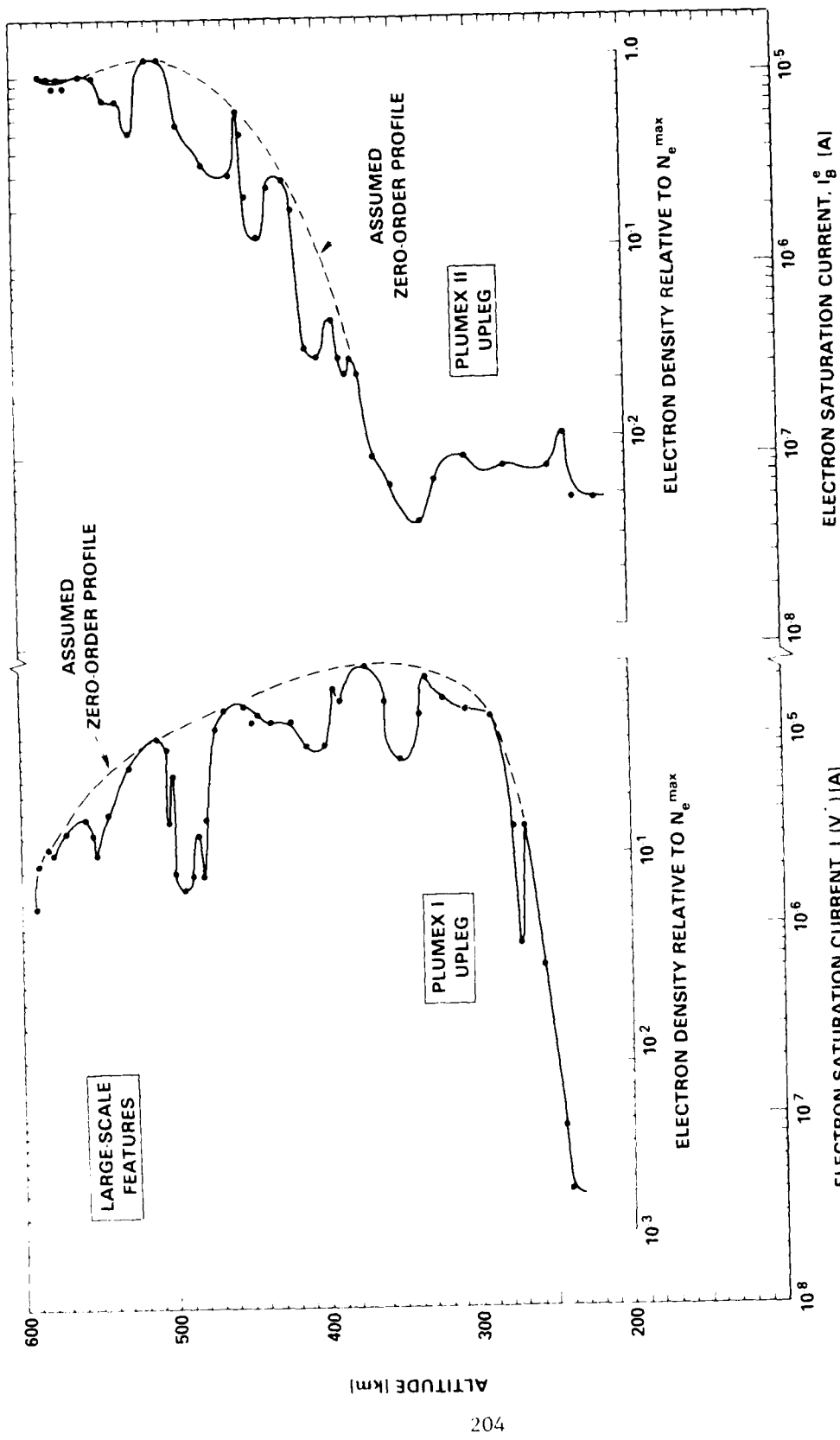


FIGURE 4 PLUMEX I AND II UPLEG ELECTRON-DENSITY PROFILES

Table 1
A COMPARISON OF CONDITIONS AND OBSERVATIONS
IN THE DNA/PLUMEX CAMPAIGN

Conditions and Observations	Rocket	
	PLUMEX I	PLUMEX II
Launch Time (LT)	17 July 1979; 0031:30.25	23 July 1979; 2157:30
Spread-F Conditions	Late time; topside radar plume in decay phase	Midphase of well-developed spread F; plumes penetrating to topside and rising with time
F_2^h max	375 km	510 km
F bottom	240 km	340 km
N_e^{\max}	$1.3 \times 10^6 \text{ cm}^{-3}$	$\approx 6 \times 10^5 \text{ cm}^{-3}$
L (Gradient scale length)	4.0 km	8.6 km
T_e	1350 K (± 250 K)	TBD
Dominant F_2 ion	O^+	O^+
Number of depletions $(\Delta N_e/N_e^0)_{\max}$	0.90	0.75
In-situ irregularity strength	± 80 percent fluctuations on bottomside gradient	Fluctuation levels appear much less intense than PLUMEX I; detailed analysis TBD
Ion signatures in holes	N^+/O^+ ratio	TBD
Plume penetration by rocket	Western wall and plume head	Eastern wall

depletions) occurred near 275 km on the bottomside ledge (± 80 percent fluctuations about an estimate N_e^0). The power spectral density in this region of intense irregularities on the bottomside was dominated by a $k^{-2.5}$ power law over the intermediate wavelength domain, $k = 2\pi/1000 \text{ m}^{-1}$ to $k = 2\pi/25 \text{ m}^{-1}$. This result supports the role of the collisional Rayleigh-Taylor instability in generating intermediate wavelength irregularities^{2,5} during the occurrence of equatorial spread F (see Szuszczewicz et al.¹ and Szuszczewicz and Holmes² for additional details.)

The PLUMEX II data have not yet received the same level of analysis already applied to the PLUMEX I data, a result largely caused by the complications of uncontrolled payload tumble and ACS jet firings that arose when a subsystem failed to separate the payload from the second-stage rocket motor. A number of important conclusions can, however, be drawn at this time. In the upleg density profile (Figures 2 and 4) of the PLUMEX II flight, a number of depletions ($\Delta N_e/N_e^0 \lesssim 0.75$) were distributed throughout the F region with the F peak ($F_{2h_{\max}}$) at 510 km and $N_e^{\max} \approx 6 \times 10^{13} \text{ cm}^{-3}$. In PLUMEX II the bottomside gradient was substantially softer than in PLUMEX I with F bottom at 340 km and $L = 8.6 \text{ km}$. A qualitative review of analog records (uncorrected for tumble and jet firings) indicates that smaller-scale in-situ irregularities were much less intense than corresponding observations in PLUMEX I. This result, if substantiated by a more complete analysis, will support current interpretations (e.g., Tsunoda⁶) of east-west plume asymmetry which suggest that the western wall of a plume (the PLUMEX I case) is more unstable than its eastern counterpart (the PLUMEX II case).

- Ion composition. PLUMEX I and II provided the very first vertical profiles of ion composition during the occurrence of equatorial spread F. The data pertain particularly to the subjects of plasma bubble formation, vertical transport, and ion signatures of source domains for topside F-region depletions. Previous in-situ measurements of ion composition within plasma depletions came only from satellite-borne mass spectrometers⁷⁻⁹ with results that suggested that topside holes formed at lower altitudes, where $[NO^+]$, $[O_2^+] > [O^+]$, and rise to greater heights maintaining (to the first order) their original ion composition. In the final analysis, the composition can be different because it depends on the bubble-formation process, the source domain, and the bubble age as manifested by time-dependent chemical processes.

In both PLUMEX operations O^+ was the dominant F-region ion down to the very bottom of the F ledge (F bottom). At altitudes below F bottom, molecular ions dominated with a scale height that approached infinity. (Detailed ion chemical results and analyses that go beyond discussions presented here are available in Szuszczewicz et al.¹ and Narcisi et al.⁴

The connection of the foregoing observation to topside bubbles and instabilities mechanisms is that the Rayleigh-Taylor and $\vec{E} \times \vec{B}$ gradient drift instabilities, which have been proposed for bubble formation, require a steep bottomside gradient. The PLUMEX results, however, show that the molecular ions are dominant only at altitudes below the bottomside F-region gradient, where scale heights are very large and inhibit the instability process. If the bubble does indeed form on the F-region ledge, and if it transports only local ions to higher altitudes, then molecular ions will never dominate topside depletions. This apparent dichotomy has a number of explanations:

- (a) Relatively small depletions (i.e., $\Delta N_e/N_e^0 \lesssim 0.9$) originating on the F ledge with initially small horizontal extent can transport the local ion composition to higher altitudes by the Rayleigh-Taylor process; but molecular ions will not be the dominant positive species. Instead, the $[N^+]/[O^+]$ ratio will indicate the original source domain as suggested by McClure et al.⁷ and Szuszczewicz et al.,¹ and discussed in detail by Narcisi et al.⁴
- (b) For molecular ions to be dominant in a topside F-region depletion, it appears that one of two mechanisms must apply: (i) An initially small depletion (i.e., $\Delta N_e/N_e^0 \lesssim 0.9$) of large horizontal scale size can result in much higher depletion levels (e.g., References 7 through 9) by fringing fields that draw up the lower densities and molecular ions that populate altitude regimes lower than the sight of the initial perturbation. This mechanism has been studied by Zalesak and Ossakow¹⁰ and appears in substantial agreement with observations, (ii) an alternate mechanism for molecular ion dominance in topside depletions has been proposed by Chin and Straus.¹¹ They suggest that plasma bubbles in the nighttime equatorial ionosphere originate as wind-driven waves at one of the highly variable density gradients below 200 km, rather than at the bottomside F-region ledge. Once the bubble is formed, with the low densities and molecular ion dominance characterized by the lower altitude, it can propagate into the bottomside F region and provide the initial perturbation required for the onset of the Rayleigh-Taylor mode.¹²⁻¹⁴

Current analyses of PLUMEX ion composition results support conclusion a as the operating principle on the nights of in-situ investigations. This does not negate b(i) and b(ii) as candidates for other conditions; it leaves the question open for further experimental tests.

ACKNOWLEDGMENTS

Support for the plasma probe analysis was provided by the Defense Nuclear Agency (DNA) under Subtask Code 125AAXHX640, Communications Effects Experiments. The ALTAIR radar analysis was also supported by DNA under contract DNA 001-C-0153. Support for the ion composition measurements was supplied mostly by the Air Force Office of Scientific Research under Task 2310-G3 and partially by DNA under Subtask 125AAXHX640, Work Unit 06. We also wish to acknowledge the dedicated technical support of E. Trzcinski, G. Federico, L. Wlodyka, L. Kegley, D. Walker and C. S. Lin, who, independently and as a team, contributed significantly to the success of the rocket-borne plasma probe and mass spectrometer experiments. Development of the plasma probe technique was provided by the Office of Naval Research under Work Unit A02-11.11 (71-0949-0-0), Ionospheric and Stratospheric Interactions, Task Area RR 043-02-044.

REFERENCES

1. E. P. Szuszczewicz, R. T. Tsunoda, R. Narcisi, and J. C. Holmes, "PLUMEX I: Coincident Radar and Rocket Observations of Equatorial Spread F," Proceed. of the Summer Equatorial Experiment Data Review Meeting, 18 March 1980 (1980); also published in Geophys Res. Lett., Vol. 7, No. 7, pp. 537-540 (July 1980).
2. E. P. Szuszczewicz and J. C. Holmes, "The Pulsed-Plasma-Probe Experiment: In-Situ Measurements of Electron Density, Temperature and Density Fluctuation Power Spectra," Proceed. of the Summer Equatorial Experiment Data Review Meeting, 18 March 1980 (1980); also published in NRL Memorandum, Report 4289 (July 1980).
3. R. T. Tsunoda, M. J. Baron, J. Owen, and D. M. Towle, "ALTAIR: An Incoherent Scatter Radar for Equatorial Spread-F Studies," Radio Sci., Vol. 14, No. 6, pp. 1111-1120 (November-December 1979).
4. R. Narcisi, E. Trzcinski, G. Federico, L. Wlodyka, and P. Bench, "Structure and Composition Measurements in Equatorial Ionospheric Bubbles," Proceed. of the Summer Equatorial Experiment Data Review Meeting, 18 March 1980 (1980).

5. M. J. Keskinen, S. L. Ossakow, and P. K. Chaturvedi, "Preliminary Report on Numerical Simulations of Intermediate Wavelength Collisional Rayleigh-Taylor Instability in Equatorial Spread F," J. Geophys. Res., Vol. 85, No. A4, pp. 1775-1778 (April 1980).
6. R. T. Tsunoda, "Time Evolution and Dynamics of Equatorial Backscatter Plumes--Growth Phase," Report, SRI International, Menlo Park, CA 94025, (in press, 1980).
7. J. P. McClure, W. B. Hanson, and J. H. Hoffman, "Plasma Bubbles and Irregularities in the Equatorial Ionosphere," J. Geophys. Res., Vol. 82, No. 19, pp. 2650-2656 (July 1977).
8. H. C. Brinton, H. G. Mayr, and G. P. Newton, "Ion Composition in the Nighttime Equatorial F Region: Implications for Chemistry and Dynamics," (abstract), EOS Trans. AGU, Vol. 56, No. 12, p. 1038 (December 1975).
9. E. P. Szuszczewicz, "Ionospheric Holes and Equatorial Spread F: Chemistry and Transport," J. Geophys. Res., Vol. 83, No. A6, pp. 2665-2670 (June 1978).
10. S. T. Zalesak and S. L. Ossakow, "Nonlinear Equatorial Spread F: Spatially Large Bubbles Resulting from Large Horizontal Scale Initial Perturbations," NRL Memorandum, Rpt. 4154 (February 6, 1980); J. Geophys. Res. (1980).
11. Y. T. Chiu and J. M. Straus, "Rayleigh-Taylor and Wind-Driven Instabilities of the Nighttime Equatorial Ionosphere," J. Geophys. Res., Vol. 83, No. A7, pp. 3283-3290 (July 1979).
12. A. J. Scannapieco and S. L. Ossakow, "Nonlinear Equatorial Spread F," Geophys. Res. Lett., Vol. 3, No. 9, pp. 451-454 (August 1976).
13. E. Ott, "Theory of Rayleigh-Taylor Bubbles in the Equatorial Ionosphere," J. Geophys. Res., Vol. 83, No. A5, pp. 2066-2070 (May 1978).
14. P. K. Chaturvedi and S. L. Ossakow, "Nonlinear Theory of the Collisional Rayleigh-Taylor Instability in Equatorial Spread F," Geophys. Res. Lett., Vol. 4, No. 12, pp. 558-560 (December 1977).

BACKSCATTER MEASUREMENTS OF 11-cm EQUATORIAL SPREAD-F IRREGULARITIES

Roland T. Tsunoda
Radio Physics Laboratory
SRI International
Menlo Park, CA 94025

ABSTRACT

An important objective of the Defense Nuclear Agency is to understand the physical processes that control the dissipation of turbulent structure in plasmas. Such turbulent structures occur as a consequence of high-altitude nuclear events as well as in the natural, disturbed equatorial ionosphere. Analysis and understanding of those processes in the nighttime equatorial nuclear environment can lead to an intelligent extrapolation of equatorial findings to the nuclear case. In the equatorial F-region ionosphere, the turbulent cascade process had been found previously to extend from irregularity spatial wavelengths longer than tens of kilometers down to wavelengths as short as 36 cm. To investigate the small-scale regime of wavelengths less than 36 cm, a radar backscatter experiment was conducted in the Kwajalein Atoll, Marshall Islands, using a frequency that corresponds to an irregularity wavelength of 11 cm.

The first observations of radar backscatter from 11-cm equatorial field-aligned irregularities (FAI) are described. These measurements extend the spatial wavelength regime of F-region FAI to lengths that approach both the electron gyro-radius and the Debye length. Agreement of these results with the theory of high-frequency drift waves suggests that these observations may be unique to the equatorial ionosphere. That is, the requirement for low-electron densities that the theory calls for may preclude the existence of 11-cm FAI elsewhere in the F-region ionosphere, except in equatorial plasma bubbles.

I INTRODUCTION

During July 1979, a coordinated field program was sponsored by the Defense Nuclear Agency to investigate the phenomena of equatorial spread F.

The experiment included the use of two high-power backscatter radars, ALTAIR and TRADEX, located in the Kwajalein Atoll, Marshall Islands. ALTAIR operates at 155.5 MHz and 415 MHz, and has been used previously to characterize the 1-m and 36-cm field-aligned irregularities (FAI) that produce the backscatter at those frequencies.^{1,2,3*} TRADEX was employed for the first time in this kind of experiment to extend radar observations of equatorial FAI to 1320 MHz—the highest frequency ever used. Backscatter at this frequency corresponds to an FAI wavelength of 11 cm.

A primary objective of extending radar observations to higher frequencies is to seek the "inner scale" of equatorial plasma turbulence. That is, TRADEX measurements were directed toward answering the question, "what is the smallest wavelength at which equatorial FAI can exist?"

The background of radar backscatter observations of equatorial FAI and the rationale for interest in characterizing the small-scale end of the FAI power spectrum is given in Section II. The experiment utilizing both ALTAIR and TRADEX radars is described in Section III, and the preliminary results are presented in Section IV. In Section V, the results are discussed in relation to an existing plasma instability model that has been proposed as the source mechanism for these small-scale FAI that exist, with spatial wavelengths, below the ion gyroradius.⁴

II BACKGROUND

Radar backscatter has been used to study equatorial spread-F irregularities for more than four decades first in the form of vertical-incidence ionosondes⁵ and high-frequency (HF) backscatter radars,^{6,7} and most recently in the form of high-power backscatter radars that operate in the very-high-frequency (VHF) and ultra-high-frequency (UHF) bands.^{8,9,1,2} A characteristic trend apparent in these measurements is the use of increasingly higher transmitter power at higher radar frequencies. The

*References are listed at the end of the paper.

need for increased radar sensitivity underscores the waning strength of these FAI as their spatial wavelength decreases.

The implied decrease in FAI strength with decreasing spatial wavelengths is not surprising. Measurements of the power spectral density associated with larger-scale ($\gtrsim 1$ km) equatorial irregularities have already indicated a power-law dependence on spatial wavelength.¹⁰ It is by no means apparent, however, that the rate of decrease (characterized by a power-law spectral index) in FAI strength should be constant over the entire range of spatial wavelengths. In fact, it is perhaps natural to expect significant decreases in FAI strength when the FAI spatial wavelength becomes comparable to or less than the characteristic plasma scale lengths. Drastic decreases (or "cutoffs") in FAI strength might be envisioned whether we think in terms of an "inner scale" to a spectrum of turbulence, or whether we consider source mechanisms for FAI generation and growth.

For example, intuitively, it is apparent that gradients in plasma density do not produce rapid growth of irregularities when the wavelength is much smaller than the gradient scale length. It is also apparent that gradients or irregularities in plasma density are difficult to maintain if their scale sizes are comparable to (or less than) the ion or electron gyroradius. This happens because we can no longer treat particle motion by its "guiding center." And finally, any organized motion involving electrons and ions is not possible at spatial distances less than the Debye length. From these heuristic arguments, we might expect possible cutoffs in FAI strength at spatial wavelengths comparable to (1) the ion gyroradius, (2) the electron gyroradius, or (3) the Debye length.

The largest of the three characteristic lengths in ionospheric plasma is the ion gyroradius. The nighttime equatorial F-layer ionosphere typically consists of O^+ ions at a temperature of 1000 K. For this case, the ion gyroradius is 5.6 m. Irregularities with this spatial wavelength produce radar backscatter at a frequency of 26.8 MHz. On this basis, radar backscatter at frequencies above 26.8 MHz (which

includes all of the VHF and UHF bands) must occur from FAI with spatial wavelengths less than the ion gyroradius.

Woodman and Basu¹¹ considered the possible existence of a cutoff in FAI strength near the ion gyroradius. They compared in-situ measurements of large-scale FAI to 50-MHz backscatter strength and found that 3-m FAI was much weaker in strength than expected from extrapolation of the large-scale FAI strength using the observed power-law dependence of the in-situ irregularity spectrum. They suggested that an explanation for this discrepancy might be a cutoff in FAI strength near the ion gyro-radius. Since then, however, Tsunoda et al.¹ and Towle² have pointed out that the Woodman and Basu model,¹¹ which contains a Gaussian-shaped cutoff near the ion gyroradius precludes the existence of 1-m and 36-cm FAI. Observations of 1-m and 36-cm FAI by Tsunoda et al.¹ and Towle² refute the accuracy of the Gaussian cutoff model. These observations do not, however, shed further light on the nature of FAI strength dependence on spatial wavelength near to or less than the ion gyroradius.

With the demonstrated existence of radar backscatter from FAI as short as 36 cm, Huba et al.⁴ proposed that high-frequency drift waves driven by the lower-hybrid-drift instability could account for these small-scale FAI. In their model, Huba et al.⁴ assume that $k^2 r_i^2 \gg 1$ and find that maximum linear growth rates occur near $kr_e \sim 1$, where k is the wave number and r_i (r_e) is the ion (electron) gyroradius. For an electron temperature of 1000 K, r_e in the equatorial ionosphere is 3.3 cm. Consequently, their model predicts maximum growth rate for FAI with a spatial wavelength of 20.7 cm, and probably strong backscatter at the corresponding radar frequency of 725 MHz.

The condition $k^2 r_i^2 \gg 1$ implies damping of this instability at the longer wavelengths that approach the ion gyroradius. Huba and Ossakow¹² and Goldman and Sperling¹³ have shown that electron viscosity (from electron-electron collisions) can control the growth of FAI at the short-wavelength end of the spectrum. A detailed analysis is required to determine whether the cutoff occurs at wavelengths that approach the electron gyroradius.

Even as we approach the electron gyroradius, we need to consider the effects produced by proximity to the Debye length. This is particularly true in the case of the lower-hybrid-drift instability because electron viscosity is small when the plasma density is low. That is, low plasma densities favor growth of high-frequency drift waves.¹³ Experimentally, Tsunoda^{14,15} and Szuszczewicz et al.¹⁶ have shown that small-scale FAI are spatially coincident with large-scale (tens of kilometers) plasma depletions, or "bubbles"^{17,18} that exist in the equatorial ionosphere. The plasma density within these bubbles has been found as low as 10^3 el/cm^3 . For an electron temperature of 1000 K, the Debye length would be 6.9 cm. Therefore, dissipative effects on FAI growth may be compounded at wavelengths that approach the Debye length.

To the author's knowledge, a source mechanism that produces FAI with spatial wavelengths in the range between the electron gyroradius and the Debye length has never been proposed.

III THE EXPERIMENT

The experiment to detect the existence of 11-cm FAI was conducted on Roi-Namur Island in the Kwajalein Atoll, Marshall Islands. Two high-power radars were used: ALTAIR (ARPA Long-Range Tracking and Instrumentation Radar) and the TRADEX (Target Resolution and Discrimination Experiments) radar. Both are support radars for the Kwajalein Missile Range under the technical supervision of MIT Lincoln Laboratory. ALTAIR is a fully steerable backscatter radar that operates at two frequencies, 155.5 MHz (VHF) and 415 MHz (UHF), simultaneously. ALTAIR has been the source of all observations of equatorial FAI with spatial wavelengths of 1 m and 36 cm. TRADEX is also a fully steerable backscatter radar. It operates at 1320 MHz (L band) and is located within a hundred meters of ALTAIR. The pertinent ALTAIR and TRADEX radar parameters are listed in Table 1.

Tsunoda et al.¹ and Towle² have shown that ALTAIR is sensitive enough to perform incoherent-scatter (IS) measurements at both VHF and

Table 1
RADAR SYSTEMS CHARACTERISTICS

Parameters	Value	
	ALTAIR	TRADEX
Frequency, MHz	415	1320
Peak power, MW	20	4
Pulse width, μ s	40	50/1.7 μ s (chirp)
Antenna:		
Diameter, m (ft)	45.7 (150)	25.6 (84)
Beamwidth, deg	1.1	0.65
Gain, dB	42.4	48.5
Effective Aperture, m^2	722	283
Temperature, K	785	622
Polarization	LC/RC	LC/RC

UHF. Consequently, ALTAIR is easily capable of detecting backscatter from FAI. On the other hand, TRADEX with its extremely short transmitted waveform is less sensitive than ALTAIR, and is not capable (as configured) of IS measurements. In fact, because of the very short pulse width, the TRADEX sensitivity is considered marginal for detection of 11-cm FAI. For example, if we assume a wavelength dependence of FAI of $\lambda^{2.3}$ (inferred from past ALTAIR data), we expect detectable backscatter with TRADEX only under the most disturbed spread-F conditions.

Because of the marginal TRADEX sensitivity, the experiment was conducted as follows. ALTAIR was operated in a continuous (magnetic) east-west scan, maintaining the radar beam perpendicular to the geomagnetic field lines at F-region altitudes. TRADEX was kept in a standby mode during the ALTAIR scans. TRADEX was turned on and operated only when strong backscatter was observed with ALTAIR at UHF.

The procedure for directing the TRADEX antenna beam to the region of strong UHF backscatter consisted of storing the ALTAIR beam position

at which the strong backscatter was observed. That position was selected in real time during an ALTAIR scan by pushing a "zap" button. TRADEX was then immediately directed to the zap coordinates and operated in a limited elevation scan. The elevation scan consisted of seven discrete beam positions with the center position at the zap point. The beam positions were spaced in elevation at intervals of half a beamwidth ($\sim 0.3^\circ$). Data were recorded at each beam position for 1 min at a PRF of 125 s^{-1} , thereby completing a scan in 7 min.

TRADEX data were taken at 150-m range intervals to maintain the range resolution (and backscatter detectability) of the $1.7\text{-}\mu\text{s}$ chirp waveform. To reduce the high data rates, 1024 range samples were recorded beginning at a start range that was specified in real time to match the altitude interval of the strong UHF backscatter. In this burst sampling mode, TRADEX data taken over any selected 153-km range interval could be recorded.

This dual-radar experiment was conducted as a part of a larger coordinated rocket program (designed to investigate equatorial spread-F phenomena), sponsored by the Defense Nuclear Agency. Data were collected over a two-week period in mid-July 1979.

IV RESULTS

For this short report, a data set obtained on 17 July 1979 between 1102 UT and 1110 UT (2212 to 2220 local solar time) was selected. During this period, ALTAIR backscatter approached 50 dB above IS levels at VHF and 40 dB above IS levels at UHF. The backscatter strengths are some of the strongest observed with ALTAIR. (In comparison, the Jicamarca 50-MHz radar has observed backscatter strengths up to about 50 dB above IS levels.¹¹

The backscatter distribution observed with ALTAIR at UHF is shown in Figure 1. The backscatter strength is represented by contours of constant signal strength (after range-squared correction). The contours,

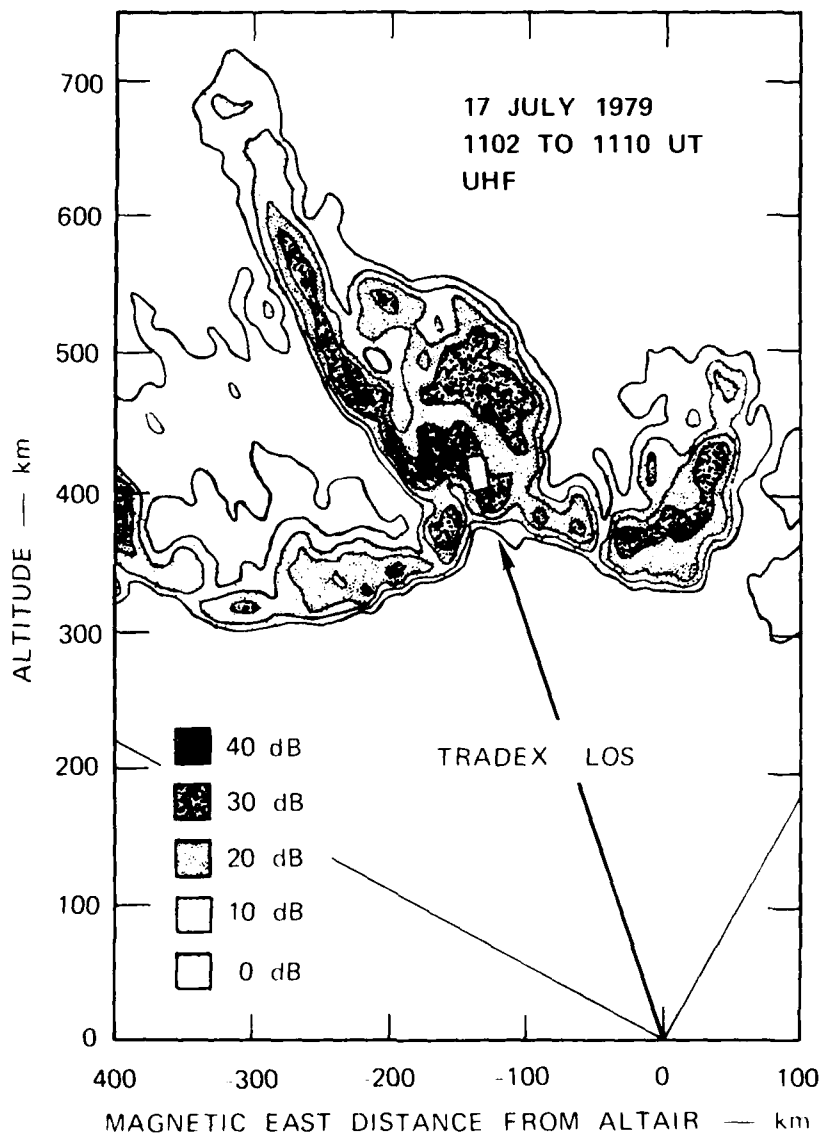


FIGURE 1 SPATIAL DISTRIBUTION OF RADAR BACKSCATTER FROM EQUATORIAL FAI OBTAINED AT 415 MHz WITH ALTAIR. The TRADEX radar line-of-sight (LOS) vector points to region of backscatter at 1320 MHz.

shown in decade increments of backscatter strength, are calibrated with reference to IS signal strength. The zero-dB contour is equivalent to IS from an electron density of 10^6 el/cm^3 . In this map, the altitude-modulated bottomside backscatter is centered around the 350-km altitude and backscatter "plumes" extend upward from the bottomside into the topside of the F layer. (Tsunoda² presents the basis for these inferences.) The intense, altitude-extended plume just west of ALTAIR contains the region of interest.

The TRADEX line of sight (LOS), also shown in Figure 1, passes through the intense backscatter plume mapped by ALTAIR. The white bar located just beyond the arrow head on the LOS vector shows the range extent from which L-band backscatter was observed and coincides with a region of strong UHF backscatter ($\gtrsim 30 \text{ dB}$).

Figure 2 shows the TRADEX measurements made along the LOS in Figure 1. In the upper panel, we have displayed the backscatter strength versus range record obtained by time averaging the TRADEX data for one minute. The range resolution is 150 m with this kind of data processing. The lower panel contains the same backscatter profile after range-averaging to simulate the ALTAIR range resolution of approximately 5 km. Backscatter extends in range from 437 km to 457 km with a peak in backscatter strength located at 447 km. Peak backscatter strength is about -46 dBsm. The noise level is only a fraction of a decibel below the peak in spread-F backscatter.

Despite the small signal-to-noise ratio, it is clear from Figure 2 that backscatter from 11-cm FAI was indeed detected with TRADEX. There is no remaining doubt when we note the spatial collocation (Figure 1) of the L-band backscatter with one of the strongest backscatter regions found in the plume at both UHF and VHF.

To compare the TRADEX measurement with those by ALTAIR, we must convert the -46 dBsm discrete target cross section into volume reflectivity. If we assume that the radar scattering volume is filled with FAI, we obtain a value of about $5 \times 10^{-15} \text{ m}^2/\text{m}^3$, which is approximately 32 dB above IS levels (for an electron density of 10^6 el/cm^3). The extent to

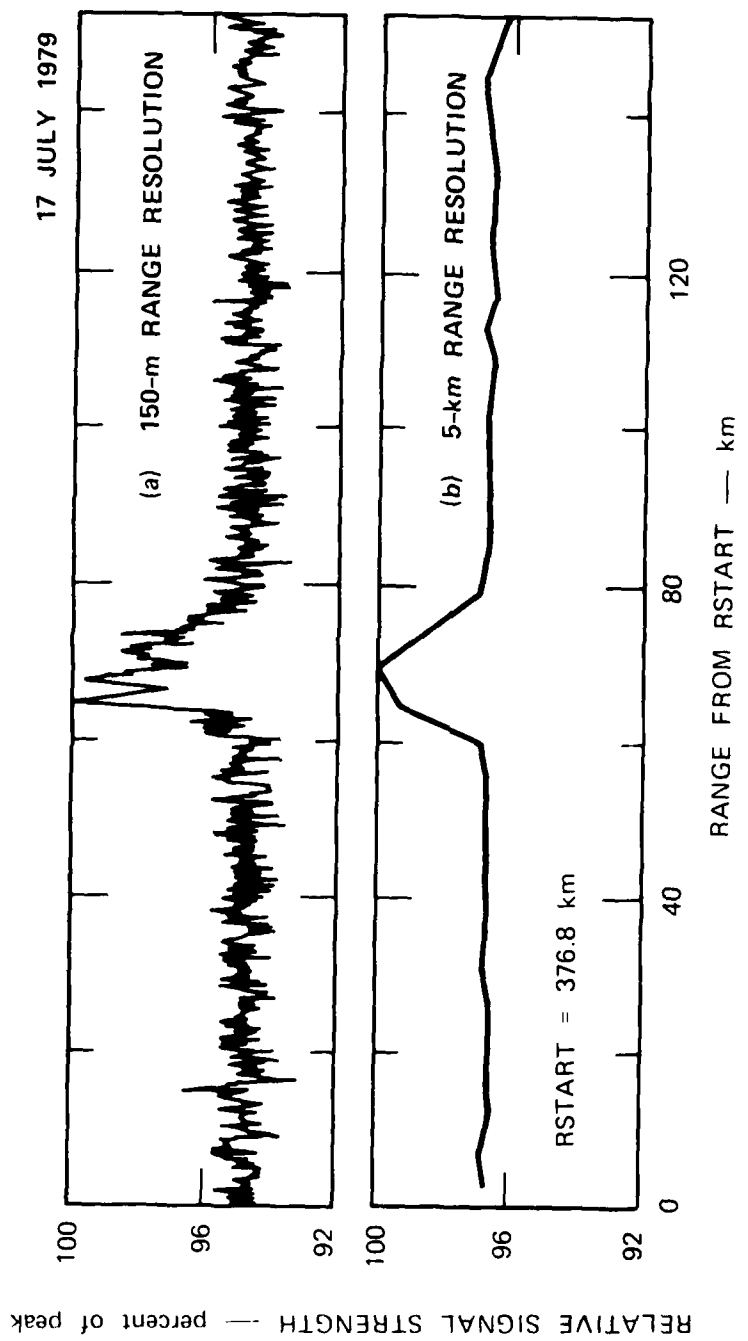


FIGURE 2 RANGE-POWER PROFILE OF L-BAND BACKSCATTER OBTAINED FROM 11-cm FAJ

which the scattering volume is actually filled is dependent on the magnetic aspect sensitivity of equatorial FAI. The filled volume approximation is obviously less valid with increasing radar beamwidth. Using the same assumption (filled scattering volume) for the VHF and UHF data, we can estimate a wavelength dependence of FAI strength. We find that the wavelength dependence between L band and UHF is $\lambda^{1.3}$ and that between UHF and VHF is $\lambda^{2.3}$.

The implication that the power-law spectral index decreases at the shorter spatial wavelengths is important if shown to be real. Rough estimates to correct for magnetic aspect sensitivity and unscaled antenna beamwidths indicate that although the spectral index does increase, there remains a decrease in the spectral index at shorter FAI wavelengths. Results of a more complete analysis of the wavelength dependence of small-scale FAI will be presented in a future paper.

V DISCUSSION AND CONCLUSIONS

We have described the first observations of radar backscatter from 11-cm FAI. The preliminary results on 36-cm and 11-cm FAI appear to be consistent with the theoretical model for high-frequency drift waves.⁴ Backscatter has now been observed on either side of the frequency at which maximum backscatter might be expected on the basis of the condition, $kr_e \sim 1$. The relatively flat wavelength dependence implied by the results ($\lambda^{1.3}$)--if proven accurate--supports the idea that the driving point is indeed $kr_e \sim 1$.

If these small-scale FAI are indeed produced by high-frequency drift waves, the occurrence of 11-cm FAI might very well be unique to the equatorial ionosphere. A more generalized analysis of the high-frequency drift wave theory^{1, 2, 12} has shown that viscous damping of the electrons (via electron-electron collisions) will damp out the instability for cases in which the electron density is much greater than 10^4 el/cm^3 (for a moderate electron-density gradient). On this basis, 11-cm FAI will occur primarily within the equatorial plasma bubbles where the electron

densities are low. Whether FAI with much smaller spatial wavelengths can exist even in the equatorial case depends on the existence of steeper electron density gradients and the Debye length effects.

The requirement of low electron density will preclude the presence of small-scale FAI (via high-frequency drift waves) in barium ion clouds. Although the striations in barium clouds are initiated by the gradient-drift instability,¹⁹ which is a direct analog of the Rayleigh-Taylor instability that initiates equatorial spread F,²⁰ both the striations and the background ionosphere (into which the barium cloud is injected) have higher electron densities than required to trigger high-frequency drift waves. This conclusion is consistent with available experimental evidence. Bates²¹ operated step-frequency sounders in Alaska as part of the Secede III barium release program. Using oblique-incidence backscatter sounders that operated between 4 MHz and 64 MHz, backscatter was found occurring up to a frequency near 45 MHz, with a maximum in backscatter strength around 30 MHz. (Of course, we do not know what a more sensitive radar would have seen.)

Aside from the consideration of the source mechanism, the observation of 11-cm FAI is also noteworthy because it represents detection of FAI with a spatial wavelength that is closer to the electron gyroradius and, possibly, also closer to the Debye length than any other measurement of ionospheric FAI. As discussed in Section II, 11-cm FAI in the equatorial ionosphere is within a factor of 3 of the electron gyroradius and perhaps as close as a factor of 1.5 of the Debye length.

The only observations of ionospheric FAI that approaches the measurements reported here were those made at 3000 MHz from auroral electrojet irregularities.²² Although the radar frequency for the auroral backscatter measurements is a factor of 2.3 higher than that used in this experiment, the ratios of FAI wavelength to electron gyroradius and of FAI wavelength to Debye length are larger than found in this experiment. The reason is that auroral backscatter occurs in the E layer in which the electron temperature is lower than in the F layer, and in polar regions where the magnetic flux density is higher than in the equatorial region. Typical E-region electron densities are also higher than those in plasma bubbles.

In the auroral case, the electron gyroradius for an electron temperature of 300 K is 1 cm. The FAI wavelength (5 cm) is, therefore, a factor of 5 greater than the electron gyroradius. There are, of course, conditions of intense particle precipitation during which the electron temperature can reach 1200 K. In this case, the electron gyroradius is 2 cm and the factor drops to 2.5, which is slightly smaller than for the equatorial results. However, Tsunoda and Presneill²³ have shown that the conditions for FAI growth via the two-stream instability (source mechanism for E-region electrojet FAI) is not favorable when the E-region conductivity is high (because of particle precipitation) or when the electron temperature is high. High conductivity tends to short out the ionospheric electric field that drives the two-stream instability. High temperatures also inhibit two-stream growth because they raise the ion-acoustic speed, which controls the instability threshold. Therefore, if we allow high electron temperatures, we introduce difficulties in FAI generation via the two-stream instability.

In the auroral case, the Debye length is also smaller because of lower electron temperatures and higher electron densities. For example, for an electron temperature of 300 K and an electron density of 10^5 el/cm^3 , the Debye length is 0.38 cm. For an electron density of 10^6 el/cm^3 , the Debye length decreases to 0.12 cm. The ratio of FAI wavelength to Debye length is, therefore, between 13 and 42 for the auroral case. For the equatorial case, the Debye length can range between 3.3 cm and 2.2 cm for electron densities between 10^3 el/cm^3 and 10^4 el/cm^3 . The ratio of FAI wavelength to Debye length, therefore, ranges between 1.5 to 5.

ACKNOWLEDGMENTS

The author would like to thank the TRADEX and ALTAIR staffs for their support during this experiment. The author also thanks Dr. G. Ahlgren (MIT/Lincoln Laboratory) for providing in-the-field data analysis support including the TRADEX results presented in this report.

REFERENCES

1. Tsunoda, R. T., M. J. Baron, J. Owen, and D. M. Towle, "ALTAIR: An Incoherent Scatter Radar for Equatorial Spread-F Studies," Radio Sci., Vol. 14, No. 6, pp. 1111-1120 (November-December 1979).
2. Towle, D. M., "VHF and UHF Radar Observations of Equatorial F-Region Ionospheric Irregularities and Background Densities," Radio Sci., 15, No. 1, pp. 71-86 (January-February 1980).
3. Tsunoda, R. T., "Time Evolution and Dynamics of Equatorial Backscatter Plumes--I," Growth phase, submitted to J. Geophys. Res., 1980c.
4. Huba, J. D., P. K. Chaturvedi, S. L. Ossakow, and D. M. Towle, "High-Frequency Drift Waves with Wavelengths Below the Ion Gyroradius in Equatorial Spread F," Geophys. Res. Lett., 5, No. 8, pp. 895-697 (August 1978).
5. Booker, H. G. and W. H. Wells, "Scattering of Radio Waves by the F Region of the Ionosphere," Terr. Magn. Atmos. Electr., Vol. 43, p. 249, 1938.
6. Clemesha, B. R., "An Investigation of the Irregularities in the F Region Associated with Equatorial-Type Spread F," J. Atmos. Terr. Phys., Vol. 26, No. 1, pp. 91-112 (January 1964).
7. Kelleher, R. F. and N. J. Skinner, "Studies of F-Region Irregularities at Nairobi, II--By Direct Backscatter at 27.8 MHz," Ann. Geophys., Vol. 27, No. 2, pp. 195-200 (1971).
8. Farley, D. T., B. B. Balsley, R. F. Woodman, and J. P. McClure, "Equatorial Spread F: Implications of VHF Radar Observations," J. Geophys. Res., Vol. 75, No. 34, pp. 7199-7206 (December 1970).
9. Woodman, R. F. and C. La Hoz, "Radar Observations of F-Region Equatorial Irregularities," J. Geophys. Res., Vol. 81, No. 31, pp. 5447-5466 (November 1976).
10. Basu, S., S. Basu, and B. K. Khan, "Model of Equatorial Scintillations from In-Situ Measurements," Radio Sci., Vol. 11, No. 10, pp. 821-832 (October 1976).
11. Woodman, R. F. and S. Basu, "Comparison Between In-Situ Spectral Measurements of F-Region Irregularities and Backscatter Observations at 3-m Wavelength," Geophys. Res. Lett., Vol. 5, No. 10, pp. 869-873 (October 1978).

12. Huba, J. D. and S. L. Ossakow, "Destruction of Cyclotron Resonances in Weakly Collisional, Inhomogeneous Plasmas," Phys. Fluids, Vol. 22, No. 7, pp. 1349-1354 (July 1979).
13. Goldman, S. R. and J. L. Sperling, "Aspects of Late-Time Striation Behavior and Satellite Communication Effects," Final Report, DNA 4923F, Contract DNA001-76-C-0186-P00005, JAYCOR, Del Mar, CA (1979).
14. Tsunoda, R. T., "On the Spatial Relationship of 1-m Equatorial Spread-F Irregularities and Plasma Bubbles," J. Geophys. Res., Vol. 85, No. A1, pp. 185-190 (January 1980).
15. Tsunoda, R. T., "Magnetic-Field-Aligned Characteristics of Plasma Bubbles in the Nighttime Equatorial Ionosphere," accepted for publication, J. Atmos. Terr. Phys. (1980b).
16. Szuszczewicz, E. P., R. T. Tsunoda, R. Narcisi, and J. C. Holmes, "Coincident Radar and Rocket Observations of Equatorial Spread F," submitted to Geophys. Res. Lett. (1980).
17. Hanson, W. B. and S. Sanatani, "Large Ni Gradients below the Equatorial F Peak," J. Geophys. Res., Vol. 78, No. 7, pp. 1167-1173 (March 1973).
18. McClure, J. P., W. B. Hanson, and J. H. Hoffman, "Plasma Bubbles and Irregularities in the Equatorial Ionosphere," J. Geophys. Res., Vol. 82, No. 19, pp. 2650-2656 (July 1977).
19. Linson, L. M. and J. B. Workman, "Formation of Striations in Ionospheric Plasma Clouds," J. Geophys. Res., Vol. 75, No. 16, pp. 3211-3219 (June 1970).
20. Ossakow, S. L. and P. K. Chaturvedi, "Morphological Studies of Rising Equatorial Spread-F Bubbles," J. Geophys. Res., Vol. 83, No. A5, pp. 2085-2090 (May 1978).
21. Bates, H. F., "Step Frequency Radar Study of Secede III Barium Release," Final Report, DASA 2409, Contract DASA01-69-C-P001, SRI Project 7784, Stanford Research Institute, Menlo Park, CA (1969).
22. Chesnut, W. G., J. C. Hodges, and R. L. Leadabrand, "Auroral Backscatter Wavelength Dependence Studies," Final Report, Contract AF 30(602)-3734, SRI Project 5535, Stanford Research Institute, Menlo Park, CA (1968).
23. Tsunoda, R. T. and R. I. Presnell, "On a Threshold Electric Field Associated with the 398-MHz Diffuse Radar Aurora," J. Geophys. Res., Vol. 81, No. 1, pp. 88-96 (January 1976).

ON THE GENERATION AND GROWTH
OF EQUATORIAL BACKSCATTER PLUMES

Wave Structure in the Bottomside F Layer

by

Roland T. Tsunoda and Barbara R. White

SRI International
Menlo Park, CA 94025

ABSTRACT

We examine the initial conditions that lead to backscatter plume development in the equatorial F-region ionosphere. By analyzing ALTAIR radar data we obtained the following principal results: (1) Prior to plume development, an altitude modulation of electron-density contours exists in the bottomside F layer. These quasi-periodic variations were mapped spatially over a 1200-km east-west distance using incoherent-scatter measurements and found to consist of three cycles with an average spatial wavelength of 400 km; (2) Bottomside backscatter developed on the west walls of all three altitude-modulated regions followed by plume development from near the crests of these regions; (3) Spatial resonance as a "seed" mechanism for the large-scale distribution of equatorial spread-F structures can be discounted because vertical velocity components of atmospheric gravity waves and bulk plasma motion are mismatched.

I INTRODUCTION

The scientific community has shown considerable interest in the initial ionospheric conditions that lead to the development of equatorial spread-F (ESF) irregularities, because observed ESF structures do not appear to result simply from the amplification of thermal fluctuations in the F-region plasma. Equatorial spread-F structures almost always appear in patches rather than in some extended and uniform spatial

distribution. The patchy nature of ESF structures was noted by Clemesha¹* using an 18-MHz backscatter radar, by Röttger² from a transequatorial propagation experiment, and most dramatically by Woodman and La Hoz,³ Tsunoda et al.,⁴ and Towle⁵ using VHF and UHF backscatter radars. The observations indicate that the irregularity growth rates of the primary source mechanisms, believed to be the collisional Rayleigh-Taylor and gradient drift instabilities,^{6,7,8} are not very large. Consequently, the initial ionospheric conditions, such as the strength and spatial wavelengths of nonthermal geophysical noise that act as input signals to the primary instability mechanisms, appear to control the large-scale characteristics of ESF structures.

In an earlier paper,⁹ we suggested that equatorial backscatter "plumes," i.e., VHF and UHF radar backscatter signatures of ESF structures that extend from the bottomside into the topside F layer are initiated or enhanced by an eastward neutral wind blowing through the west walls of altitude-modulated electron-density contours in the bottomside F layer. The structuring mechanism again is believed to be the gradient-drift instability that leads to a cascade process involving a hierarchy of plasma instabilities.⁶ This model was based on the fact that (1) most backscatter plumes were associated with altitude-modulated bottomside backscatter, and (2) bottomside-backscatter strength was stronger on the west wall rather than elsewhere within the altitude-modulated backscatter region. By assuming that an altitude-modulated, bottomside-backscatter region is associated with similarly modulated contours of constant electron density in the F layer, we argued earlier⁹ that the observed east-west asymmetry in bottomside-backscatter strength could be produced by an eastward neutral wind. If we allow for the action of an eastward neutral wind, we can account for the large-scale characteristics of ESF structures. We inferred⁹ that the bottomside F layer is often altitude modulated by referring to 6300-A depletions reported by Weber et al.¹⁰

* References are listed at the end of this paper.

In this paper, we present the first direct evidence that the bottom-side F layer is indeed altitude modulated, and that the altitude modulation actually leads to the observed large-scale characteristics of equatorial backscatter plumes. The evidence presented is in the form of spatial maps of constant electron-density contours constructed from incoherent-scatter measurements made with the ALTAIR radar.^{4,5}

II EXPERIMENTAL CONSIDERATIONS

The ALTAIR radar and its system characteristics have been described in earlier papers;^{4,5} therefore, a detailed description will not be repeated here. Instead, we briefly summarize the pertinent radar parameters and describe the modifications in ALTAIR operation that allowed collection of the data on which we report in this paper.

ALTAIR is a dual-frequency radar that operates simultaneously at 155.5 MHz (VHF) and 415 MHz (UHF). Its peak power together with an effective antenna aperture allows incoherent-scatter measurements to be made at both radar frequencies. Although data were collected for this experiment at both frequencies, we present only data collected at 415 MHz. We made this choice because the radar is slightly more sensitive at UHF than at VHF, and because ESF backscatter is about 10 dB weaker at UHF than at VHF. Consequently, the use of UHF data provides a more accurate measure of the ionospheric electron-density distribution. The pulse-width used at UHF was 40 μ s (6-km range resolution).

The experiment consisted of scanning ALTAIR repeatedly in east-west direction. The scans were made with the radar beam directed perpendicular to the geomagnetic field at F-region altitudes. As shown by Tsunoda et al.,⁴ these scans provide incoherent-scatter measurements of the F-layer electron density in the absence of ESF irregularities, and map the ESF irregularities under disturbed conditions. Therefore, by operating ALTAIR before and during ESF development, mapping of the ionospheric conditions that just preceded the development of ESF was possible.

The scans differed from those previously reported^{4,5} in that the scans were both continuous (rather than in discrete beam positions) and significantly expanded in east-west extent. The continuous scan allowed for improved angular resolution. The expanded angular width of 120° (compared with 45° and 72° used previously) provided an east-west coverage of over 1200 km (compared with 600 km) at an altitude of 400 km.

III RESULTS

This section is divided into six parts. In the first subsection, we present a map of the nighttime equatorial ionosphere (constructed from incoherent-scatter measurements) in which we found the first direct evidence that wave structure develops in the bottomside F layer prior to the development of ESF irregularities. The map is the first of five ALTAIR backscatter maps taken in time sequence that show the time evolution of backscatter plumes from the wave structure in electron density. The following four subsections are devoted to description and brief discussions of the remaining four backscatter maps. Supporting evidence is introduced when needed during the course of the discussion of the results. The final subsection is a summary of the results.

A. First Map (0743 to 0803 UT)

The first backscatter map, presented in Figure 1, was obtained during a slow east-to-west scan (20-min duration). There is no obvious evidence of enhanced backscatter from ESF irregularities. In the absence of ESF backscatter, the contours of constant backscatter strength correspond identically to constant electron-density values. The map, therefore, represents the distribution of F-layer electron density as a function of east-west distance and altitude. The contour values in Figure 1 range from 3.2×10^4 el/cm³ ($\text{Deg} \log_{10} N_e = 4.5$) to 10^6 el/cm³.

The contours, particularly those in the bottomside F layer, can be characterized by the superposition of a quasi-periodic wave structure on a mean tilt that is higher in the east than in the west. The altitude

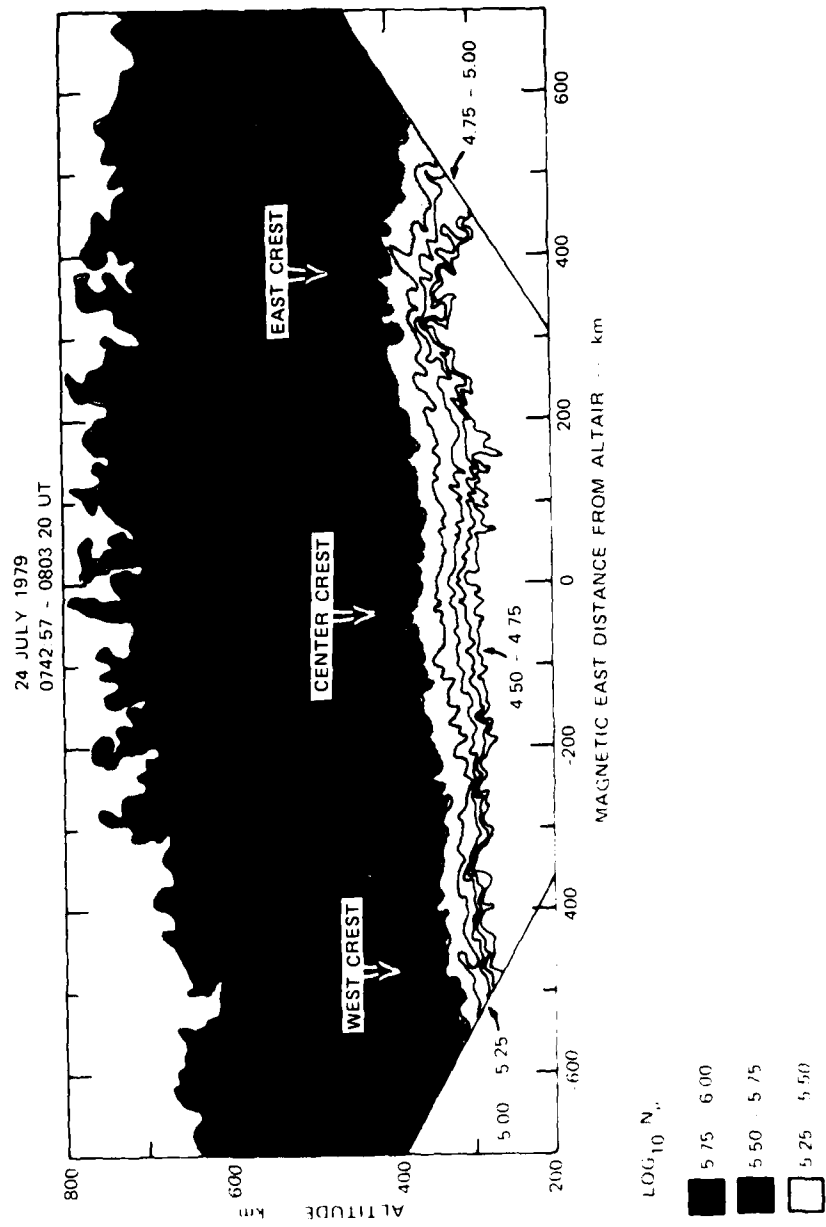


FIGURE 1 EVIDENCE OF WAVE STRUCTURE IN CONTOURS OF CONSTANT ELECTRON DENSITY FOUND IN THE F LAYER PRIOR TO EQUATORIAL SPREAD-F DEVELOPMENT

of the bottomside F-layer contours is centered around 300 km at the west end and a few tens of kilometers higher at the east end of the scan.

The wave structure consists of three oscillations that can be found in most of the contours in the bottomside F layer. The crests associated with the three oscillations are spaced approximately 400 km apart in east-west distance. The crest of each oscillation has been labeled west, center, and east for discussion purposes. Whether wave structure also occurs in the contours in the topside F layer is debatable, because the data from those altitudes are quite noisy.

The nature of the wave structure can be inferred from the electron-density gradients associated with the crests. The steepness of the gradient can be estimated from the closeness of the adjacent contours in the crest region. For example, the gradients appear steeper in the east and west crests than in the center crest, particularly if we examine the lower electron-density contours. On the other hand, the spacings of the higher electron-density contours (all in the bottomside F layer) appear to be nearly the same in both crest and trough regions. An interpretation is that after the wave structure was impressed upon the bottomside layer, the crests experienced additional upward force resulting in further upwelling in the crest region (relative to the trough region). This interpretation is consistent with the behavior of the collisional Rayleigh-Taylor instability or the gradient drift instability, the latter operating when the F layer is rising.

The large-scale mean tilt of the F layer contours appears to be associated with the postsunset rise of the F layer.^{11,12} If we assume a simple model in which the F layer is rising at a uniform velocity, the observed altitude difference (or the apparent tilt) corresponds to a vertical rise velocity of several tens of meters per second. This estimate (for such a simple model) is in reasonable agreement with a rise velocity of 30 m/s estimated from changes in $h'F$, the minimum virtual height of the F layer, scaled from ionograms taken during the same time period. Woodman¹¹ and Tsunoda¹² found that 40 m/s is a representative value for the postsunset rise of the F layer.

Another consistency check as to the nature of the tilt can be made by noting that Fejer et al.¹⁸ showed that the peak upward velocity associated with the postsunset rise of the F layer is time coincident with E-region sunset. The solar zenith angle at the east and west ends of the scan was 104° (start of scan) and 98° (end of scan), respectively. The shadow heights of the solar terminator corresponding to those angles are 187 and 45 km; therefore, the scan was made around the time of E-region sunset. Because a maximum tilt angle would be associated with the time of maximum rise velocity, we conclude that the tilt seen in Figure 1 is indeed a direct result of the lifting of the F layer.

From the map in Figure 1, altitude modulation clearly occurs in the bottomside F layer prior to the development of ESF backscatter. The time development of ESF backscatter associated with the three crests is shown in Figure 2. Five maps are stacked: the scan made earliest is at the bottom and that made last is at the top. All maps are cut off below 250-km altitude to allow a closer intercomparison of backscatter features in the various maps. The top of each map is cut off at an altitude above which backscatter was not observed. The maps are drawn with contours of constant backscatter strength. The contour of weakest backscatter (dashed curve) corresponds to equivalent incoherent-scatter returns from an electron density of 10^5 el/cm^3 (as labeled in the bottom panel). The other contours represent 10-dB steps above that level of backscatter strength. Although the contours are not labeled, the stronger backscatter regions are evident because the contours are, in most cases, concentric. For continuity and intercomparison with the other maps, we have reproduced the map shown in Figure 1 with only the $\log_{10} N_e = 5$ contour, in Figure 2(a). The remaining four maps are described and discussed in the following subsections.

B. Second Map (0805 to 0825 UT)

The map in Figure 2(b) obtained during a slow west-to-east scan, shows the same wavy contour with a large-scale tilt found in the first map. There are two important changes that appear in the second map regarding the wave structure. First, the altitude of the dashed contour

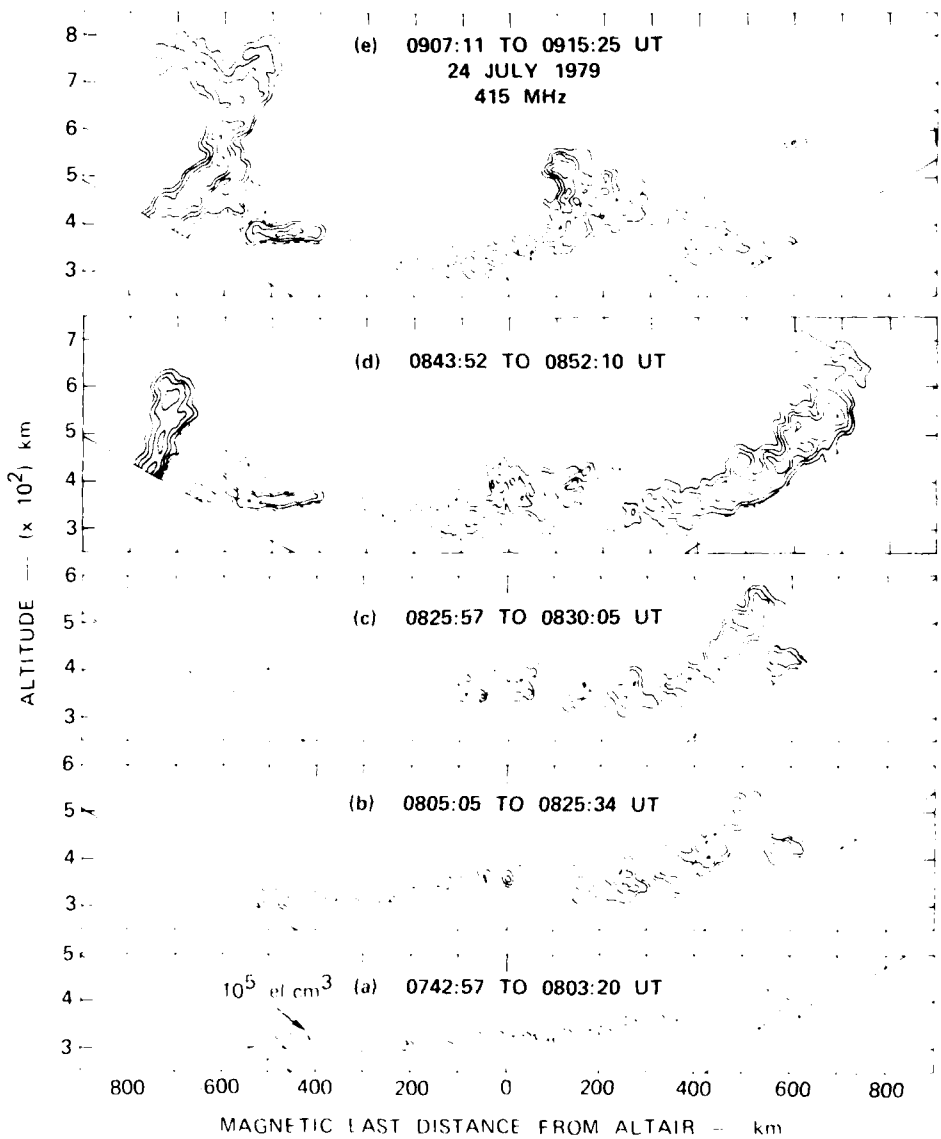


FIGURE 2 SEQUENCE OF ALTAIR BACKSCATTER MAPS SHOWING (a) QUASI-PERIODIC ALTITUDE MODULATION OF THE BOTTOMSIDE F LAYER, (b) INCREASE IN AMPLITUDE OF THE WAVE STRUCTURE, (c) DEVELOPMENT OF BOTTOMSIDE BACKSCATTER ON THE WEST WALLS OF ALTITUDE-MODULATED REGIONS, (d) PLUME DEVELOPMENT FROM CRESTS

has increased. This increase becomes evident if we note that the west and center crests have risen in altitude by 25 and 50 km, respectively. The trough (lowest altitude portion of the contour) between those two crests has also increased by about 15 km. All points on the dashed curve in the first map, therefore, have been displaced upward. This observation supports our original supposition of a rising F layer deduced from the large-scale tilt of the contour.

Second, the wave amplitude has increased. The wave amplitude as estimated from the altitude difference between the west crest and the trough (right of the west crest) has increased from 30 km to 50 km. Similarly, the altitude difference between the same trough and the center crest has increased from 40 km to 70 km. The increases in wave amplitude correspond to e-fold growth times of 10 and 25 min, respectively. A 10-min e-fold growth time for the linear gradient-drift instability can be obtained with an upward velocity of 40 m/s and a gradient scale length in electron density of 20 km. For the same gradient scale length, the upward velocity would have to be reduced to 16 m/s to obtain an e-fold growth time of 25 min.

As a consistency check, we measured the gradient scale length of the bottomside F layer from electron-density profiles obtained near overhead of ALTAIR, i.e., associated with the center crest. Three profiles obtained at elevation angles above 75° are plotted in Figure 3. The gradient scale length near the 10^5 el/cm^3 value (corresponding to the contour value in Figure 2) was measured to be about 20 km. On this basis alone, the upward velocity in the center crest region should be closer to 16 m/s. (The required upward velocity would be even smaller if we note that the collisional Rayleigh-Taylor instability contributes an effective velocity of 15 m/s at an altitude of 300 km.)

The gradient scale length associated with electron-density profiles in the west crest region was also found to be about 20 km (near the 10^5 el/cm^3 value). (The smaller gradient scale lengths suggested by the contours in Figure 1 are associated with lower electron densities.) The estimated e-fold growth time of the west crest, therefore, appears to be

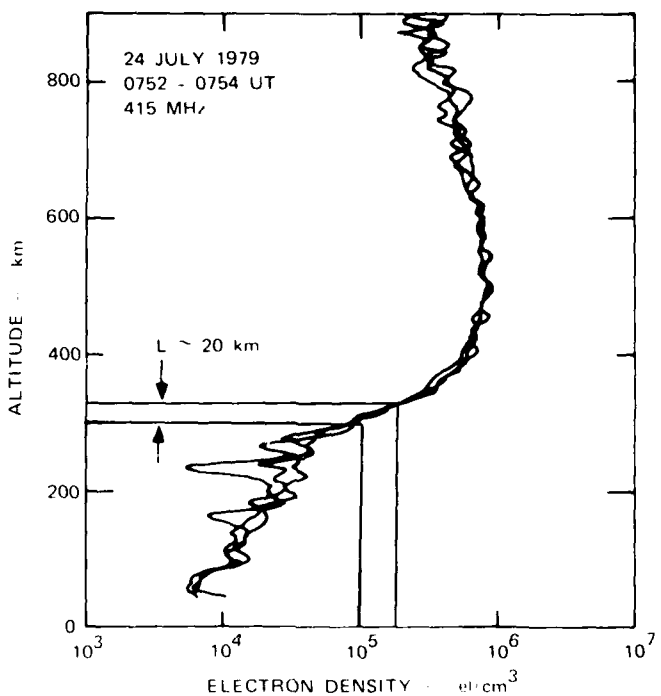


FIGURE 3 ELECTRON-DENSITY PROFILES FROM THE CENTER CREST REGION OVER ALTAIR [Figure 1(a)]

in reasonable agreement with the growth time predicted by the gradient-drift and Rayleigh-Taylor instabilities, using an upward velocity of 30 m/s (from ionogram data) and the observed gradient scale length.

Other qualitative conclusions can be drawn from Figure 2(b). The development of ESF backscatter in the east sector of the second map where the altitude of the bottomside F layer is higher than in the western sector is consistent with the concept that the collisional Rayleigh-Taylor instability is an initiating mechanism for ESF structure. We note, however, that ESF backscatter did not develop at the top of the eastern crest, as would be predicted by the Rayleigh-Taylor instability. Instead,

we find that backscatter developed on the west wall of the east crest, consistent with the findings reported earlier.³ The ESF backscatter structures, which resembles a plume with an eastward (from vertical) tilt, is actually bottomside backscatter that extends upward to an altitude of about 500 km. The tilt of the bottomside backscatter contours is more vertical than that found in the 10^5 el/cm^3 electron-density contour shown in the first map, indicating continued upwelling of the east crest. Because the amplitude of the east crest has grown faster than the amplitude of the other two crests, amplitude growth seems to depend on the altitude, which is again consistent with the Rayleigh-Taylor instability.

A few words of clarification are perhaps necessary regarding terminology used in this paper and in the earlier one to describe bottomside wave structure, plasma bubbles, and associated backscatter. The backscatter that develops on the bottomside of a horizontally stratified F layer can unambiguously be called bottomside backscatter. The term bottomside backscatter is appropriate when describing backscatter within an altitude-modulated region, provided that the bottomside F-layer contours have not penetrated the nominal altitude for the F-layer peak. If the contours have penetrated this nominal altitude, the term bottomside backscatter no longer describes accurately the altitude region in which backscatter is occurring. This complication also extends into the choice of the words plasma bubble and upwelling (or crest).

In this paper, the definitions are based on the sketch of the F-layer contours shown in Figure 4. We differentiate an upwelling from a plasma bubble by the ratio of its dimensions transverse to the geomagnetic field. If the length (or height) of the plasma-depleted region is much longer than its width (or east-west dimension), we define that feature as a plasma bubble (e.g., dashed contour in Figure 4). When the width is comparable to or greater than its length, we define that plasma-depleted region as an upwelling, or crest associated with wave structure in the bottomside F layer. In Figure 4, the backscatter that develops

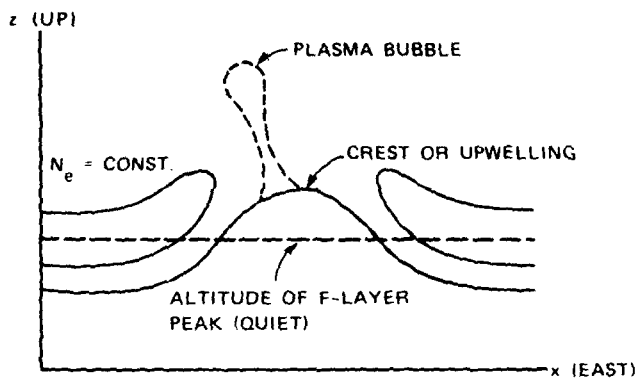


FIGURE 4 SCHEMATIC MODEL OF THE DISTURBED F-LAYER IONOSPHERE USED TO DEFINE THE TERMS CONTAINED IN THIS PAPER [i.e., the terms upwelling (or crest), plasma bubble, bottomside backscatter, and backscatter plumes].

along the bottomside F layer or within the upwelling is called bottomside backscatter. The backscatter that develops along walls or within plasma bubbles is called a backscatter plume.

C. Third Map (0826 to 0830 UT)

The map in Figure 2(c), obtained during a fast east-to-west scan (4-min duration), shows the continued upward development of bottomside backscatter associated with the west wall of the east crest. The bottomside backscatter now extends up to an altitude of 570 km. Because the tilt angle of the backscatter region is east of vertical and nearly constant with altitude, we infer that a plume has not yet developed. The upwelling of the bottomside F layer continues to develop, indicated for example by the increased amplitude of the east crest.

A similar upwelling of the altitude modulation is also evident in the west crest. The west crest in Figure 2(c) has reached an altitude

of 450 km, approximately 100 km higher than in the previous map. From the time difference between scans (25 min), we estimated the upwelling growth-velocity to be 67 m/s. Despite the high altitude of the west crest, ESF backscatter has not yet developed. In contrast, we note that the development of backscatter in the second map at altitudes as low as 350 km.

Finally, the small backscatter patch associated with the center crest, first evident in the second map, has developed, but is not associated with the west wall of the center crest. This development pattern may be related to the correspondingly slow development in amplitude of the center crest. Although the amplitude of the center crest has increased (as is evident by comparing the first three maps), it is not nearly as large as that for the other two crests. The altitude dependence of wave-amplitude growth, suggested above, does not appear to hold if we compare growth rates of the west and center crests. We believe that the wave growth does depend on altitude, as is indicated by the growth of individual crests, and that the slow development of the center crest is caused by other factors, such as growth suppression by electric fields of adjacent plumes.

D. Fourth Map (0844 to 0852 UT)

The map in Figure 2(d), obtained during a medium-speed east-to-west scan (lasting 8 min), reveals the first development of a plume from the east crest. (Towle⁵ and Tsunoda^{12,14} showed that plumes and plasma bubbles are virtually collocated.) As mentioned previously, this inference of plume development is based on the change in tilt angle of the backscatter region at altitudes above 600 km. The near verticality in direction of the plume suggests that an eastward neutral wind is no longer effective at those altitudes, and that the growth velocity vector is controlled primarily by the gravitational term (collisional Rayleigh-Taylor instability). The predicted plasma bubble velocity (extrapolated from the results of Ossakow and Chaturvedi,¹⁵ even for a moderate percentage depletion in electron density, exceeds 100 m/s.

The patchy bottomside backscatter associated with the center crest has become stronger and spatially more extensive in the fourth map. Note that the structure has now developed a tilt that is similar to that of the bottomside backscatter associated with the east crest. Its altitude is also higher than that shown in the third map, indicating continued upwelling of the center crest.

While the time evolution of the center crest is gradual, that associated with the west crest is not. The upwelling of the west crest is another 100 km higher in altitude than is presented in the previous map. The corresponding growth velocity of the upwelling is 75 m/s, slightly faster than the velocity estimated from the two previous maps. The observed acceleration of the upwelling supports our interpretation in terms of an altitude-dependence in wave-amplitude growth.

In the fourth map, we also observe the development of bottomside backscatter along the west wall of the west crest. The tilt angle is closer to vertical than those found in the other two crests. This observation is consistent with the rapid development of strong backscatter that is expected if a large component of the eastward neutral wind acts to drive the gradient-drift instability. We have shown, therefore, that all three crests are associated with bottomside-backscatter development along their west walls.

E. Fifth Map (0907 to 0915 UT)

In Figure 2(e), the fifth and final map of this sequence, obtained during a medium-speed west-to-east scan, we find that a plume has developed from the bottomside backscatter region associated with the west crest. As in the case of the plume associated with the east crest, the orientation of the plume is nearly vertical. As discussed previously, this near-verticity seems to result from a dominance of the gravitational term over the eastward neutral wind in the collisional Rayleigh-Taylor instability.

The relatively slow development of backscatter associated with the center crest is still apparent in the fifth map. Neither the tilt angle

nor the altitude of the bottomside backscatter has changed, when compared to that in the fourth map. A plume has begun to develop; however, it is much smaller than those that developed from the west and east crests, and is characterized by a slight westward tilt (from vertical). We interpret its slight westward tilt with the low-altitude development of the plume. At low altitudes, the gravitational term is not as dominant as at high altitudes. Contributions of an eastward neutral wind to the tilt of the low-altitude plume is, therefore, probably significant; furthermore, the F layer was not rising at that time, also reducing the vertical velocity even more.

F. Summary of Results

Analysis of ALTAIR data taken on 24 July 1979, in the form of expanded east-west scans, has produced the following results:

- (1) Incoherent-scatter measurements have shown that electron-density contours in the bottomside F layer were tilted and altitude modulated in east-west direction.
- (2) The observed altitude modulation was quasi-periodic, containing three crests with an average spatial east-west wavelength of 400 km.
- (3) The altitude modulation was observed around E-region sunset and during the postsunset rise of the F layer.
- (4) The initially observed peak-to-peal plitude of the wave was 15 to 30 km, a significant fraction of the scale height of the neutral gas (~ 50 km).
- (5) The amplitude of the wave-like structures as characterized by constant electron-density contours grow with time. The growth rates of the west crest agreed well with those that were computed from the linearized collisional Rayleigh-Taylor and gradient-drift instability models. The growth rate of the center crest appeared smaller than expected from the same instability models.
- (6) The rate of amplitude growth depended on altitude, with increased rates at higher altitudes.
- (7) Bottomside backscatter developed on the west walls of all three crests. Their development times, however, differed.
- (8) Plumes developed from each of the three crests, but with very different rates of growth.

IV DISCUSSION AND CONCLUSIONS

In this paper, we have presented the first direct evidence that electron-density contours in the bottomside F layer are altitude-modulated prior to ESF backscatter development. That is, incoherent-scatter measurements of the F-layer electron density were used to plot the contours of its spatial distribution (altitude, east-west distance). These contours were shown to have a wave structure. Related measurements by Weber et al.¹⁰ showed that 6300-A equatorial airglow depletions could be explained in terms of an altitude-modulated F layer; however, they used the virtual heights of the F layer and the range to oblique reflections to construct an altitude-modulated F layer.

The observed spatial wavelength of 400 km associated with the wave structure suggests that the results presented in this paper might be more typical rather than the exception. Röttger² used a transequatorial propagation experiment to characterize the wave-like properties of ESF structure. He found that the median east-west spacings of ESF patches was 380 km, and that the number of patches observed at any given time ranged from one to ten. We note, however, that most of his observations were made during the night when the F layer was descending; therefore, although the spatial wavelength found in our data set appears typical, the observation during a time when the F layer was rising, is not.

We pointed out earlier⁹ that most backscatter plumes appear to develop during the postsunset rise of the F layer. Major plumes did not develop over ALTAIR at later times when the F layer was descending. Plumes, however, did continue to drift eastward, passing over ALTAIR during the period when the F layer was descending. These observations seem to indicate that most major plumes are generated close to E-region sunset (during the lifting of the F layer) and that they continue to develop and decay thereafter. We, therefore, conclude that the results reported here probably represent the typical case for plume generation.

The conclusion that an upward-moving F layer represents typical initial ionospheric conditions for wave growth and plume generation is crucial in the determination of the wave amplification mechanism. One

mechanism, spatial resonance,¹⁵⁻¹⁸ would be eliminated or at least its effectiveness can be reduced severely by this conclusion. The key to spatial resonance is to allow "infinite" interaction time between a neutral-gas disturbance (e.g., atmospheric gravity waves) and the F-region plasma by matching the phase velocity of the wave to the bulk plasma motion. Because typical atmospheric gravity waves have a downward component of phase velocity, the rising F layer would be antiparallel to this component, thus resulting in a mismatch that appears to reduce drastically the effectiveness of spatial resonance.¹⁸

On the other hand, there appears to be no need for further contributions to wave growth other than the generalized gradient-drift instability (which includes the collisional Rayleigh-Taylor instability). We found from the data in Figure 2 that the observed growth in wave amplitude (upwelling of altitude-modulated regions) was in good agreement with theoretical estimates based on the generalized gradient-drift instability.

The apparent ineffectiveness of the spatial resonance mechanism under the ionospheric conditions described does not mean it does not have a role in ESF phenomena. It might still represent a viable means of sustaining ESF structures during the descent of the F layer. At the moment, however, spatial resonance does not appear to be the "seed" mechanism that establishes the character of the geophysical noise that is amplified by the generalized gradient-drift instability.

The upwelling of crests to altitudes as high as 570 km has never before been reported. With the bottomside F layer located at a 350-km altitude, the upwelling represents a 220-km upward displacement. This result suggests that many of the plasma bubble signatures through an altitude-modulated bottomside F layer. For example, McClure et al.¹⁹ reported AE-C measurements made at altitudes ranging from 650 km down to 200 km; therefore, some care must be taken in interpreting in-situ data.

The growth in wave amplitude was followed by the development of ESF backscatter on the west walls of all three upwellings. We have thus shown that not only is the F layer altitude modulated, but that ESF

structuring is indeed initiated on the west wall of the upwellings. We earlier⁹ that the source of the east-west asymmetry was the eastward neutral wind blowing through the west wall of the upwellings. Allowance for an east-west neutral wind in the reference frame of the moving plasma has been proposed previously as the explanation of the tilt of backscatter plumes and the electrodynamics of plasma bubbles.^{3,20,8} The development of east-west asymmetry in the spatial distribution of ESF irregularities, however, has not been considered previously. Because of the cascading process by which large-scale ESF structures lead to the development of small-scale ESF irregularities (e.g., radar backscatter), it is likely that a similar east-west asymmetry exists in larger-scale ESF structures, e.g., as measured by in-situ probes and by scintillations of transionospheric signals.

Several important questions remain to be answered. First, F-region neutral-wind measurements must be made in conjunction with plasma drift and ESF backscatter measurements to verify that the eastward neutral wind does blow through the upwellings. F-region neutral winds were measured simultaneously with this ALTAIR data set, by researchers from the University of Pittsburgh.²¹ The results of the comparative analysis will be presented in a future paper.

Second, there is still the question of the source of the wave structure observed in the maps in Figure 2. Because the wave amplitude was already large at E-region sunset, it is not clear whether the source operates under daytime or nighttime conditions or both. It is important to know, for example, whether F-region polarization electric fields could be set up at the time of the observations by the F-region dynamo.²²

And third, is the generation and time evolution of backscatter plumes influenced by coupling processes between adjacent plumes in a multiple-plume environment? In this data set, there appeared to be a suppression of plume development in the center crest.

REFERENCES

1. B. R. Clemesha, "An Investigation of the Irregularities in the F-Region Associated with Equatorial Type Spread F," J. Atmos. Terr. Phys., Vol. 26, No. 1, pp. 91-112 (January 1964).
2. J. Röttger, "Wave-Like Structures of Large-Scale Equatorial Spread-F Irregularities," J. Atmos. Terr. Phys., Vol. 35, No. 6, pp. 1195-1206 (June 1973).
3. R. F. Woodman and C. La Hoz, "Radar Observations of F-Region Equatorial Irregularities," J. Geophys. Res., Vol. 81, No. 31, pp. 5447-5466 (November 1976).
4. R. T. Tsunoda, M. J. Baron, J. Owen, and D. M. Towle, "ALTAIR: An Incoherent Scatter Radar for Equatorial Spread F Studies," Radio Sci., Vol. 14, No. 6, pp. 1111-1120 (November/December 1979).
5. D. M. Towle, "VHF and UHF Radar Observations of Equatorial F-Region Ionospheric Irregularities and Background Densities," Radio Sci., Vol. 15, No. 1, pp. 71-86 (January/February 1980).
6. G. Haerendel, "Theory of Equatorial Spread F," preprint, Max-Planck (Institut fur Physik und Astrophysik, Institut fur Extraterrestrische Physik, 8046 Garching, Germany, 1973).
7. A. Scannapieco and S. L. Ossakow, "Nonlinear Equatorial Spread F," Geophys. Res. Lett., Vol. 3, No. 8, pp. 451-454 (August 1976).
8. S. L. Ossakow and P. K. Chaturvedi, "Morphological Studies of Rising Equatorial Spread F Bubbles," J. Geophys. Res., Vol. 83, No. A5, pp. 2085-2090 (May 1978).
9. R. T. Tsunoda, "Time Evolution and Dynamics of Equatorial Backscatter Plumes--I. Growth Phase," Accepted for Publication, J. Geophys. Res..
10. E. J. Weber, J. Buchau, R. H. Eather, and S. B. Mende, "North-South Aligned Equatorial Airglow Depletions," J. Geophys. Res., Vol. 83, No. A2, pp. 712-716 (February 1978).
11. R. F. Woodman, "Vertical Drift Velocities and East-West Electric Fields at the Magnetic Equator," J. Geophys. Res., Vol. 75, No. 31, pp. 6249-6259 (November 1970).
12. R. T. Tsunoda, "Magnetic-Field-Aligned Characteristics of Plasma Bubbles in the Nighttime Equatorial Ionosphere," J. Atmos. Terr. Phys., Vol. 42, No. 8, pp. 743-752 (August 1980).

13. B. G. Fejer, D. T. Farley, R. F. Woodman, and C. Calderon, "Dependence of Equatorial F-Region Vertical Drift on Season and Solar Cycle," J. Geophys. Res., Vol. 84, No. A10, pp. 5792-5796 (October 1979).
14. R. T. Tsunoda, "On the Spatial Relationship of 1-m Equatorial Spread F Irregularities and Plasma Bubbles," J. Geophys. Res., Vol. 85, No. A1, pp. 185-190 (January 1980).
15. J. D. Whitehead, "Ionization Disturbances Caused by Gravity Waves in the Presence of an Electrostatic Field and Background Wind," J. Geophys. Res., Vol. 76, No. 1, pp. 238-241 (January 1971).
16. T. Beer, "Spatial Resonance in the Ionosphere," Planet. Space Sci., Vol. 21, No. 3, pp. 297-308 (March 1973).
17. J. Klostermeyer, "Nonlinear Investigation of the Spatial Resonance Effect in the Nighttime Equatorial F-Region," J. Geophys. Res., Vol. 83, No. A8, pp. 3753-3760 (August 1978).
18. J. Röttger, "Drifting Patches of Equatorial Spread-F Irregularities--Experimental Support for the Spatial Resonance Mechanism in the Ionosphere," J. Atmos. Terr. Phys., Vol. 40, No. 10/11, pp. 1103-1112 (October/November 1978).
19. J. P. McClure, W. B. Hanson, and J. H. Hoffman, "Plasma Bubbles and Irregularities in the Equatorial Ionosphere," J. Geophys. Res., Vol. 82, No. 19, pp. 2650-2658 (July 1977).
20. E. Ott, "Theory of Rayleigh-Taylor Bubbles in the Equatorial Ionosphere," J. Geophys. Res., Vol. 83, No. A5, pp. 2066-2070 (May 1978).
21. D. P. Sipler and M. A. Biondi, "Equatorial F-Region Neutral Winds from Nightglow OI 630.0 nm Doppler Shifts," Geophys. Res. Lett., Vol. 5, No. 5, pp. 373-376 (May 1978).
22. H. Rishbeth, "Polarization Fields Produced by Winds in the Equatorial F Region," Planet. Space Sci., Vol. 19, No. 3, pp. 357-371 (March 1971).

A THEORETICAL EXPLANATION FOR 11-cm IRREGULARITIES DURING EQUATORIAL SPREAD F

J. D. Huba

Science Applications, Inc.
McLean, VA 22101

and

S. L. Ossakow

Geophysical and Plasma Dynamics Branch
Plasma Physics Division
Naval Research Laboratory
Washington, D.C. 20375

ABSTRACT

The recent Kwajalein radar backscatter observations on 17 July 1979 of 11-cm irregularities at high altitudes during equatorial spread F are explained in terms of the kinetic lower-hybrid-drift instability. The instability depends on there being regions of steep plasma density gradients and low plasma density. The absence of radar backscatter from 11-cm irregularities at lower altitudes can be attributed to the stabilizing influence of electron-neutral collisions.

I INTRODUCTION

During the past several years, high-frequency radar backscatter experiments have revealed a spectrum of short-wavelength (i.e., below the ion gyroradius) irregularities during equatorial spread F (ESF). Radar backscatter observations at 50 MHz, 155 MHz, and 415 MHz indicate that density fluctuations exist with scale sizes of 3 m, 1 m, and 36 m, respectively.^{1-5*} Most recently, on 17 July 1979 between 1102 and 1110 UT

*References are listed at the end of this paper.

(one and one-half hours prior to rocket launch), R. T. Tsunoda⁶ observed radar backscatter from 11-cm irregularities at high altitudes, during ESF using the TRADEX radar with a frequency of 1320 MHz. These observations were part of the coordinated Defense Nuclear Agency campaign at Kwajalein to study ionospheric irregularities during ESF. The program was designed to obtain simultaneous radar backscatter results and in-situ rocket measurements of density and fluctuating fields. Because the 11-cm observations were made prior to the rocket launch, but during ESF, coincidental in-situ plasma and fluctuation data are not available. However, presumably ionospheric plasma conditions were similar during the various measurements.

Sharp density gradients were observed during this campaign⁷ and have been observed during past ESF events.^{3,4} The scale lengths of these gradients range from tens of meters to several hundred meters and presumably are due to primary longer-wavelength instabilities such as the Rayleigh-Taylor instability. Because the typical ion gyroradius is $r_{Li} \sim 5$ m, it is found that $r_{Li}/L_n \lesssim 0.02$ where L_n is the density gradient scale length. Based upon this evidence, it has been suggested that various drift instabilities are responsible for the short-wavelength irregularities,^{3-5,8,9} depending upon the wavelength observed. Although collisionless drift waves would easily be excited under these circumstances, collisional effects have a stabilizing influence on the instabilities thus far investigated.³⁻¹⁰ Specifically, the lower-hybrid-drift instability is the prime candidate to explain the 1-m, 36-cm, and 11-cm irregularities. However, recent work¹⁰ has indicated that electron-electron, electron-ion, and electron-neutral collisions stabilize the instability and an approximate threshold condition has been derived.¹⁰

In the light of the July 1979 observations of 11-cm irregularities and theoretical results, we show that the lower-hybrid-drift instability is the most probable cause of the small-scale irregularities, i.e., 11 cm, 36 cm, and 1 m, observed during ESF. Moreover, we discuss the role of these irregularities on the large-scale plasma behavior during these periods.

II THEORY

We consider a plasma immersed in a homogeneous, unidirectional field, $\bar{B} = B_0 \hat{e}_z$, with an inhomogeneous density profile, $n = n(x)$, and a constant temperature, $T_e = T_i = T$. Each species, α (i.e., electrons and O^+ ions), has a diamagnetic drift velocity, $\bar{v}_{d\alpha} = (v_\alpha^2/2\omega_\alpha) d \ln n/dx$ where $v_\alpha = (2T_\alpha/m_\alpha)^{1/2}$ is the thermal velocity, $\omega_\alpha = e_\alpha B_0/m_\alpha c$ is the cyclotron frequency and $n = n_e \approx n_i$. A net current exists in the plasma, $\bar{j}_o = en(v_{di} - v_{de})\hat{e}_y \approx 2en v_{di} \hat{e}_y$, that provides the free energy to drive an instability. Perturbed quantities are assumed to vary as $\exp[iky - j\omega t]$ and we consider electrostatic oscillations only because $\beta \ll 1$. We make use of the local approximation, which requires $kL_n \gg 1$, where $L_n = (d \ln n/dx)^{-1}$ is the density gradient scale length. The ions are considered unmagnetized while the electrons are considered magnetized. The ions behave as unmagnetized particles for the wavelengths under consideration ($k r_{Li} \sim 10^2$) because of ion-ion collisions.³ Electron-neutral, electron-electron and electron-ion collisions are included in the analysis via an effective collision frequency, $\nu_e = \nu_{en} + \nu_{ei}(1 + 0.15k^2 r_{Le}^{-2})$, where $r_{Le} = v_c/|v_c|$ is the mean electron Larmor radius.^{10,11} We note that our coefficient of $k^2 r_{Le}^{-2}$ differs from that of Sperling and Goldman¹⁰ because of a different definition of the thermal velocity.

Based upon these assumptions, we obtain the following dispersion equation for the lower-hybrid-drift instability

$$D(\omega, k) = 1 + x_i + x_e \quad (1)$$

where⁵

$$x_i = \frac{2\omega_{pi}^2}{k^2 v_i^2} \left[1 + \frac{\omega - kv_{di}}{kv_i} Z \left(\frac{\omega - kv_{di}}{kv_i} \right) \right] \quad (2)$$

and¹⁰

$$x_e = \frac{2\omega_{pe}^2}{k^2 v_e^2} \left[1 - \frac{\omega - kv_{de} + i\nu_e}{\omega + i\nu_e} \Gamma_o(b_e) \right] \left[1 - \frac{i\nu_e}{\omega + i\nu_e} \tilde{\Gamma}_o(b_e) \right]^{-1} \quad (3)$$

where $\omega_{p\alpha}^2 = 4\pi n_\alpha e_\alpha^2/m_\alpha$, $v_\alpha^2 = 2T_\alpha/m_\alpha$, $\Omega_\alpha = e_\alpha B_\alpha/m_\alpha c$, $v_{d\alpha} = (v_\alpha^2/2\lambda_\alpha)d\ln n/dx$, $v_e = v_{en} + v_{ei}(1 + 0.3 b_e)$, $b_e = k^2 r_{Le}^{2/2}$, $\Gamma_o(x)e^{-x}$, I_n is the modified Bessel function of order n , and Z is the plasma dispersion function. We note that Eq. (3) is based upon the BGK collision model and, strictly speaking, does not correctly treat electron-electron collisions.¹² However, electron viscosity is modeled approximately via the term¹³ proportional to $k^2 r_{Le}^{2/2}$. Because the 11-cm irregularities correspond to $k r_{Le} \approx 2$, it is clear that electron viscous effects are only moderately important; moreover, the BGK model is adequate in the absence of temperature gradients,¹² as is the situation in the F region. Thus, Eq. (3) can confidently be used to describe the electron response qualitatively. The quantitative results based upon Eq. (3) are approximately correct because a model Fokker-Planck equation is used to describe the collisionality.

Because $v_{di} \ll v_i$ (which corresponds to $r_{Li} \ll L_n$), we can expand the plasma dispersion function in the small argument limit (e.g., $Z(\Psi) \approx i\Psi/\lambda$). The dispersion equation assumes the form

$$D(\omega, k) = 1 + \frac{2\omega_{pi}^2}{k^2 v_i^2} \left[1 + i\sqrt{\lambda} \frac{\omega - kv_{di}}{kv_i} \right] + \frac{2\omega_{pe}^2}{k^2 v_e^2} \left[1 - \frac{\omega - kv_{de} + iv_e}{\omega + iv_e} \Gamma_o(b_e) \right] \left[1 - \frac{iv_e}{\omega + iv_e} \Gamma_o(b_e) \right]^{-1} = 0. \quad (4)$$

In the limit $\gamma \sim v_e \ll \omega_r$, $\omega = \omega_r + i\gamma$, Eq. (4) has the following solution

$$\omega_r = \Gamma_o kV_{di} \left[1 + k^2 \lambda_{di}^2 + (T_i/T_e)(1 - \Gamma_o) \right] \quad (5)$$

$$\gamma = -\omega_r (\omega_r/kV_{di}) \left[\frac{i\lambda}{\Gamma_o} \frac{\omega_r - kv_{di}}{kv_i} + \frac{T_i}{T_e} \frac{v_e}{\omega_r} (1 - \Gamma_o) \left(1 + \frac{kV_{di}}{\omega_r} \frac{T_e}{T_i} \right) \right] \quad (6)$$

where $\lambda_{di}^2 = v_i^2/2\omega_{pi}^2$ and the argument of Γ_o has been suppressed. In the absence of collisions ($v_c = 0$), instability occurs for $\omega_r < kV_{di}$,

and there is no threshold requirement. However, electron collisions are stabilizing and place a threshold condition on the drift velocity to excite the mode.^{8,10} Substituting Eq. (5) into Eq. (6), the critical drift velocity (i.e., such that $\gamma > 0$) is given by

$$\left(\frac{v_{di}}{v_i}\right)_{cr} > \left[\frac{v_e}{v_i} \left(\frac{m_e}{m_i} \right)^{1/2} \frac{1}{\sqrt{\pi}} \frac{(1 - \Gamma_o) (2 + k^2 \lambda_{di}^2 - \Gamma_o^2)^2 (2 + k^2 \lambda_{di}^2)}{kr_{Le} \Gamma_o^2 (1 - \Gamma_o)^2 + k^2 \lambda_{di}^2} \right]^{1/2} \quad (7)$$

This corresponds to a critical density gradient scale length via

$$L_n^{cr} < (v_i/v_{di})_{cr} (r_{Le}/2).$$

We now apply Eq. (7) to plasma conditions relevant to equatorial spread F to determine whether or not the lower-hybrid-drift instability is responsible for the 11-cm radar backscatter observations. We choose $B = 0.3$ G, $T_e = T_1 = 0.1$ eV and $m_i = 16 m_p$. The collision frequency is given by

$$v_c = v_{en} + v_{ei} (1 + 0.15 k^2 r_{Le}^{-2}) \quad (8)$$

where^{14,15}

$$v_{en} = 5.0 \times 10^{-8} n_n T_e^{1/2} s^{-1} \quad (9)$$

$$v_{ei} = (\lambda/3.5 \times 10^5) (n_e/T_e)^{3/2} s^{-1} \quad (10)$$

and n_n is the neutral density, n_e is the electron density, $\lambda = 23.4 - 1.15 \log n_e + 3.45 \log T_e$, and T_e is given in eV. We plot $(v_{di}/v_i)_{cr}$ and L_n^{cr} (meters) versus kr_{Le} in Figure 1 for the following values: $n_e = 10^4, 10^5, 10^6 \text{ cm}^{-3}$ and $n_n = 10^8, 5 \times 10^9 \text{ cm}^{-3}$. The range in electron density corresponds to the range from ambient density ($n_e \sim 10^6 \text{ cm}^{-3}$) to the density within ionospheric bubbles or plasma depletions ($n_e \sim 10^4 \text{ cm}^{-3}$). The values of the neutral density are for altitudes ~ 450 km ($n_n \sim 10^8 \text{ cm}^{-3}$) and 250 km ($n_n \sim 5 \times 10^9 \text{ cm}^{-3}$) during sunspot maximum.¹⁶ The altitude ~ 450 km corresponds to the region from which

the 11-cm radar backscatter returns were observed⁵ (severe backscatter on 17 July 1979 between 1102 and 1110 UT extended from 437 km to 457 km in altitude with a peak in backscatter strength at 447 km); whereas, the 250-km altitude corresponds to the bottom of the F region on that same night. Also, we have marked the values of kr_{Le} , which correspond to 1 m, 36 cm, and 11 cm, respectively. Several interesting features of Figure 1 are as follows.

First, minimum values of $(v_{di}/v_i)_{cr}$ and L_n^{cr} exist for $kr_{Le} \sim 0.6$ as noted by Sperling and Goldman.¹⁰ The minimum is rather broad for low n_e , but becomes sharper as n_e is increased. This indicates that for a given density and density-gradient scale length, only a certain range of kr_{Le} can be excited linearly. Second, larger values of the neutral density require larger drift velocities (or shorter density-gradient scale lengths) as expected. This is a more dramatic effect at lower electron densities ($n_e \sim 10^4 \text{ cm}^{-3}$) than higher electron densities ($n_e \sim 10^6 \text{ cm}^{-3}$) simply because v_{ei}/v_n scales as n_e . Finally, for $n_e = 10^4 \text{ cm}^{-3}$ there is a cutoff at $kr_{Le} \approx 1.5$, because $k\lambda_{de} \approx 1$ for these values, and collective plasma phenomena are not expected to occur on length scales shorter than a Debye length. Thus, for electron densities less than 10^4 cm^{-3} , there will be no density fluctuations with scale lengths shorter than 20 cm, other than thermal fluctuations.

III DISCUSSION

During the DNA-coordinated 17 July 1979 ground-based, rocket and satellite campaign to study ionospheric irregularities during equatorial spread F at Kwajalein, Tsunoda⁶ observed radar backscatter from 11-cm irregularities. These are the smallest-scale irregularities observed thus far and are comparable to the mean electron Larmor radius ($r_{Le} \sim 3 \text{ cm}$). An important feature of the experimental results is that these irregularities were only observed at high altitudes ($\sim 450 \text{ km}$). During the rocket flight, which occurred subsequent to the 11-cm radar backscatter measurements, in-situ probes detected sharp density gradients⁷ ($L_n \gtrsim 45 \text{ m}$) and large density depletions^{7,16,17} ($n_e \sim \text{several} \times 10^4 \text{ cm}^{-3}$).

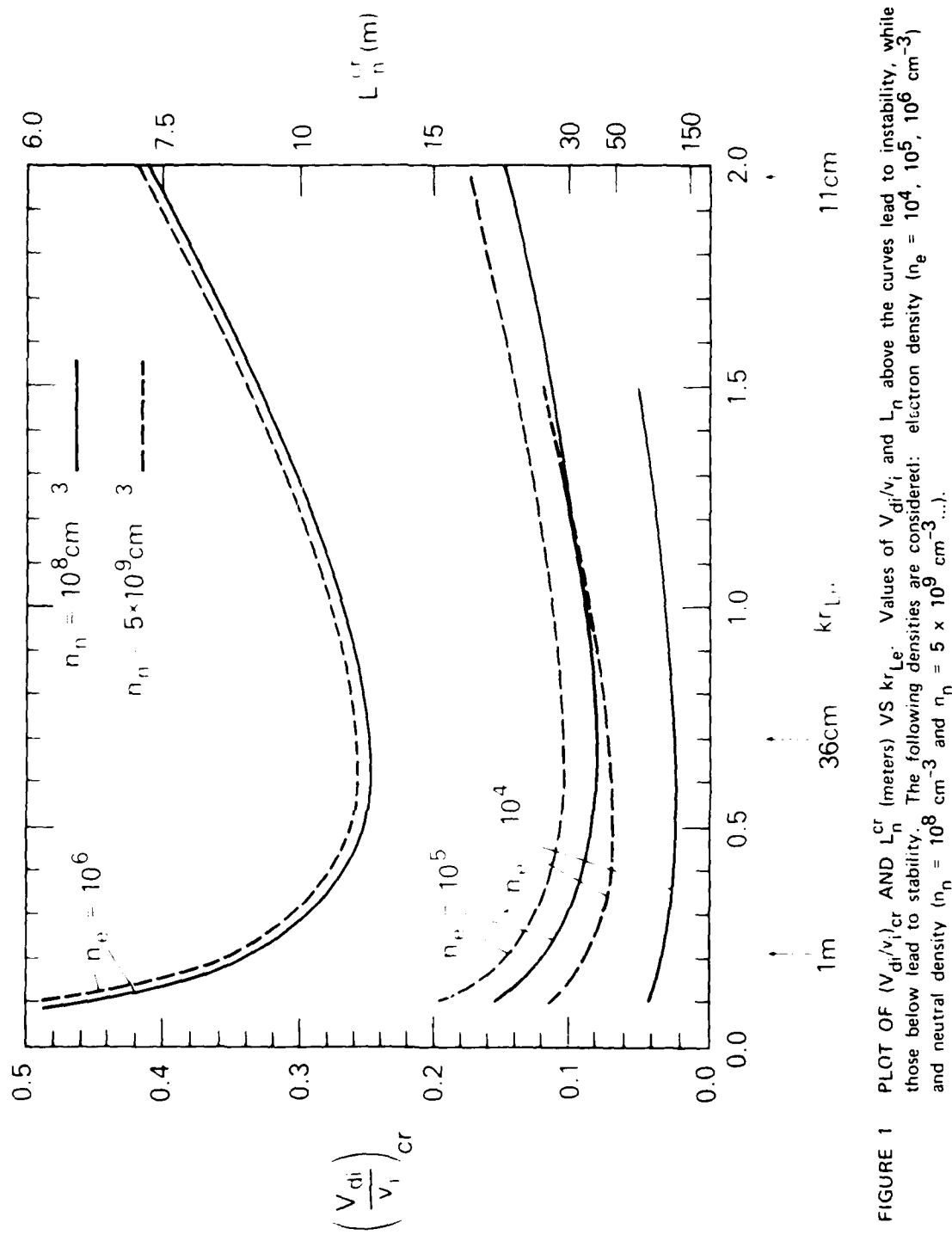


FIGURE 1 PLOT OF $(V_{di}/V_i)_{cr}$ AND L_n^{cr} (meters) VS $k_r L_e$. Values of V_{di}/V_i and L_n^{cr} above the curves lead to instability, while those below lead to stability. The following densities are considered: electron density ($n_e = 10^4, 10^5, 10^6 \text{ cm}^{-3}$) and neutral density ($n_n = 10^8 \text{ cm}^{-3}$ and $n_n = 5 \times 10^9 \text{ cm}^{-3}$).

at high altitude (~ 500 km). We note that previous in-situ rocket measurements have found density-gradient scale lengths³ as small as 30 m.

These data suggest the following scenario: As ESF develops, density depletions rise to the topside of the F region where the neutral density is low (~ 450 km). Within these plasma bubbles (where electron collisional effects are minimal) sharp density gradients exist that can excite the lower-hybrid-drift instability. The density fluctuations associated with the instability give rise to the radar backscatter measurements at 1 m, 36 cm, and 11 cm. This can occur for $L_n \gtrsim 20$ m, $n_e < 10^5 \text{ cm}^{-3}$ and $n_n \sim 10^8 \text{ cm}^{-3}$ (Figure 1), which is consistent with observational results to within a factor of two. This is quite good considering the approximations involved in deriving the electron response [Eq. (3)]. At lower altitudes (< 250 km) the increased neutral density requires a sharper density-gradient scale length for a given value of n_e (or lower values of n_e for fixed density-gradient scale length), especially for the 11-cm irregularities (Figure 1), and the mode is stable. Also, it is possible that the density within the lower altitude density depletions is $n_e \lesssim 10^4 \text{ cm}^{-3}$ and radar backscatter is not observed at 11 cm because this is smaller than the Debye length. Thus, based upon the linear theory of the lower-hybrid-drift instability, it is found that this mode is the most probable cause of the small-scale irregularities ($\lesssim 1$ m) observed during ESF.

Finally, we discuss the possible role of this instability in the evolution of the large-scale plasma phenomena occurring during ESF. Typically, plasma microturbulence influences the plasma via its anomalous transport properties (i.e., scattering of particles by the collective fields associated with the instability). A recent theoretical study of the lower-hybrid-drift instability¹⁵ indicates that this mode can produce irreversible electron heating and diffusion only when $e\Phi/T \gtrsim 0.2$ to 0.5 where Φ is the fluctuating electrostatic potential. Producing this level of turbulence requires very sharp density gradients ($L_n \lesssim r_{Li}$), which do not exist during ESF. For typical ionospheric conditions (i.e., $L_n \gg r_{Li}$), the instability will saturate at a low level of turbulence and not be an effective anomalous transport mechanism. Thus, the

small-scale density and field fluctuations associated with this mode are possibly no more than a signature of EFS, under the proper conditions, and will probably not significantly influence the macroscopic fluid evolution of the plasma for scale sizes $\gtrsim L_n$.

ACKNOWLEDGMENTS

This work was supported by the Defense Nuclear Agency. We wish to thank Drs. M. C. Kelley, E. P. Szuszczewicz, and R. T. Tsunoda for valuable discussions concerning the data obtained during the 1979 DNA-supported Kwajalein equatorial campaign.

REFERENCES

1. D. T. Farley, B. B. Balsley, R. F. Woodman, and J. P. McClure, "Equatorial Spread F: Implications of VHF Radar Observations," J. Geophys. Res., Vol. 75, No. 34, pp. 7199-7216 (December 1970).
2. R. F. Woodman and C. La Hoz, "Radar Observations of F-Region Equatorial Irregularities," J. Geophys. Res., Vol. 81, No. 31, pp. 5447-5466 (November 1976).
3. E. Costa and M. C. Kelley, "On the Role of Steepened Structures and Drift Waves in Equatorial Spread F," J. Geophys. Res., Vol. 83, No. A9, pp. 4359-4364 (September 1978).
4. E. Costa and M. C. Kelley, "Linear Theory for the Collisionless Drift Wave Instability with Wavelengths Near the Ion Gyroradius," J. Geophys. Res., Vol. 83, No. A9, pp. 4365-4368 (September 1978).
5. J. D. Huba, P. K. Chaturvedi, S. L. Ossakow, and D. M. Towle, "High Frequency Drift Waves with Wavelengths Below the Ion Gyroradius in Equatorial Spread F," Geophys. Res. Lett., Vol. 5, No. 8, pp. 695-698 (August 1978).
6. R. T. Tsunoda, "Backscatter Measurements of 11-cm Equatorial Spread-F Irregularities," Proceed. of the Summer Equatorial Experiment Data Review Meeting, 18 March (1980).
7. M. C. Kelley and E. P. Szuszczewicz, private communication (1980).
8. J. D. Huba and S. L. Ossakow, "Destruction of Cyclotron Resonances in Weakly Collisional, Inhomogeneous Plasmas," Phys. Fluids, Vol. 22, No. 7, pp. 1349-1354 (July 1979).

9. J. D. Huba and S. L. Ossakow, "On the Generation of 3-m Irregularities During Equatorial Spread F by Low-Frequency Drift Waves," J. Geophys. Res., Vol. 84, No. A11, pp. 6697-6709 (November 1979).
10. J. L. Sperling and S. R. Goldman, "Electron Collisional Effects on Lower Hybrid Drift Instabilities in the Ionosphere," J. Geophys. Res., Vol. 85, No. 47, pp. 3494-3498 (July 1980).
11. B. B. Kadomtsev, Plasma Turbulence (Academic Press, New York, 1965).
12. A. A. Rukhadze and V. P. Sulin, "Kinetic Theory of Drift-Dissipative Instabilities of a Plasma," Sov. Phys. Uspekhi, Vol. 11, p. 659 (1969).
13. A. B. Mikhailovskii and O. P. Pogutse, "Kinetic Theory of Oscillations of an Inhomogeneous Plasma with Collisions," Sov. Phys.-Tech. Phys., Vol. 11, p. 153 (1966).
14. S. I. Braginskii, Reviews of Plasma Physics, Vol. I, p. 215, M. A. Leontovich, ed., (Consultants Bureau, New York, 1965).
15. F. S. Johnson, Satellite Environment Handbook, Chap. I, F. S. Johnson, ed., Stanford University Press, Stanford, CA (1961).
16. E. P. Szuszczewicz, R. T. Tsunoda, R. Narcisi, and J. C. Holmes, "PLUMEX I--Coincident Radar and Rocket Observations of Equatorial Spread F," DNA Report, Proceed. of the Summer Equatorial Experiment Data Review Meeting, 18 March (1980).
17. E. P. Szuszczewicz and J. C. Holmes, "The Pulsed Plasma Probe Experiment: In-Situ Measurements of Electron Density, Temperature and Density Fluctuation Power Spectra," DNA Report, Proceed. of the Summer Equatorial Experiment Data Review Meeting, 18 March (1980).
18. J. F. Drake, "Irreversibility and Transport in the Lower-Hybrid-Drift Instability," U. of Md. preprint PL80-033 (submitted to Phys. Fluids), 1980.

NUMERICAL SIMULATIONS OF EQUATORIAL SPREAD F,
USING ALTAIR INCOHERENT-BACKSCATTER-MEASURED
ELECTRON-DENSITY PROFILES

S. T. Zalesak

and

S. L. Ossakow

Geophysical and Plasma Dynamics Branch
Plasma Physics Division
Naval Research Laboratory
Washington, DC 20375

ABSTRACT

Using electron-density profiles measured by the ALTAIR radar on 17 July 1979, we have performed global large-scale-size numerical simulations of the nonlinear evolution of the collisional Rayleigh-Taylor instability in the equatorial ionosphere. The ALTAIR profiles were taken approximately four and one-half hours prior to the launch of a rocket equipped with plasma diagnostics instrumentation, and about one hour prior to the onset of equatorial spread F. Using 5-percent amplitude sinusoidal initial perturbations in our numerical simulations, we find fully developed spread-F bubbles (plumes) on time scales of approximately one-half hour for both small (8 km) and large (200 km) horizontal scale lengths.

I INTRODUCTION

During the 17 July 1979 DNA PLUMEX I experiment, coordinated measurements of equatorial spread F (ESF) were carried out by (1) radar backscatter using the ALTAIR radar, (2) plasma diagnostics using in-situ rocket probes, and (3) scintillation measurements using the DNA Wideband satellite. Prior to the rocket launches, however, ALTAIR was used to monitor the equatorial environment into which the rockets would be launched. In particular, off-perpendicular "incoherent" scans were made, giving direct profiles of electron density versus altitude, as well as coherent-backscatter measurements. Using a background laminar-electron-density profile of this type, which was taken before the onset

of spread F, as the ambient laminar ionospheric profile, we have performed numerical simulations of the nonlinear evolution of the collisional Rayleigh-Taylor instability. This phenomenon is believed to be the cause¹⁻⁵ of the large-scale irregularities during ESF.

Our results indicate fully developed spread-F plumes (bubbles) on time scales of approximately one-half hour, using initial sinusoidal perturbations of 5-percent amplitude and two different horizontal wavelengths (8 km and 200 km). ALTAIR radar and ionosonde data indicate fully developed spread F at approximately one hour after the aforementioned profile was taken.⁶ The difference in times could easily be accounted for simply by assuming a smaller initial perturbation, i.e., the present measurements do not provide us with all the pertinent initial conditions prior to ESF onset. Other factors, such as (1) the significant differences between local and magnetic-field-line integrated Pedersen conductivities, (2) the shorting effects of background E-region conductivities, and (3) the effect of inertial terms in the ion-momentum equation (ignored in our simulations) could also delay the progress of the instability. Notwithstanding these effects, our aim was to show that these types of global large-scale numerical simulations of the collisional Rayleigh-Taylor mechanism are consistent with the onset time and morphology of ESF during the 17 July 1979 campaign. We also find that the large-horizontal-scale-length bubbles consist of plasma which originated at much lower altitudes than that of their small-horizontal-scale-length counterparts, resulting in bubbles with much greater depletion in the large-horizontal-scale-length case. This last effect is explained by using scaling arguments similar to those that apply to the fringe field at the edge of a parallel plate capacitor.⁵

In Section II we briefly review the relevant theory and equations used in the numerical simulations; in Section III we present and analyze the numerical results; and in Section IV a summary is presented.

II THEORY

A complete description of our theoretical and numerical model of the equatorial spread-F phenomenon has already been published.⁴ To explain the phenomenon briefly, we assume that the magnetic-field-line integrated Pedersen conductivity in the equatorial ionosphere is dominated by, and is therefore proportional to, the local (equatorial) Pedersen conductivity, which in turn is proportional to the product of the local ion-neutral collision frequency and the local electron density. This enables us to carry out our simulations in a two dimensional (x,y) coordinate system. The constant magnetic field \bar{B} is aligned along the \hat{z} axis (pointing north). Gravity is directed along the negative \hat{y} axis. $n(y)$, $v_R(y)$, and $v_{in}(y)$ are the ambient electron density, recombination coefficient, and ion-neutral collision frequency respectively. Magnetic-field lines are assumed to terminate at both ends in an electrically insulated medium (currents must close in the two-dimensional plane, not in some distant E region).

Following Ossakow et al.,⁴ we describe the system with the two-fluid plasma continuity and momentum equations:

$$\frac{\partial n_\alpha}{\partial t} + \nabla \cdot (n_\alpha \bar{v}_\alpha) = - v_R n_\alpha , \quad (1)$$

and

$$\left(\frac{\partial}{\partial t} + \bar{v}_\alpha \cdot \nabla \right) \bar{v}_\alpha = \frac{q_\alpha}{m_\alpha} \left(\bar{E} + \frac{\bar{v}_\alpha \times \bar{B}}{c} \right) \bar{g} - v_{on} (\bar{v}_\alpha - \bar{U}_n) , \quad (2)$$

where the subscript, α , denotes the species (i for ions, e for electrons), n is the species number density, \bar{v} is velocity, v_R is the recombination coefficient, \bar{E} is the electric field, \bar{g} is the gravitational acceleration, q is the species charge, v_{on} is the species collision frequency with the neutral atmosphere, \bar{U}_n is the neutral wind velocity, c is the speed of light, and m is the species mass.

Note that, in contrast to Ossakow et al.,⁴ we have dropped the term $+ v_R n_{\alpha 0}$ from Eq. (1). This is the equivalent of dropping the assumption of the existence of an ionization source given by that term. This ionization source was such that the ambient ionization profiles, $n_{\alpha 0}(y)$, was an equilibrium profile, $(\partial n_{\alpha 0} / \partial t = 0)$. Our present model, therefore, has instead

$$\frac{\partial n_{\alpha 0}}{\partial t} = - v_R n_{\alpha 0} . \quad (3)$$

Hence, when normalized results $n_{\alpha}(x,y)/n_{\alpha 0}(y)$ are later presented, it should be understood that both the numerator and denominator are time dependent.

Figure 1 shows the recombination rate, v_R , and ion-neutral collision frequency, v_{in} , used in our simulations. It will be seen presently that v_{en} need not be specified as long as it is much smaller than the electron gyrofrequency, ω_e . For details on the form of v_{in} and v_R , as depicted in Figure 1, see Ossakow et al.⁴ If we neglect the inertial terms (the left-hand side) of Eq. (2) by assuming the inertial time scales are much larger than either the gyroperiods or the mean time between collisions, then the equation can be inverted to give an algebraic expression for \tilde{v}_{α} . In two-dimensional (x,y) geometry with \vec{B} along the \hat{z} axis, the solution is, for our problem, with $m_e \ll m_i$, $v_{in}/v_i \ll 1$, $v_{en}/\omega_e = 0$ (where $\alpha = eB/m_{\alpha}c$), and $\tilde{v}_n = 0$,

$$\tilde{v}_e = \frac{c}{B} \vec{E} \times \hat{z}, \quad \hat{z} = \frac{\vec{B}}{|\vec{B}|} , \quad (4)$$

and

$$\tilde{v}_i = \left(\frac{g}{i} + \frac{c}{B} \vec{E} \right) \times \hat{z} + \frac{v_{in}}{i} \left(\frac{g}{i} + \frac{c}{B} \vec{E} \right) . \quad (5)$$

We now make the electrostatic approximate,

$$\vec{E} = \nabla \phi , \quad (6)$$

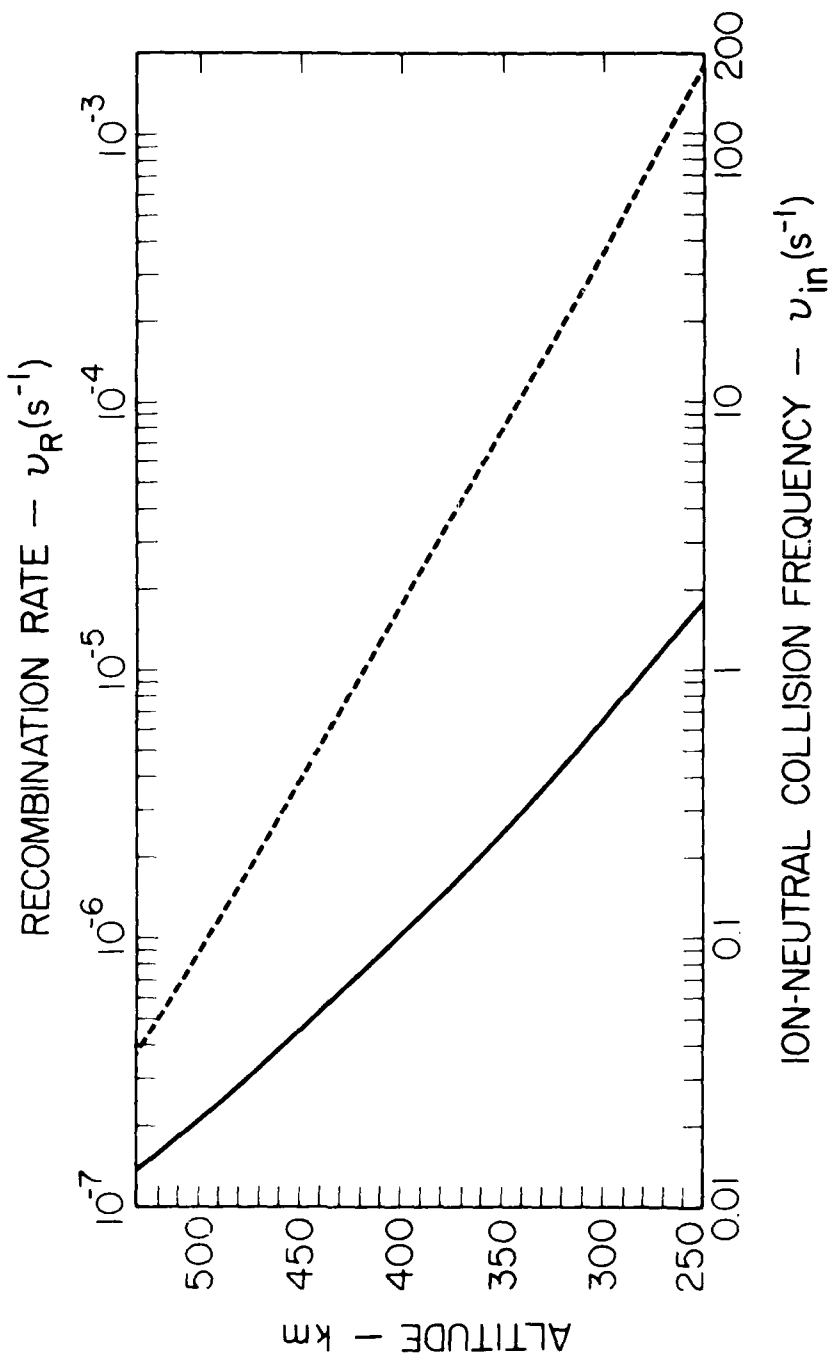


FIGURE 1 ION-NEUTRAL COLLISION FREQUENCY (SOLID LINE), v_{in} , AND RECOMBINATION COEFFICIENT (RATE), v_R , AS A FUNCTION OF ALTITUDE

where

$\nabla_{\perp} \equiv \hat{x}(\partial/\partial x) + \hat{y}(\partial/\partial y)$, and the quasi-neutrality approximation $n_e \approx n_i \equiv n$.

We then have

$$\nabla_{\perp} \cdot \bar{j} = 0 , \quad (7)$$

and

$$\bar{j} \equiv en(\bar{v}_i - \bar{v}_e) . \quad (8)$$

Substituting Eq. (4) and Eq. (5) into Eq. (8) and evaluating Eq. (7), we have for the electrostatic potential:

$$\nabla_{\perp} \cdot (v_{in} n \nabla_{\perp} \phi) = - \frac{m_i}{e} g \frac{\partial}{\partial y} (v_{in} n) - \frac{B}{c} g \frac{\partial n}{\partial x} \quad (9)$$

As in Ossakow et al.,⁴ we set $\phi = \phi_0 + \phi_1$, where $\nabla_{\perp} \phi_0 = - (m_i g/e) \hat{y}$. Because $\nabla_{\perp}^2 \phi_0 = 0$, our final potential equation becomes

$$\nabla_{\perp} \cdot (v_{in} n \nabla_{\perp} \phi_1) = - \frac{Bg}{c} \frac{\partial n}{\partial x} . \quad (10)$$

The effect of ϕ_0 is merely to superimpose a bulk westward plasma velocity g/m_i on the electron velocity field, determined from ϕ_1 , without affecting the morphology of the developing structures; hence, we ignore this motion. In addition, we have ignored any upward or downward bulk motion of the ionospheric plasma, i.e., any ambient eastward or westward electric field. This is done because we have chosen a starting time for our simulation, which, while prior to ESF onset, coincides⁶ with essentially no upward or downward bulk motion of the ionospheric plasma.

Our assumption of quasi-neutrality has made one of our two continuity equations, Eq. (1), redundant; therefore, we choose the electron equation for its simplicity:

$$\frac{\partial n}{\partial t} - \frac{\partial}{\partial x} \left(\frac{nc}{B} \frac{\partial \phi_1}{\partial y} \right) + \frac{\partial}{\partial y} \left(\frac{nc}{B} \frac{\partial \phi_1}{\partial x} \right) = - v_R n . \quad (11)$$

III NUMERICAL SIMULATION RESULTS AND DISCUSSION

Equations (10) and (11), together with appropriate boundary conditions, constitute the nonlinear system of equations we shall solve numerically. The numerical calculations to be presented were performed on a two-dimensional cartesian (x,y) mesh, using 42 points on the x (east-west) axes and 142 points on the y (vertical) axis. The (uniform) grid spacing was 2 km on the y axis for all calculations. The grid spacing on the x axis was 200 m in the "small" horizontal-scale-length cases and 5 km in the "large" cases. The bottom of the grid corresponds to 282-km altitude and the top of the grid to 564-km altitude in all simulations. Periodic boundary conditions were imposed on both n and ϕ_1 on the x-axis. In the y axis, transmittive boundary conditions were imposed on n ($\partial n / \partial y = 0$) and Neumann boundary conditions ($\partial \phi_1 / \partial y = 0$) were imposed on ϕ_1 .

Three kinds of plots will be presented: (1) contours of constant $n(x,y,t)$; (2) contours of constant $n(x,y,t)/n_o(y,t)$; and (3) contours of constant electrostatic potential ϕ_1 . Superimposed on each contour plot is a broken line depicting $n_o(y,t)$ for reference purposes. Our initial electron density profile $n_o(y,0)$ is taken from data supplied to us by Tsunoda,⁷ and is derived from an off-perpendicular VHF ALTAIR scan taken at 0804 UT on 17 July 1979. We found it necessary to introduce some smoothing of the raw data by using a standard Shuman filter, to eliminate spurious regions of stability and instability in the initial profile. In general, the bottomside gradient scale lengths associated with this profile are quite a bit larger than those we have used in previous simulations.^{4,5} This factor by itself would tend to give us smaller linear growth rates for the collisional Rayleigh-Taylor instability. This decrease in linear growth rate is, however, offset by the fact that the whole ionosphere is somewhat higher (an effect that tends to increase the linear growth rate) than that used in our previous work.⁴

The higher altitude of the ionosphere, however, will not offset one other effect of the large initial gradient scale lengths: viz., the displacement of a plasma fluid element vertically for a given distance will result in a smaller relative depletion level. All other things being equal, larger gradient scale lengths in the initial electron density profile will therefore produce bubbles with less depletions. To summarize, we expect approximately equal growth times, but bubbles with less depletion than we have seen in our previous work.

Our initial perturbation is given by a pure sine wave of wavelength $40(\Delta x)$, our system length on the x axis:

$$\frac{n(x,y,0)}{n_0(y,0)} = 1 - e^{-3} \cos\left(\frac{\pi x}{20\Delta x}\right) . \quad (12)$$

Two simulations have been run:

- (1) S, with $\Delta x = 200$ m; and
- (2) L, with $\Delta y = 5$ km.

These two cases are meant to span the range of actual observed horizontal scale lengths. Figure 2 shows isodensity contours of calculation S at six times during the simulation. Figure 3 shows the same contours at six different times for calculation L. The presence of lower density plasma in the bubble in calculation L is obvious. It is also obvious that calculation S seems to proceed in two separate stages, with a small, low-depletion-level bubble going through the F2 peak at about 1200 s, followed by the main, somewhat more depleted, bubble 800 s later. This is in contrast to calculation L, where plasma from much lower altitudes is drawn up into the bubble in one stage. Note that in both cases we have fully developed plumes (bubbles) in 2000 s.

Late-time contours of relative electron density, $n(x,y,t)/n_0(y,t)$, are shown for calculations S and L in Figures 4(a) and 4(b), respectively. Solid lines define depleted regions, and broken lines define enhancements. For depletions, the contour levels are such that for the first (outermost) contour, n/n_0 is 0.5; and for each succeeding contour,

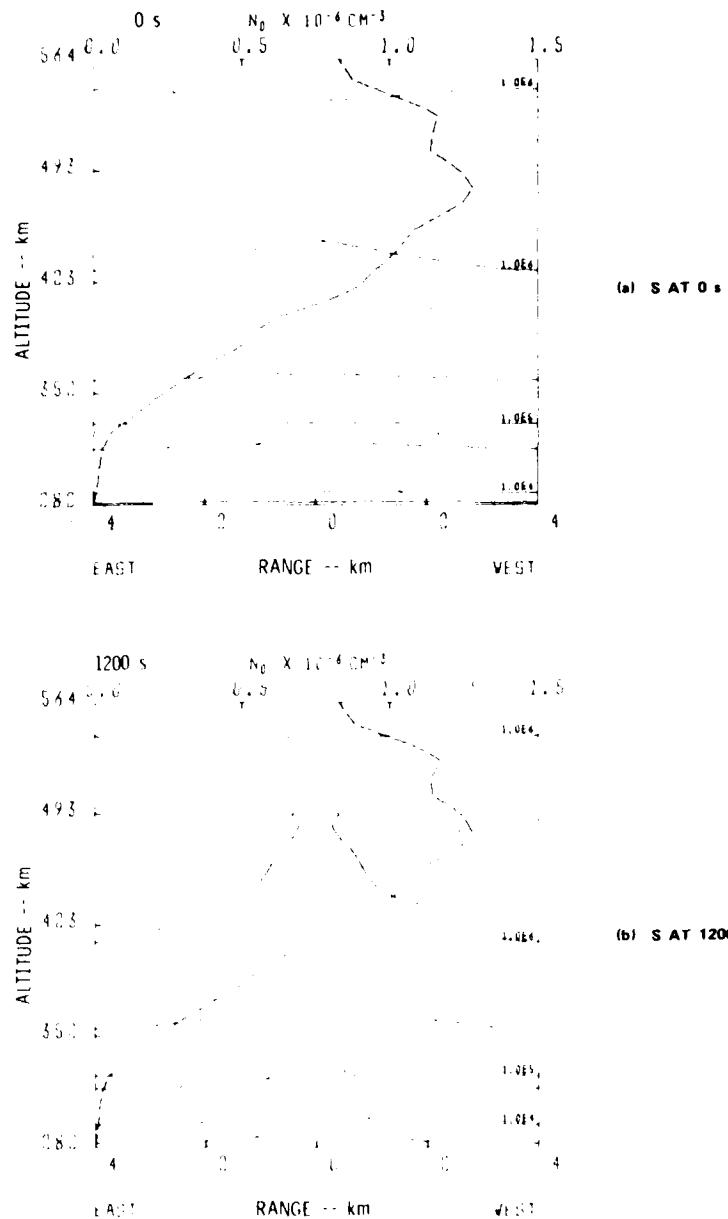


FIGURE 2 SEQUENCE OF SIX PLOTS SHOWING ISOELECTRON-DENSITY CONTOURS OF CALCULATION S AT 0, 1200, 1650, 1850, 1950, AND 2050 s. Superimposed on each plot is a long dashed line depicting $n_0(y,t)$. Electron densities are given in cm^{-3} . The observer is looking southward.

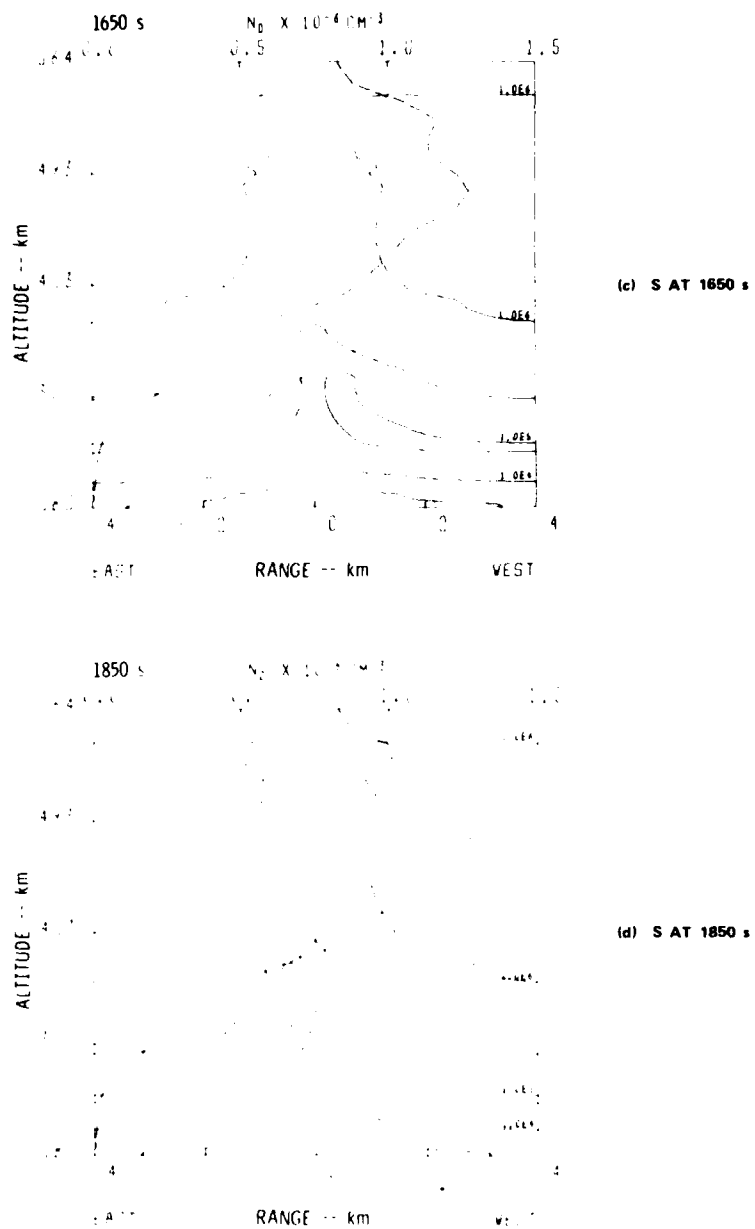


FIGURE 2 (continued) SEQUENCE OF SIX PLOTS SHOWING ISOELECTRON-DENSITY CONTOURS OF CALCULATION S AT 0, 1200, 1650, 1850, 1950, AND 2050 s. Superimposed on each plot is a long dashed line depicting $n_0(y,t)$. Electron densities are given in cm^{-3} . The observer is looking southward.

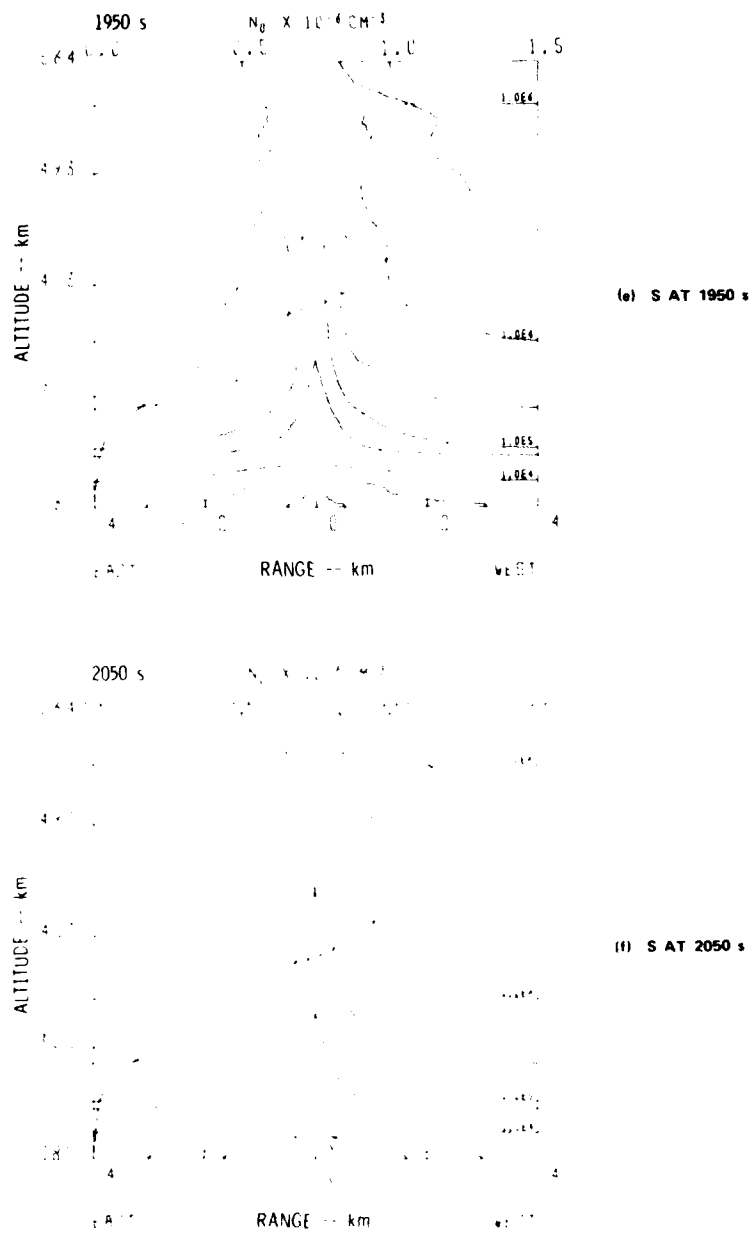


FIGURE 2 (concluded) SEQUENCE OF SIX PLOTS SHOWING ISOELECTRON-DENSITY CONTOURS OF CALCULATION S AT 0, 1200, 1650, 1850, 1950, AND 2050 s. Superimposed on each plot is a long dashed line depicting $n_0(y,t)$. Electron densities are given in cm^{-3} . The observer is looking southward.

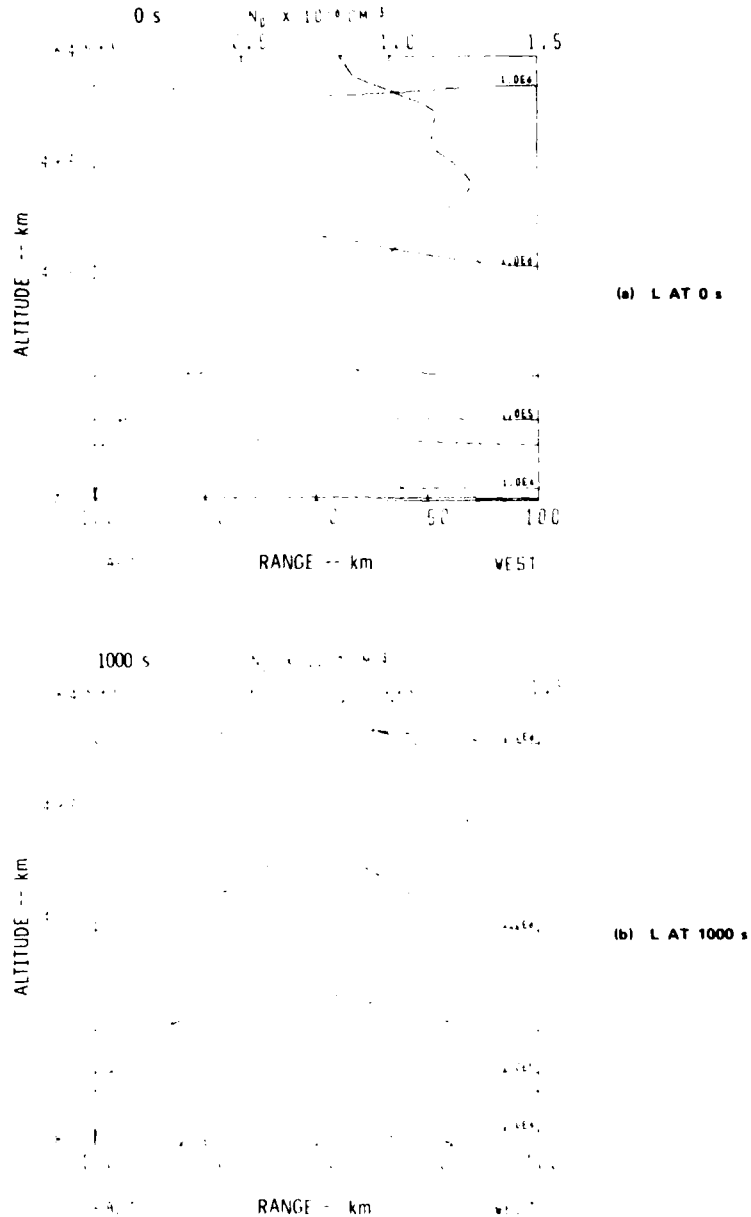


FIGURE 3 SEQUENCE OF SIX PLOTS SHOWING ISOELECTRON-DENSITY CONTOURS OF CALCULATION L AT 0, 1000, 1500, 1750, 1850, AND 1946 s. Superimposed on each plot is a long dashed line depicting $n_0(y,t)$. Electron densities are given in cm^{-3} . The observer is looking southward.

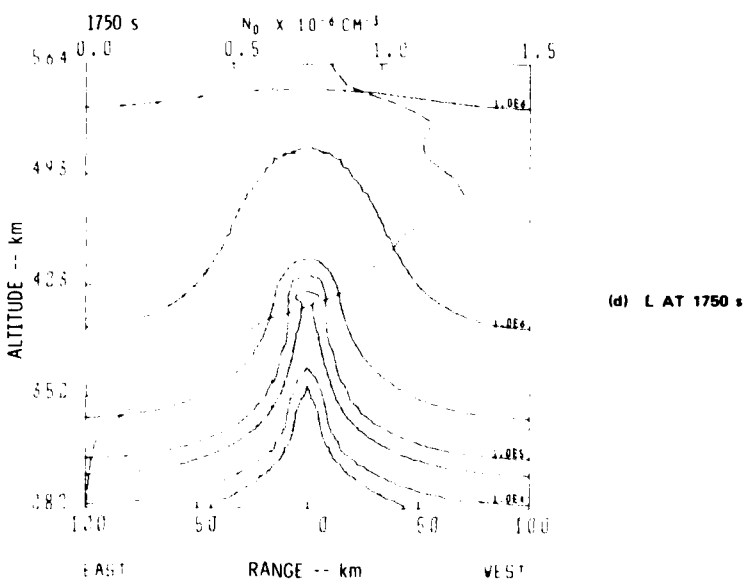
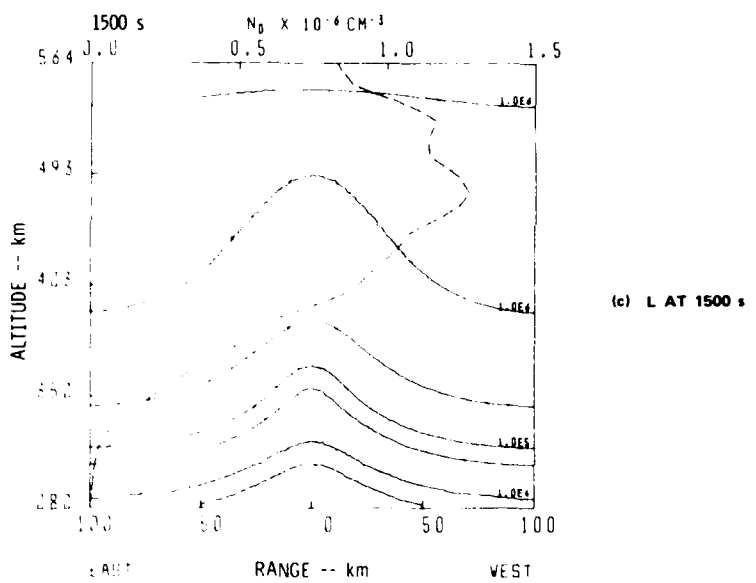


FIGURE 3 (continued) SEQUENCE OF SIX PLOTS SHOWING ISOELECTRON-DENSITY CONTOURS OF CALCULATION L AT 0, 1000, 1500, 1750, 1850, AND 1946 s. Superimposed on each plot is a long dashed line depicting $n_0(y,t)$. Electron densities are given in cm^{-3} . The observer is looking southward.

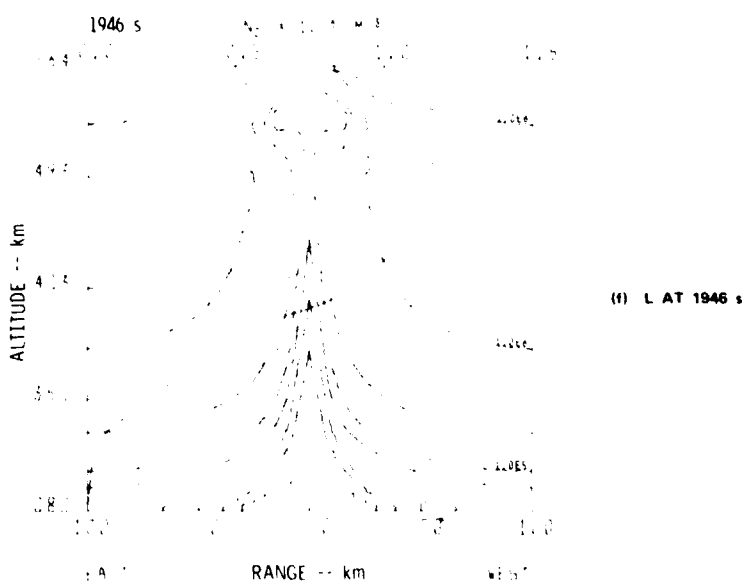
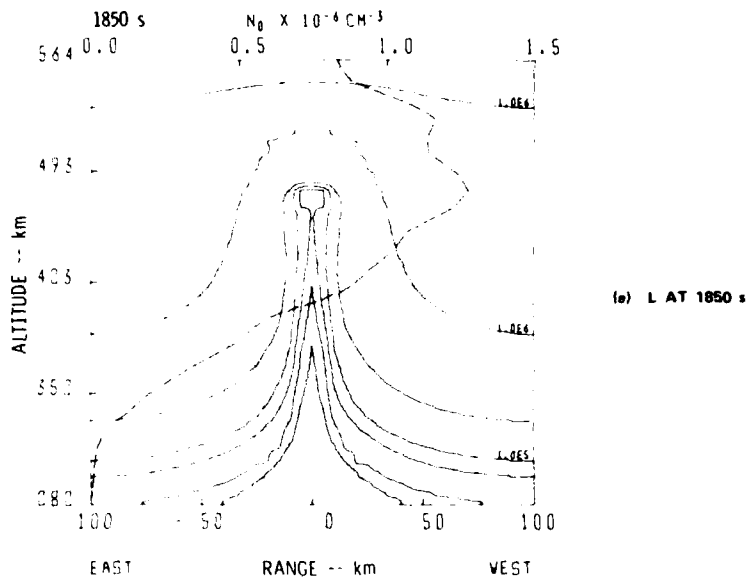


FIGURE 3 (concluded) SEQUENCE OF SIX PLOTS SHOWING ISOELECTRON-DENSITY CONTOURS OF CALCULATION L AT 0, 1000, 1500, 1750, 1850, AND 1946 s. Superimposed on each plot is a long dashed line depicting $n_0(y,t)$. Electron densities are given in cm^{-3} . The observer is looking southward.

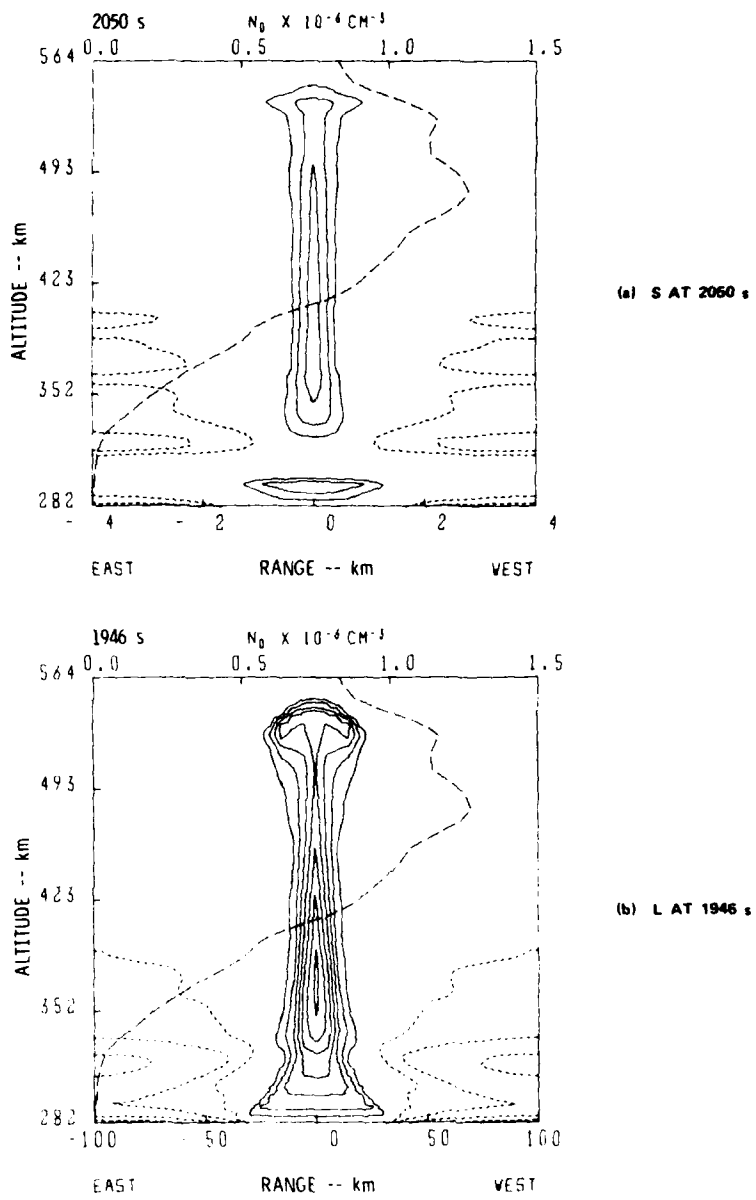


FIGURE 4 CONTOURS OF THE CONSTANT, $n(x,y,t)/n_0(y,t)$, FOR (a) CALCULATION S AT 2050 s, AND (b) CALCULATION L AT 1946 s. Depletions, $n/n_0 < 1$, are shown in solid lines while enhancements, $n/n_0 > 1$, are shown as broken lines. The first (outermost) depletion contour is for $n/n_0 = 0.5$, and each succeeding contour is for a value of n/n_0 , a factor of 0.5 times the previous one. The first enhancement contour is for $n/n_0 = 2.0$, and each succeeding contour is for a value of n/n_0 , a factor of 2.0 times the previous one. The superimposed long dashed line depicts $n_0(y,t)$.

n/n_o is multiplied by 0.5. The third solid contour line thus represents a value of n/n_o that is equal to $(0.5)^3 = 0.125$, or an 87.5-percent depletion. For the first broken contour line, n/n_o is 2.0; and for each succeeding contour line, n/n_o is multiplied by 2.0. Percentage enhancements and depletions are obtained by subtracting 1.0 from n/n_o . Comparison of Figures 4(a) and 4(b) shows that the depletion level of the large-horizontal-scale bubble is greater than that of the small-horizontal-scale bubble. Neither of these calculations, furthermore, attain the depletion levels seen in our previous work (Figure 7 in Zalesak and Ossakow⁵). For instance, in the calculation shown in Figure 7(b) of Zalesak and Ossakow,⁵ which is identical to our calculation (except for the initial ambient electron density profile), a plume of almost 200-km vertical extent can be found with depletion levels of 99.9 percent or greater. A look at Figure 4(b) shows that a plume of similar dimensions can be found only for depletion levels of 94 percent or greater. These smaller depletion levels for the ALTAIR profile were expected, based on our analysis of the effects of larger gradient scale lengths in the initial electron-density profile, which was presented earlier in this section.

An explanation for the reason that larger horizontal-scale-lengths produce more severely depleted bubbles is given in Zalesak and Ossakow.⁵ To summarize briefly, scale analysis is invoked to show that the vertical extent of the polarization electric field produced by a perturbation in the ionosphere scales as the horizontal extent of that perturbation. Because the electric field produces plasma movement, the vertical extent of the polarization electric field will determine the depth in the ionosphere from which a bubble may draw plasma. The lower the altitude that a plasma fluid element originates, the lower its density is; therefore, the higher the depletion level is of any plume into which it is drawn. To illustrate this point, we show in Figures 5(a) and 5(b) contours of the polarization potential, ϕ_1 , for calculation S at 1650 s, and for calculation L at 1750 s, respectively. Contours of constant ϕ_1 are in fact streamlines for this flow [see Eqs. (4) and (6)]. Calculation S consists of two convective cells, each mixing plasma over a fairly

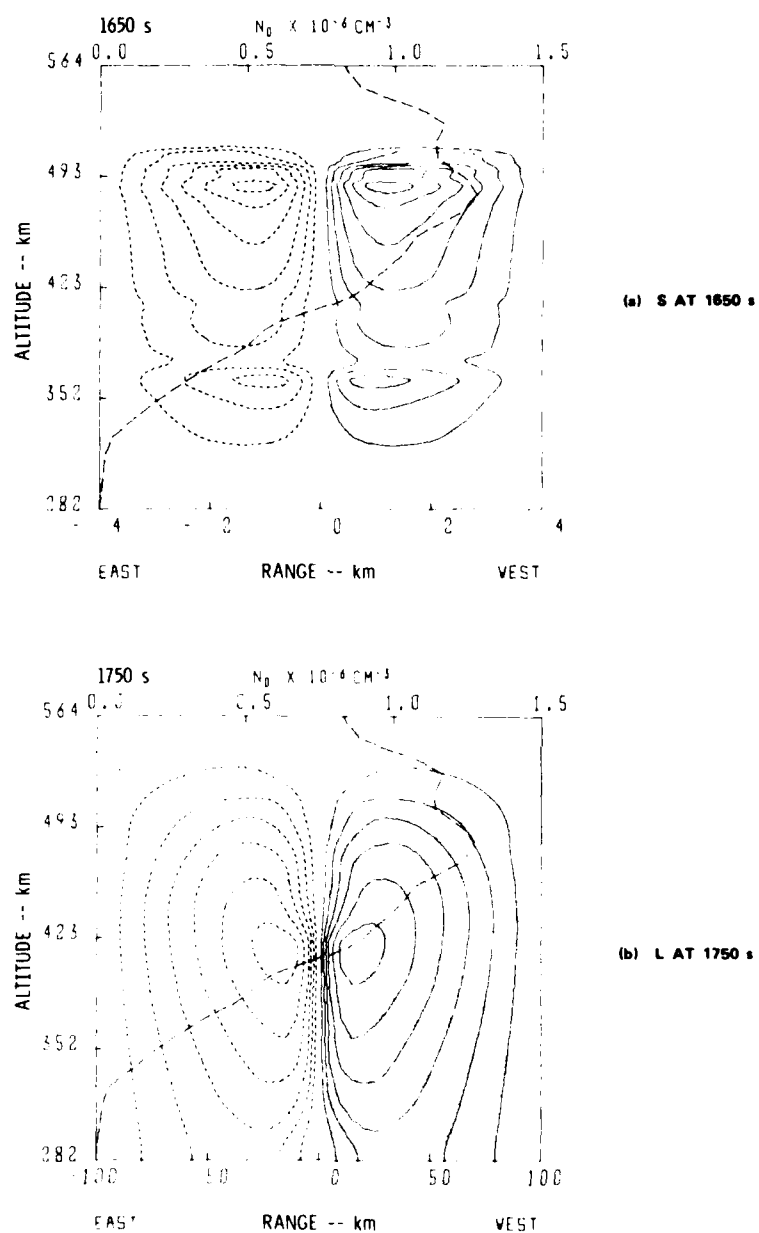


FIGURE 5 CONTOURS OF THE CONSTANT ELECTROSTATIC POTENTIAL, ϕ_1 , FOR (a) CALCULATION S AT 1650 s, AND (b) CALCULATION L AT 1750 s. Positive potentials are shown as solid lines, and negative potentials are shown as broken lines. The contour levels are spaced equally from minimum to maximum, except that the zero contour is suppressed. Superimposed on each plot is a long dashed line depicting $n_0(y,t)$.

narrow altitude range, whereas calculation L has formed a deep convective cell that draws plasma into the plume from very low altitudes.

IV SUMMARY

Both of our global large-scale collisional Rayleigh-Taylor nonlinear simulations, using a background electron-density profile from ALTAIR incoherent radar measurements on 17 July 1979 (prior to spread F onset), indicate fully developed ESF bubbles in approximately one-half hour. ALTAIR radar and ionosonde measurements indicated fully developed spread-F backscatter about one hour after the profile was taken. The most obvious explanation is that we have possibly chosen a perturbation amplitude that was too large, but because no in-situ measurements were made prior to ESF, the measurements do not provide us with all the pertinent initial conditions prior to ESF onset. Other factors, such as (1) the shorting effects of background E-region conductivities, or (2) the neglect of inertial terms in the ion-momentum equation, could also influence the speed with which the instability proceeds. In addition, neither the chain of events that leads from kilometer-scale bubbles to 1-m backscatter irregularities, nor the associated time delays, are well understood. Our simulations, nevertheless, exhibit results which are consistent with the onset time of ESF during the 17 July 1979 Kwajalein campaign.

A word of caution is in order here with regard to a comparison of the bubbles we show in our simulations and the actual structures into the PLUMEX I rocket was launched⁵,⁶ at 1231 UT on 17 July 1979. According to ALTAIR measurements,⁸ starting with the onset of spread F at about 0900 UT and lasting until approximately the time of rocket launch, the bottomside of the F region moved downward approximately 140 km, and at the same time developed much smaller gradient scale lengths⁹ than we have used in the present simulation. In addition, the bubbles detected by the in-situ plasma probe at these later times shows depletions $\lesssim 90$ percent. At least three factors are in competition here: (1) the downward movement of the ionospheric plasma indicates the presence of an electric field, which would tend to reduce the growth rate of the

instability; (2) lower altitudes mean larger v_{in} , which again would reduce the growth rate; and (3) the development of smaller bottomside gradient scale lengths enhances the growth rate. In addition, the ALTAIR radar operating in the coherent mode showed that VHF plumes (looking at 1-m field-aligned irregularities) at this late time during ESF were in a decay phase of development. Decaying plumes that had been generated early (while the ionosphere was high) would not disappear simply because the plasma had been displaced downward later in the evening. Obviously, the actual physical situation at the rocket launch time is more complex than that addressed by the simulations presented here; many of these complexities will be treated accurately in forthcoming versions of our simulation model.

ACKNOWLEDGMENTS

This work was supported by the Defense Nuclear Agency.

REFERENCES

1. B. B. Balsley, G. Haerendel, and R. A. Greenwald, "Equatorial Spread F: Recent Observations and a New Interpolation," J. Geophys. Res., Vol. 77, No. 28, pp. 5625-5628 (October 1972).
2. G. Haerendel, "Theory of Equatorial Spread F" (Max-Planck Inst. für Phys. and Astrophys., Garching, German, 1974).
3. A. J. Scannapieco and S. L. Ossakow, "Nonlinear Equatorial Spread F," Geophys. Res. Lett., Vol. 3, No. 8, pp. 451-454 (August 1976).
4. S. L. Ossakow, S. T. Zalesak, B. E. McDonald, and P. K. Chaturvedi, "Nonlinear Equatorial Spread F: Dependence on Altitude of F Peak and Bottomside Background Electron Density Gradient Scale Length," J. Geophys. Res., Vol. 84, No. A1, pp. 17-30 (January 1979).
5. S. T. Zalesak and S. L. Ossakow, "Nonlinear Equatorial Spread F: Spatially Large Bubbles Resulting from Large Horizontal Scale Initial Perturbations," J. Geophys. Res., Vol. 85, No. A5, pp. 2131-2140 (May 1980).
6. R. T. Tsunoda, "ALTAIR Radar Measurements in Support of the PLUMEX Rocket Campaign," Proceed. of the Summer Equatorial Experiment Data Review Meeting, 18 March 1980 (1980).

7. R. T. Tsunoda, private communication (1980).
8. E. P. Szuszczewicz, R. T. Tsunoda, R. Narcisi, and J. C. Holmes, "PLUMEX I: Coincident Radar and Rocket Observations of Equatorial Spread F," Proceed. of the Summer Equatorial Experiment Data Review Meeting, 18 March 1980 (1980).
9. E. P. Szuszczewicz and J. C. Holmes, "The Pulsed Plasma-Probe Experiment: In-Situ Measurements of Electron Density, Temperature, and Density Fluctuation Power Spectra," Proceed. of the Summer Equatorial Experiment Data Review Meeting, 18 March 1980 (1980).

NONLINEAR EVOLUTION OF THE COLLISIONAL RAYLEIGH-TAYLOR INSTABILITY FOR INTERMEDIATE WAVELENGTHS IN THE 17 JULY 1979 KWAJALEIN DESCENDING SPREAD-F IONOSPHERE

M. J. Keskinen

Berkeley Research Associates
Arlington, VA 22209

S. L. Ossakow

Geophysical and Plasma Dynamics Branch
Plasma Physics Division
Naval Research Laboratory
Washington, DC 20375

ABSTRACT

The nonlinear evolution of the collisional Rayleigh-Taylor instability in the intermediate-wavelength (100 m to 1 km) regime in local unstable regions of downward-moving equatorial F layers has been studied using numerical simulation. For ambient bottomside electron-density gradient scale lengths, $L = 8$ and 25 km, large percentage depletions and spatial power spectra that agree with the *in-situ* rocket observations during the DNA sponsored 17 July 1979 Kwajalein equatorial spread-F campaign.

I INTRODUCTION

Recently on 17 July 1979 coincident rocket^{1,2*} and radar³ observations of equatorial spread F were made at the Kwajalein Atoll in the Marshall Islands. The *in-situ* rocket data indicated that major depletions were distributed throughout the downward-moving F layers with

*References are listed at the end of this paper.

intermediate-wavelength ($\lambda \sim 25$ m - 1 km) irregularity spatial power spectra that are well described by inverse power laws. The VHF radar measurements showed that the backscatter "plumes," in addition to having a large vertical extent from the bottomside to the topside [see Kelley et al.,⁴ McLure et al.,⁵ and Woodman and La Hoz⁶], were collocated spatially with the plasma depletions^{7,8} and could be characterized by both a growth and a decay phase.³

Several features of the small-scale-irregularity ($\lambda \lesssim 3$ m) signatures seen by the radar backscatter can be explained by various plasma kinetic instabilities [for a review, Ossakow⁹] that presumably are driven by steep gradients within developing plasma bubbles. On the other hand, there is now evidence that the large-scale irregularities result from a collisional Rayleigh-Taylor instability^{10,11} that is driven by the ambient bottomside plasma density gradient. Global^{12,13,14} and local¹⁵ numerical simulations of the collisional Rayleigh-Taylor instability have reproduced successfully the large plasma-density depletions (bubbles) and associated spatial power spectra that have been experimentally observed. However, the aforementioned in-situ rocket observations^{1,2} were made in an F layer that was moving downward,¹ which implies the existence of a large-scale westward electric field. The importance of this electric field in describing the development of plasma bubbles has been discussed by several authors.^{13,16,17,18} However, the previous analytical and numerical studies of the nonlinear collisional Rayleigh-Taylor instability have not included the effects of an upward- or downward-moving F layer in realistic geometries.

In this paper we study the effects of a downward-moving F layer on the development of the intermediate-wavelength (100 m to 1 km) collisional Rayleigh-Taylor instability. In addition we compare our results with the recent 17 July 1979 DNA Kwajalein in-situ rocket data.^{1,2}

II SUMMARY OF DATA

On 17 July 1979 by 2100 LT, the bottomside of the F region had risen to an approximate altitude of 400 km. The F layer then began a

downward drift at an approximate velocity^{1,19} of $v_D \cong 10$ m/s with a simultaneous onset of spread F. With the F layer drifting downward and spread-F conditions continuing, a rocket was launched (1231:30 UT, 17 July 1979) when the bottomside F layer had descended to an altitude below 300 km. The upleg-rocket data indicated that major depletions ($\delta n_e/n_e^{Bo} \leq 90\%$) were distributed throughout the F region, with the highest percentage of the fluctuations located in the bottomside near the 260-km altitude. In a particular bottomside region centered near 270 km (Region C of Szuszczewicz and Holmes), whose density gradient scale length was $L \cong 8$ km, but which was surrounded by an $L \cong 25$ km region, the irregularity spatial spectra were described by an inverse power law, $\sim k^{-2.5}$, over the wave-number domain² between $2\pi/1 \text{ km}^{-1}$ and $2\pi/25 \text{ m}^{-1}$.

III EQUATIONS AND RESULTS

The two fluid equations describing the collisional Rayleigh-Taylor instability in the presence of a zeroth-order horizontal westward electric field, \bar{E}_o , have been given (S. F. Ossakow et al.¹³ and Anderson and Haerendel¹³). These equations can be written as follows:

$$\frac{\partial n}{\partial t} - \frac{c}{B} (\nabla_{\perp} \phi_1 \times \hat{z}) \cdot \nabla_{\perp} n = - v_R (n - n_o) \quad (1)$$

$$\nabla_{\perp} \cdot (v_{in} n \nabla_{\perp} \phi_1) = \bar{E}_o \cdot \nabla_{\perp} (v_{in} n) + \frac{B}{c} (\bar{g} \times \hat{z}) \cdot \nabla_{\perp} n \quad (2)$$

where n , ϕ_1 , v_R , v_{in} , B , \bar{g} , and ∇_{\perp} are the ion density, the perturbed electrostatic potential, the recombination coefficient, the ion-neutral collision frequency, the magnetic field, gravity, and the two-dimensional derivative perpendicular to the magnetic field, respectively. All other symbols retain their conventional meaning. Because we are interested in studying intermediate wavelengths ($\lambda \sim 100$ m - 1 km), we have ignored inertial and temperature effects in Eqs. (1) and (2). We have written Eqs. (1) and (2) in a downward-moving frame whose velocity is $\bar{v}_D = c \bar{E}_o \times \bar{B}/B^2 \cong 10$ m/s and made the separation¹³ $\nabla \phi_i = \nabla \phi - m_i \bar{g}/c + \bar{E}_o$,

where φ is the total electrostatic potential defined by $\bar{E} \equiv -\nabla\varphi$. Furthermore, we have adopted the following coordinate system: the magnetic field, \bar{B} , is the z -axis (north), the y -axis (vertical) denoted altitude with $\bar{g} \approx -\hat{g}\hat{y}$, and the x -axis points westward. By linearizing Eqs. (1) and (2) and writing $n_1 \equiv n - n_o$, $\varphi_1 \propto \exp[i(k_x x + k_y y) + \gamma_k t]$, $\bar{k} \cdot \bar{B} = 0$, and $|\bar{k}|L \gg 1$ we find

$$\gamma_k = \left(\frac{\bar{g}}{v_{in}} \pm \frac{cE_o}{B} \right) \left(\frac{k_x}{k} \right)^2 \frac{1}{L} - v_R \quad (3)$$

$$\text{where } \bar{E}_o = \pm E_o \hat{x}, \quad L = \left(\frac{1}{n_o} \frac{\partial n_o}{\partial y} \right)^{-1}, \quad k^2 = k_x^2 + k_y^2$$

From Eq. (3) we note that we recover the usual collisional Rayleigh-Taylor instability if $E_o \rightarrow 0$. The growth rate, γ_k , is enhanced (reduced) by an eastward (westward) electric field, \bar{E}_o . We are concerned only with a westward electric field, $\bar{E}_o = E_o \hat{x}$, which produces a downward moving F layer.

By defining $n(x,y) = n(x,y)/n_o(y)$, $\varphi_1(x,y) = \varphi_1(x,y)/BL$, $x' = x/L$, $y' = y/L$, and $t' = ct/L$ where $n_o(y) = n_o(1 + y/L)$ with $n_o = \text{constant}$ in an equilibrium solution of Eqs. (1) and (2), we can write Eqs. (1) and (2) in dimensionless form as follows (after dropping primes for clarity):

$$\frac{\partial n}{\partial t} - \frac{\partial \varphi_1}{\partial y} \frac{\partial n}{\partial x} - \frac{\partial \varphi_1}{\partial x} \frac{\partial n}{\partial y} = \frac{n}{n_o} \frac{\partial n_o}{\partial y} \frac{\partial \varphi_1}{\partial x} - \beta_1(n - 1) \quad (4)$$

$$\frac{\partial^2 \varphi_1}{\partial x^2} + \frac{\partial^2 \varphi_1}{\partial y^2} + \left(\frac{1}{n} \frac{\partial n}{\partial y} + \frac{1}{n_o} \frac{\partial n_o}{\partial y} \right) \frac{\partial \varphi_1}{\partial y} + \frac{1}{n} \frac{\partial n}{\partial x} = -\beta_2 \frac{1}{n} \frac{\partial n}{\partial x} \quad (5)$$

where $\beta_1 = Lv_R/c$ and $\beta_2 = g/cv_{in} - E_o/B$ are dimensionless constants. Eq. (4) was integrated forward in time using a flux-corrected¹⁰ leapfrog-trapezoidal scheme.¹¹ Eq. (5) was solved for the self-consistent potential, φ_1 , using a Chebyshev semiiterative multigrid technique.¹² The computational grid described a small vertical slice of the bottomside

equatorial F layer and is defined by 64 by 64 points with a constant mesh spacing of $\Delta x = \Delta y = 15$ m, which gives an altitude and east-west extent of 960 m. Periodic boundary conditions were imposed on n/n_0 and φ_1 in both the x (east-west) and y (vertical) directions.

The in-situ rocket data of Szuszczewicz and Holmes do not reveal the initial conditions from which the observed irregularities developed. Many sets of initial conditions are possible. In the context of the experimental observations of an initially upward- and then downward-moving F layer,^{1,2,3} we make the reasonable assumption that the irregularities, whose spatial power spectra are sampled² in Region C of the bottomside, originate at a higher altitude(s), y_0 , at earlier time(s) and are convected downward by the ambient F layer. From previous numerical simulations¹⁵ of the intermediate-wavelength collisional Rayleigh-Taylor instability for bottomside gradient scale lengths, $L = 5$ km - 15 km, at an altitude of 300 km, we found that a well-developed nonlinear regime could be achieved after a time, $\Delta t \geq 10 - 15 \gamma_m^{-1}$, where γ_m is the maximum linear growth rate. We compute the altitude, y_0 , as that altitude from which after approximately 10 to 15 growth times, the bottomside will have moved downward to the vicinity of 270 km. This, of course, neglects the fact that $v(y)$ will be decreasing because v_{in} and v_R will be increasing [Eq. (3)] for a downward-moving F layer. In other words, we wish to determine an altitude, $y_0 - 15\gamma^{-1}(y)v_D = 270$ km, where $v_D = 10$ m/s. For $L = 8$ km (25 km), we find $y_0 \cong 335$ km (365 km). From the Jacchia model²³ neutral atmosphere,¹³ $v_R(335 \text{ km}) \cong 0.3 \text{ s}^{-1}$, $v_{in}(365 \text{ km}) \cong 0.18 \text{ s}^{-1}$, $v_R(335 \text{ km}) \cong 1 \times 10^{-4} \text{ s}^{-1}$, $v_R(365 \text{ km}) \cong 10^{-5} \text{ s}^{-1}$ with $\omega_e = 5 \times 10^6 \text{ s}^{-1}$ and $\omega_i = 300 \text{ s}^{-1}$. From these considerations two different numerical simulations were made using² different equilibrium density gradient scale lengths, $L = 8$ km and 25 km. Both simulations were initialized with the following density profile: $n(x,y,t=0)/n_0 = 1 + (y/L) + \epsilon(x,y)$ where $\epsilon(x,y)$ is a random function of position in the x-y plane with a white-noise-like spatial power spectrum (no preferred wavelength) and an rms amplitude of 0.03. This noise-like power spectrum and amplitude were adopted given that long-wave length Rayleigh-Taylor irregularities existed (in that spread F was already exhibited).

Because the real-space dimensions of the computational grid are 960 m by 960 m, the altitude-dependent quantities, $v_{in}(y)$ and $v_R(y)$, do not, at any fixed time, vary appreciably over the grid. Their scale lengths are much greater than the grid dimensions. In fact, these quantities can be fit very well with exponential variation in y , i.e., $v_{in}(y) \propto \exp(-y/L_{in})$ and $v_R(y) \propto \exp(-y/L_R)$ with $L_{in} \cong 55$ km and $L_R \cong 33$ km between the altitudes of 250 and 500 km using a Jacchia model²³ neutral atmosphere.¹³ However, over several thousands of seconds, v_{in} and v_R will change (increase) in a frame moving downward with velocity $v_D = 10$ m/s. To compensate for this effect, we convert the spatial (altitude) dependence of v_{in} and v_R into functions of time by making the substitution $y \rightarrow -v_D t$. In other words, during the course of the simulations, $v_{in}(t) = v_{in}(t_0) \exp(v_D \Delta t / L_R)$ where Δt is the elapsed time and $v_{in}(t_0)$, $v_R(t_0)$ are the initial values depending upon initial altitude. In this simple model we ignore the variation of the bottom-side density-gradient scale length with altitude. We now present the important nonlinear aspects of these simulations.

Figure 1 gives an isodensity contour plot of $\delta n(x,y)/n_o(y)$, $\delta n = n(x,y) - n_o(y)$, at $t = 800$ s for $L = 8$ and shows that the random nature of the initial perturbations still prevails. The contours of the random initial perturbations in $\delta n(x,y)/n_o(y)$ at $t = 0$ s are very similar to Figure 1, but with more smaller-scale structure. Figure 2 displays the evolution of $\delta n(x,y)/n_o(y)$ at $t = 2000$ s in which some vertical elongation and steepening can be seen together with small-scale irregularities. Figure 3 illustrates the perturbation density contours at $t = 4500$ s in which further steepening and vertical elongation have occurred. This late-time density configuration is similar to recent numerical simulations of the intermediate-wavelength collisional Rayleigh-Taylor instability¹⁵ under almost monochromatic initial conditions, i.e., with only two waves initially excited. The maximum percentage depletion ($\delta n/n_o < 0$) in Figure 3 was 56 percent. Similar density-contour development and late-time percentage depletion were found using $L = 25$ km, again starting from random initial conditions. These large depletions were also noted in the in-situ rocket data.²

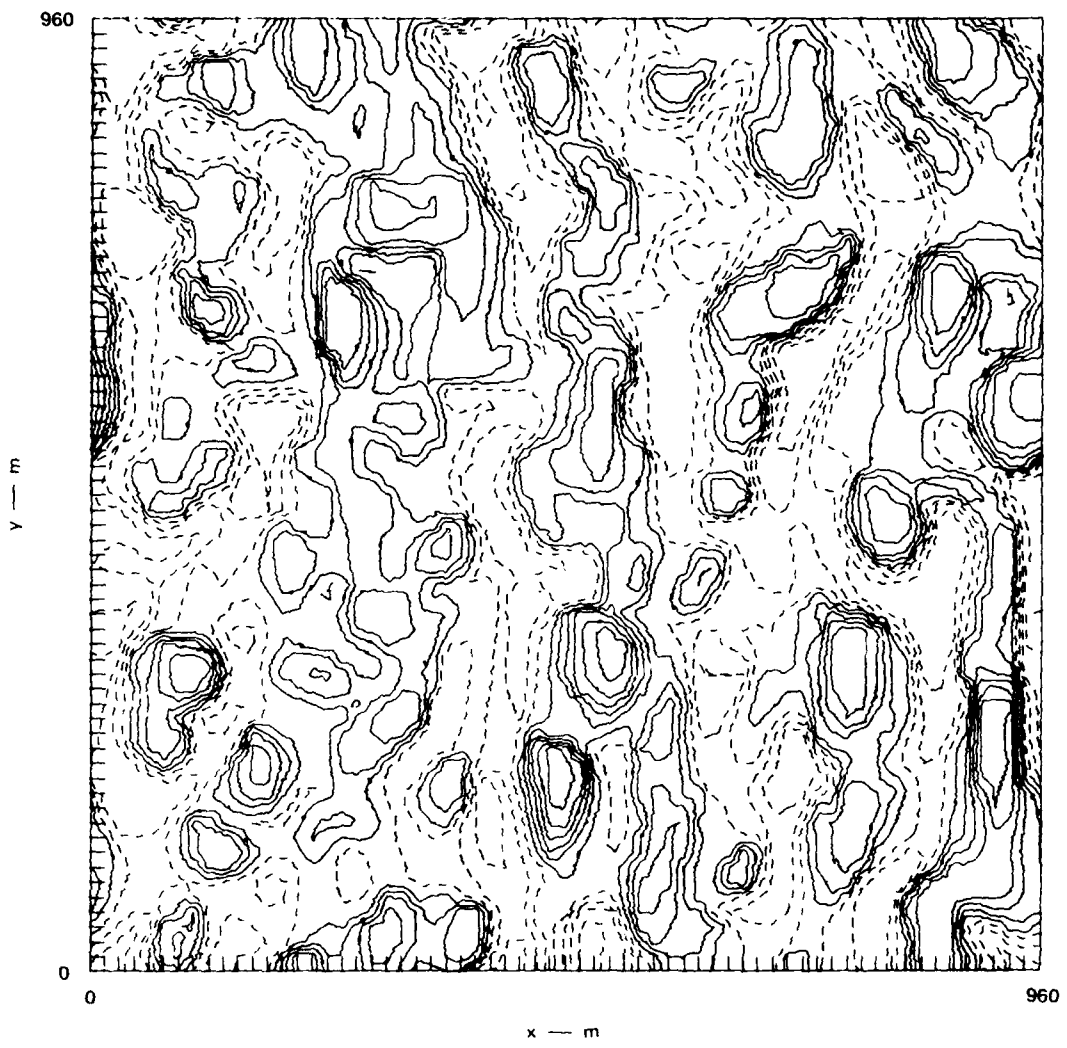


FIGURE 1 DENSITY CONTOURS AT $t = 800$ s

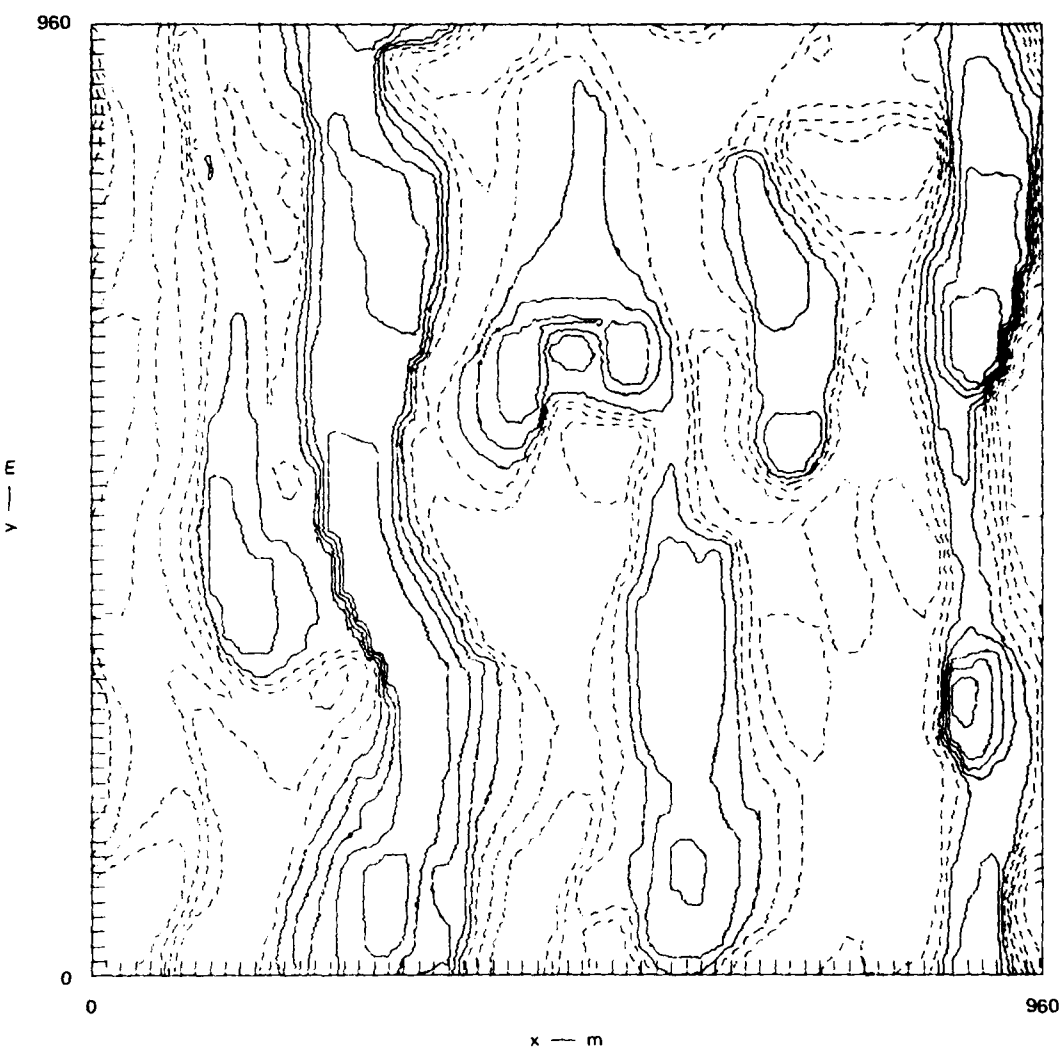


FIGURE 2 DENSITY CONTOURS AT $t = 2000$ s

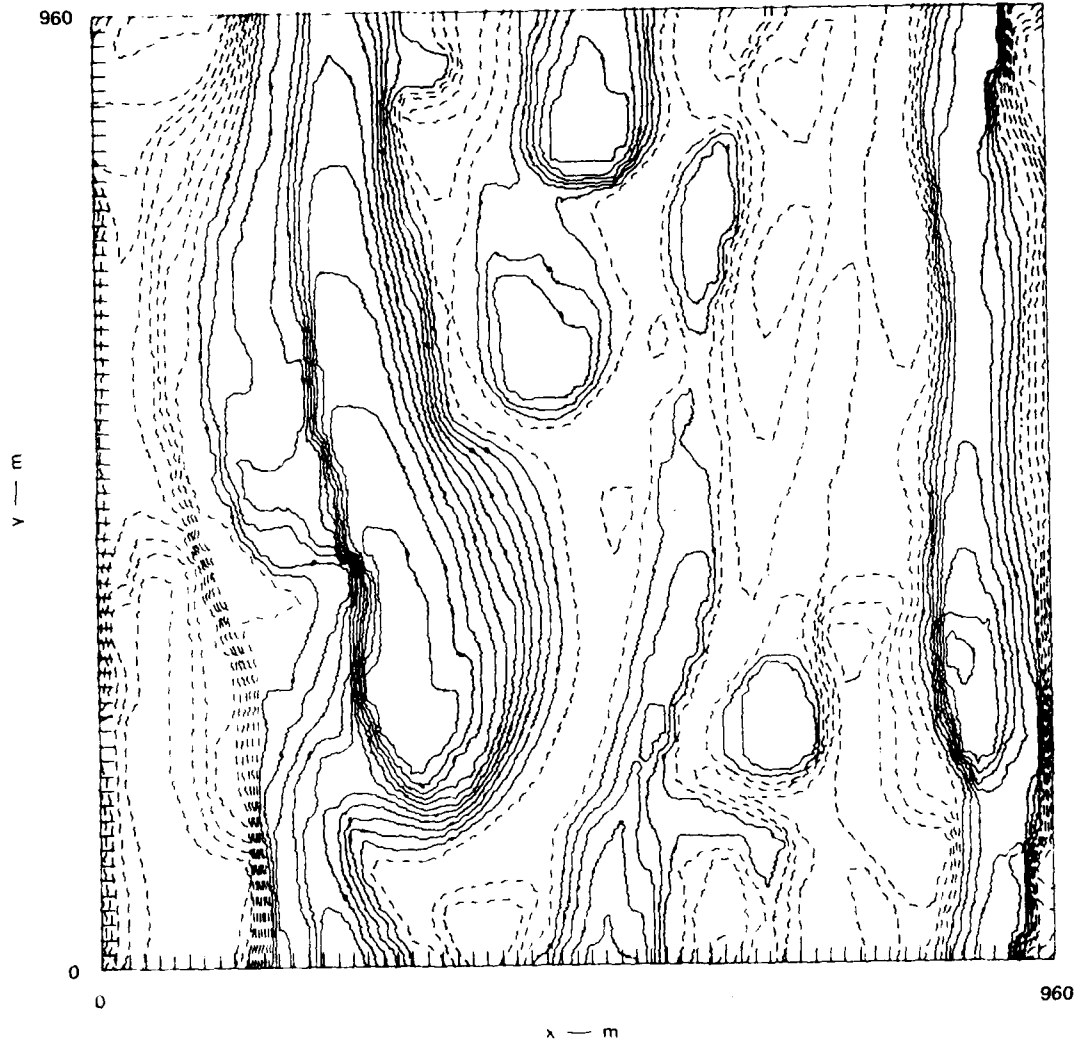


FIGURE 3 DENSITY CONTOURS AT $t = 4500$ s

In Figures 4(a) and 4(b), we have plotted sample one-dimensional horizontal $P(k_x)$ and vertical $P(k_y)$ spatial power spectra for $2\pi/k_x$, $2\pi/k_y$ between approximately 100 m and 960 m in the nonlinear regime for $L = 8$ km at $t = 4000$ s. These power spectra are obtained by integrating $|\delta n(k_x, k_y)/n_0|^2$ over k_x and k_y , respectively. These power spectra are in agreement with the bottomside-irregularity power spectra as determined from rocket observations [Region C of Szuszczewicz and Holmes²] in the wavelength domain $\lambda: 100$ m - 1 km and recent simulations.¹⁵ Similar power laws were found for the $L = 25$ km case at a later time.

IV SUMMARY

We performed numerical simulations of the collisional Rayleigh-Taylor instability in local unstable regions of downward-moving equatorial F layers that model the downward-moving 17 July 1979 Kwajalein ionosphere into which the rocket was fired. For ambient bottomside plasma-density gradient scale lengths, $L = 8$ km and 25 km, the values that were obtained from the rocket in-situ measurements,² we have demonstrated that large percentage of the relative depletions (large irregularity intensity) can develop on time scales of several thousands of seconds from purely random initial conditions. In addition, we have shown that the one-dimensional spatial power spectra of these irregularities in the vertical and east-west directions conform to power laws $\propto k^{-n}$, where $n = 2$ to 2.5 for $2\pi/k$ between 100 m and 1 km. These results are in good agreement with the recent in-situ rocket observations² of intermediate-wavelength ($\lambda: 25$ m - 1 km) irregularities in the 17 July 1979 Kwajalein equatorial spread-F environment, complement previous local numerical simulations,¹⁵ and lend further support to the belief that the collisional Rayleigh-Taylor instability is responsible for large and intermediate scale-size irregularities in equatorial spread F. Given the uncertainties in initial conditions, the present numerical simulations match the in-situ rocket data of Szuszczewicz and Holmes² quite well.

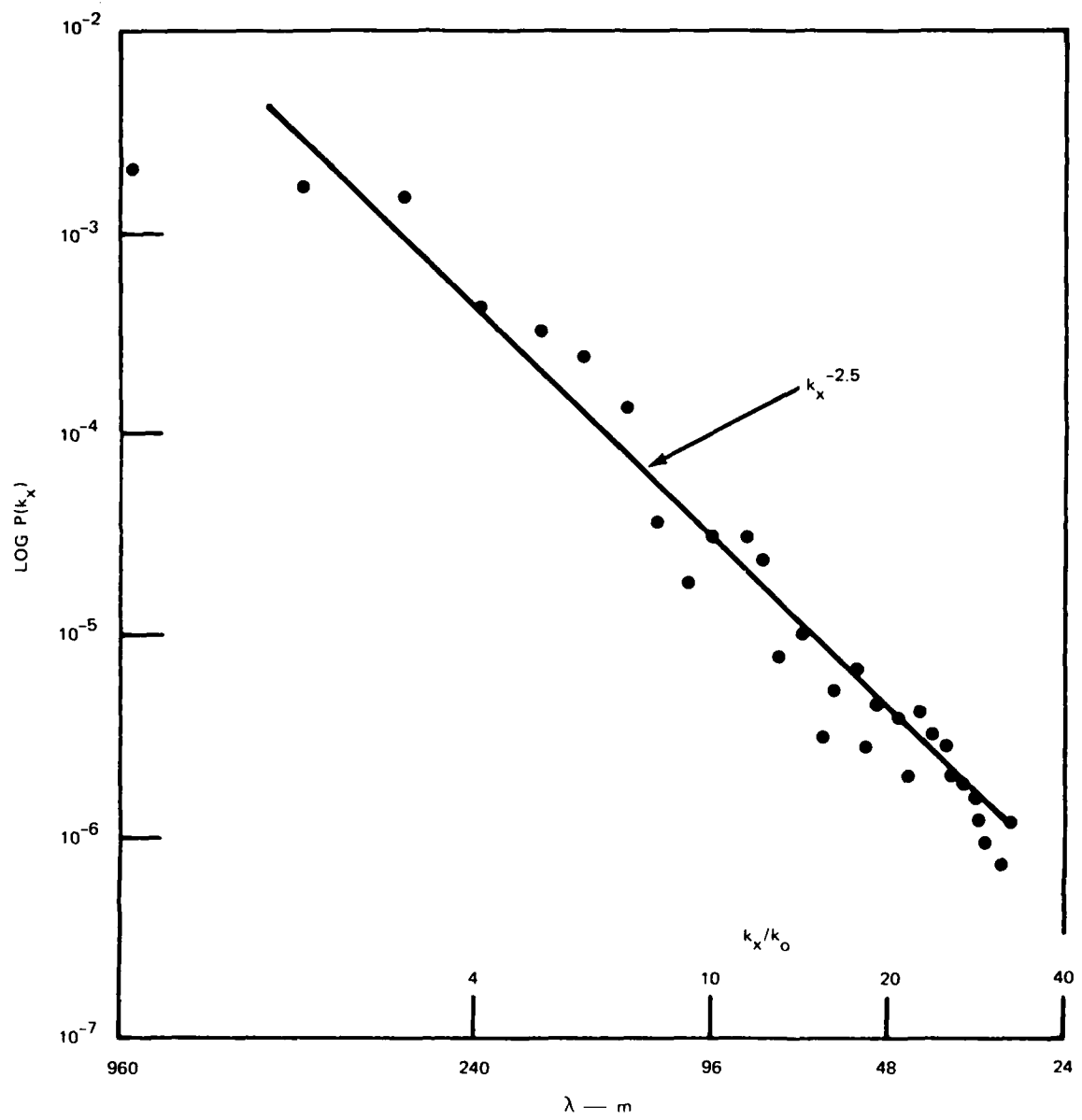


FIGURE 4(a) HORIZONTAL SPATIAL POWER SPECTRA AT $t = 4000$ s

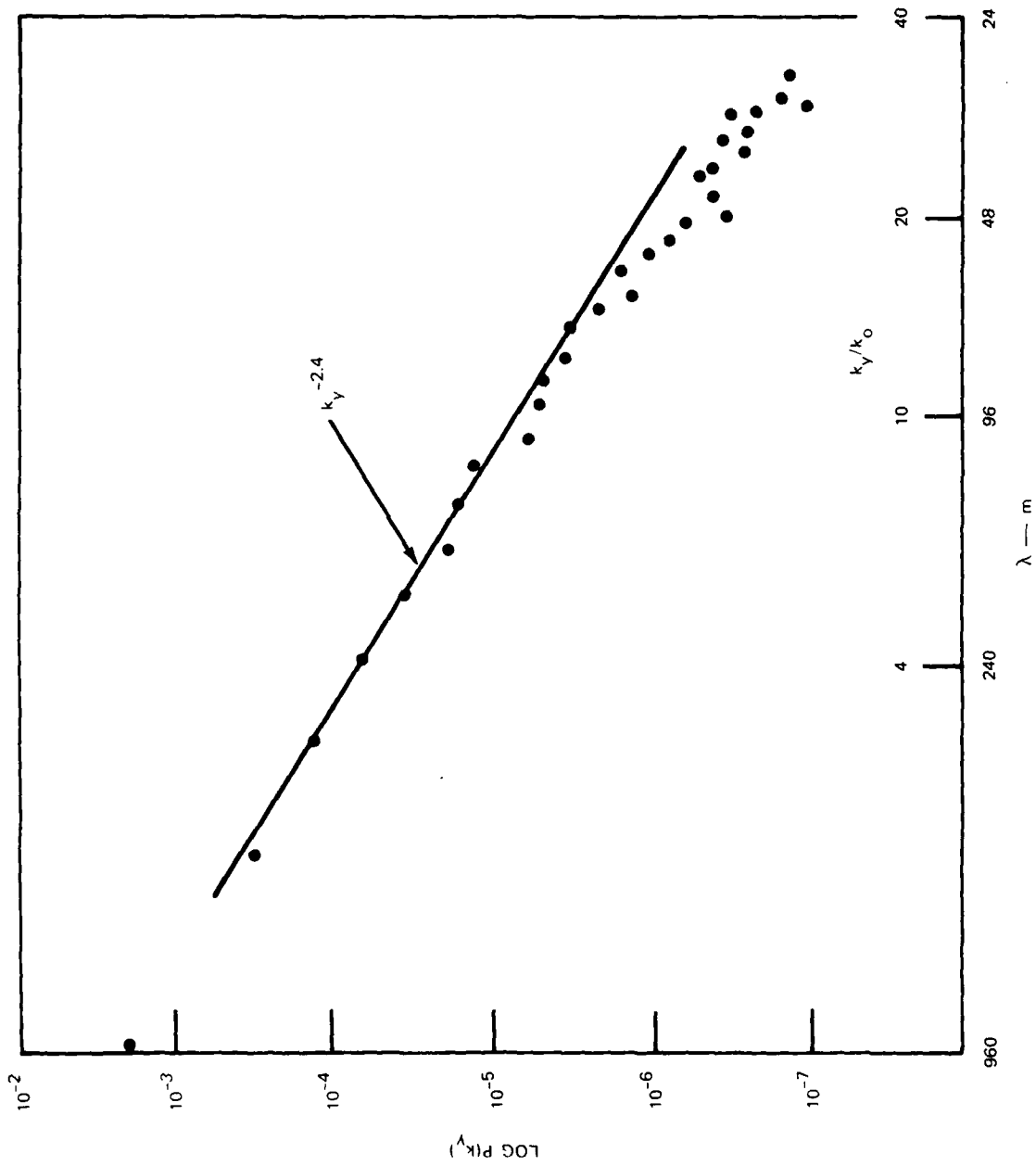


FIGURE 4(b) VERTICAL SPATIAL POWER SPECTRA AT $t = 4000$ s

ACKNOWLEDGMENTS

We wish to thank E. P. Szuszczewicz, R. T. Tsunoda, B. E. McDonald, and S. T. Zalesak for useful discussions. This work was supported by the Defense Nuclear Agency.

REFERENCES

1. E. P. Szuszczewicz, R. T. Tsunoda, R. Narcisi, and J. C. Holmes, "PLUMEX I: Coincident Radar and Rocket Observations of Equatorial Spread F," Proceed. of the Summer Equatorial Experiment Data Review Meeting (18 March 1980).
2. E. P. Szuszczewicz and J. C. Holmes, "The Pulsed Plasma Probe Experiment: In-Situ Measurements of Electron Density, Temperature, and Density Fluctuation Power Spectra," Proceed. of the Summer Equatorial Experiment Data Review Meeting (18 March 1980).
3. R. T. Tsunoda and B. R. White, "Generation and Growth of Equatorial Backscatter Plumes--Growth Phase," submitted to J. Geophys. Res. (1980); Proceed. of the Summer Equatorial Experiment Data Review Meeting, 18 March 1980 (1980).
4. M. C. Kelley, G. Haerendel, H. Kappler, A. Valenzuela, B. B. Balsley, D. A. Carter, W. L. Ecklund, C. W. Carlson, B. Hausler, and R. Torbert, "Evidence for a Rayleigh-Taylor Type Instability and Up-welling of Depleted Density Regions During Equatorial Spread F," Geophys. Res. Lett., Vol. 3, No. 8, pp. 448-450 (August 1976).
5. J. P. McClure, W. B. Hanson, and J. H. Hoffman, "Plasma Bubbles and Irregularities in the Equatorial Ionosphere," J. Geophys. Res., Vol. 82, No. 19, pp. 2650-2656 (July 1977).
6. R. F. Woodman and C. La Hoz, "Radar Observations of F Region Equatorial Irregularities," J. Geophys. Res., Vol. 81, No. 31, pp. 5447-5466 (November 1976).
7. R. T. Tsunoda and D. M. Towle, "On the Spatial Relationship of 1-Meter Equatorial Spread-F Irregularities and Depletions in Total Electron Content," Geophys. Res. Lett., Vol. 6, No. 11, pp. 873-876 (November 1979).
8. R. T. Tsunoda, "On the Spatial Relationship of 1-Meter Equatorial Spread-F Irregularities and Plasma Bubbles," J. Geophys. Res., Vol. 85, No. A1, pp. 185-190 (January 1980).
9. S. L. Ossakow, "Ionospheric Irregularities," Rev. Geophys. and Space Phys., Vol. 17, No. 4, pp. 521-533 (June 1979).

10. B. B. Balsley, G. Haerendel, and R. A. Greenwald, "Equatorial Spread F: Recent Observations and a New Interpretation," J. Geophys. Res., Vol. 77, No. 28, pp. 5625-5628 (October 1972).
11. G. Haerendel, "Theory of Equatorial Spread F," Report, Max-Planck Inst. fur Phys. and Astrophys., Garching, Germany (1974).
12. A. J. Scannapieco and S. L. Ossakow, "Nonlinear Equatorial Spread F," Geophys. Res. Lett., Vol. 3, No. 8, pp. 451-454 (August 1976).
13. S. L. Ossakow, S. T. Zalesak, B. E. McDonald, and P. K. Chaturvedi, "Nonlinear Equatorial Spread F: Dependence on Altitude of F Peak and Bottomside Background Electron Density Gradient Scale Length," J. Geophys. Res., Vol. 84, No. A1, pp. 17-30 (January 1979).
14. S. T. Zalesak and S. L. Ossakow, "Nonlinear Equatorial Spread F: Spatially Large Bubbles Resulting from Large Horizontal Scale Initial Perturbations," J. Geophys. Res., Vol. 85, No. A5, pp. 2131-2142 (May 1980).
15. M. J. Keskinen, S. L. Ossakow, and P. K. Chaturvedi, "Preliminary Report of Numerical Simulations of Intermediate Wavelength Collisional Rayleigh-Taylor Instability in Equatorial Spread F," J. Geophys. Res., Vol. 85, No. A4, pp. 1775-1778 (April 1980).
16. S. L. Ossakow and P. K. Chaturvedi, "Morphological Studies of Rising Equatorial Spread F Bubbles," J. Geophys. Res., Vol. 83, No. A5, pp. 2085-2090 (May 1978).
17. E. Ott, "Theory of Rayleigh-Taylor Bubbles in the Equatorial Ionosphere," J. Geophys. Res., Vol. 83, No. A5, pp. 2066-2071 (May 1978).
18. D. N. Anderson and G. Haerendel, "The Motion of Depleted Plasma Regions in the Equatorial Ionosphere," J. Geophys. Res., Vol. 84, No. A8, pp. 4251-4258 (August 1979).
19. R. T. Tsunoda, private communication, 1980.
20. J. P. Boris and D. L. Book, "Flux-Corrected Transport, I, Shasta, a Transport Algorithm that Works," J. Comput. Phys., Vol. 11, p. 38 (1973).
21. S. T. Zalesak, "Fully Multidimensional Flux-Corrected Transport Algorithms for Fluids," J. Comput. Phys., Vol. 31, No. 3, pp. 335-392 (June 1979).
22. B. E. McDonald, "Explicit Chebychev-Iterative Solution of Nonself-Adjoint Elliptic Equations on a Vector Computer," J. Comput. Phys. (in press), 1980.
23. L. G. Jacchia, "Static Diffusion Models of the Upper Atmosphere with Empirical Temperature Profiles," Smithson, Contrib. Astrophys., Vol. 8, p. 215 (1965).

AD-A099 998

SRI INTERNATIONAL MENLO PARK CA
PROCEEDINGS OF THE SUMMER EQUATORIAL EXPERIMENT DATA REVIEW MEE--ETC(U)
NOV 80 D R McDANIEL

F/G 22/2
DNA001-78-C-0379

NL

UNCLASSIFIED

A...4
A1
A300146

DNA-5528P

END
DATE
ENTERED
n 81
DTIC

STRUCTURE AND COMPOSITION MEASUREMENTS IN EQUATORIAL IONOSPHERIC BUBBLES

R. Narcisi, E. Trzcinski, G. Federico
L. Wlodyka and P. Bench

Aeronomy Division, Air Force Geophysics Laboratory
Hanscom Air Force Base, Bedford, MA 01731

ABSTRACT

Two multiinstrumented (including an ion mass spectrometer) Terrier Malemute rockets were launched from Kwajalein on the nights of 17 and 23 July 1979 during equatorial spread-F events. Detailed ionospheric structure and composition measurements were made between about 100 and 590 km. The first flight penetrated six areas of "bite-outs" spread over the range from 265 to 560 km on the upleg as well as several more depletions on the down-leg. The strongest irregularities, up to 90 percent depletion, occurred at the altitudes from 265 to 285 km, just above the F-region ledge at 250 km. There was no evidence of enhanced bottomside tracer ions (NO^+ , O_2^+ or meteoric ions) in any of the holes which were composed mostly of O^+ and smaller amounts of N^+ . From the composition signatures, the source of the bubbles appeared to be near the F-region ledge. Within the higher-altitude holes the N^+/O^+ ratios were smaller than the adjacent ionosphere ratios, indicating not only that the source regions were near the ledge, but also that the bubbles had started to form earlier when the ledge was at higher altitudes. Although O^+ and N^+ exhibited strong fluctuations, NO^+ and O_2^+ had fairly smooth profiles with scale heights similar to N_2 and O_2 , respectively--demonstrating steady-state conditions and a stable neutral atmosphere with an exospheric temperature of about 1100 K. This suggests that neutral atmospheric turbulence is not a major source of the ionospheric irregularities. Time periods for ion-chemical processes to achieve the observed composition are discussed in terms of bubble-formation times and rise velocities. The second flight showed an F-region ledge near 350 km and irregularities only near the ledge, with O^+ dominating.

I INTRODUCTION

The ion composition inside and outside equatorial depletions has been measured with satellite retarding-potential analyzers and ion mass spectrometers.^{1-4*} Fe^+ ions were found to be either enhanced or depleted within the holes. Molecular ions (NO^+) were often more abundant than O^+ , which predominated outside the holes. Depletions in O^+ up to 10^3 have been observed. The bite-outs varied from a few kilometers to tens of kilometers in width.

The position of the F-region ledge was generally unknown during the satellite measurements. In the equatorial region, the ledge altitude could be greater than 450 km during certain times, while outside this particular region the ledge could be at much lower altitudes. This perhaps explains both the magnitude and shape of some of the measured bite-outs, especially those of large scale, as well as the changes in composition.

To determine the processes of equatorial irregularities more clearly, it was recognized that detailed vertical profiles of the ionospheric plasma parameters were needed (as well as the satellite measurements), coincident with radar, ionosonde, and neutral wind measurements. Such an effort, designated "PLUMEX," was conducted by the Defense Nuclear Agency.

The PLUMEX program, designed to measure equatorial ionospheric irregularities and their effects on communications channels and radar, was conducted at the Kwajalein Atoll (4.3°N dip latitude) during July 1979. As part of this effort two multiinstrumented Terrier Malemute rockets, each with a plasma diagnostics complement of plasma probes, ion mass

*References are listed at the end of this paper.

3

spectrometer, electric-field sensors and a four-frequency beacon were flown during equatorial spread-F events. The first rocket, PLUMEX I, was launched 17 July (0031:30.25 local time) and the second, PLUMEX II, 23 July (2157:30.4 local time). In this paper we present the results from the ion mass spectrometer experiments only. We believe that these represent the first vertical profile measurements of the detailed ion mass composition and structure in equatorial ionospheric plumes.

II INSTRUMENTATION AND MEASUREMENT PROGRAM

Figure 1 shows a schematic of the quadrupole ion mass spectrometer. The two important data outputs of the spectrometer were the total positive ion current collected on the aperture plate that was essentially a dc probe for ionospheric structure measurements and the mass spectra output for species composition. The mass program for the instrument is presented in Figure 2. Five mass numbers were sampled in sixteen sequences. Each programmed mass number was measured for 10 ms so that the total program period was 0.8 s, covering 80 separate mass numbers including mass repetitions for altitude resolution. The species associated with the mass numbers are 1(H⁺), 4(He⁺), 14(N⁺), 16(O⁺), contaminants from water vapor of 17(OH⁺), 18(H₂O⁺), and 19(H₃O⁺), 23(Na⁺), 24-25-26(Mg⁺), 27(Al⁺), 28(Si⁺), 30(NO⁺), 32(O₂⁺) and 54-56(Fe⁺). The remaining mass numbers were sampled to establish background levels. Between 110 and 588 km, the altitude resolution of the aperture plate output decreased from 1.5 to 0.2 m while that for the important ion species decreased from 150 to 20 m each varying with the vehicle velocity, which diminished with increasing altitude. The instrument was mounted on the rocket axis at the forward end of the payload. The PLUMEX payload configuration and flight scenario are described in Figure 3.

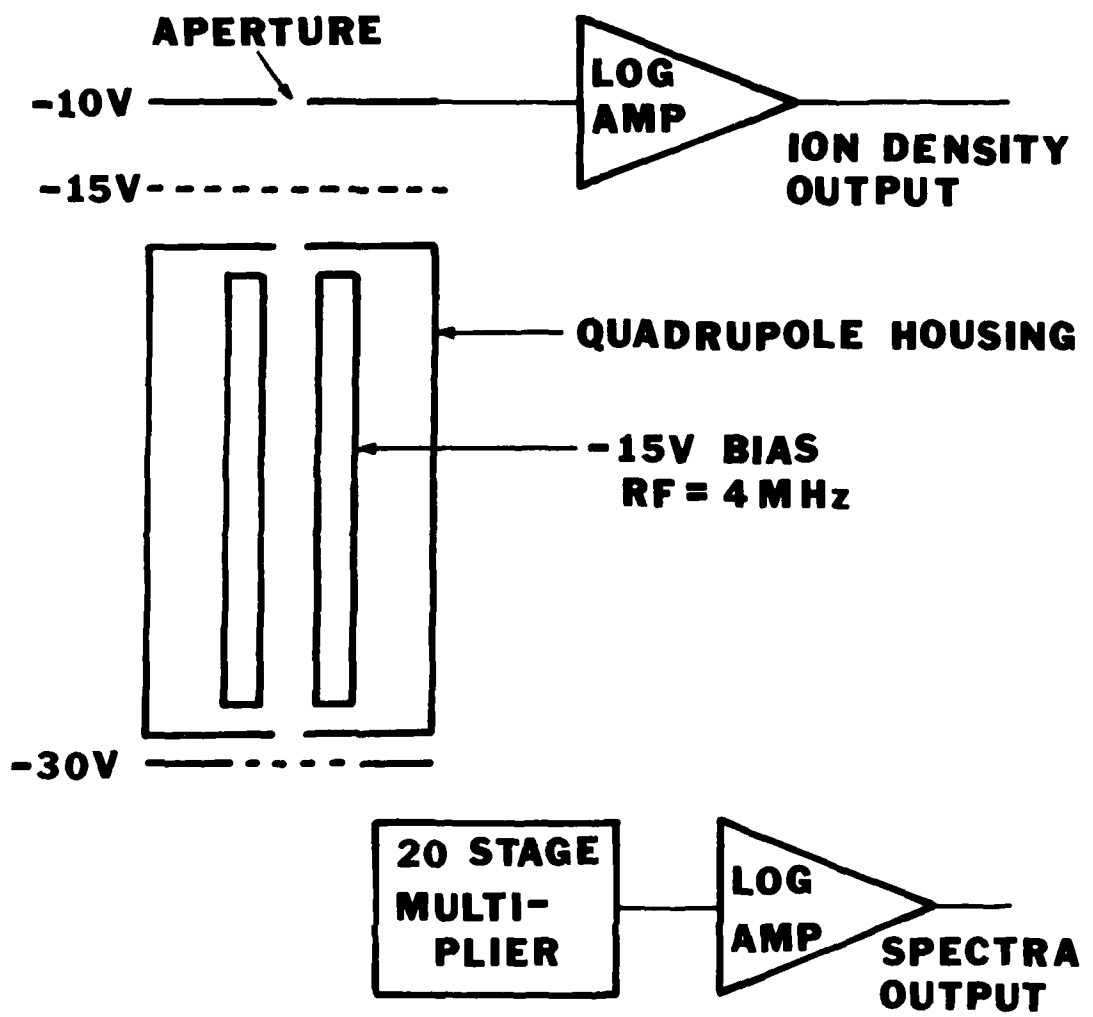


FIGURE 1 SCHEMATIC OF THE QUADRUPOLE ION-MASS SPECTROMETER

MASS PROGRAM

<u>SEQUENCE #</u>	<u>MASS # - AMU</u>				
1.	1	4	14	16	30
2.	1	4	14	16	32
3.	14	16	28	54	56
4.	1	4	14	16	30
5.	1	4	14	16	32
6.	14	16	28	54	56
7.	1	4	14	16	30
8.	1	4	14	16	32
9.	14	16	28	54	56
10.	1	4	14	16	30
11.	1	4	14	16	32
12.	1	4	7	8	56
13.	13	14	15	16	17
14.	18	19	20	21	22
15.	23	24	25	26	27
16.	28	29	30	31	32

SAMPLE RATE: 10 MS/AMU

PROGRAM TIME: 0.8 SECONDS

**FIGURE 2 SPECTROMETER PROGRAM FOR THE MEASUREMENT OF
SELECTED ION-MASS NUMBERS AT HIGH-SPATIAL RESOLUTION**

III MEASUREMENTS AND DISCUSSION

A. PLUMEX I

Figure 4 shows the altitude versus current profiles of the aperture plate output (digitized at 2 kHz and plotted) and the species of O^+ , N^+ ,

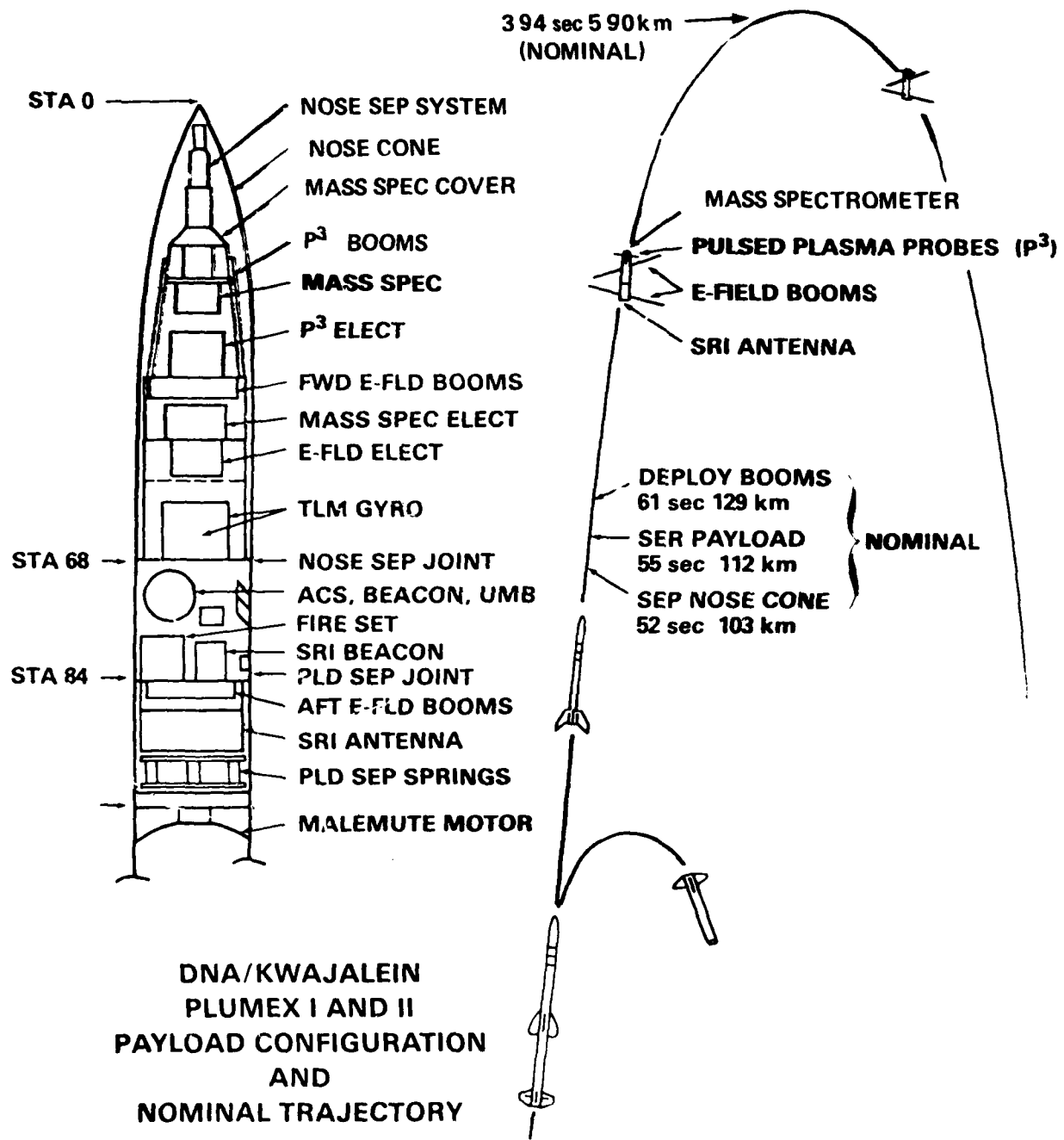


FIGURE 3 PLUMEX PAYLOAD INSTRUMENTATION AND FLIGHT FUNCTIONS

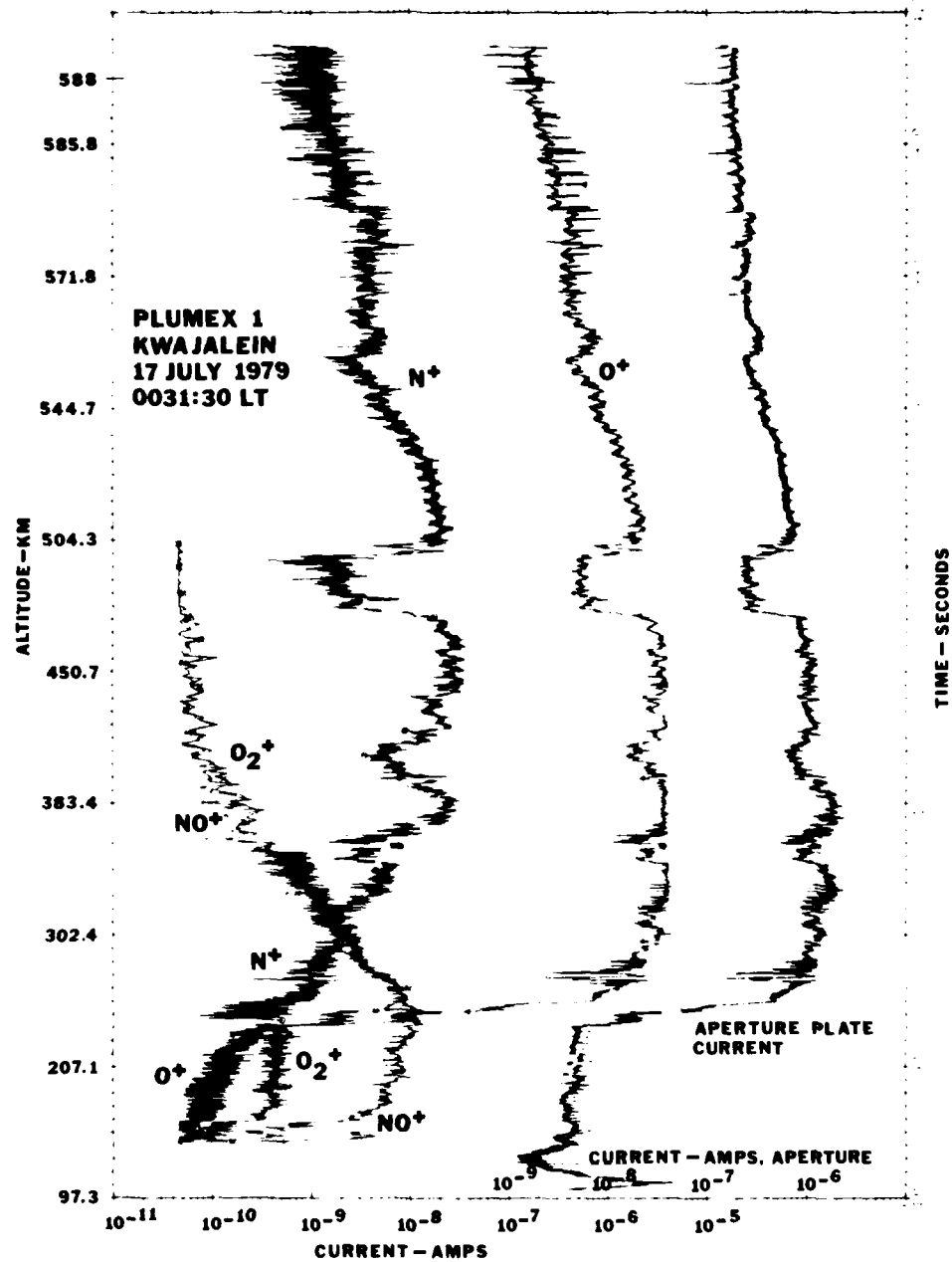


FIGURE 4 ASCENT MEASUREMENTS OF PLUMEX I SHOWING THE APERTURE PLATE, O^+ , N^+ , NO^+ AND O_2^+ CURRENT PROFILES. Baseline current is 4×10^{-11} amps.

and NO^+ measured on ascent on PLUMEX I. The positive spikes on the aperture current below 250 km and the negative spikes at higher altitudes are caused by the nitrogen gas bursts from the attitude control jets. The rocket penetrated six areas of bite-outs in the F region. In no case was there any evidence of enhanced bottomside ions (NO^+ , O_2^+ , nor meteoric ions). The steep F-region ledge was created by O^+ ions where density rose by more than three orders of magnitude over a space of less than 20 km. Estimated ion densities were about 6×10^5 ions/cc at the F peak and about 1100 ions/cc below the ledge with an accuracy of roughly a factor of 2. NO^+ measurements at higher altitudes where the NO^+ was produced during the N_2 jet bursts by the reaction of $\text{O}^+ + \text{N}_2 \rightarrow \text{NO}^+ + \text{N}$ were not plotted in Figure 4.

The strongest ionospheric fluctuations with up to 90 percent depletion occurred between 265 and 285 km. An expanded plot of this region is given in Figure 5. Note that the O^+ and N^+ ions generally follow the ionospheric fluctuations as depicted by the aperture plate current while NO^+ and O_2^+ do not. It can be shown that the NO^+ and O_2^+ have steady-state distributions under the prevailing ionospheric conditions.

Figure 6 depicts the NO^+ and O_2^+ chemistry. Because the recombination coefficients (α) and reaction rates (k) vary mainly with temperature that is relatively constant over the altitude range 250 to 400 km, the NO^+ and O_2^+ concentrations should be directly proportional to the N_2 and O_2 concentrations respectively, as long as

$$[\text{O}^+] \approx N_e \gg ([\text{NO}^+] + [\text{O}_2^+]) .$$

The molecular ions can achieve their steady state values in a relatively short time. An estimate of this time may be made by referring to Figure 5. Assuming first a zero order ionosphere, removal of 90 percent of the plasma (the hole near 273 km) causes a 90 percent depletion in O^+ , NO^+ and O_2^+ . The time required for the molecular ions to return to their steady-state values by the chemistry in Figure 6 is approximately 8 to 9 min. Note that this time is not necessarily the age of the hole because it could have been in steady state longer. Note also that this

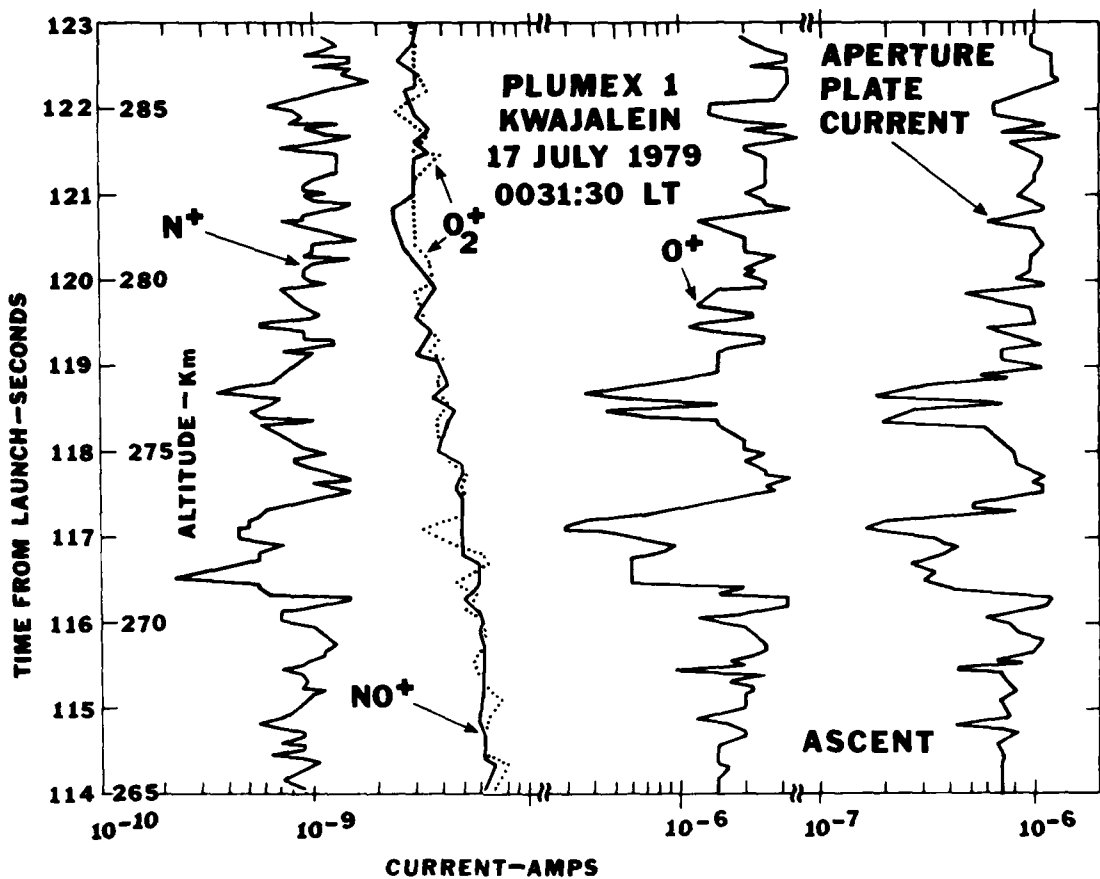


FIGURE 5 AN EXPANDED PLOT OF THE STRONGEST IRREGULARITIES IN THE UPLEG 265 TO 288-km REGION. Note the relatively smooth molecular ion profiles. Meteoric ions were negligible.

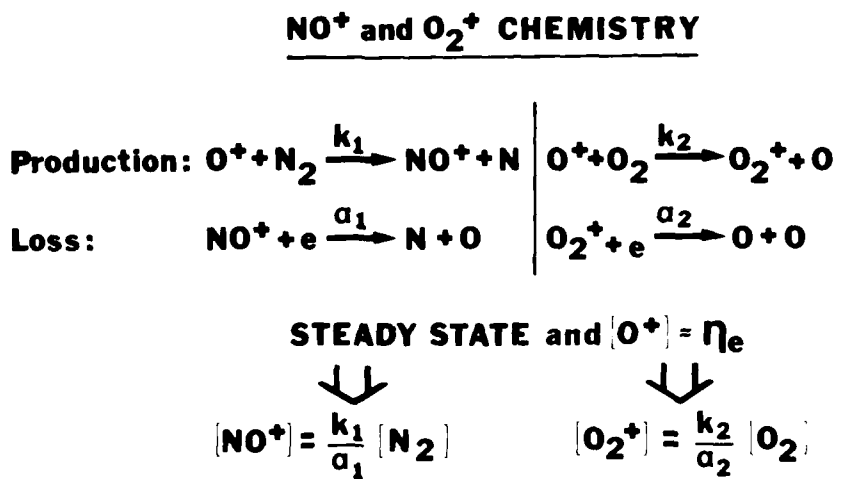


FIGURE 6 F-REGION CHEMISTRY OF NO⁺ AND O₂⁺

time is not necessarily a lower limit on the hole's age because the hole may not have been formed by an abrupt depletion mechanism. However, the NO^+ and O_2^+ distributions do indicate normal, relatively smooth N_2 and O_2 profiles, and this suggests that neutral atmospheric turbulence is not a major source for bottomside ionospheric plasma irregularities.

In Figures 7 and 8 it is shown that the NO^+ and O_2^+ density profiles, and, in particular, the slopes calculated from N_2 and O_2 concentrations taken from the 1976 Standard Atmosphere match rather closely with the measured slopes. From the scale heights determined from slopes fit to the data, an exospheric neutral temperature of $1100 \text{ K} \pm 150 \text{ K}$ is inferred. Not only can the neutral concentrations of N_2 and O_2 be determined from the ion composition measurements but the concentrations of $\text{N}^4(\text{S})$ and NO from the bottomside ion composition can be determined as well.⁵ This latter determination, however, will not be performed here.

Atomic nitrogen ions may perhaps be the more useful species for inferring ionospheric irregularities processes.⁴ In Figure 5, N^+ shows similar irregularity structure as O^+ . The presence of N^+ in this lower altitude range indicates the need for appreciable downward transport of N^+ because there are no significant chemical sources of N^+ at night and N^+ is rapidly destroyed in reactions with O_2 . For example, the lifetimes of N^+ at 250 and 300 km are about 1 and 7 min, respectively. There was indeed a significant downward ionospheric drift of 10 m/s, as indicated by simultaneous radar observations.⁶ Because both chemistry and ionospheric motions play equally important roles, the N^+ distribution can only be calculated properly with a detailed F-region chemical-transport model. However, considering the short lifetimes of N^+ , it is perhaps unlikely that the irregularity structure in Figure 5 is very much greater than ten minutes old.

The N^+ distribution at higher altitudes also presents some interesting features as shown in the N^+/O^+ ratio versus altitude in Figure 9. It is seen that the N^+/O^+ ratio is considerably smaller in the large scale depletions than in the adjacent "zero order" areas. This and the magnitude of the O^+ and N^+ concentrations suggest that the depletions

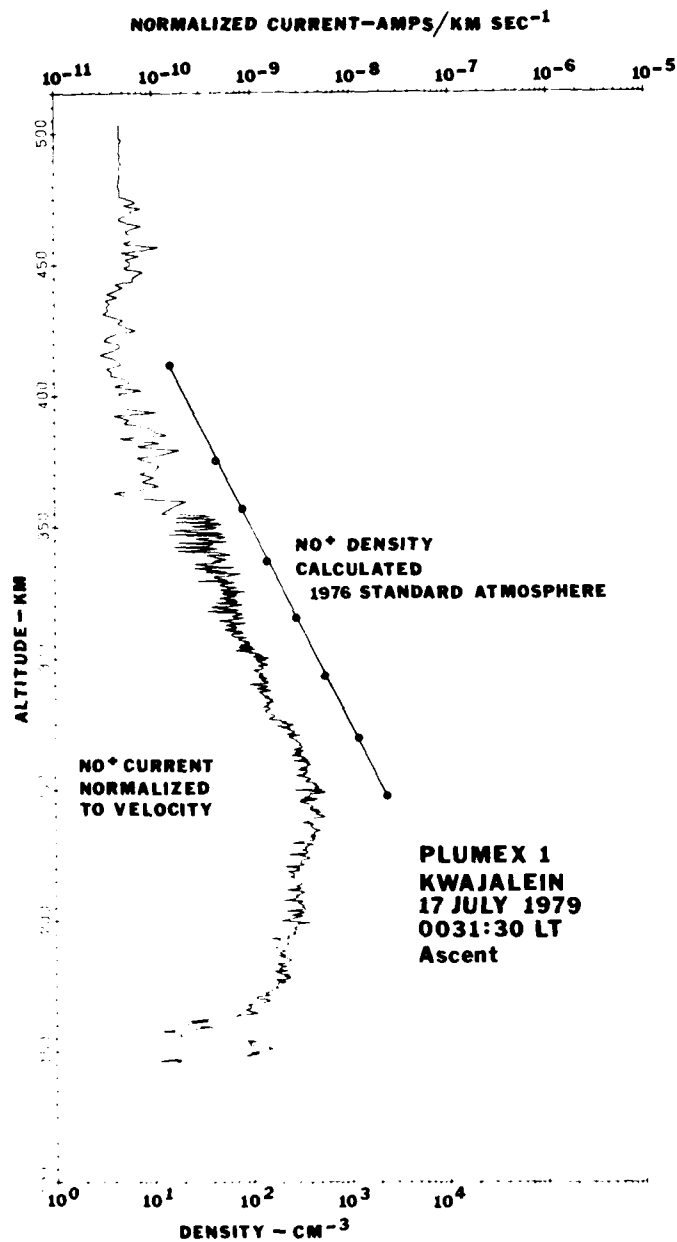


FIGURE 7 A COMPARISON OF THE NORMALIZED NO⁺ CURRENT (PROPORTIONAL TO DENSITY) WITH A CALCULATED NO⁺ DENSITY. The slope yields the N₂ scale height and temperature.

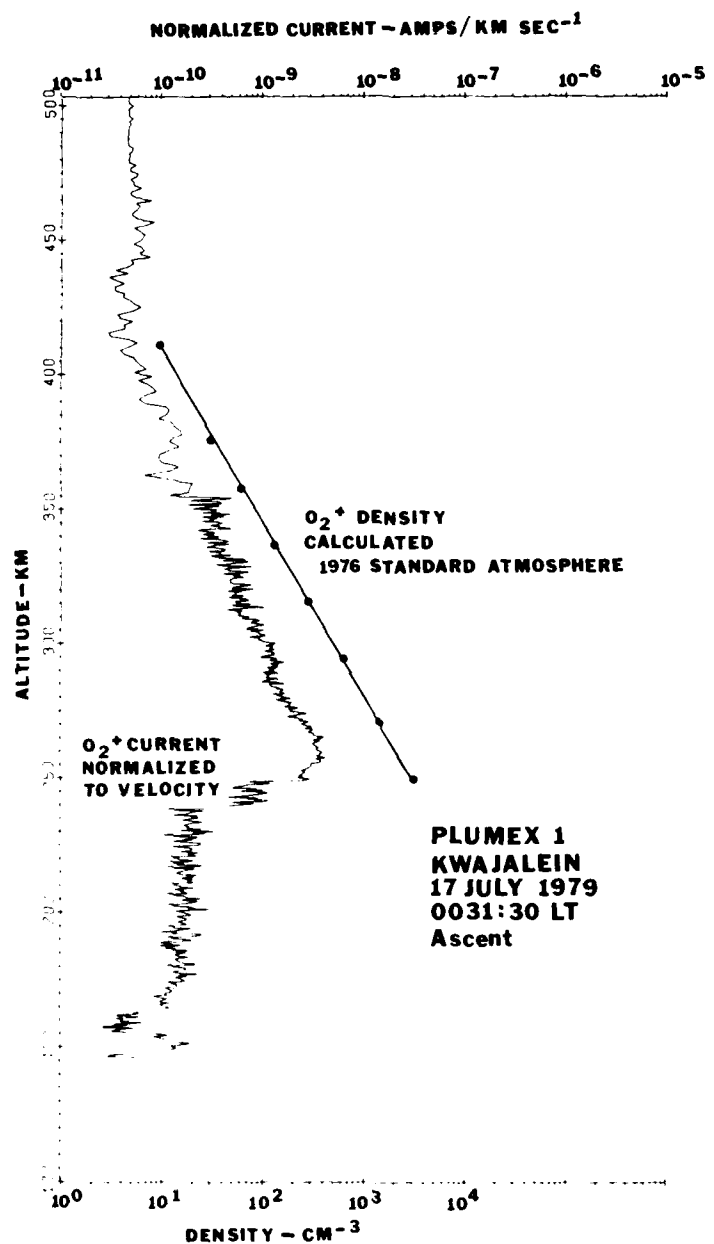


FIGURE 8 A COMPARISON OF THE NORMALIZED O_2^+ CURRENT (PROPORTIONAL TO DENSITY) WITH A CALCULATED O_2^+ DENSITY. The O_2^+ calculated density profile must be reduced by a factor of 1.5 to yield the correct values.

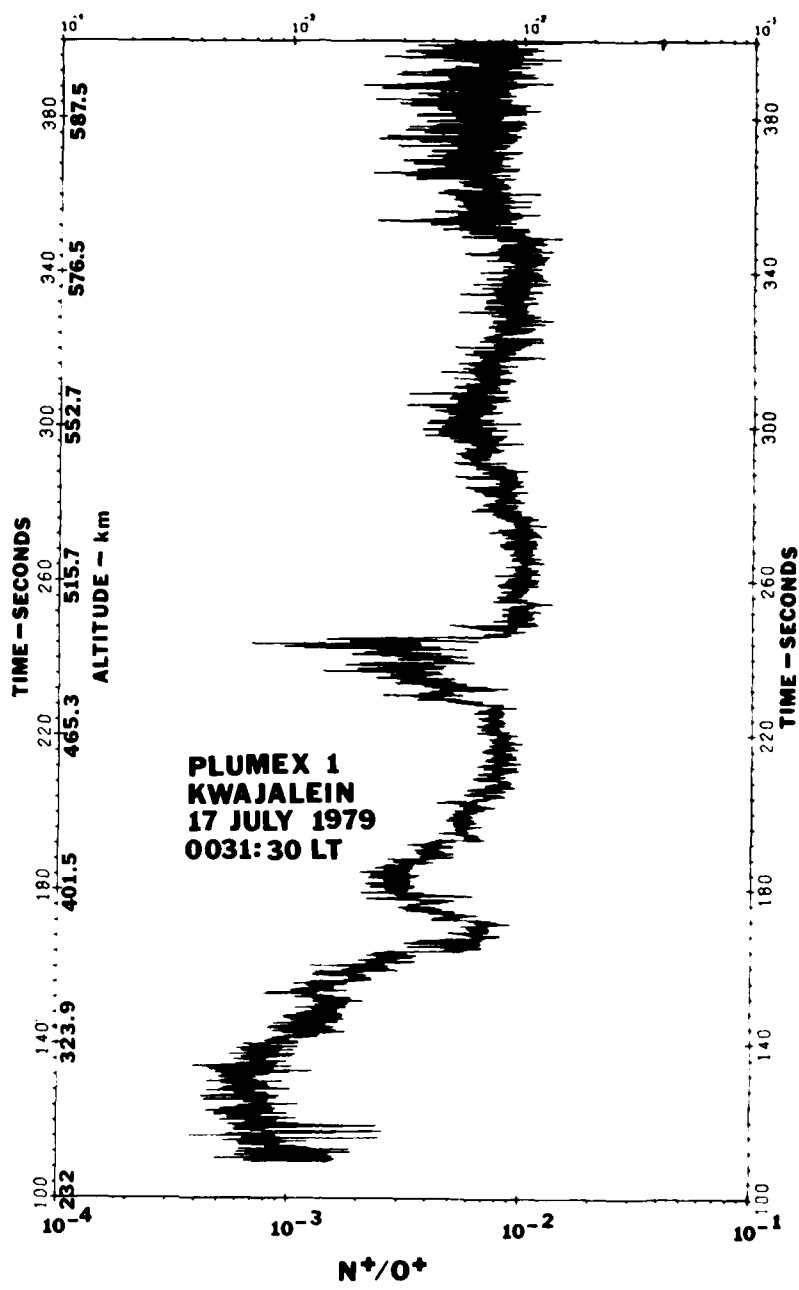


FIGURE 9 THE N^+/O^+ RATIO ON UPLEG DEMONSTRATING THE DIMINISHED RATIOS IN THE HOLES

originated at or near the bottomside region

$$\left[O^+ \right] \approx \left[O^+ \right]$$

hole. The radar data revealed that the large-scale depletion at 475 to 500 km was at nominal altitude for more than 30 min and that its upward rise velocity was essentially zero.⁷ Furthermore, the radar measurements indicated that spread F occurred shortly after ionospheric motion reversal from upward to downward when the F-region ledge was at much higher altitudes.⁷ Thus, although it is still true that the ion composition indicates that the source region of this bubble was at or near the F-region ledge, the ledge was probably at much higher altitudes than 250 km when these bubbles formed. The picture here seems to be that the bubbles are generated somewhat continuously near the ledge and then move upward while the ledge is drifting downward during the night. Our particular rocket launch took place when the irregularities were in the decay phase, which is defined as the period after the upward motion of the depletion has stopped.

If the radar measurements were unavailable and it was presumed that the 475 to 500-km depletion originated near 262 km, where similar O^+ concentrations prevailed, an upper limit of the bubble vertical drift velocity could be calculated by utilizing the source region levels of NO^+ and O_2^+ . The molecular ion concentrations in the source region are not preserved at higher altitudes because of losses by dissociative recombination and a simultaneous loss in production by ion-atom interchange and charge exchange reactions because $[N_2]$ and $[O_2]$ decrease markedly with altitude. The longer it takes a bottomside depletion to move upward, the more likely the elimination of molecular ion signatures when

$$\left[O^+ \right] \approx N_e \gg \left(\left[NO^+ \right] + \left[O_2^+ \right] \right) .$$

In the case of the 475-to-500-km depletion, a vertical transport time somewhat greater than 360 s would account for the molecular ion deficiency. This estimate is based on an instantaneous displacement of the bottomside ion composition to the 475-to-500-km range and a calculation showing that

in about 6 min the molecular ion levels would be comparable to those in the depletion. This time estimate would then suggest an upper limit of about 600 m/s for average vertical drift velocity of the depletion. However, the radar measurements showed the bubble was essentially stationary for some time. Considering the short lifetime of N^+ in the lower-altitude region near 275 km, it is unlikely that the lower-altitude N^+ levels could be maintained if the source region was at this low altitude with the bubble subsequently rising to about 500 km, even if the upward drift velocity was 600 m/s. Further, the $[N^+]$ in the higher-altitude hole is somewhat larger than in the source region $[O^+] \approx [O^+]$ hole. Although the O^+ in the source would be preserved during the upward traversal time, N^+ would not and would certainly show a decay. This all indicates that the source region for the 475-to-500-km hole was indeed at the ledge, but when this ledge was at higher altitudes where the N^+ concentrations could endure. The exact altitude of the ledge also depends on the vertical velocity of the bubble; a faster upward drift means the bubble could have initiated at lower heights.

Meteoric species measured on PLUMEX I are shown in Figure 10. Iron and magnesium ions were present up to 180 km with peak concentrations of up to about 100 ions/cc. Meteoric ions, mainly Mg^+ , were detected at much higher altitudes, but only in concentrations of 5 to 10 ions/cc.

Figure 11 shows the contaminant species, OH^+ (17) and H_2O^+ (18), which were about one percent of the total plasma density. The H_2O^+ ions are produced through the rapid charge transfer reaction of O^+ with H_2O outgassing from the rocket. This had only a very small effect on the ambient species measurements. It is not clear how the OH^+ ion was produced; the O^+ reaction with H_2O to produce OH^+ is slightly endothermic.

Figure 12 presents the NO^+/O_2^+ ratio exhibiting values of 10 to 20 in the F1 region and rapidly decreasing at the ledge to a steady value of 1 ± 0.2 from 260 to 450 km.

Finally, Figure 13 shows the upleg and downleg aperture current measurements. The negative spikes on descent are the N_2 gas bursts from the attitude control system. Note that there are several depletions seen on downleg also and that the ledge is about 25 km lower.

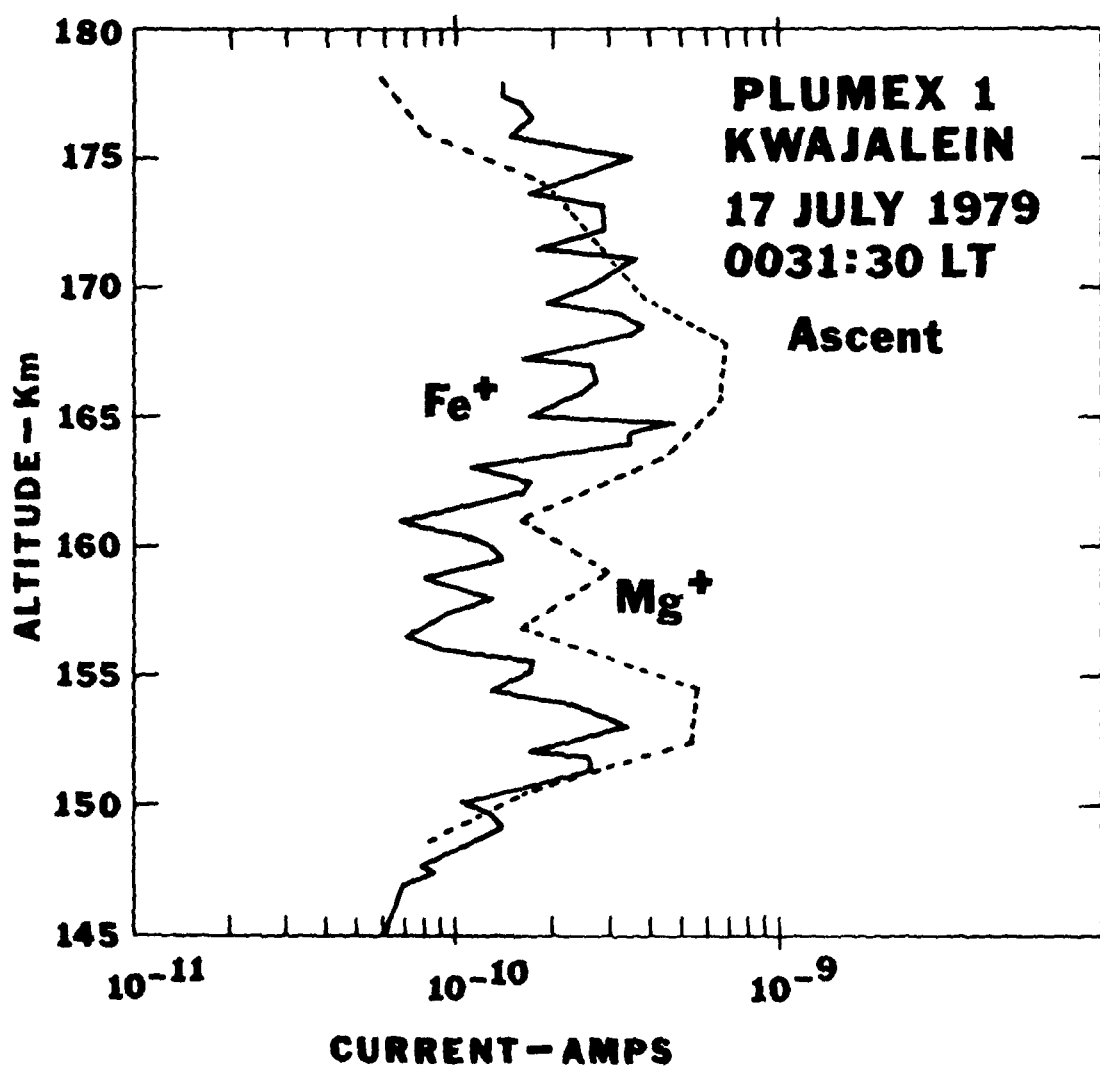


FIGURE 10 METEORIC SPECIES MEASURED ON UPLEG. Mg^+ was also detected at higher altitudes with peak currents in the vicinity of 4×10^{-11} amps.

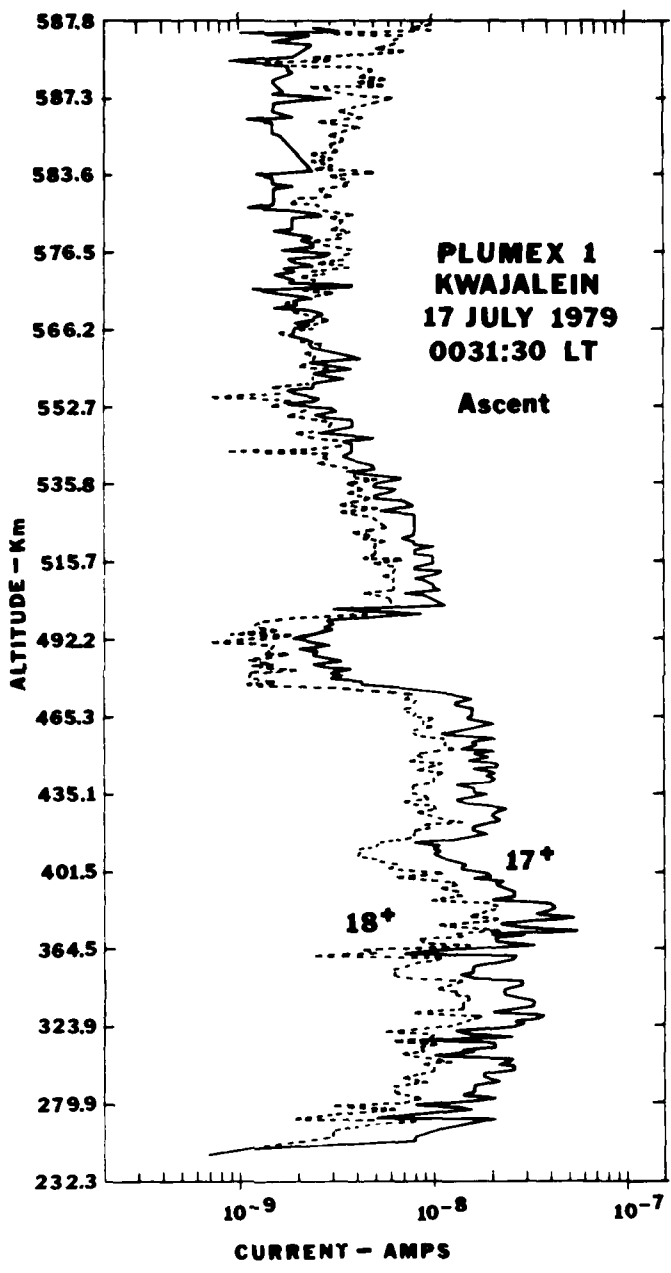


FIGURE 11 CONTAMINANT IONS OF OH^+ AND H_2O^+
MEASURED ON UPLEG

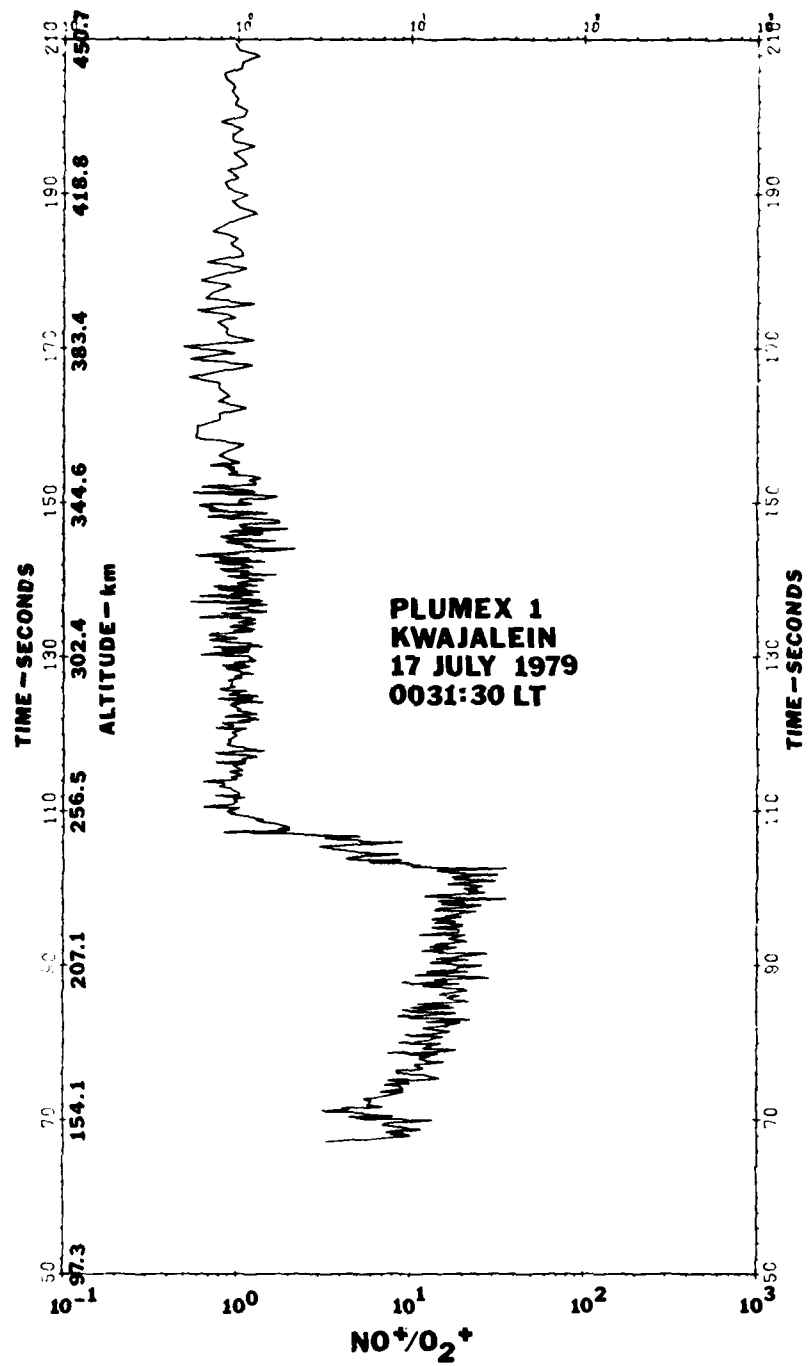


FIGURE 12 THE NO^+/O_2^+ RATIO ON ASCENT

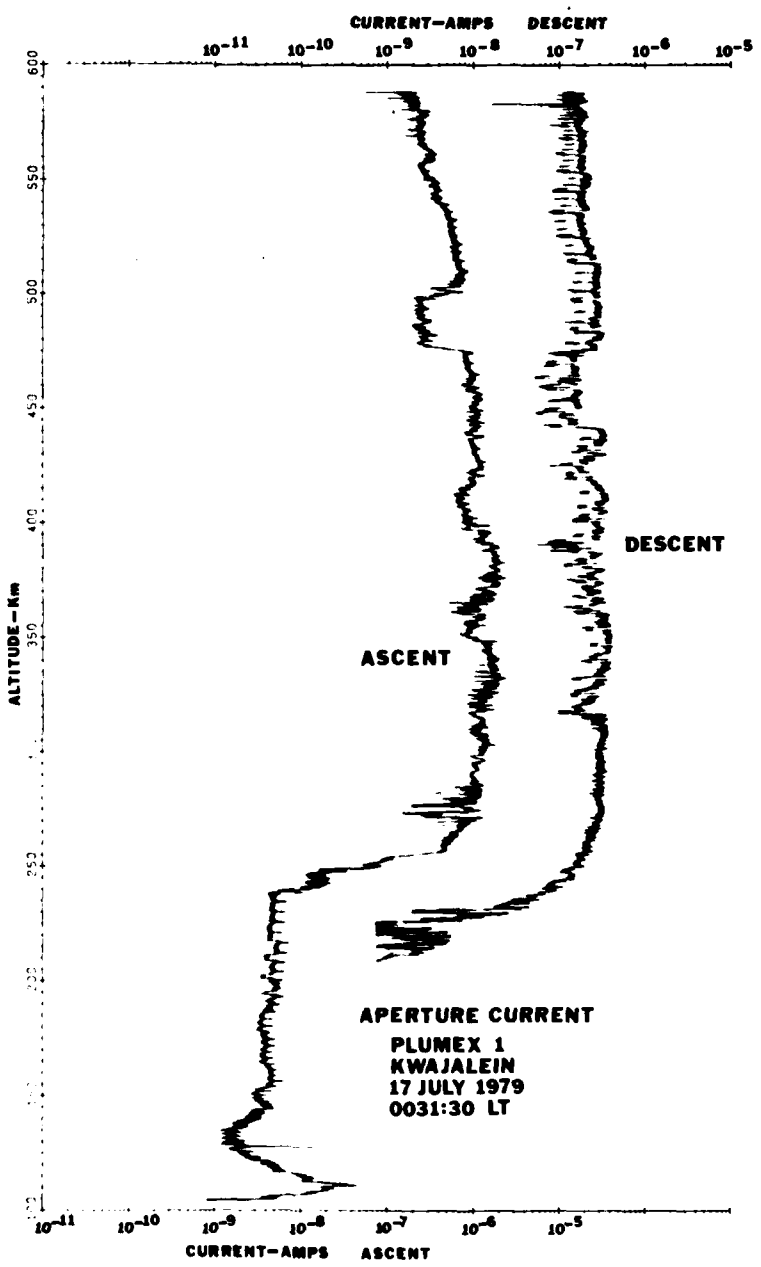


FIGURE 13 A COMPARISON OF THE ASCENT AND DESCENT APERTURE PLATE CURRENT MEASUREMENTS SHOWING SEVERAL DEPLETIONS PENETRATED ON DESCENT

B. PLUMEX II

The PLUMEX II payload was launched six days later and about 2-1/2 hours earlier in the evening. Figure 14 shows the altitude-versus-current ascent measurements of the aperture plate output and the species, O^+ , N^+ , NO^+ and O_2^+ . In this flight the payload did not separate from the rocket motor, which rendered the attitude control system ineffective. The attitude of the vehicle was stable up to 300 km above which the angle of the attack increased and varied causing the modulations in the data. Nevertheless the F-region ledge is now seen to be near 350 to 360 km. If a 10 m/s downward drift was still prevalent, then this ledge would appear near that of PLUMEX I two and one-half hours later, the time of the PLUMEX I launch.

Figure 15 presents the upleg and downleg measurements of the aperture plate current. The irregularities, especially those of smaller scale between 350 and 400 km, cannot be explained entirely by vehicle aspect modulations and are probably real, representative of bottomside spread F. The descent measurements depict a quiet, unperturbed ionosphere.

The meteoric species measured on PLUMEX II are shown in Figure 16. Significant concentrations of iron and magnesium ions are seen in layers up to 260 km, about 80 km higher than PLUMEX I. These species were perhaps moved to higher altitudes by earlier upward ionospheric drift and essentially remained there because the downward motion after ionospheric drift reversal did not last long enough to drag them to lower altitudes.

All these data are still being reduced and analyzed. Descent species measurements, current-density conversions, and removal of the aspect modulation in PLUMEX II remain to be performed. Finally, these data need to be fit to an F-region chemical-transport model from which detailed irregularities processes may be determined.

IV CONCLUSION

A considerable amount of information on ionospheric plumes and processes can be obtained from ion-composition and structure measurements

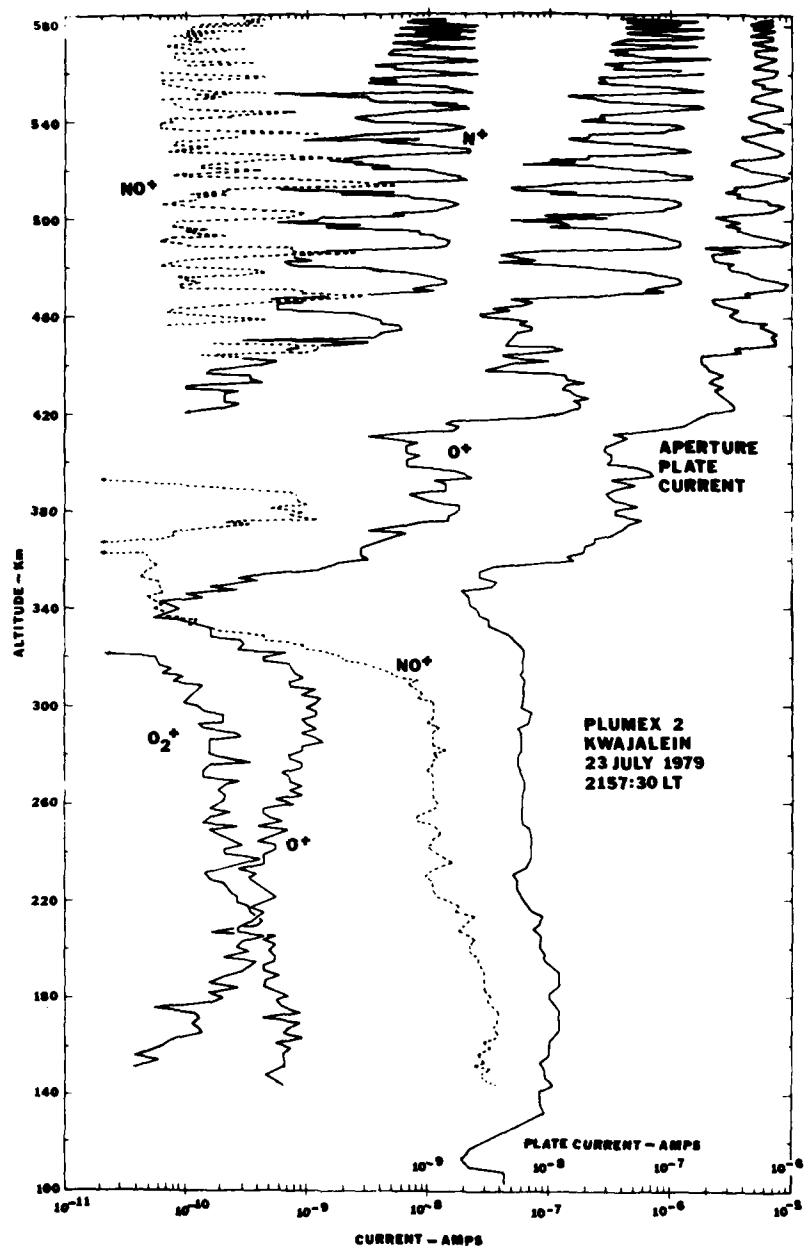


FIGURE 14 ASCENT MEASUREMENTS OF PLUMEX II PRESENTING THE APERTURE PLATE, O^+ , N^+ , NO^+ AND O_2^+ CURRENT PROFILES. Only a portion of the data (points every 0.8 s) was used to generate the profiles. The vehicle became unstable above 300 km, the variations in aspect causing the current modulations.

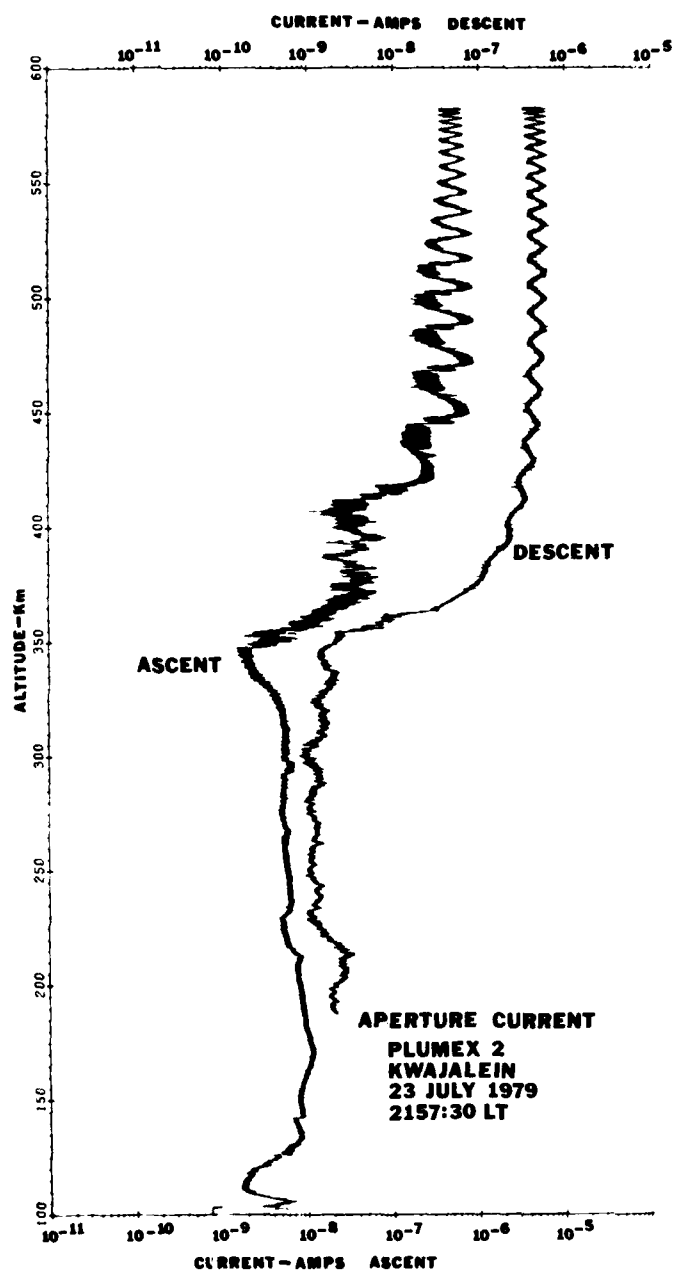


FIGURE 15 A COMPARISON OF THE ASCENT AND DESCENT APERTURE PLATE CURRENT PROFILES. The descent profile depicts a quiescent ionosphere.

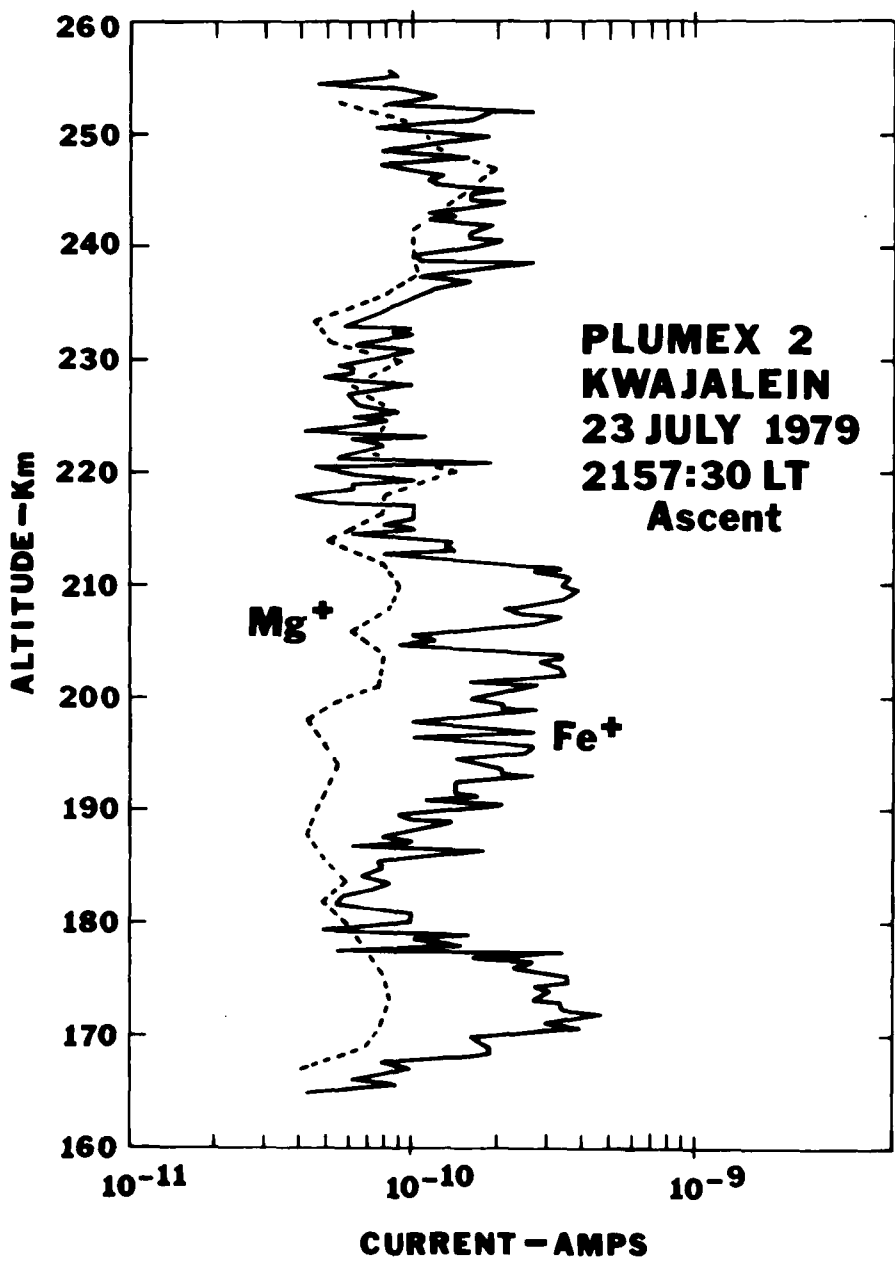


FIGURE 16 METEORIC SPECIES MEASURED ON ASCENT

during such events. Preliminary analysis of the results leads to the following comments and conclusions:

- (a) The measurements clearly demonstrated that not all holes contain enhanced bottomside molecular and metal ion species, indeed none of the holes had such signatures.
- (b) The composition signatures not only proved that the source region of the depletion is at or near the F-region ledge, but also that they can be used to determine the altitude of the ledge at the time of depletion formation.
- (c) Evidence was presented from the molecular ion distributions that showed a stable neutral atmosphere in the simultaneous presence of strong ionospheric fluctuations, suggesting that neutral atmospheric turbulence is not a major source of bottomside plasma irregularities.
- (d) From the ion composition measurements, it is possible to derive N₂, O₂, N(⁴S), and NO neutral concentrations as well as the atmospheric neutral temperature.
- (e) Utilizing the composition measurements and ion chemistry, the limits on bubble lifetimes and rise velocities under certain conditions can be estimated.
- (f) The in-situ measurements along with the radar measurements of ionospheric motions will allow a more detailed determination of ionospheric irregularities processes when coupled to F-region chemical-transport model calculations.

REFERENCES

1. W. B. Hanson and S. Sanatani, "Relationship between Fe⁺ Ions and Equatorial Spread F," J. Geophys. Res., Vol. 76, No. 31, pp. 7761-7768 (November 1971).
2. W. B. Hanson and S. Sanatani, "Large Ni Gradients below the Equatorial F Peak," J. Geophys. Res., Vol. 78, No. 7, pp. 1167-1173 (March 1973).

3. H. C. Brinton, H. G. Mayr, and G. P. Newton, "Ion Composition in the Nighttime Equatorial F-Region: Implications for Chemistry and Dynamics (abstract), EOS Trans. AGU, Vol. 56, No. 12, p. 1038 (December 1975).
4. J. P. McClure, W. B. Hanson, and J. H. Hoffman, "Plasma Bubbles and Irregularities in the Equatorial Ionosphere," J. Geophys. Res., Vol. 82, No. 19, pp. 2650-2656 (July 1977).
5. D. N. Anderson and D. W. Rusch, "Composition of the Nighttime Ionospheric F1 Region Near the Magnetic Equator," J. Geophys. Res., Vol. 85, No. A2, pp. 569-574 (February 1980).
6. E. P. Szuszczewicz, R. T. Tsunoda, R. Narcisi, and J. C. Holmes, "Coincident Radar and Rocket Observations of Equatorial Spread F," Geophys. Res. Lett. (in press, 1980); Proceed. of the Summer Equatorial Experiment Data Review Meeting, 18 March 1980 (1980).
7. R. T. Tsunoda, private communication.

DISTRIBUTION LIST

DEPARTMENT OF DEFENSE

Assistant Secretary of Defense
 Comm, Cmd, Cont & Intell
 ATTN: Dir of Intelligence Sys, J. Babcock

Assistant to the Secretary of Defense
 Atomic Energy
 ATTN: Executive Assistant

Command & Control Technical Center
 ATTN: C-650, G. Jones
 ATTN: C-650
 ATTN: C-312, R. Mason
 3 cy ATTN: C-650, W. Heidig

Defense Communications Agency
 ATTN: Code 480
 ATTN: Code 480, F. Dieter
 ATTN: Code 810, J. Barna
 ATTN: Code 205
 ATTN: Code 101B

Defense Communications Engineer Center
 ATTN: Code R820
 ATTN: Code R410, N. Jones
 ATTN: Code R410, J. McLean
 ATTN: Code R410, R. Craighill
 ATTN: Code R123

Defense Intelligence Agency
 ATTN: DT-5
 ATTN: DB-4C, E. O'Farrell
 ATTN: DB, A. Wise
 ATTN: DT-1B
 ATTN: HQ-TR, J. Stewart
 ATTN: DC-7D, W. Wittig

Defense Nuclear Agency
 ATTN: STNA
 ATTN: RAEE
 ATTN: NATD
 ATTN: NAFO
 2 cy ATTN: RAAE
 4 cy ATTN: TITL
 5 cy ATTN: RAAE

Defense Technical Information Center
 Cameron Station
 12 cy ATTN: DD

Field Command
 Defense Nuclear Agency
 ATTN: FCPR

Field Command
 Defense Nuclear Agency
 Livermore Branch
 ATTN: FCPL

Interservice Nuclear Weapons School
 ATTN: TIV

Joint Chiefs of Staff
 ATTN: C3S, Evaluation Office
 ATTN: C3S

DEPARTMENT OF DEFENSE (Continued)

Joint Strat Tgt Planning Staff
 ATTN: JLA
 ATTN: JLW-2

National Security Agency
 ATTN: W-32, O. Bartlett
 ATTN: B-3, F. Leonard
 ATTN: R-52, J. Skillman

NATO School
 SHAPE
 ATTN: U.S. Documents Officer

Undersecretary of Defense for Rsch & Engrg
 Department of Defense
 ATTN: Strategic & Space Sys (OS)

WWMCCS System Engineering Org
 ATTN: R. Crawford

DEPARTMENT OF THE ARMY

Assistant Chief of Staff for Automation & Comm
 Department of the Army
 ATTN: DAAC-ZT, P. Kenny

Atmospheric Sciences Laboratory
 U.S. Army Electronics R&D Command
 ATTN: DELAS-EO-ME, K. Ballard
 ATTN: DELAS-EO, F. Niles
 ATTN: DELAS-EO-MO, M. Heaps

BMD Advanced Technology Center
 Department of the Army
 ATTN: ATC-T, M. Capps
 ATTN: ATC-O, W. Davies

BMD Systems Command
 Department of the Army
 2 cy ATTN: BMDSC-HW

Deputy Chief of Staff for Ops & Plans
 Department of the Army
 ATTN: DAMO-ROC

Electronics Tech & Devices Lab
 U.S. Army Electronics R&D Command
 ATTN: DELET-ER, H. Bomke

Harry Diamond Laboratories
 Department of the Army
 ATTN: DELHD-N-RB, R. Williams
 ATTN: DELHD-N-P, F. Wimenitz
 ATTN: DELHD-N-P
 ATTN: DELHD-I-TL
 ATTN: DELHD-I-TL, M. Weiner

U.S. Army Comm-Elec Engrg Instal Agency
 ATTN: CCC-CED-CCO, W. Neuendorf
 ATTN: CCC-EMEO-PED, G. Lane

U.S. Army Communications Command
 ATTN: CC-OPS-W
 ATTN: CC-OPS-WR, H. Wilson

DEPARTMENT OF THE ARMY (Continued)

U.S. Army Ballistic Research Labs
ATTN: DRDAR-BLT, J. Vanderhoff
ATTN: DRDAR-BLB, M. Kregel
ATTN: DRDAR-BLP, J. Heimerl
ATTN: DRDAR-TSB-S

U.S. Army Communication R&D Command
ATTN: DRDCO-COM-RY, W. Kesselman

U.S. Army Foreign Science & Tech Ctr
ATTN: DRXST-SD
ATTN: DRXST-SD-3

U.S. Materiel Dev & Readiness Cmd
ATTN: DRCLDC, J. Bender

U.S. Army Missile Intelligence Agency
ATTN: J. Gamble

U.S. Army Missile R&D Command
ATTN: Redstone Scientific Info Ctr

U.S. Army Nuclear & Chemical Agency
ATTN: Library

U.S. Army Research Office
ATTN: R. Mace

U.S. Army Satellite Comm Agency
ATTN: Document Control

U.S. Army TRADOC Sys Analysis Actvty
ATTN: ATAA-TCC, F. Payan, Jr.
ATTN: ATAA-PL
ATTN: ATAA-TDC

White Sands Missile Range
Department of the Army
ATTN: STEWS-TE-AN, M. Squires

DEPARTMENT OF THE NAVY

Joint Cruise Missiles Project
Department of the Navy
ATTN: JCMG-707

Naval Air Development Center
Johnsville
ATTN: Code 6091, M. Setz

Naval Air Systems Command
ATTN: PMA 271

Naval Electronic Systems Command
ATTN: PME-106-13, T. Griffin
ATTN: PME-117-2013, G. Burnhart
ATTN: PME-117-211, B. Kruger
ATTN: Code 501A
ATTN: PME-106-4, S. Kearney
ATTN: Code 3101, T. Hughes
ATTN: PME-117-20
ATTN: ELEX-03

Naval Intelligence Support Ctr
ATTN: Document Control
ATTN: NISC-50

DEPARTMENT OF THE NAVY (Continued)

Naval Ocean Systems Center
ATTN: Code 532
ATTN: Code 532, J. Bickel
ATTN: Code 5322, H. Hughes
ATTN: Code 5322, M. Paulson
ATTN: Code 5321, I. Rothmuller
ATTN: Code 5324, W. Moler
ATTN: Code 4471, Tech Lib
ATTN: Code 532, J. Richter
ATTN: Code 532, R. Pappert
3 cy ATTN: Code 5323, J. Ferguson

Naval Postgraduate School
ATTN: Code 1424, Library

Naval Research Laboratory
ATTN: Code 7120, R. Kinzer
ATTN: Code 4700, T. Coffey
ATTN: Code 7122, D. McNutt
ATTN: Code 7500, B. Wald
ATTN: Code 6790, J. Fedder
ATTN: Code 7101, P. Mange
ATTN: Code 6750, K. Hain
ATTN: Code 7175, J. Johnson
ATTN: Code 7175H, D. Horan
ATTN: Code 1434, E. Brancato
ATTN: Code 7550, J. Davis
ATTN: Code 4701, J. Brown
ATTN: Code 6750, D. Strobel
ATTN: Code 2627
ATTN: Code 4709, W. Ali
2 cy ATTN: Code 4187
5 cy ATTN: Code 4780, S. Ossakow

Naval Space Surveillance System
ATTN: J. Burton

Naval Surface Weapons Center
White Oak Laboratory
ATTN: Code F46, D. Hudson
ATTN: L. Rudlin
ATTN: Code R41, D. Land
ATTN: Code F31

Naval Telecommunications Command
ATTN: Code 341

Nuclear Weapons Tng Group Pacific
Naval Air Station North Island
ATTN: Nuclear Warfare Department

Office of Naval Research
ATTN: Code 421
ATTN: Code 420
ATTN: Code 464, G. Joiner
ATTN: Code 421, B. Junker
ATTN: Code 465

Office of the Chief of Naval Operations
ATTN: OP 65
ATTN: OP 941D
ATTN: OP 981N

Strategic Systems Project Office
Department of the Navy
ATTN: NSP-43
ATTN: NSP-2722, F. Wimberly
ATTN: NSP-2141

DEPARTMENT OF THE AIR FORCE

Aerospace Defense Command
Department of the Air Force
ATTN: DC, T. Long

Air Force Geophysics Laboratory
ATTN: OPR, J. Kennealy
ATTN: LKD, C. Philbrick
ATTN: OPR-1
ATTN: SULL
ATTN: LKB, T. Keneshea
ATTN: LKB, E. Murad
ATTN: LKB, J. Paulson
ATTN: LKB, K. Champion
ATTN: LKB, W. Swider, Jr.
ATTN: LKO, R. Huffman
ATTN: PHG, F. Innes
ATTN: LKO, R. Van Tassel
ATTN: OPR, H. Gardiner
ATTN: OP, J. Garing
ATTN: OPR, A Stair
ATTN: OPR, F. Delgreco
ATTN: PHI, J. Buchau
ATTN: OPR, R. O'Neill
ATTN: OPR, T. Connolly
ATTN: PHP
5 cy ATTN: LKD, R. Narcisi

Air Force Technical Applications Ctr
ATTN: TN
ATTN: TD
ATTN: TF, L. Seiler
ATTN: STINFO Office/TF

Air Force Weapons Laboratory
Air Force Systems Command
ATTN: NTN
ATTN: NTYC
ATTN: SUL
ATTN: DYV, E. Copus

Air Force Wright Aeronautical Lab
ATTN: A. Johnson
ATTN: W. Hunt

Air Logistics Command
Department of the Air Force
ATTN: OO-ALC/MM, R. Blackburn

Air University Library
Department of the Air Force
ATTN: AUL-LSE

Assistant Chief of Staff
Intelligence
Department of the Air Force
ATTN: INED

Assistant Chief of Staff
Studies & Analyses
Department of the Air Force
ATTN: AF/SASC, W. Keaus

Ballistic Missile Office
Air Force Systems Command
ATTN: MNNXH, J. Allen
ATTN: MNNL, S. Kennedy

DEPARTMENT OF THE AIR FORCE (Continued)

Deputy Chief of Staff
Operations Plans and Readiness
Department of the Air Force
ATTN: AFXOKCD
ATTN: AFXOKS
ATTN: AFXOXFD
ATTN: AFXOKT

Deputy Chief of Staff
Research, Development, & Acq
Department of the Air Force
ATTN: AFRDSP
ATTN: AFROSS
ATTN: AFRDS

Electronic System Division
Department of the Air Force
ATTN: DCKC, J. Clark

Electronic Systems Division
Department of the Air Force
ATTN: XRW, J. Deas

Electronic Systems Division
Department of the Air Force
ATTN: YSEA
ATTN: YSM, J. Kobelski

Foreign Technology Division
Department of the Air Force
ATTN: TQTD, B. Ballard
ATTN: NIIS Library
ATTN: WE

Headquarters Space Division
Air Force Systems Command
ATTN: SKA, D. Bolin
ATTN: SKY, C. Kennedy

Headquarters Space Division
Air Force Systems Command
ATTN: YZJ, W. Mercer

Headquarters Space Division
Air Force Systems Command
ATTN: E. Butt

Rome Air Development Center
Air Force Systems Command
ATTN: OCS, V. Coyne
ATTN: OCSA, J. Simons
ATTN: TSLD

Rome Air Development Center
Air Force Systems Command
ATTN: EEP

Strategic Air Command
Department of the Air Force
ATTN: DCXT
ATTN: ADWATE, B. Bauer
ATTN: NRT
ATTN: DCX
ATTN: DCXR, T. Jorgensen
ATTN: XPFS
ATTN: XPFS, B. Stephan

USAFETAC
Department of the Air Force
ATTN: CBTL Stop 825

OTHER GOVERNMENT AGENCIES

Research Director
Bureau of Mines
ATTN: J. Murphy

Central Intelligence Agency
ATTN: OSWR/NED

Department of Commerce
National Bureau of Standards
ATTN: W. Lineberger
ATTN: S. Leone
ATTN: A. Phelps

Department of Commerce
National Bureau of Standards
ATTN: Sec Ofc for R. Hampson, Jr.
ATTN: Sec Ofc for D. Garvin
ATTN: Sec Ofc for S. Abramowitz
ATTN: Sec Ofc for M. Krauss
ATTN: Sec Ofc for M. Scheer
ATTN: Sec Ofc for R. Moore
ATTN: Sec Ofc for J. Cooper
ATTN: Sec Ofc for J. Devoe
ATTN: Sec Ofc for L. Gevantman

Department of Commerce
National Oceanic & Atmospheric Admin
ATTN: L. Machta
ATTN: J. Angell

Department of Commerce
National Oceanic & Atmospheric Admin
ATTN: Assistant Administrator, RD

Department of Commerce
National Oceanic & Atmospheric Admin
ATTN: D. Albritton
ATTN: R. Grubb
ATTN: E. Fergerson
ATTN: F. Fehsenfeld
ATTN: W. Spjeldvik

Department of Transportation
ATTN: F. Marmo

Institute for Telecommunications Sciences
ATTN: W. Utlauf
ATTN: A. Jean
ATTN: L. Berry

NASA
Goddard Space Flight Center
ATTN: S. Bauer
ATTN: Technical Library
ATTN: Code 625, M. Sugiura
ATTN: Code 625, J. Heppner
ATTN: J. Vette
ATTN: A. Aikin

NASA
George C. Marshall Space Flight Center
ATTN: W. Roberts

NASA
ATTN: E. Schmerling
ATTN: N. Roman
ATTN: R. Schiffer

OTHER GOVERNMENT AGENCIES (Continued)

NASA
Johnson Space Center
ATTN: Code JM6, Technical Library

NASA
Ames Research Center
ATTN: W. Starr
ATTN: N-245-3, R. Whitten
ATTN: G. Poppoff

National Science Foundation
ATTN: R. Sinclair
ATTN: Div of Atmos Sci, k. McNeal

U.S. Coast Guard
Department of Transportation
ATTN: G-DOE-3/TP54, B. Romine

DEPARTMENT OF ENERGY CONTRACTORS

Lawrence Livermore National Lab
ATTN: L-71, J. Chang
ATTN: Technical Info Dept Library
ATTN: L-31, R. Hager
ATTN: L-389, R. Ott

Los Alamos National Scientific Lab
ATTN: J. Wolcott
ATTN: MS 668, J. Malik
ATTN: R. Jeffries
ATTN: P. Keaton
ATTN: D. Simons
ATTN: MS 212, W. Barfield
ATTN: R. Taschek
ATTN: MS 560, W. Hughes
ATTN: MS 664, J. Zinn
ATTN: MS 670, J. Hopkins
ATTN: MS 668, H. Hoerlin
ATTN: E. Jones
ATTN: D. Westervelt

Sandia National Laboratories
Livermore Laboratory
ATTN: B. Murphey
ATTN: T. Cook

Sandia National Lab
ATTN: ORG 4241, T. Wright
ATTN: D. Thornbrough
ATTN: D. Dahlgren
ATTN: Space Project Div
ATTN: ORG 1250, W. Brown
ATTN: 3141

DEPARTMENT OF DEFENSE CONTRACTORS

Aero-Chem Research Labs, Inc
ATTN: A. Fontijn

Aerodyne Research, Inc
ATTN: F. Bien
ATTN: Librarian, B. Duston
ATTN: M. Camac
ATTN: M. Faist

Aeronautics Rsch Assoc of Princeton, Inc
ATTN: H. Pergament

DEPARTMENT OF DEFENSE CONTRACTORS (Continued)

Aerospace Corp

ATTN: R. Cohen
ATTN: T. Salmi
ATTN: Library
ATTN: D. Olsen
ATTN: H. Mayer
ATTN: M. Whitson
ATTN: S. Bower
ATTN: N. Stockwell
ATTN: J. Straus
ATTN: R. Slaughter
ATTN: V. Josephson
ATTN: I. Garfunkel

University of Alaska

ATTN: R. Parthasarathy
ATTN: N. Brown
ATTN: Technical Library
ATTN: T. Davis

Analytical Systems Engineering Corp

ATTN: Radio Sciences

Analytical Systems Engineering Corp

ATTN: Security

AVCO Everett Research Lab, Inc

ATTN: C. Von Rosenberg, Jr

Barry Research Corporation

ATTN: J. McLaughlin

BDM Corp

ATTN: T. Neighbors
ATTN: L. Jacobs

Berkley Research Associates, Inc

ATTN: C. Prettie
ATTN: J. Workman

Betac

ATTN: J. Hirsch

Boeing Co

ATTN: G. Hall
ATTN: S. Tashird
ATTN: M/S 42-33, J. Kennedy

Boeing Co

ATTN: D. Clauson

Booz-Allen & Hamilton, Inc

ATTN: B. Wilkinson

Boston College

ATTN: Chairman Dept of Physics
ATTN: Dept of Chemistry, D. McFadden
ATTN: Science Library, F. McElory

University of California at San Diego

ATTN: H. Booker
ATTN: D. Miller

University of California at Santa Barbara

ATTN: M. Steinberg

California Institute of Technology

ATTN: V. Anicich
ATTN: S. Trajmar

DEPARTMENT OF DEFENSE CONTRACTORS (Continued)

University of California

ATTN: H. Johnston

Calspan Corp

ATTN: C. Treanor
ATTN: Library
ATTN: W. Wurster

Charles Stark Draper Lab, Inc

ATTN: D. Cox
ATTN: J. Gilmore

Chem Data Research

ATTN: K. Schofield

University of Colorado

ATTN: V. Bierbaum

Columbia University

ATTN: H. Foley

Computer Sciences Corp

ATTN: C. Nail
ATTN: J. Spoor
ATTN: H. Blank

Comsat Labs

ATTN: R. Taur
ATTN: G. Hyde

Cornell University

ATTN: D. Farley, Jr
ATTN: M. Kelley

University of Denver

ATTN: B. Van Zyl
ATTN: D. Murcay

EG&G, Inc

ATTN: P. Lucero
ATTN: D. Wright
ATTN: J. Colvin

Electrospace Systems, Inc

ATTN: H. Logston
ATTN: P. Phillips

Epsilon Labs, Inc

ATTN: C. Accardo

ESL, Inc

ATTN: W. Bell
ATTN: J. Marshall

General Electric Co

Space Division
ATTN: M. Linevsky
ATTN: A. Harcar
ATTN: R. Edsall
ATTN: J. Burns
ATTN: P. Zavitsanos
ATTN: M. Bortner
ATTN: J. Peden

General Electric Co

Re-Entry Systems Division
ATTN: C. Zierdt
ATTN: A. Steinmayer

DEPARTMENT OF DEFENSE CONTRACTORS (Continued)

General Electric Co
ATTN: F. Reibert

General Electric Co
Corporate Research & Development Ctr
ATTN: J. Schroeder

General Electric Tech Service Co, Inc
Electronic Park
ATTN: G. Millman

General Research Corp
Santa Barbara Division
ATTN: J. Ise, Jr.
ATTN: J. Garbarino

General Research Corp
ATTN: T. Zakrzewski

Horizons Technology, Inc
ATTN: R. Kruger

Howard University
ATTN: W. Jackson

HSS, Inc
ATTN: D. Hansen
ATTN: M. Shuler

IBM Corp
ATTN: F. Ricci

University of Illinois
ATTN: Security Supervisor for K. Yen

Information Science, Inc
ATTN: W. Dudziak

Institute for Defense Analyses
ATTN: H. Wolfhard
ATTN: E. Bauer
ATTN: J. Bengston
ATTN: J. Aein

International Tel & Telegraph Corp
ATTN: Technical Library
ATTN: G. Wetmore

ION Physics Corp
ATTN: C. Hauer

IRT Corp
ATTN: R. Overmyer
ATTN: R. Neynaber
ATTN: D. Vroom
ATTN: J. Rutherford

JAYCOR
ATTN: J. Sperling

JAYCOR
ATTN: J. Doncarlos

Johns Hopkins University
ATTN: P. Komiske
ATTN: T. Potemra
ATTN: T. Evans
ATTN: J. Newland
ATTN: J. Phillips

DEPARTMENT OF DEFENSE CONTRACTORS (Continued)

John Hopkins University
ATTN: J. Kaufman

Kaman Sciences Corp
ATTN: D. Foxwell
ATTN: W. Rich

Kaman TEMPO
ATTN: M. Dudash
ATTN: M. Stanton
ATTN: D. Reitz
ATTN: D. Chandler
ATTN: J. Thompson
ATTN: W. Knapp
ATTN: T. Stephens
ATTN: W. McNamara
ATTN: B. Gambill
ATTN: DASIAC

KMS Fusion, Inc
ATTN: Library

Linkabit Corp
ATTN: I. Jacobs

Litton Systems, Inc
ATTN: R. Grasty

Lockheed Missile & Space Co, Inc
ATTN: D. Divis

Lockheed Missiles & Space Co, Inc
ATTN: J. Evans
ATTN: J. Kumer
ATTN: M. Walt
ATTN: R. Johnson
ATTN: R. Gunton
ATTN: R. Sears
ATTN: W. Imhof
ATTN: J. Reagan
ATTN: T. James
ATTN: B. McCormac

Lockheed Missiles & Space Co, Inc
ATTN: D. Churchill
ATTN: Dept 60-12

University of Lowell
ATTN: G. Best

M.I.T. Lincoln Lab
ATTN: D. Towle
ATTN: B. Watkins
ATTN: L. Loughlin

M.I.T. Lincoln Lab
2 cy ATTN: R. Miller

Martin Marietta Corp
ATTN: R. Heffner

University of Maryland
ATTN: Chemistry Dept, J. Vanderslice

University of Massachusetts
ATTN: H. Sakai

DEPARTMENT OF DEFENSE CONTRACTORS (Continued)

McDonnell Douglas Corp
ATTN: J. Moule
ATTN: W. Olson
ATTN: Technical Library Services
ATTN: G. Mroz
ATTN: N. Harris
ATTN: R. Halprin

Meteor Communications Consultants
ATTN: R. Leader

University of Minnesota
ATTN: J. Winkler

University of Minnesota
Morris Campus
ATTN: M. Hirsch

Mission Research Corp
ATTN: V. Van Lint
ATTN: D. Archer
ATTN: Tech Library
ATTN: F. Fajen
ATTN: M. Schiebe
ATTN: M. Messier
ATTN: R. Hendrick
ATTN: R. Bogusch
ATTN: D. Sappenfield
ATTN: R. Kilb
ATTN: W. White
ATTN: S. Gutsche

Mitre Corp
ATTN: C. Callahan
ATTN: B. Adams
ATTN: G. Harding
ATTN: A. Kymmel

Mitre Corp
Westagate Research Park
ATTN: W. Hall
ATTN: M. Horrocks
ATTN: W. Foster
ATTN: J. Wheeler

National Academy of Sciences
ATTN: J. Sievers

State University of New York at Buffalo
ATTN: G. Brink

Nichols Research Corp, Inc
ATTN: N. Byrn

Pacific-Sierra Research Corp
ATTN: F. Thomas
ATTN: E. Field, Jr
ATTN: H. Brode

Panametrics, Inc
ATTN: B. Sellers

Pennsylvania State University
ATTN: L. Hale
ATTN: J. Nisbet

Pennsylvania State University
Ionosphere Research Lab
ATTN: Ionospheric Research Lab

DEPARTMENT OF DEFENSE CONTRACTORS (Continued)

Photometrics, Inc
ATTN: I. Kofsky

Physical Dynamics, Inc
ATTN: E. Fremouw

Physical Science Lab
ATTN: W. Berning

Physical Sciences, Inc
ATTN: K. Wray
ATTN: G. Caledonia
ATTN: R. Taylor

University of Pittsburgh
ATTN: W. Fite
ATTN: F. Kaufman
3 cy ATTN: M. Biondi

Quantum Systems, Inc
ATTN: S. Ormonde

R & D Associates
ATTN: R. Turco
ATTN: M. Gantsweg
ATTN: R. Lelevier
ATTN: F. Gilmore
ATTN: W. Karzas
ATTN: W. Wright
ATTN: C. Greifinger
ATTN: H. Ory
ATTN: B. Gabhard
ATTN: P. Haas

R & D Associates
ATTN: J. Rosengren
ATTN: L. Delaney
ATTN: B. Yoon

Radiation Research Associates, Inc
ATTN: N. Schaeffer

Rand Corp
ATTN: E. Bedrozian
ATTN: C. Crain

Riverside Research Institute
ATTN: V. Trapani

Rockwell International Corp
ATTN: R. Buckner

Rockwell International Corp
Collins Telecommunications Sys Div
ATTN: S. Quilici

Santa Fe Corp
ATTN: D. Paolucci

Science Applications, Inc
ATTN: C. Smith
ATTN: D. Hamlin
ATTN: E. Straker
ATTN: L. Linson

Science Applications, Inc
ATTN: N. Byrn

DEPARTMENT OF DEFENSE CONTRACTORS (Continued)

Science Applications, Inc
ATTN: R. Johnston

Science Applications, Inc
ATTN: SZ

Science Applications, Inc
ATTN: J. Cockayne

University of Illinois
ATTN: S. Bowhill
ATTN: C. Sechrist

SRI International
ATTN: V. Gonzales
ATTN: R. Hake, Jr
ATTN: W. Chesnut
ATTN: T. Slanger
ATTN: R. Leadabrand
ATTN: G. Price
ATTN: A. Burns
ATTN: G. Smith
ATTN: G. Black
ATTN: A. Peterson
ATTN: V. Wickwar
ATTN: W. Jaye
ATTN: M. Baron
ATTN: D. Hildenbrand
ATTN: D. Neilson
ATTN: E. Kindermann
ATTN: J. Peterson
ATTN: A. Whitson
ATTN: J. Moseley
2 cy ATTN: R. Tsunoda
2 cy ATTN: C. Rino
2 cy ATTN: J. Petrickes
2 cy ATTN: R. Livingston
10 cy ATTN: D. McDaniels

SRI International
ATTN: C. Hulbert

Sylvania Systems Group
ATTN: M. Cross

Technology International Corp
ATTN: W. Boquist

DEPARTMENT OF DEFENSE CONTRACTORS (Continued)

University of Texas System
ATTN: J. Browne

TRI-Com, Inc
ATTN: D. Murray

TRW Defense & Space Sys Group
ATTN: J. Frichtenicht
ATTN: Technical Information Center
ATTN: R. Plebuch
ATTN: D. Dee

Utah State University
ATTN: L. Jensen
ATTN: J. Dupnik
3 cy ATTN: K. Baker

University of Virginia
ATTN: R. McKnight
ATTN: R. Ritter
ATTN: H. Kelly

Visidyne, Inc
ATTN: H. Smith
ATTN: J. Carpenter
ATTN: T. Degges
ATTN: O. Manley
ATTN: C. Humphrey

University of Washington
ATTN: Physics FM15, K. Clark

Wayne State University
ATTN: R. Kummier
ATTN: P. Rol

Westinghouse Electric Corp
ATTN: P. Chantry

William Marsh Rice University
ATTN: R. Stebbings

William Marsh Rice University
ATTN: J. Chamberlain

